Study of dry sliding wear characteristics of boron carbide and ilmenite mineral reinforced AMCs

A Dissertation Submitted
In Partial Fulfillment of the Requirements
for the Degree of

Doctor of Philosophy

Submitted by

Rahul Gupta
Regd. No. 901708019

Under the guidance of

Dr. Tarun Nanda
Professor,
MED, TIET, Patiala

Dr. O. P. Pandey
Senior Professor,
SPMS, TIET, Patiala

Mechanical Engineering Department
Thapar Institute of Engineering and Technology
(Deemed to be University), Patiala
September, 2023

CERTIFICATE

Certified that the work presented in the thesis entitled **"Study of dry sliding wear characteristics of boron carbide and ilmenite mineral reinforced AMCs"** being submitted by Mr Rahul Gupta (Regd. No. 901708019) in fulfilment of the requirements for the award of the degree of 'Doctor of Philosophy' in the Department of Mechanical Engineering, Thapar Institute of Engineering and Technology, Patiala, is an authentic record of the candidate's own work carried out during the period from January, 2018 to May, 2023 at this institute under my supervision. The matter presented in this dissertation has not been submitted for the award of any other degree in any university.

20/9/23

Dr. Tarun Nanda
Professor,
MED, TIET, Patiala

20/09/23

Dr. O. P. Pandey
Senior Professor,
SPMS, TIET, Patiala

DECLARATION

I hereby certify that the work which is being presented in this thesis, entitled "**Study of dry sliding wear characteristics of boron carbide and ilmenite mineral reinforced AMCs",** in the fulfilment of the requirements for the award of degree of 'Doctor of Philosophy' in Mechanical Engineering submitted to the Department of Mechanical Engineering of Thapar Institute of Engineering and Technology (Deemed to be University), Patiala is an authentic record of my own work carried out under the supervision of Dr. Tarun Nanda, Professor, Mechanical Engineering Department, Thapar Institute of Engineering and Technology, Patiala and Dr. O. P. Pandey, Senior Professor, School of Physics and Materials Science, Thapar Institute of Engineering and Technology, Patiala.

The matter presented in this dissertation has not been submitted in part or full to any other university or institute for the award of any degree in India or abroad.

Rahul Gupta

Rahul Gupta

ACKNOWLEDGEMENT

First of all, I would like to express my gratitude to my supervisors Dr. Tarun Nanda, Professor, Mechanical Engineering Department, Thapar Institute of Engineering and Technology, Patiala and Dr. O. P. Pandey, Senior Professor, School of Physics and Materials Science, Thapar Institute of Engineering and Technology, Patiala for their invaluable guidance, moral support and encouragement during the entire period of this research which cannot adequately be expressed in words in this acknowledgement.

I would like to extend my acknowledgment to my doctoral committee member Dr. Kishore Khanna, Dr. H. L. Bhowmick, and Dr. R. K. Gupta for their feedback. I am very much grateful to my friends Dr. Bhupinder Singh, Manpreet Singh, Ashutosh Bist, Rajat Kumar, Deepak Sharma, Hitesh Mittal, Ayush Singla, and Navneet Goyal for their help and support.

I would like to thank my seniors Dr. Sandeep Sharma, Dr. Suresh Kumar, and Dr. Karanbir Singh and my fellow PhD scholars Dr. Daksh Shelly, Dr. Vikas Deep Mann, Dr. Sandeep Bansal, Pushpinder Kumar, and Sachin Jaidka who provided a great support during my dissertation writing.

I would like to thank my parents, Sh. Mohan Lal and Smt. Sunita Rani whose consistent love and support motivated me throughout the period of research. I would also like to thank my brother, Er. Raman Gupta for his understanding, patience and valuable support which helped me in achieving the goal.

Above all, I thank almighty whose blessings have enabled me to accomplish this research work.

Rahul Gupta

Rahul Gupta

LIST OF PUBLICATIONS

PUBLICATIONS RELATED TO PRESENT WORK:

- ***Rahul Gupta**, Tarun Nanda, O.P. Pandey (2021) Comparison of wear behaviour of LM13 Al−Si alloy based composites reinforced with synthetic (B_4C) and natural (ilmenite) ceramic particles. Transactions of Nonferrous Metals Society of China 31(12), 3613–3625.* ***Impact Factor 3.752***
- ***Rahul Gupta**, Tarun Nanda, O.P. Pandey (2022) Effect of high operating temperatures on the wear characteristics of boron carbide and ilmenite reinforced LM13 alloy-based composites. Journal of Tribology 144(10), 101703.* ***Impact Factor 1.891***
- ***Rahul Gupta**, Tarun Nanda, O.P. Pandey (2023) Tribological properties of hybrid aluminium matrix composites reinforced with boron carbide and ilmenite particles for brake rotor applications. Archives of Civil and Mechanical Engineering 23, 47* ***Impact Factor 4.257***
- ***Rahul Gupta**, Tarun Nanda, O.P. Pandey (2023) Tribological characteristics of LM13 alloy based ilmenite-boron carbide reinforced hybrid composites for brake drum applications. Wear, 522, 204851.* ***Impact Factor 4.695***

OTHER PUBLICATIONS:

- ***Rahul Gupta**, Sandeep Sharma, Tarun Nanda, O.P. Pandey (2020) Wear studies of hybrid AMCs reinforced with naturally occurring sillimanite and rutile ceramic particles for brake-rotor applications. Ceramics International 46(10B), 16849–16859.* ***Impact Factor 5.532***
- ***Rahul Gupta**, Sandeep Sharma, Tarun Nanda, O.P. Pandey (2020) A comparative study of dry sliding wear behaviour of sillimanite and rutile reinforced LM27 aluminium alloy composites. Materials Research Express. 7(1), 016540.* ***Impact Factor 2.025***
- *Sandeep Sharma,* ***Rahul Gupta**, Tarun Nanda, O.P. Pandey (2021) Influence of two different range of sillimanite particle reinforcement on tribological characteristics of LM30 based composites under elevated temperature conditions. Materials Chemistry and Physics 258, 123988.* ***Impact Factor 4.778***

ACRONYMS AND SYMBOLS

MMC = Metal matrix composite

AMC = Aluminium matrix composite

HAMC = Hybrid metal matrix composites

Wt.% = Weight percentage

SPS = Single particle size

DPS = dual particle size

SEM = Scanning electron microscopy

EDS = Energy dispersion spectroscopy

℃ = Degree celsius

% = Percentage

Kg = Kilogram

Rpm = Revolution per minute

Min. = Minute

BHN = Brinell hardness number

ANOVA = Analysis of variance

µ = Micro

COF = Coefficient of friction

AFM = Atomic force microscopy

XRD = X-ray powder diffraction

VHN, HV = Vickers hardness number

EDAX/EDX = Energy dispersion X-ray analysis

ANN = Artificial neural network

TOPSIS = Technique for order performance by similarity to ideal solution

UTS = Ultimate tensile strength

RSM = Response surface methodology

CTE = Coefficient of thermal expansion

MML = Mechanical mixed layer

SWR = Specific wear rate

ARB = Accumulative roll bonding

MA = Mechanically alloying

TEM = Transmission Electron Microscope

SAD = Selected area diffraction

UCS = Ultimate compression strength

FEM = Finite element method

vol.% = Volume percentage

α = Alpha

R_a = Roughness value

F = Applied load

v = Sliding velocity

a = Constant

T_o = Constant

AT = Ambient temperature condition

λ = Lattice misfit

d_r = d spacing of reinforced particle

d_b = d spacing of base alloy

DD = Dislocation density

b = Burgers vector

V_H = Volume Fraction

GND = Geometrically necessary dislocations

ABSTRACT

Dry sliding wear behaviour of stir-cast aluminium matrix composites (AMCs) containing LM13 alloy as matrix and synthetic ceramic particles and mineral particles as reinforcements was investigated at room temperature as well as at high temperature operating conditions. Particles were reinforced in three different ways viz. (a) only synthetic ceramic particles (boron carbide; B_4C), (b) only mineral particles (ilmenite; $FeTiO_3$), and (c) combination of synthetic and mineral particles in various mixing proportions. Composites processed using these reinforcements were designated as 'BR' composites, 'IR' composites, and 'BI' composites respectively. Particle size for both types of reinforcements was categorized into two classes viz. (a) 'fine' and (b)'coarse' whose range was 20–32 µm and 106–125 µm respectively. For each particle size, the weight percentage of reinforcement was varied from 0–15 wt.%, with a step size of 5 wt.%. For combination of synthetic and mineral particles, reinforcements with same particle size were mixed in three different weight proportions of 1:3, 1:1, and 3:1.

For processing of AMCs, the base alloy (LM13) was melted in the stir casting set-up using an electric furnace maintained at 700 ℃. Ceramic particles to be reinforced were pre-heated in another electric furnace maintained at 450 ℃ to eliminate moisture or volatile matter (if present) from the particles. Before addition of pre-heated particles, a vortex was developed in the molten mass by using a three-blade graphite stirrer. Uniform stirring at 625 rpm was maintained for 10 min. Thereafter, the required amount of particles (wt.%) was added to the molten mass by reducing the stirring speed to 250 rpm. Again, stirrer speed was maintained at 625 rpm for 10 min. Finally, molten mass was poured in a cast iron mould to allow cooling till room temperature.

SEM images of ball milled reinforced particles were used to obtain the average particle size whereas EDS was used to obtain the elemental composition of reinforcements. For boron carbide particles, the average particle size of 'fine' and 'coarse' categories was 25.52±3.48 µm and 115.64±5.70 respectively. For ilmenite particles, the average particle size for 'fine' and 'coarse' categories was 25.24±2.85 µm and 116.60±5.72 µm respectively. EDS analysis confirmed 100% purity of both the reinforcements after ball milling process. XRD analysis of 'IR' composites showed presence of silicon oxide (SiO_2), iron oxide (FeO), and titanium-silicon ($TiSi_2$) phases. These phases were formed due to interfacial reaction between ilmenite and silicon of base alloy. In hybrid composites, ilmenite particles caused a transition in phases in the presence of boron carbide particles leading to formation of iron oxide (Fe_3O_4), silicon

oxide (SiO_2), and titanium oxide (TiO). The formation of interfacial products resulted in strong interfacial bonding between ilmenite and matrix material. Reinforced particles were also responsible for reduction in crystallite size and rise in crystallinity. Relatively lower crystallite size and higher crystallinity were obtained on addition of boron carbide particles in comparison to ilmenite particles. Similar results were obtained with reduction in particle size from 'coarse' to 'fine'. Optical micrographs of 'BR' composites, 'IR' composites, and 'BI' composites showed uniform dispersion of reinforced particles in the matrix material. Reinforced particles refined the eutectic silicon grain size (of matrix material) and changed its morphology from acicular to globular type. Increase in reinforcement level and reduction in particle size decreased the grain size for all the composites. Out of 'BR' and 'IR' composites, lower grain size was obtained for 'BR' composites. Further, for hybrid AMCs, increase in concentration of boron carbide in the reinforcement mixture resulted in lower grain size ('15FBI-31' composite showed the lowest grain size).

For room temperature conditions, hardness of AMCs showed an increasing trend with rise in reinforcement level and reduction in particle size. For the case of individual reinforcements (single particle reinforced AMCs), maximum increase in hardness was obtained for '15FBR' composite and '15FIR' composite which was 41.07% and 34.77% higher than the base alloy. In case of 'BI' hybrid composites (dual particle reinforced composites) also, rise in reinforcement level resulted in higher hardness. At 15 wt.%, the hardness of '15FBI-31' composite showed an increase of 39.87% over the base alloy. Increase in hardness of AMCs was attributed to increase in plastic deformation of the matrix material and rise in dislocation density in AMCs in the presence of reinforced particles. Coefficient of thermal expansion (CTE) showed reduction with increase in reinforcement level, both for single particle as well as hybrid AMCs. For any increase in temperature over the entire range (50–300 ℃), CTE values showed an increasing trend for 'IR' and 'BI' composites. For 'BR' composites, CTE values showed an increasing trend till 100 ℃ beyond which values started decreasing. This variation in CTE was attributed to increase in solubility of silicon in aluminium of base alloy under the presence of boron carbide particles. For a particular combination of reinforcements in hybrid AMCs, highest reduction in CTE value was obtained at higher level of reinforcement (15 wt.%), with 'fine' particles of reinforcement, and with higher content of boron carbide in the reinforcement mixture (B_4C:$FeTiO_3$ wt.% equal to 3:1). Maximum improvement in CTE of '15FBR', '15FIR', and '15FBI-31' composites was 49.67%, 60.02%, and 55.18%, respectively (over the base alloy). Dry sliding wear behaviour of 'BR', 'IR', and 'BI' composites significantly improved over the base alloy under room temperature conditions. In the context

of individual reinforcements, addition of boron carbide particles helped in providing increased stability to the mechanical mixed layer. The low thermal conductivity of ilmenite particles resulted in early oxidation and provided a protective layer on the surface of composites. So, both types of reinforcements led to improvement in wear characteristics of AMCs, though the mechanisms involved were very different. The wear rate of '15FBR', '15FIR', and '15FBI-31' composites showed a maximum improvement of 61%, 52%, and 90% over the base alloy. Comparison of '15FBI-31' composite with the commercially used brake rotor material under room temperature conditions showed superior wear behaviour (14% lower wear rate), lower processing cost, and lower materials cost. These characteristics make the developed composites a suitable substitute for commercial material being used for brake rotor applications (under ambient conditions). With regards to coefficient of friction (COF) values, lower values were obtained on addition of ilmenite particles (i.e. 'IR' composites). COF values reduced with lower particle size, lower applied load, higher reinforcement level, and higher concentration of boron carbide particles in the reinforcement mixture. COF of '15FIR', '15FBR' and '15FBI-31' composites resulted in a maximum reduction of 35.18%, 27.45%, and 46.21% over the base alloy. These improvements were caused by (a) early oxidation of sliding surface and formation of strong interfacial bonding by ilmenite particles, and (b) increased stability provided to mechanical mixed layer by boron carbide particles. SEM images of wear tracks and worn debris revealed increase in plastic deformation with rise in applied load conditions. This was attributed to rise in formation of craters (delamination wear). EDS analysis signified the formation of mechanical mixed layer (MML) on sliding surfaces. MML was relatively more stable for boron carbide reinforced 'BR' composites.

For high temperature conditions, wear rate of AMCs showed an increasing trend with increase in applied load and operating temperature. For all the samples, transition temperature was 200 ℃ after which wear rate showed a sharp increase. Improvement in wear characteristics of AMCs (compared to base alloy) at high operating temperatures conditions was attributed to higher restriction to micro-cracks by refined grain structure, higher pinning effect causing restriction to thermal softening, strong interfacial bonding between matrix-reinforced particles, and early formation of oxide layer. At transition temperature of 200 ℃, the maximum improvement in steady state wear rate of '15FBR', '15FIR', and '15FBI-31' composites was 82%, 75%, and 87% respectively (over base alloy). The composite having lowest wear rate ('15FBI-31' composite) showed comparable wear rate behaviour with commercially used brake rotor material (only 23% higher). COF of AMCs showed an increasing trend with rise in applied load and operating temperature. However, at a given testing condition, a reduction in

COF values was observed with increase in reinforcement level and proportion of boron carbide particles. Similar observations were noted with reduction in particle size. Maximum reduction in COF values was obtained for '15FBI-31' composite (with reduction of 46.15% at 100 ℃), which was followed by '15FIR' composite (with reduction of 37.16% at 200 ℃) and '15FBR' composite (with reduction of 32.33% at 100 ℃). SEM analysis of wear tracks and debris at 200 ℃ revealed the change in mechanism of wear with increase in applied load conditions. At 200 ℃-9.8 N, abrasive wear was dominant mechanism for removal of material which changed to delamination wear for 49.0 N at 200 ℃.

For each property under a given testing condition, the hybrid composites showed superior results than the single particle reinforced AMCs. This signified that each type of reinforcement in the hybrid AMCs played a significant and diverse role in improving the properties. Boron carbide particles were responsible for higher stability of MML, higher refinement of eutectic silicon and increased resistance to softening of matrix material at high temperatures. On the other hand, ilmenite particles helped in early oxidation of the pin surface and formed strong interfacial bonding between matrix-reinforced ilmenite particles.

LIST OF TABLE

LIST OF FIGURES

TABLE OF CONTENTS

Chapter 1
INTRODUCTION

Overview

This chapter presents a general introduction to the field of tribology. It discusses the role of metal matrix composites (MMCs) as suitable materials for reducing the wear and friction related issues. Different categories of materials which are used as reinforcement in MMCs are discussed. An overview of various techniques used for processing of MMCs are presented. The chapter also discusses the various factors which affect the wear characteristics of MMCs. The applications of MMCs as wear resistant materials are also discussed. Finally, the origin of present research and the organization of thesis are presented.

1.1. Introduction

Tribology is the study of interacting surfaces sliding against each other under the action of an applied load. During this relative motion, sliding surfaces interact with each other to affect the contact surfaces and the interfacial region between them [1–3]. The study of tribology influences the functioning and life of various components used in many mechanical systems. Further, it also impacts the technical safety and maintenance costs for industry [2,4,5]. In recent developments in the field of tribological materials, metal matrix composites (MMCs) are considered as suitable materials for reducing the wear and friction related issues [6–8]. For improving the wear characteristics of MMCs, solid lubricants (graphite, MoS_2, graphene etc.) [9–11], ceramics (SiC, Al_2O_3, TiC etc.) [12–17], and/or natural minerals (rutile, garnet, sillimanite etc.) [13,18–20] are used as reinforcement in MMCs. In the context of matrix, the available metals are aluminium, magnesium, titanium, copper, nickel, and iron etc. For applications where wear behaviour is an important characteristic, aluminium and magnesium are mainly used as the matrix material. However, applications of magnesium based MMCs are restricted because of their low fracture toughness and ductility [6,21,22]. Wear characteristics of metal matrix composites mainly depend on the reinforcement type, reinforcement loading (weight percentage), and the particle size of reinforced particles [13,23,24].

Several methods including stir casting, powder metallurgy, liquid metal infiltration, diffusion bonding, spray deposition etc. are available for processing of MMCs. These fabrication methods are classified into three categories viz. (i) liquid state processing techniques, (ii) solid state processing techniques, and (iii) phase deposition processing techniques [25–27]. Various factors which improve the properties of processed MMCs include uniform dispersion of reinforcement in the matrix material, minimum porosity, and good interfacial bonding between the reinforcement and matrix [28–32]. Powder metallurgy and stir casting routes are the most commonly used processes. Stir casting is used because of its simplicity, proven processing methodology, low cost of production, and mass production capability. Stir cast composites can have issues related to non-wettability of reinforced particles, presence of porosity, and non-uniform distribution of reinforced particles in the matrix. These problems can be avoided by suitable selection of stir casting process parameters such as stirrer design, stirring speed, stirring time, and correct placement of stirrer in the molten mass during processing. Besides this, using different coatings on the reinforced particles, preheating the reinforced particles before addition to the molten mass, and using ultrasonic vibrations for effective dispersion of

reinforced particles are other measures used to improve the quality of the cast MMCs [29,33–35].

Powder metallurgy route for processing of MMCs tends to offer homogeneity in composition and microstructure along with more control over reinforcement distribution. The powder metallurgy process suffers from some limitations also. The powder of pre-alloyed metals comes at a high cost. The hot isostatic pressing method of powder metallurgy which produces full dense compact in one go is very expensive. Finally, the properties obtained by powder metallurgy process are anisotropic due to the uniaxial compressive forces [36,37].

Similarly other techniques used for processing of MMCs have their own advantages and disadvantages. Manufacturers generally prefer the low cost route with adequate quality making stir casting route a preferred choice.

1.2. Factors affecting the wear characteristics of AMCs

Aluminium and its alloys are a preferred matrix material for MMCs because of their high strength to weight ratio, high corrosion resistance, and high specific stiffness. The properties of aluminium matrix composites (AMCs) can be tailored as per the needs of a particular application. AMCs are generally reinforced with discontinuous particles [38,39]. The main factors which affect the wear characteristics of AMCs are as follows:

- Type of reinforcement
- Particle size of reinforcement
- Weight percentage of reinforcement

1.2.1 Type of reinforcement

It is well reported in literature that there are three main categories of reinforced particles which are used to improve the wear behaviour of AMCs. These include (i) synthetic ceramic particles, (ii) natural ceramic particles, and (iii) solid lubricant particles. Further, to take advantage of different types of reinforced particles, some researchers have even used more than one category of reinforced particles in the matrix material (reinforcing two or more types of reinforcements in the metal/alloy matrix) resulting in the development of hybrid metal matrix composites (HMMCs) [18,40,41].

1.2.1.1 Synthetic ceramic particles

Synthetic ceramic particles which are generally used as a reinforcement in MMCs include SiC, TiC, TiB_2, B_4C, WC, and Al_2O_3 particles etc. [13–15,42]. Synthetic ceramics have high inherent hardness and also improve the hardness of metal/alloy matrix on being reinforced. This provides strengthening to the MMC system and improves its wear characteristics [9,24,43]. Synthetic ceramics also have good chemical and thermal stability [44,45]. However, these particles can show poor wettability with the matrix material. Poor wettability results in weak interfacial bonding between the matrix and reinforcement [46,47]. Also, synthetic ceramics are available at a high cost [13]. Addition of synthetic ceramics also reduces the anti-friction capability of AMCs (coefficient of friction etc.) under high operating temperature conditions. This results in increased materials removal rate under high temperature conditions, and thus, increases the overall maintenance cost of the components [48].

1.2.1.2 Natural ceramic particles

Natural minerals which are generally used as a reinforcement in MMCs include zircon, sillimanite, rutile, and garnet etc. [13,18,19]. These particles possess almost similar desirable properties (high hardness, thermal stability, melting point, and strength) as are possessed by synthetic ceramics. This is attributed to their formation under extreme conditions of pressure and temperature [49]. Natural ceramics provide additional benefits like relatively lower coefficient of friction, lower thermal conductivity, and lesser difference in coefficient of thermal expansion values of matrix and reinforced particles [18,19,50]. Further, natural ceramics are abundantly present in the coastal areas of the Indian subcontinent and are available at a low cost. This makes processing of AMCs extremely economical [18,51]. Under high-temperature conditions, these particles help in increasing the wear transition temperature of AMCs by providing thermal stability to the base alloy [24,52].

1.2.1.3 Solid lubricant particles

Various authors have reported on the addition of graphite, silver, calcium fluoride, or molybdenum disulfide particles as reinforcement in AMCs. These particles improve the wear behaviour of resulting AMCs by creating a lubricating layer between the sliding surfaces [9–11]. However, the improvements achieved in hardness and wear characteristics are relatively lesser than those achieved through reinforcement of hard ceramic particles [48].

1.2.2 Particle size of reinforcement

Various authors have investigated the effect of change in particle size of reinforced particles on the mechanical properties and wear characteristics of AMCs. Several range of particle sizes are reported where those greater than 110 μm generally referred to as coarse particle size and those lesser than 40 μm referred to as fine particle size. With relatively coarse particle reinforcement, the processed composites are superior in hardness, wear resistance, and fracture toughness. Also, the level of porosity present in AMCs due to reinforced particles is relatively lower [53,54]. On the other hand, with relatively fine particle reinforcement, the processed composites have higher tensile strength, creep resistance, fatigue strength, and ductility. However, fine particle reinforcement causes increased porosity levels and agglomeration of reinforced particles [55–57]. Researchers have also developed bi-modal and tri-modal particle reinforced AMCs to take advantages of large and fine particle sizes [23,58,59].

1.2.3 Weight percentage of reinforcement

Several authors have investigated the effect of change in reinforcement loading (weight percentage of reinforced particles; wt.%) on the mechanical properties and wear characteristics of AMCs. Increase in weight percentage of reinforced particles till an optimum level shows a direct relationship with improvements in wear behaviour and mechanical properties like hardness etc. [18,24,60]. For reinforcement loading, beyond the optimum level, the properties start degrading. This is attributed to agglomeration of reinforced particles which decrease the potential of load transfer from matrix material to reinforced particles [57,61].

1.3. Application of MMCs

In 1970s, many countries started recognizing the need to develop advanced materials which were economical and could be commercialized [62,63]. Metal matrix composite materials system was one such development. These materials (i.e. MMCs) are superior in structural efficiency, wear characteristics, and thermal/electrical properties compared to the matrix material [62,64]. MMCs find applications in aerospace, automobile, marine, military, and sports sectors [6,39,65]. The specific applications of MMCs as a wear resistant materials in various industrial sectors is presented in Table 1.1.

Table 1.1 Applications of MMCs as wear resistant materials.

Industrial application	Desirable properties	Related references
Brake discs and brake rotors	High wear resistance and high strength	P. Rohatgi [66], Allison and Cole [67], G. S. Cole and A. M. Sherman [68], Deuis *et al.* [69], Sujith *et al.* [70]
Machining tools, ammunition and surgical instruments	High wear and abrasion resistance, high rigidity, high impact resistance, and good thermal conductivity	Samal *et al.* [6], Miracle [62], Ravi *et al.* [71]
Ceramic tubes, cylinder liners, connecting rods, and thermal insulation	High wear resistance, high corrosion resistance and high fracture toughness	Samal *et al.* [6], Miracle [62], Suthan and Patel [72],
Structural applications in aerospace and automobile sector	High wear resistance and high strength	Samal *et al.* [6], Miracle [62]
Wrist pins	High specific stiffness, high wear resistance, and high creep resistance	P. Rohatgi [66], Allison and Cole [67]
Rail wheels, cylinder heads and blocks	High wear resistance and low friction	P. Rohatgi [66], Allison and Cole [67], G. S. Cole and A. M. Sherman[68], Deuis *et al.* [69], Sujith *et al.* [70], Arslan *et al.* [73]
Pistons	High wear resistance and high strength	P. Rohatgi [66], Allison and Cole [67], G. S. Cole and A. M. Sherman [68], Deuis *et al.* [69], Sujith *et al.* [70], Arslan *et al.* [73]

1.4. Origin of the present research

In many applications such as aerospace industry, the mechanical components work under extreme environmental conditions of wear because of high applied loads and operating temperatures. Due to these extreme operating conditions, components like pistons, gas turbine seals, bearings etc. fail which reduces the working efficiency and increases the overall maintenance cost [38,74,75]. To improve the life of such components, researchers have used a combination of metallic alloys (as matrix material) and ceramic particles (as reinforcement) resulting in superior tribological properties of the resulting MMCs [76,77]. However, the disadvantage of adding ceramic particles is that their reinforcement reduces the anti-friction capabilities of MMCs at high operating temperatures [48]. These friction related characteristics are improved by reinforcing self-lubricating particles (solid lubricant particles) such as graphite, silver, calcium fluoride, molybdenum disulfide etc. [9–11]. However, with this type of reinforcement, the improvements achieved in hardness and wear resistance are relatively lower in comparison to the hard ceramic particle reinforced composites [48]. In order to obtain a synergetic effect of ceramic particles and solid lubricants reinforcement, a combination of both the particles is also used and reported in literature. Addition of two different types of reinforcements in aluminium alloy matrix leads to development of hybrid aluminium matrix composites (HAMCs). Each type of reinforcement when added to the matrix material plays

different and specific roles in improving the properties of resulting hybrid composites. Synthetic ceramic particle reinforcement causes microstructural changes (grain size refinement) and assists in formation of mechanical mixed layer (tribolayer) [78,79]. Natural ceramic particle reinforcement results in formation of strong interfacial bonding between matrix and reinforced particles and assists in early formation of oxide layer [24,80]. Further, these oxide based particles (TiO_2, Al_2O_3, Fe_2O_3 etc.) on reinforcement provide increased lubricity and decrease the friction coefficient of composites [18,75].

So, hybrid AMCs can provide superior properties by using a combination of synthetic and natural mineral reinforcements. In the present research work, it was envisaged that addition of the synthetic particles will improve the hardness/wear behaviour whereas natural mineral particles will improve the coefficient friction values of resulting AMCs. The present research work uses boron carbide (B_4C) as the synthetic ceramic particle reinforcement and ilmenite ($FeTiO_3$) as the natural mineral particle reinforcement. Ilmenite is an ore of titanium. It is an abundantly available mineral oxide present in the coastal areas of Kerala, Odisha, Andhra Pradesh, and Tamil Naidu in the Indian sub-continent [81]. Ilmenite particles have high hardness (5–6 Mohs), low thermal conductivity (1.49 W/mK), high thermal stability, high chemical stability, and high corrosion resistance [82,83]. Boron carbide was selected as the ceramic particle reinforcement due to its high hardness (9.49 Mohs), low density (2.52 g/cc), high impact resistance, high wear resistance, and high thermal stability [84]. Boron carbide is the third hardest material after diamond and boron nitride [85,86].

In most of the studies available in literature, AMCs are reinforced with synthetic ceramic particles. Detailed studies with single particle size (SPS; ceramic particles with one specific particle size range, i.e. either fine or coarse) and dual particle size (DPS; ceramic particles of two different particle size ranges, i.e. a combination of fine and coarse) reinforcement are available [59,87]. However, synthetic ceramics are very expensive in comparison to natural (mineral) ceramic particles, and thus, increase the cost of processing of composites. This is not desirable for large scale industrial processing of AMCs [88]. To overcome this problem, composites containing natural ceramic particles have been processed by a few researchers. The addition of minerals into AMCs is an effective and economical way of improving the properties of composites. In most of the reported work on mineral reinforced AMCs, only one type of mineral is reinforced in the AMCs. For these mineral reinforced AMCs, researchers have investigated the effect of reinforcement level and reinforcement particle size on the wear behaviour of AMCs at room temperature and also at high temperatures [88,89]. A few researchers have processed mineral reinforced AMCs with dual particle size also [59,90].

Hybrid composites containing two different types of ceramic particles have also been processed and studied by various authors [41,91,92]. However, in most of the studies, both types of reinforcements are synthetic ceramics. This increases the cost of processing and also the developed composites lack in properties like friction coefficient. To overcome these problems, the present research proposed to develop hybrid composites containing a combination of a naturally occurring mineral and a synthetic ceramic.

In the present research, LM13 alloy (a locomotive grade aluminium alloy) was used as the matrix material. It was reinforced with (a) ilmenite particles only, (b) boron carbide particles only, and also (c) both types of particles to improve the thermal and wear characteristics of resulting AMCs for brake rotor applications. The processed composites were categorized as single particle reinforced AMCs (containing only one type of particles: either boron carbide or ilmenite particles) and dual particle reinforced hybrid AMCs (containing both, boron carbide as well as ilmenite particles). In single particle reinforced AMCs, various formulations were processed by (a) varying the reinforcement type (i. ilmenite particles, or ii. boron carbide particles), (b) varying the reinforcement particles size; two different size ranges were used (i. fine: 20–32 µm, and ii. coarse: 106–125 µm), and (c) varying the weight percentage of reinforced particles (0–15 wt.%; step size of 5 wt.%). In addition to these parameters, for the dual particle reinforced hybrid AMCs, the mixing proportion of the two types of reinforcements for a given reinforcement level (wt.%) were varied as 1:3, 1:1, and 3:1.

1.5. Outline of the thesis

The present work report on development of AMCs with improved dry sliding wear characteristics for high operating temperature conditions. The subject matter pertaining to the present research is organized into six different chapters. A brief outline of the thesis is presented as follows:

Chapter 1. This chapter provides an introduction to the terms of 'tribology' and metal matrix composites'. The role of metal matrix composites (MMCs) as suitable materials for applications where the phenomenon of wear and friction are important is discussed. Various types of materials which are used as reinforcements in MMCs are discussed. The processing methods for MMCs are briefly discussed with their relative advantages/disadvantages. Different parameters which influence the wear behaviour of MMCs are discussed. The origin of present work and the outline of the thesis are finally presented in this chapter.

Chapter 2: This chapter provides the insight to aluminium and its alloy, which is followed by discussion on different combinations of reinforcements used to make AMCs. Further, a detailed review of literature is done to point out the gaps in literature. The literature review section is divided into four categories based on the reinforcement used i.e. boron carbide, ilmenite, 'synthetic particles+mineral particles' and 'synthetic particles+synthetic particles'.

Chapter 3: This chapter describes the key issues taken on the basis of gaps found in existing literature review. Further, a discussion on methodology used to make the desired AMCs is done. During fabrication of AMCs, various equipements and machines were used. The purpose of using particular equipement and machine is discussed in detail.

Chapter 4: This chapter presents the comparative study of effect of boron carbide and ilmenite particles on hardness, coefficient of thermal expansion, friction and wear property of LM13 base alloy. In addition to reinforcement, the influence of particle size on these properties are also discussed. The fabricated AMCs were characterized using X-ray Diffraction and optical microscopy. However, SEM-EDS analysis was used to analyse the worn surface and debris obtained during wear test at room and high temperature conditions.

Chapter 5: This chapter illustrates the effect of different particle sizes of hybrid reinforcement (i.e. boron carbide and ilmenite) on various properties of base alloy. Beside this, the composite having lowest wear rate at different particle size is compared with commercially used brake rotor material. The worn surfaces of AMCs were characterized by using the SEM-EDS and roughness tester. However, the debris were only analysed using SEM-EDS.

Chapter 6: This chapter summaries the outcomes of the experimental study done in this thesis. It also outlines the main implications to be made from the current study. The potential future scope of the current effort is also highlighted.

As per this outline, a detailed review of literature is presented in the next chapter.

Chapter 2
LITERATURE REVIEW

Overview

This chapter presents a detailed literature review of aluminium matrix composites (AMCs) reinforced with different types of reinforcements. The reinforcements were classified into two broad categories of (a) synthetic ceramics, and (b) naturally occurring minerals. Literature survey revealed the use of different combinations of reinforcements for enhancing the properties of aluminium alloys. The chapter provides an insight into the role of individual reinforcements in affecting the characteristics of matrix material. Based on different combinations, the literature review is divided into four sections viz. (a) AMCs reinforced with boron carbide (B_4C) ceramic particles, (b) AMCs reinforced with ilmenite ($FeTiO_3$) mineral particles, (c) hybrid AMCs reinforced with two different synthetic ceramic particles, and (d) hybrid AMCs reinforced with a combination of synthetic ceramic particles and mineral particles.

2.1. Aluminium and its alloy

In most of the industries, the requirements concerning the engineering materials include low density, good machinability, and high specific strength. These requirements are adequately fulfilled by aluminium alloys. The increase in demand for aluminium alloys in various sectors, especially auto-sector is attributed to the fulfillment of objectives like reduction in energy consumption, pollution, and fuel consumption [93,94]. The use of aluminium alloys can be extended for other applications (viz. tappets, gears, and transmission bearings) by enhancing hardness, seizure load, and wear performance. The enhancement in properties is obtained by developing aluminium matrix composites (AMCs), and around 69% of metal matrix composites are AMCs only [95,96].

Without reinforcement, the properties of aluminium alloys can be altered by three methods. First, selection of an optimum age hardening process can enhance the properties of heat treatable aluminium alloys. Second, the properties of non-heat treatable aluminium alloys can be altered by performing work hardening process. Third, the addition of different alloying elements help in attaining a variety of properties for aluminium alloys [6,97]. The primary alloying element used to enhance aluminum's casting characteristics is silicon. Silicon forms a eutectic composition with aluminium and enhances the fluidity of molten mass. This improvement in fluidity reduces the defects caused by shrinkage during the casting process. In addition to this, Al-Si alloys have high corrosion resistance, low coefficient of thermal expansion, and good weldability. These properties allow the use of Al-Si alloy in 80% of the casted aluminium alloys [97,98].

The eutectic composition of Al-Si alloy is based on silicon content as shown in Figure 2.1. Aluminium alloys having silicon content less than 11 wt.%, between 11–13 wt.%, and more than 13 wt.% are classified as hypoeutectic, eutectic, and hypereutectic Al-Si alloys respectively. The exact eutectic composition of Al-Si alloy is obtained at 12.6 wt.% which melts at 577 ℃. When casted components have a complex design and variable thickness, the silicon content is kept at 4 wt.% to 11 wt.%. Besides this, hypoeutectic Al-Si alloys are also preferred for general applications [97,99]. The casted components are manufactured by eutectic Al-Si alloy when high fluidity and low shrinkage are more important than strength. For example, pistons, pump casting, domestic cookware, manifolds, etc. are made by using eutectic Al-Si alloy [97,100]. Further, hypereutectic Al-Si alloys are found to have high specific stiffness, high temperature wear resistance, and low coefficient of thermal expansion. Due to

these properties, hypereutectic Al-Si alloys are used to make rocker arms, valve retainers, cylinders and connecting rods [97,101].

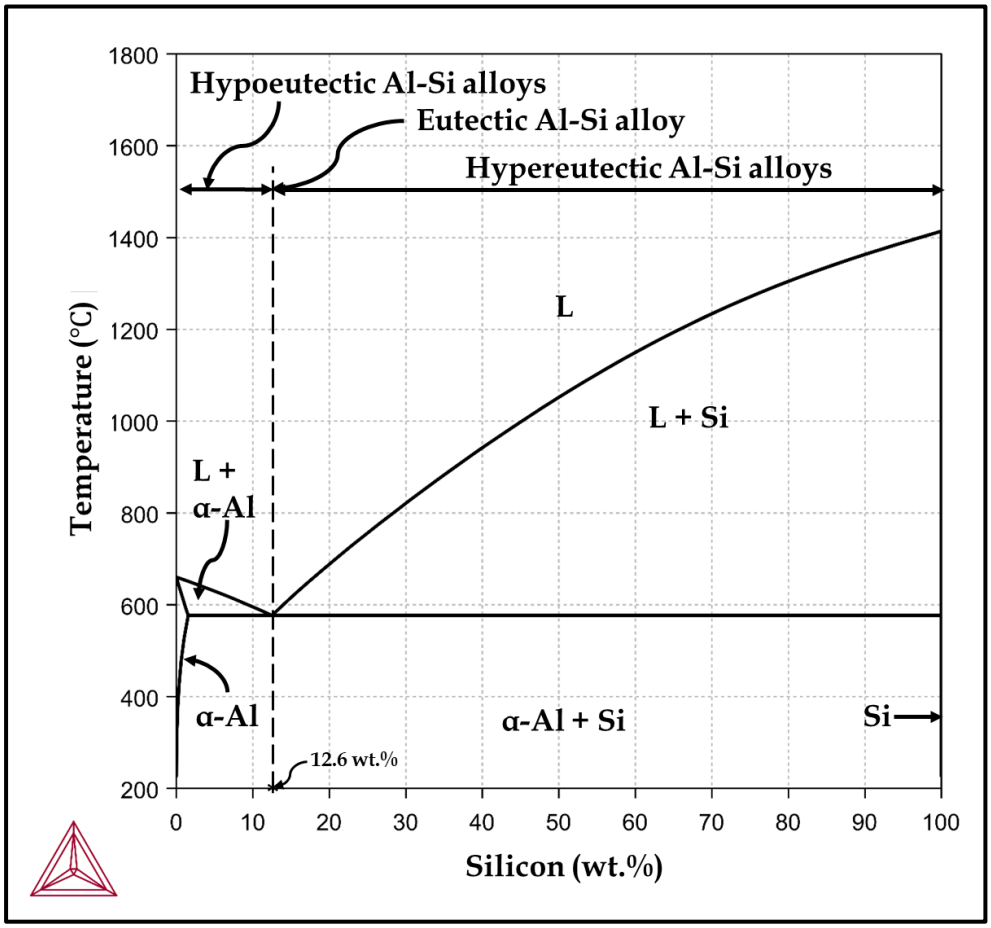

Figure 2.1 Al-Si phase diagram constructed using Thermo-calc software.

The properties of AMCs depend upon the type, nature, shape, and size of reinforced particles in the matrix material. Reinforced particles bring about changes in the microstructure, interfacial bonding strength, and load transfer capability. AMCs are generally categorized as (i) single particle reinforced AMCs, and (b) dual particle reinforced AMCs (hybrid AMCs). In single particle reinforced AMCs, matrix is reinforced with only one particular type of reinforcement. Properties of a given type of single particle reinforced AMCs can be varied by changing the reinforcement level (i.e. weight percentage) and/or particle size. Though slight differences are reported in different sources of literature but generally reinforcement particle size is divided into three categories viz. fine (1–30 µm), medium (32–60 µm), and coarse (70–120 µm). Authors have successfully improved the properties of AMCs by mixing particles of various size ranges into the matrix material [23,80,102].

Dual particle reinforced AMCs (hybrid AMCs or HAMCs) contain two different types of reinforcements in a particular matrix [18,103]. Literature reveals that each reinforcement plays

a significant role in improving the properties of HAMCs. Usually, one reinforcement refines the microstructure of matrix material, and the other increases the load transfer capability by forming strong interfacial bonding [18,104]. Different combinations of reinforcements are reported in literature to enhance the properties of HAMCs. Some of the combinations used by researchers for enhancing the mechanical and tribological properties are 'SiC + Al_2O_3', 'SiC + TiB_2', 'SiC + B_4C', 'SiC + TiC' and 'AlN + $Y_2W_3O_{12}$' etc. The mixing proportions of the two types of particles in the reinforcement mixture, particle size, and reinforcement levels are changed to affect the properties [38,105–107].

2.2. Literature review

This section discusses the literature review on discontinuous particle reinforced aluminium matrix composites. The literature has been divided into four main sections:

(a) AMCs reinforced with boron carbide (B_4C) ceramic particles

(b) AMCs reinforced with ilmenite ($FeTiO_3$) mineral particles

(c) Hybrid AMCs reinforced with two different types of synthetic ceramic particles

(d) Hybrid AMCs reinforced with a combination of synthetic ceramic particles and mineral particles

(a) AMCs reinforced with boron carbide (B_4C) ceramic particles

This section provides a summary of literature pertaining to reinforcement of boron carbide particles in aluminium alloy matrix for analyzing the improvements obtained in resulting AMCs.

Tang *et al.* [108] in **2008** investigated the friction and wear characteristics of AMCs containing Al-5083 as matrix and B_4C particles as reinforcement. Mixture of boron carbide and stearic acid was blended using cryo-milling process followed by degasification, hot isostatic pressing and rolling. Boron carbide particles were added in weight percentage of 5 wt.% and 10 wt.%. Both the compositions were made by mixing B_4C with 0.2 wt.% of stearic acid. Figure 2.2a and Figure 2.2b show the variation of reduction in length with respect to change in sliding distance for composite having 5 and 10 wt%. The change in concentration of B_4C particles from 5 wt.% to 10 wt.% led to reduction in wear rate of about 40%. The wear rate of AMCs was divided into two stages based on variation of pin length reduction with respect to sliding distance. The first stage was for sliding distance range of 0–500 m or 0–1000 m whereas second stage was for sliding distance range of 500–3000 m or 1000–3000 m. The wear rate of first

stage was one to two orders of lower magnitude in comparison to second stage. The first stage was observed for all specimens for composite A and for some specimens of composite B tested at 50 N–0.8 m/s, and 65 N–1.25 m/s.

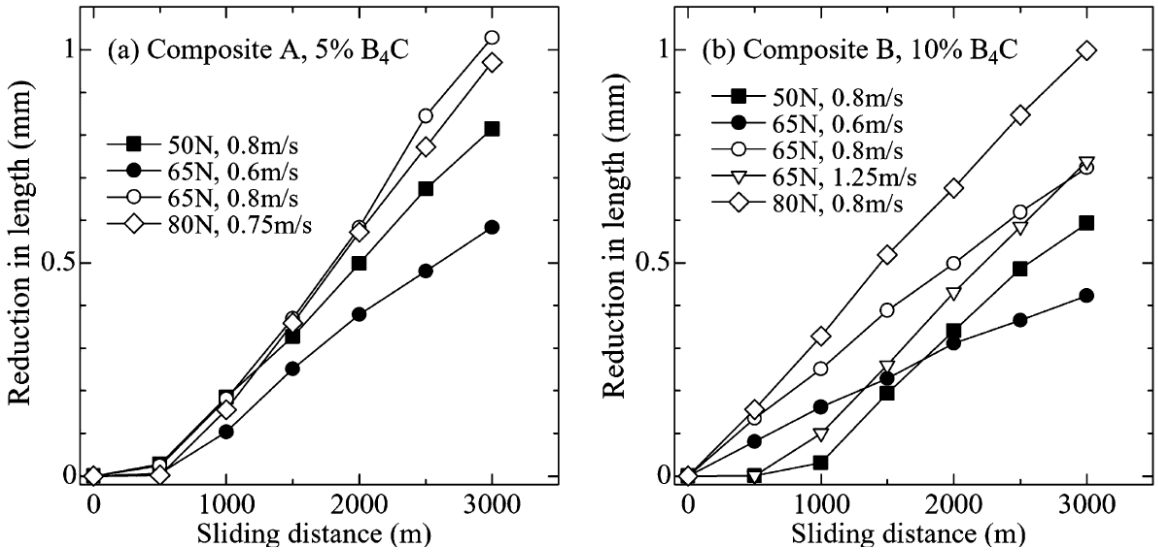

Figure 2.2 Variation of reduction in pin length with respect to change in sliding distance for (a) composite A and (b) composite B [108].

Absence of first stage was observed for composite with 10 wt.% of B_4C tested under 65 N–0.6 m/s, 65 N–0.8 m/s, and 80 N–0.8 m/s. The low length reduction rate in the first stage corresponded to a flat stage with low coefficient of friction (COF) in the COF/sliding distance curve. This was attributed to stand proud of B_4C particles from pin surface as its COF with steel disc is around 0.29. However, in second stage, composite surface was no longer covered with B_4C particles which resulted in increase of COF value. Thus, transition from the first stage to the second stage was attributed to the change in the wear mechanism from abrasive wear to adhesive wear.

Nie *et al.* [46] in **2008** investigated the microstructural and interfacial characteristics of boron carbide reinforced AMCs. Al alloy (2024 Al) was reinforced with 10 vol.% of B_4C particles. B_4C particles were treated with 5% hydrofluoric acid (HF) aqueous solution for 40 h and were then rinsed with deionized water. Composites were processed using treated/untreated B_4C particles. Mechanical alloying (MA) method was used for mixing of powder which was followed by hot pressing and hot extrusion. Microstructure analysis revealed uniform distribution of B_4C particles in Al matrix. The combination of high energy milling and hot extrusion led to a grain size distribution of 200−400 nm. This grain size was also possible due to restriction in grain growth provided by carbide and nano-sized oxides particles. During milling of untreated B_4C with Al alloy, the rise in temperature resulted in formation of B_2O_3

film on B_4C particles followed by formation of MgO (due to its interaction with Mg in the alloy). Presence of MgO near the particle interface was identified using EDX, TEM and SAD. Figure 2.3 shows the variation of modulus ratio with respect to strain.

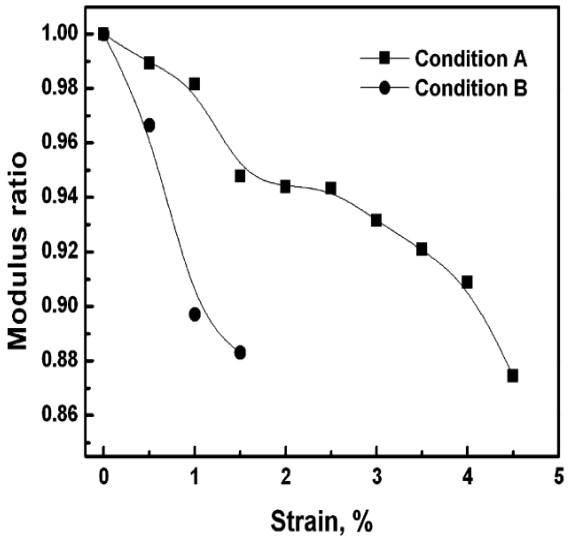

Figure 2.3 Modulus ratio as a function of strain for composite having treated B_4C (condition A) and untreated B_4C (condition B) [46].

The formation of MgO around B_4C promoted the wetting charateristics of particles with aluminium matrix but also resulted in decohesion or cracking in reinforcement even at low levels of strain (1.00%). In case of treated B_4C reinforced composite, a strong interfacial bonding was formed due to clean and oxide free aluminium alloy as the material was able to stand low levels of strain.

Sharifi *et al.* [109] in **2011** investigated the effect of boron carbide reinforcement on the hardness, compressive strength, and wear rate of AMCs. Reinforcement level of B_4C was varied in the range of 5–15 wt.% (step size of 5 wt.%). The obtained mixture of base alloy and ceramic particles was ball milled and hot pressed to fabricate different AMCs. At high temperatures of hot pressing, aluminium can react with B_4C particles to form products (detrimental to properties) such as Al_3BC, AlB_2, and Al_4C_3. However, XRD analysis revealed that no such reaction occurred between matrix and reinforced particles. The hardness, wear resistance, and ultimate compression strength (UCS) of composite showed an increasing trend with change in reinforcement from 5 to 15 wt.%. The value of hardness and UCS obtained at 15 wt.% reinforcement level was 164 HV and 485 MPa respectively. The enhancement in hardness was attributed to presence of hard B_4C particles and increase in resistance to localized matrix deformation. In case of UCS, uniform dispersion of reinforced particles helped in restricting the dislocation motion through dispersion strengthening mechanism. Further,

increase in proportion of particles led to reduction in inter-particle distance due to which the stress required for movement of dislocations increased. The increase in UCS of AMCs came at the expense of reduction in ductility. The reduction in wear rate of composites was ascribed to formation of mechanical mixed layer (MML) and oxide layer on sliding surfaces. The thickness of both the layers increased from 3 µm to 9 µm with increase in reinforcement level of B_4C from 5 wt.% to 15 wt.%. These layers prevented the exposure of base alloy to the counter disc and hence helped in reducing the wear rate of composites. Further, the lubricity effect shown by MML also resulted in reduction of friction coefficient values.

Shabani and Mazahery [110] in **2011** studied the microstructure and dry sliding wear properties of A356–B_4C composites fabricated by stir casting process. Further, the combination of finite element method (FEM) with artificial neural network (ANN) was used to predict the wear properties of AMCs. The models were developed by varying the volume percentage of B_4C (0 to 15 vol.%), average particle size of B_4C (1 to 50 µm), and sliding distance (0 to 1200 m). In molten alloy, magnesium was added to improve the wettability of aluminium alloy with reinforced particles whereas strontium was added to modify the morphology of eutectic silicon. Microstructure characterization revealed the presence of B_4C particles at the dendritic branches of Al alloy. Further, B_4C particles were found to act as sites for heterogeneous nucleation of eutectic Si and also helped in restricting the growth of eutectic Si.

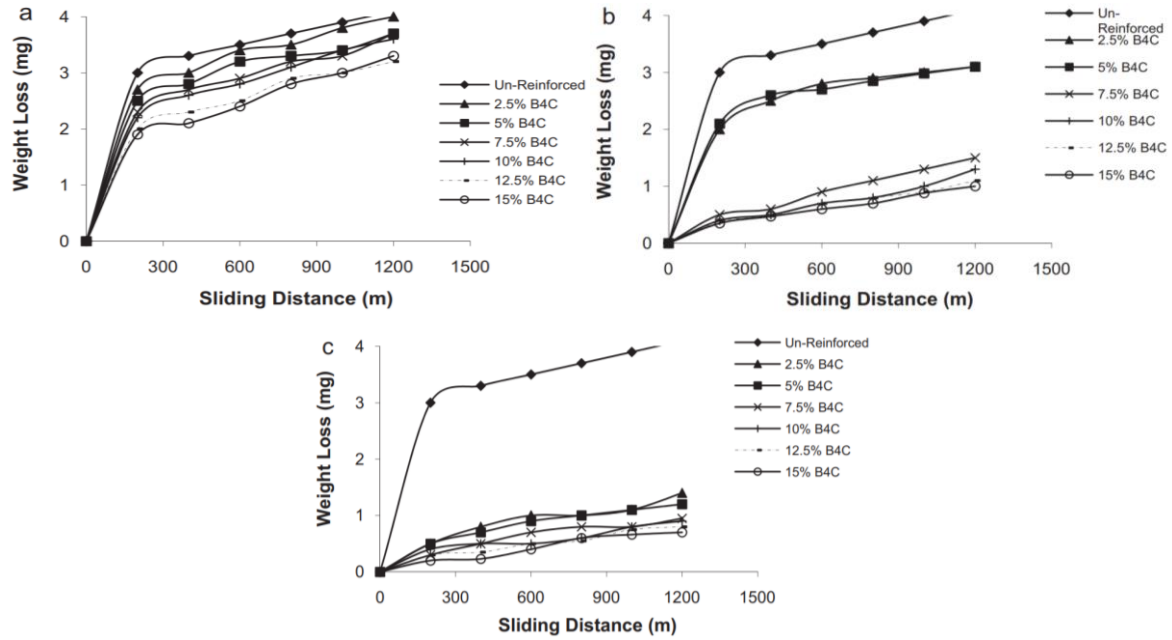

Figure 2.4 Effect of sliding distance on wear rate of AMCs at different particle size of B_4C: (a) 1 µm, (b) 30 µm, and (c) 50 µm [110].

Porosity level showed increasing trend with rise in volume percentage of B_4C and decrease in average particle size of B_4C. This was attributed to increase in probability of cluster formation by B_4C particles, air entrapment in clusters of particles, and hindrance to liquid metal flow inside them. The increase in particle size and volume fraction of B_4C led to reduction in wear rate of Al-B_4C composites. This was due to shielding of matrix by B_4C. Secondly, B_4C particles were brittle and after fracturing got distributed on surface, thus preventing wear of matrix. Al-B_4C composites with particles size of 1 µm showed highest wear rate at all volume fractions of B_4C. However, the increase in particle size led to transition in wear rate from high wear rate to low wear rate. Wear rate of base alloy and Al-B_4C composites with respect to change in sliding distance at a particle size of 1 µm, 30 µm, and 50 µm is shown in Figure 2.4a, Figure 2.4b, and Figure 2.4c, respectively. FEM method was used for discretization and evaluation of transient temperature field for quenching in heat treatment. ANN was used to predict the weight loss and porosity of AMCs. After four neurons in hidden layer, the error in measured and predicted value was observed to be minimum.

Baradeswaran and Perumal [47] in **2013** investigated the effect of B_4C particles reinforcement on mechanical and tribological properties of stir casted and T6 heat treated Al7075-B_4C composites. B_4C particles were added in amounts of 5−20 vol.% and their particle size was varied from 16–20 µm. The wettability of B_4C particles was improved by adding K_2TiF_6 flux whose function was to form interfacial products of TiC and TiB_2. The increase in volume percentage of reinforcement resulted in an increase of ceramic phase in matrix which enhanced the hardness of Al-B_4C composites. This was ascribed to increase in strain energy around the reinforced particles. Wear test results showed increase in wear resistance of composites with increase in vol.% of B_4C. This increase was attributed to the higher load bearing capacity of reinforced particles and formation of mechanical mixed layer (MML). Further, an increasing trend in ultimate tensile, compression, and flexural strength was also observed. Figure 2.5a, Figure 2.5b, Figure 2.5c, and Figure 2.5d show the variation of hardness, tensile strength, compressive strength and flexural strength with respect to change in volume fraction of B_4C, respectively. Increase in tensile strength was attributed to effective transfer of load from matrix to reinforcement. However, for compressive strength, it was an increase in obstacle density (i.e. B_4C particles) which resisted the motion of dislocations generated within the matrix. B_4C particles also helped in restricting the plastic flow during compressive test.

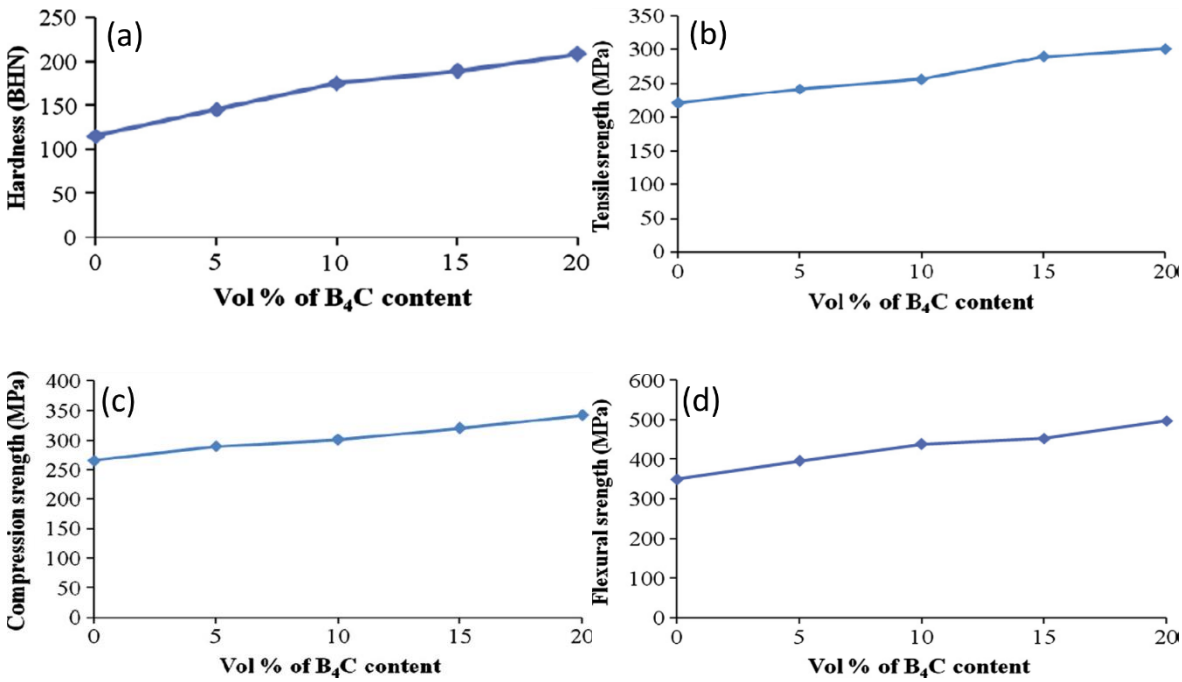

Figure 2.5 Effect of volume fraction of B_4C on (a) hardness, (b) tensile strength, (c) compressive strength, and (d) flexural strength [47].

In flexural strength, composites showed enough ductility to attain more strength. The attainment of ductility was attributed to reduction in expansion of cracks by B_4C particles which corresponded to less deformation of the AMCs. The change in flexural strength was observed to be in the range of 349–497 MPa. Composites showed decrease in coefficient of friction (COF) with increase in percentage of B_4C particles till 10 vol.% with minimum value as 0.32.

Rajesh *et al.* [111] in **2016** examined the mechanical and tribological properties of stir casted Al6061 alloy reinforced with 9 wt.% of B_4C particles. The wettability of B_4C particles was improved by adding flux (K_2TiF_6). The weight ratio of B_4C and flux was kept at 0.3. XRD analysis revealed the presence of interfacial compounds such as TiB_2 and Al_3Ti which helped in improving the wettability of B_4C particles. In comparison to base alloy, the hardness, ultimate tensile strength, and specific strength of Al6061-B_4C composite showed an improvement of 115.3%, 38.8%, and 42.8% respectively. The increase in hardness of Al-B_4C composite from 70.3 HV to 151.4 HV was attributed to reduction in plastic deformation, increment in strain energy, and particle strengthening effect shown by B_4C particles. Moreover, the enhancement in tensile strength and specific strength of composites was ascribed to the increase in work hardening and reduction of grain size of matrix by B_4C particles. This led to rise in load required for generation of voids in the material. Further, the mismatch in coefficient of thermal expansion resulted an increased dislocation density in the base alloy which was also

responsible for improvement in the strength of AMCs. During deformation of composite, reinforced particles resulted in strain hardening of the matrix which caused reduction in ductility of Al-B_4C composites. Fractographic analysis revealed the distribution of two-way dimples in AMCs. Smaller dimples represented ductile failure of matrix whereas larger dimple signified the brittle fracture of reinforced particles. The wear rate of base alloy got reduced on addition of B_4C particles at different loads and sliding distances as shown in Figure 2.6a and Figure 2.6b, respectively. This was attributed to reduction in plastic deformation due to entanglement of dislocations around the reinforced particles.

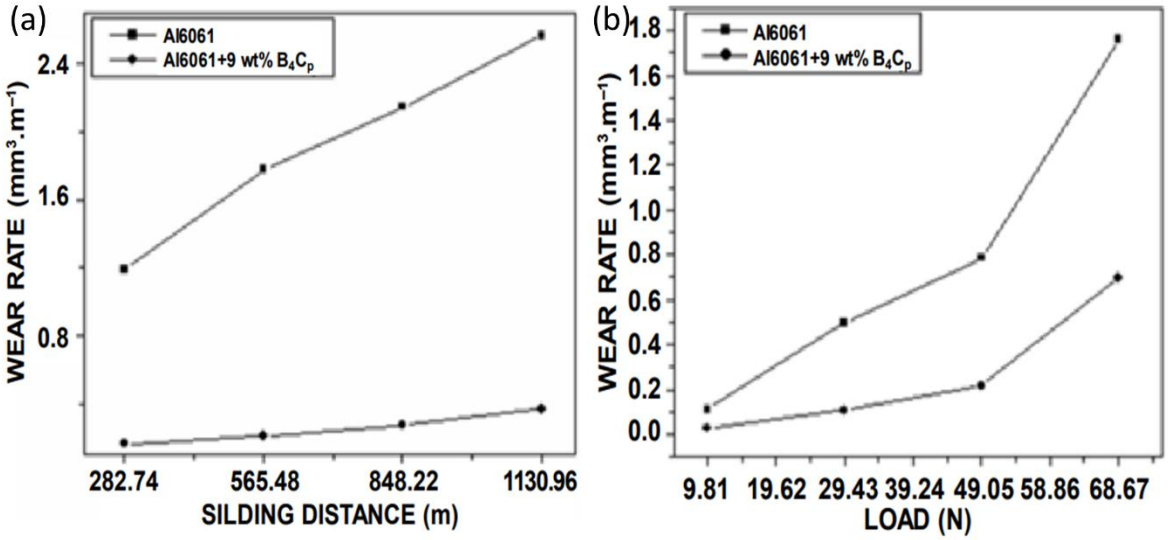

Figure 2.6 Variation of wear rate with respect to (a) sliding distance and (b) applied load for Al6061 alloy and Al6061-B_4C composite [111].

Further, the development of tribolayer between the contact surfaces helped in reducing the materials removal rate at high applied loads and sliding distances.

Harichandran *et al.* [44] in **2017** studied the effect of particle size and reinforcement level on high temperature tribological properties of AMCs. The addition of boron carbide particles in pure aluminium was done by using the ultrasonic cavitation assisted stir casting process. Boron carbide particles were added in two different particle sizes of 70 µm (micro-level) and 80 nm (nano-level). Weight percentage was varied from 2–6 wt.% (step size of 2 wt.%). Increase in hardness values was observed with increase in reinforcement level of both types of particles. The highest hardness value was attained by addition of 6 wt.% of nano-sized B_4C in pure Al. This was attributed to dispersion strengthening mechanism, Hall-Petch strengthening mechanism, Orowan strengthening mechanism and formation of strong bond by reinforced particles with the matrix material. For wear property, the rise in reinforcement level and temperature (till 200 ℃) led to reduction in wear rate of AMCs as shown in Figure 2.7. The

rise in temperature beyond 100 ℃ led to thermal softening of the matrix material whereas in the presence of reinforced particles, the matrix became soft after 200 ℃. The softening of matrix resulted in easy deformation of the material and caused rise in wear rate. Further, the rise in applied load and particles size led to increase in wear rate of AMCs. Figure 2.7a–b and Figure 2.7c–d present the effect of weight percentage of B_4C on high temperature wear rate at an applied load of 4 N and 16 N, respectively. However, the effect of particle size of 70 µm and 80 nm at particular applied load is shown by Figure 2.7a,c and Figure 2.7b,d, respectively. The mismatch in thermal properties of matrix and reinforced particles also induced thermal stresses around the reinforced particles.

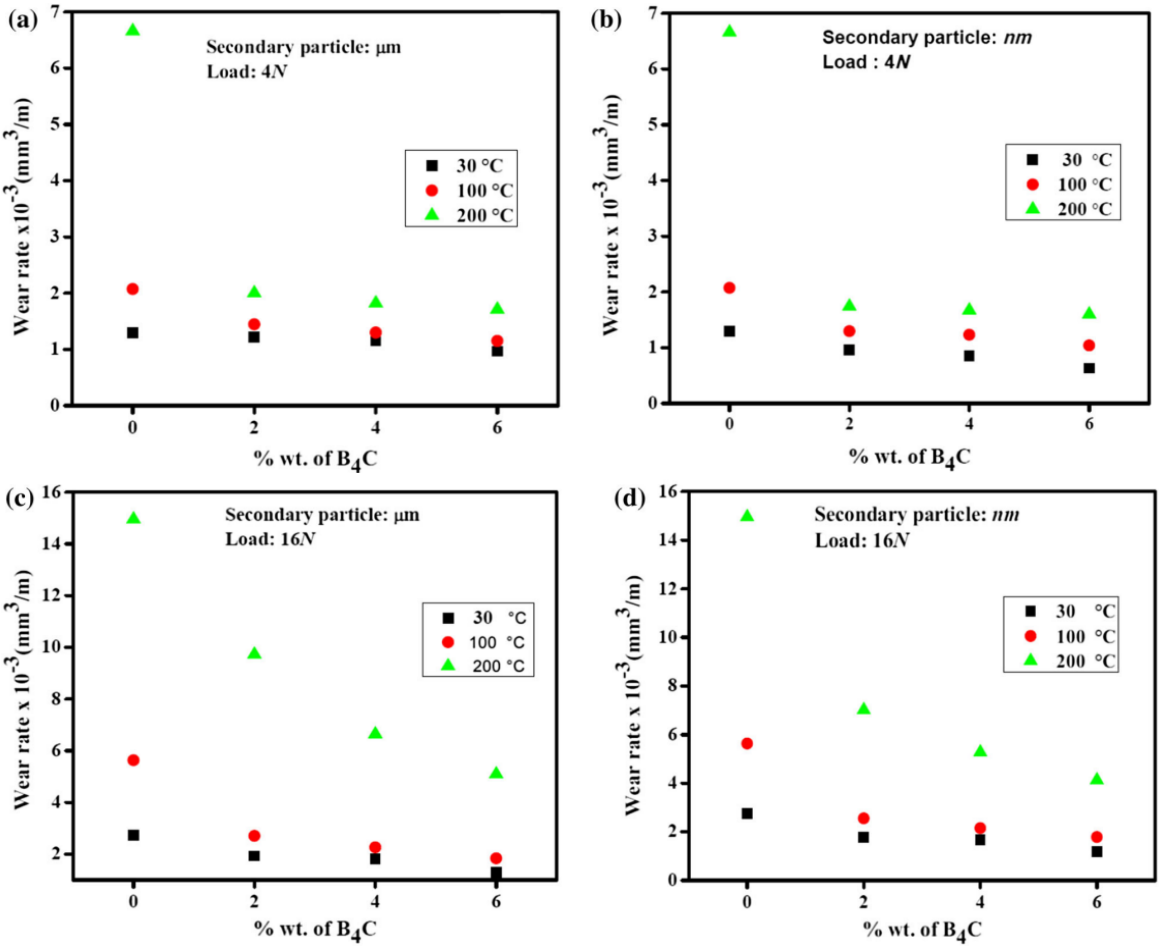

Figure 2.7 Wear rate as a function of weight percentage of B_4C and operating temperature for different combination of applied load and particle size i.e. (a) 70 µm & 4 N, (b) 80 nm & 4 N, (c) 70 µm & 16 N, and (d) 80 nm & 16 N [44].

Under the action of applied load, the increase in stress beyond the interfacial stress resulted in removal of particles from the sliding surfaces. This exposed the matrix to counter disc and caused rise in wear rate. On the other hand, the reduction in particle size provided greater thermal stability, high load bearing capacity, and high energy for dislocation movement. SEM

micrographs of wear track at room temperature revealed occurrence of abrasive wear for base alloy and its composites. However, the rise in operating temperature resulted in abrasive, adhesive and oxidation wear of AMCs.

Nieto *et al.* [112] in **2017** examined the abrasive wear characteristics of AMCs at different particle sizes of boron carbide. AA5083 alloy was used as matrix whereas boron carbide was used as reinforcement. The mixture of powder of matrix and reinforced particles were mechanically alloyed using the cryogenic medium. This process was followed by dual mode dynamic forging. The different particle sizes used for boron carbide were categorized into three types (a) micro-metric (1–7 μm), (b) sub-micron (0.5 μm), and (c) nano-metric (40 nm). The composites made by different particles were designated as Al-μB_4C, Al-sμB_4C, and Al-nB_4C respectively. The decreasing sequence of hardness obtained were Al-nB_4C, Al-sμB_4C, Al-μB_4C, and AA5083 alloy (Table 2.1).

Table 2.1 Hardness and wear volume of Al-B_4C composites [112].

Sample	Microhardness (GPa)	Wear volume (mm^3)
AA5083	1.55±0.03	118.3±0.3
Al-μB_4C composite	2.05±0.05	117.8±0.6
Al-sμB_4C composite	2.16±0.03	123.9±0.6
Al-nB_4C composite	2.42±0.03	110.1±1.1

Highest hardness shown by Al-nB_4C composite was attributed to high surface area, lower grain size, and shorter inter-particle distance. The shorter inter-particle distance led to homogeneity in the AMCs with less variation in properties. The wear property showed a dependency on hardness of AMCs as it corresponded to reduction in penetration of individual abrasive particles. The wear study of base alloy revealed the presence of silica particles on sliding surface which came from the abrasive media. This happened due to ductile nature of AA5083 alloy. However, the presence of silica particles helped in reducing the wear rate of base alloy. In the context of Al-B_4C particles, silica particles were responsible for pulling out of B_4C particles as the increase in brittleness of composite restricted the embedment of silica particles. This reduced the effect of increase in hardness for composite reinforced with larger size of B_4C particles. The reduction in particle size to sμB_4C showed the entrapment of reinforced particles which resulted in three body abrasive wear. This caused the increase in wear rate in comparison of μB_4C particle reinforced composite. In case of Al-nB_4C composite, high hardness and interfacial area with coherent bonding led to highest reduction in wear rate as given in Table 2.1.

Singh *et al.* [113] in **2019** investigated the effect of different parameters and weight fraction of B_4C reinforcement on the wear characteristics of AA5083-B_4C composites. The composites were fabricated by using the stir casting process in which boron carbide was added in different weight percentage of 5, 10, 15 and 20 wt.%. Each composition was designated as composite A, composite B, composite C, and composite D respectively. The particle size used for B_4C was 300 mesh. The wear parameters were varied in three levels of load (30, 40 and 50 N), sliding distance (1000, 2000, and 3000 m), and sliding velocity (1, 2, and 3 m/s). Figure 2.8a, Figure 2.8b, and Figure 2.8c present the effect of sliding distance, applied load, and sliding speed on volume loss of AA5083-B_4C composites, respectively. During the wear test, the increase in sliding distance, sliding speed, and applied load showed a proportional relation with wear rate of base alloy and its composites. This was attributed to fracturing of asperities which acted as abrasive medium between the sliding surfaces.

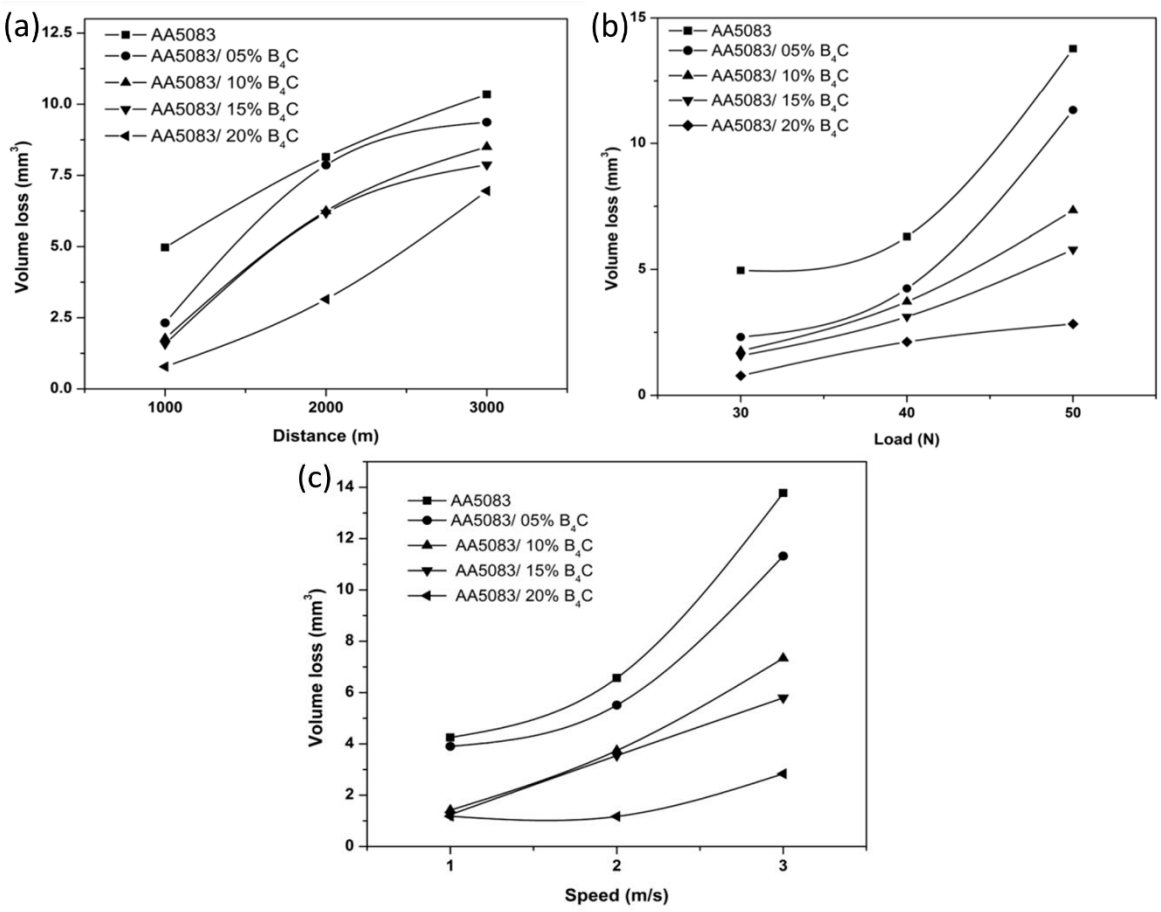

Figure 2.8 Effect of (a) sliding distance, (b) applied load, and (c) sliding speed on volume loss of base alloy and composites [113].

The trapped asperities were responsible for change in two body wear mechanism to three body wear mechanism. The rise in frictional heat by increase in sliding distance and applied load

resulted in higher removal of material by digging and deformation of softened sliding surfaces. However, this process of material removal was reduced by formation of oxide layer on the sliding surfaces. The stability to oxide layer was provided by reinforced particles whose function was to lower the deformation of matrix material. The wear track analysis revealed that the removal of material was due to abrasive, ploughing, delamination, and adhesive wear mechanisms. The occurrence of wear mechanism was dependent on the wear testing conditions. In case of composites, oxidation and three body abrasive wear mechanism were additional mechanisms responsible for deformation of sliding surfaces. Abrasive and adhesive wear mechanisms were mainly observed at lower sliding distance, applied load, and sliding velocity. However, a transition in mechanism to delamination wear was observed at the extreme values of wear parameters.

Shinde *et al.* [114] in **2020** examined the effect of applied load and sliding speed on dry sliding wear characteristics of LM6-B_4C composites fabricated by ultrasonic assisted stir casting process. Boron carbide particles were added in weight percentage of 0.5, 1, 1.5, and 2 wt.%. The microstructure analysis revealed uniform dispersion of reinforced particles in LM6 alloy. Beside this, the presence of B_4C particles led to fragmentation of silicon phase due to the Zener pinning effect and resulted in refinement of the microstructure with rise in reinforcement level. Microhardness of composites showed increasing trend with rise in concentration of B_4C particles as given in Table 2.2.

Table 2.2 Hardness and elastic modulus of LM6-B_4C composite [114].

Sample	Microhardness ($HV_{0.1}$)	Nanohardness (GPa)	Elastic Modulus (GPa)
LM6 alloy	68±5	1.2	53.6
LM6-0.5 wt.% B_4C composite	70±3	-	-
LM6-1.0 wt.% B_4C composite	75±2	2.09	72.66
LM6-1.5 wt.% B_4C composite	77±3	-	-
LM6-2.0 wt.% B_4C composite	87±4	2.46	49.8

Similar behaviour was also obtained from the load-depth curves taken by nanohardness tester. The presence of B_4C particles obstructed the dislocation motions generated by the indenter. This resulted in higher hardness values and lower penetration depth. The area under the unloading curve of load-depth curve was observed to be lowest for 2 wt.% of B_4C. This signified the attainment of higher elastic modulus for AMCs. The wear tests were performed by varying the applied load from 0.354–1.412 MPa and sliding speed from 0.16–0.66 m/s. The increase in concentration of B_4C particles and sliding speed led to reduction in wear rate whereas the rise in applied load resulted in increment of wear rate. The incorporation of reinforced particles increased the dislocation density in matrix material, refined the

microstructure, and formed strong interfacial bonding. These factors reduced the wear rate of AMCs. A sharp rise in wear rate was observed after an increase in applied load beyond 1 MPa. The increase in wear rate was attributed to breaking of the protective oxide and transfer layer which increased the metallic intimacy and enhanced the deformation of sliding surface. For sliding speed, a sharp decrease in wear rate was observed till a sliding speed of 0.33 m/s. This was attributed to the transfer of material between the two sliding surfaces which formed a protective oxide layer under high contact temperature. However, beyond 0.33 m/s, the rise in contact temperature was so significant that material got thermally soft resulting an increase in wear rate of AMCs.

Hynes *et al.* [115] in **2020** studied the effect of boron carbide addition on the mechanical properties and wear behaviour of AA6061 aluminium alloy. Stir casting process was used to incorporate different weight percentage of B_4C (5, 10, and 15 wt.%) in matrix of AA6061alloy. The addition of reinforced particles led to reduction in breaking load, ultimate tensile strength and percentage elongation by virtue of increase in yield strength. This signified the decrease in diffusivity of aluminium alloy on addition of hard reinforced particles. The bending strength, and impact strength were observed to be higher for AA6061-5wt.% B_4C composites. However, shear strength and hardness showed the highest value at 15 wt.% of B_4C particles. This was attributed to reduction in plastic deformation, ductility, and energy absorption capability of base alloy. Figure 2.9a and Figure 2.9b shows the effect of weight percentage on weight loss and coefficient of friction of AMCs, respectively.

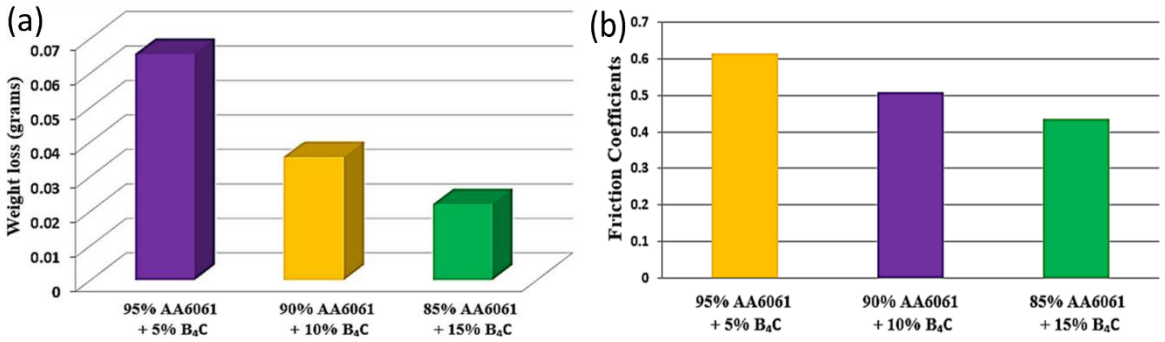

Figure 2.9 Variation of (a) weight loss and (b) friction coefficient with respect to weight percentage of B_4C [115].

The improvement in wear rate on addition of B_4C was ascribed to the reduction in area of contact of the base alloy with the counter surface and enhancement in hardness of AMCs. The coefficient of friction showed a lowest value of 0.435 at 15 wt.% of B_4C particles.

Nagaral *et al.* [116] in **2021** studied the mechanical and tribological properties of Al2024 alloy reinforced with boron carbide particles. The stir casting process was used to get uniform distribution of B_4C particles in aluminium alloy. B_4C particles with an average size of 44 µm were added in amounts of 2, 4, 6, and 8 wt.%. The incorporation of B_4C in Al2024 alloy resulted in high hardness, tensile strength, and compression strength whereas a reduction in wear rate and density was observed. The reduction in density of composites was attributed to the lower density of boron carbide particles. Further, the enhancement in hardness and compressive strength was ascribed to the refinement of grain structure and presence of hard particles. In accordance to Orowan mechanism, hard particles helped in restricting the dislocation motion whereas grain refinement provided strengthening by Hall-Petch mechanism. The improvement in tensile strength and yield strength was obtained due to mismatch in thermal properties. This led to generation of dislocation density around reinforced particles which improved the strength of AMCs. On the other hand, the increase in dislocation density was responsible for reduction in ductility of AMCs. The highest values of density, hardness, tensile strength, yield strength, and compressive strength were 2.775 g/cm^3, 285.2 MPa, 228.9 MPa, and 816 MPa respectively. Figure 2.10a and Figure 2.10b present the effect of applied load and sliding speed on wear of different AMCs whereas the effect of wt.% of B_4C on wear rate at different applied load by keeping the sliding speed at 2.09 m/s is shown in Figure 2.10c.

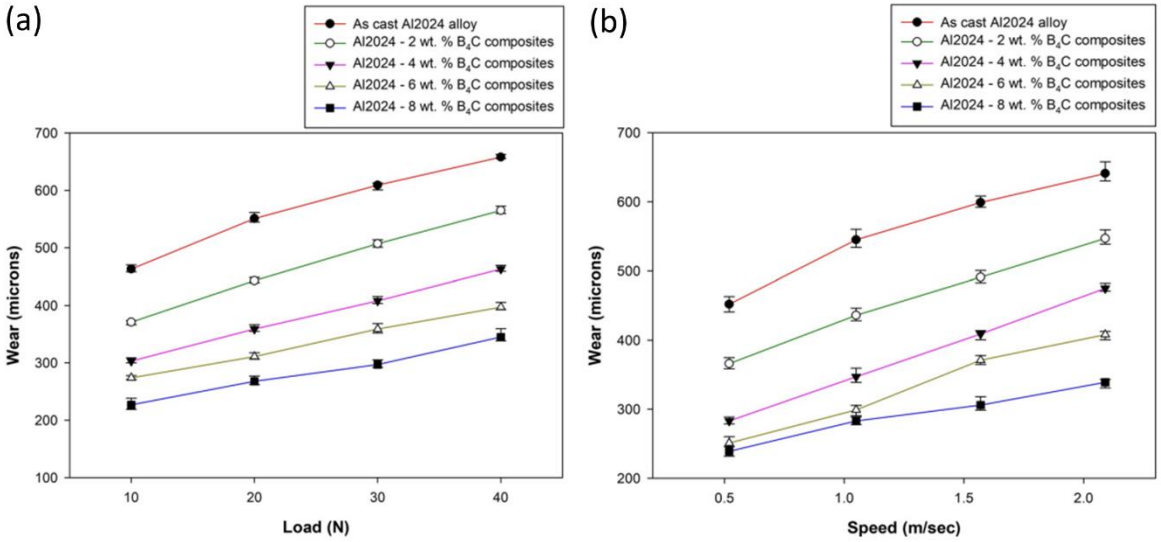

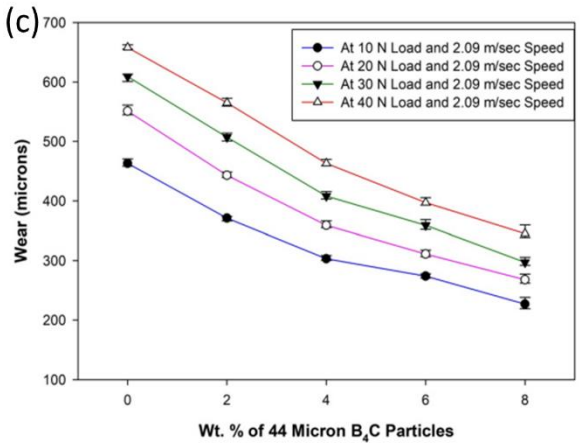

Figure 2.10 Change in wear at different (a) applied loads, (b) sliding speeds, and (c) content of B_4C for AMCs [116].

At a particular weight percentage of B_4C, wear loss showed an increasing trend with rise in applied load and sliding speed. However, the increase in weight percentage showed a decreasing trend in wear loss. This was attributed to higher obstruction to plastic deformation and dynamic recrystallization of base alloy.

Saessi *et al.* [117] in **2021** examined the high temperature wear behaviour of boron carbide reinforced Al5083 alloy composites. The average particle size used for base alloy and reinforced particle was less than 100 µm and 10 µm respectively (both constituents were in powdered form). The mixture of base alloy with 5 wt.% of B_4C particles was mechanically milled which was followed by hot pressing and hot extrusion. The comparison of microstructure of milled base alloy with un-milled base alloy revealed presence of ultra-fine grains in milled base alloy. This was attributed to severe plastic deformation and breaking of cold welding joints formed during the milling process. Similar observation was obtained for Al-B_4C composites. At room and high temperature conditions, the sequence of reduction in wear rate was obtained as un-milled Al5083 alloy, milled Al5083 alloy, and Al-B_4C composite. However, the rise in applied load and operating temperature led to increase in wear rate for all the samples. Figure 2.11a and Figure 2.11b show the effect of applied load on wear rate of Al-B_4C composites at room temperature (22–25 ℃) and high temperature (200 ℃). With rise in temperature, the movement and slipping of dislocations became easier which enhanced the plastic deformation and resulted in higher wear rate. On the other hand, the increment in applied load resulted in transition from mild to severe wear.

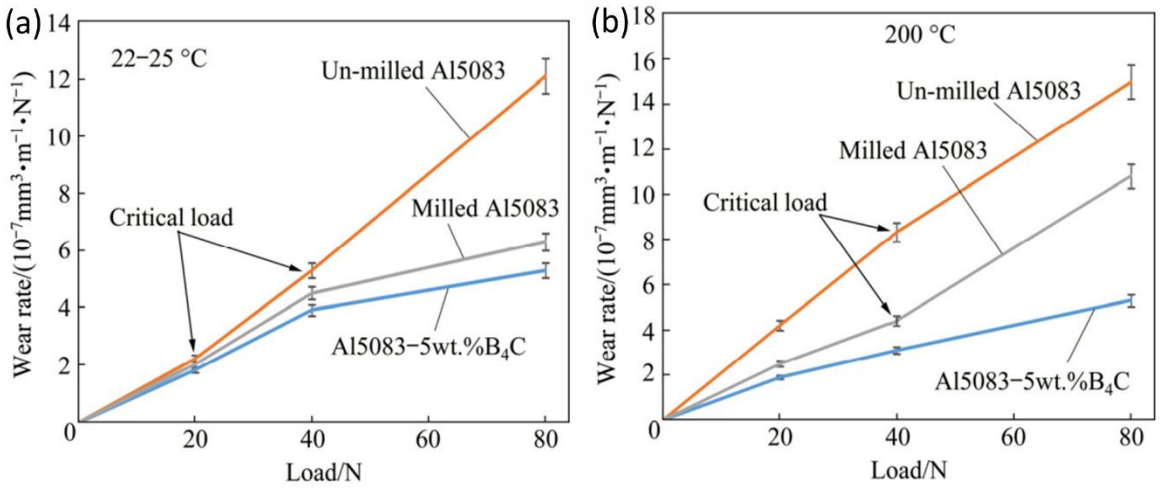

Figure 2.11 Wear rate as a function of applied load at (a) room temperature (22–25 ℃) and (b) 200 ℃ temperature for base alloy and AMCs [117].

Further, the addition of boron carbide particles resulted in early formation of protective oxide layer on sliding surfaces and increased the pinning of dislocations. This helped in reducing the plastic deformation and caused a reduction in wear rate of AMCs. The formation of oxide layer also acted as lubricant which resulted in reduction of friction coefficient values. Wear track analysis of sample tested at room temperature revealed that material removal was due to abrasive wear mechanism. However, at high temperature conditions, un-milled Al5083 alloy deformed due to severe adhesion whereas delaminated wear mechanism was responsible for deformation of milled Al5083 alloy. In case of Al-B_4C composite, the removal of material occurred due to combination of abrasion and delamination wear mechanism.

Lee *et al.* [118] in **2021** examined the tribological properties of AMCs by varying the weight percentage of boron carbide particles in Al6061 alloy. The fabrication of composites was done using stir casting which was followed by hot rolling process. Boron carbide with an average particle size of 39±1.5 µm was added in different volume percentages of 5, 10, and 20 vol.%. Microstructure of stir-cast AMCs revealed random distribution of reinforced particles. However, after hot rolling process, reinforced particles get arranged in the rolling direction which further improved the dispersion of reinforced particles. Titanium and chromium present in Al6061 were found to form multi-interfacial layer of Al_4C_3/$(Ti,Cr)B_2$ around the reinforced particles. This improved the wettability of B_4C particles with molten aluminium alloy. Vickers hardness of base alloy showed an increase in hardness from 116.5 HV to 139.9 HV when reinforcement level was kept at 20 vol.%. Further, the increase in concentration of B_4C resulted in reduction of wear depth, wear width, and coefficient of friction (COF) as given in Table 2.3. At 20 N load, the lowest wear width (856 µm) and depth (36 µm) were obtained for Al6061

alloy reinforced with 20 vol.% of B_4C. This was ascribed to formation of strong interfacial bonding and uniform dispersion of reinforced particles.

Table 2.3 Wear width, wear depth, COF, and hardness for Al6061-B_4C composites [118].

Volume percentage of B_4C	Width (µm)		Depth (µm)		COF		Hardness ($HV_{0.1}$)
	5 N	20 N	5 N	20 N	5 N	20 N	
0	1303±1.21	2101±1.44	80±0.32	165±0.29	0.38±0.02	0.42±0.02	104.2±4.63
5	1286 ±.38	1573±1.39	72±0.85	122±0.35	0.38±0.02	0.37±0.03	116.5±3.70
10	1123±2.17	1265±1.61	55±0.74	71±0.86	0.34±0.03	0.34±0.02	125.7±0.63
16	720±2.54	856±2.21	23±0.65	36±0.85	0.31±0.01	0.35±0.02	139.9±4.25

The increase in applied load resulted in rise of wear rate and slight reduction in COF. This mainly happened due to well bonded and aligned reinforced particles in base alloy which protected the matrix from deformation under the action of applied load.

V a *et al.* [119] in **2022** investigated the effect of boron carbide on mechanical and tribological properties of Al2030 aluminium alloy composites. The composites were fabricated using two stage stir casting process. In this process, mechanical stirrer was used to disperse different amount of boron carbide particles (3 wt.% and 6 wt.%) in the melted Al2030 alloy. The average particle size used for B_4C was 85–90 µm. Microstructure analysis revealed uniform dispersion of reinforced particles in the base alloy. Besides this, reinforced particles were found to be wetted by the molten alloy. The hardness, ultimate tensile strength (UTS), and yield strength showed rise in values with increase in weight percentage of B_4C particles. The highest hardness at 6 wt.% of B_4C particles was attributed to decrease in plastic deformation and increase in strain energy around the reinforced particles. The value of hardness for base alloy and Al-6 wt.% B_4C composite was 65 BHN and 87.3 BHN respectively. The UTS and yield strength of base alloy increased from 206 MPa to 244.9 MPa and 161.4 MPa to 197.7 MPa respectively after addition of extreme amount of reinforced particles respectively. The increase in UTS was ascribed to effective transfer of load from matrix to reinforced particles due to strong interfacial bonding between matrix and reinforced particles. The effective transfer of load inhibited the plastic flow of base alloy which enhanced the UTS of AMCs. Further, the rise in dislocation density by mismatch in thermal properties was responsible for enhancement in yield strength of AMCs. The decrement in percentage elongation of AMCs was attributed to increase in nucleation of voids by stress concentrators i.e. boron carbide particles. The increase in applied load and sliding speed showed rise in wear loss and coefficient of friction for all the samples. Figure 2.12a and Figure 2.12b show the effect of applied load and sliding speed on volumetric wear loss of Al2030-B_4C composite.

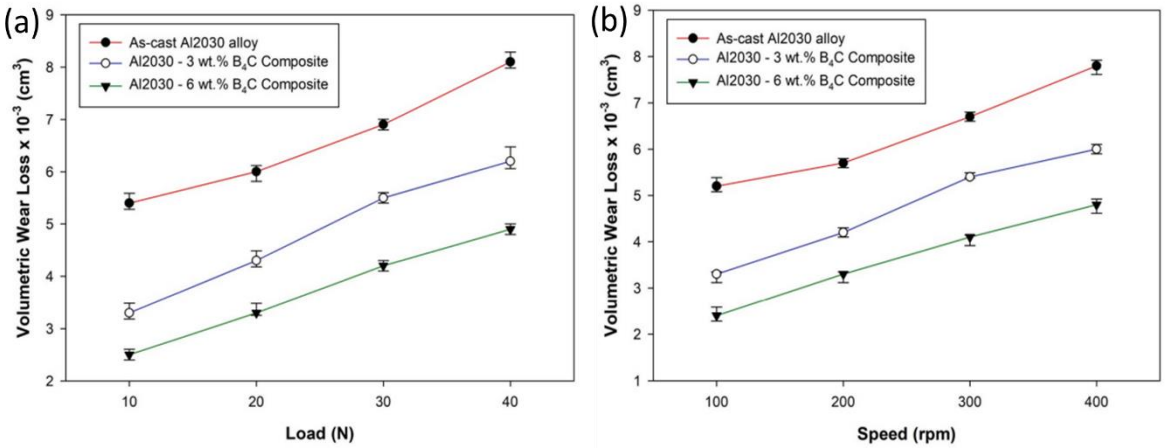

Figure 2.12 Effect of (a) applied load and (b) sliding speed on volumetric wear loss of Al2030 alloy and Al2030-B_4C composite [119].

At low load condition, removal of material happened due to three body abrasive wear. However, the rise in applied load resulted in formation of tribo-layer which reduced the contact between the two counter surfaces. The increase in weight percentage of B_4C particles resulted in reduction of wear loss. This was attributed to lower plastic deformation and stacking of dislocations at matrix-particle interface.

(b) AMCs reinforced with ilmenite ($FeTiO_3$) mineral particles

The literature survey on ilmenite reinforced AMCs revealed that very limited work has been done using ilmenite particles as reinforcement. Mainly three main research groups have worked in this area. These include Sarkar *et al*. [120,121], Rasidhar *et al.* [122–124], and Elwan *et al.* [83]. The reported work is as follows:

Sarkar *et al.* [120] in **2004** studied the effect of reinforcing ilmenite particles on the mechanical properties of different matrices viz. Al, Al-Si alloy, and Al-Mg alloy. The composites were fabricated by using the stir casting method. For different AMCs, ilmenite, magnesium, and silicon were added in weight percentage of 10 wt.%, 2 wt.% and 2 wt.% respectively. The microstructure analysis of AMCs was done at different locations of casting i.e. top, bottom, outer and inner surface. For Al-10 wt.% ilmenite composite, particles were observed to be mainly present at top, bottom and outer periphery of casting. However, uniform dispersion of particles was observed for Al-2 wt.% Mg-10 wt.% ilmenite composite and Al-2 wt.% Si-10 wt.% ilmenite composite. The X-ray data revealed the occurrence of reaction between ilmenite and molten of Al-Mg alloy. This led to formation of reaction products viz. aluminium oxide, magnesium oxide, titanium and aluminium. These reaction products grew and attained a critical size, after which they got detached from ilmenite particles. The detachment process was

initiated due to heat generated by exothermic reaction. The particles of reaction product acted as a reinforcement and also as a dispersion strengthening agent. Maximum reaction products were observed for Al-Mg alloy followed by Al-Si alloy and pure aluminium. This increased the specific surface area of reinforced particles which helped in restricting the dislocation motion, effective transfer of a load from matrix to reinforced particles, and retaining the elongation of matrix material. The mechanical properties of Al-ilmenite, Al-Si-ilmenite and Al-Mg-ilmenite composites are given in Table 2.4.

Table 2.4 Mechanical properties of different AMCs [120].

Material	Hardness (VHN)	UTS (MPa)	Percentage elongation
Al-10 wt.% ilmenite composite	42.02	60.85	14.02
Al-2 wt.% Mg-10 wt.% ilmenite composite	47.03	80.01	13
Al-2 wt.% Si-10 wt.% ilmenite composite	43.90	61.1	15

Highest values of ultimate tensile strength and hardness were shown by Al-Mg-ilmenite composite followed by Al-Si-ilmenite composite and Al-ilmenite composite. However, reduction in elongation values compared to base alloy was observed. Highest reduction was observed for Al-Mg-ilmenite composite followed by Al-ilmenite composite and Al-Si-ilmenite composite.

Sarkar *et al.* [121] in **2009** investigated the effect of different reinforcements on hardness and distribution of reinforced particles in pure aluminium matrix composites. Vertical centrifugal casting process was used to incorporate 25 g of SiC, ZrO_2 or ilmenite particles in 500 g of pure aluminium. The distribution of particles was analyzed by taking the sample along the length, inner surface, outer surface, top surface and bottom surface. Ilmenite particles were found to highly concentrated at inner, middle and outer surface of casting. However, silicon carbide particles were mostly present at the bottom and middle surface of the casting. The presence of high concentration at middle of casting was attributed to the high metallostatic pressure at the bottom and centrifugal forces at the periphery. These forces pushed the particles away from the bottom and allowed the particles to be trapped by the solid wave front at middle of the casting. The microstructure of ilmenite reinforced AMCs revealed the presence of porosity around the particles except for top and bottom surface of casting. This was attributed to the occurrence of interfacial reaction which led to generation of gas porosity. At top and bottom, the contact time of liquid aluminium with reinforced particles was less due to which gaseous products were not formed for generating porosity. Moreover, the presence of zirconia and SiC showed no interfacial reaction between the particles and matrix. The addition of reinforced particles resulted in increase in hardness of composites. Highest hardness was obtained for SiC

particles which was followed by ilmenite and zirconia particles. For pure Al and Al-zirconia composite, hardness decreased from bottom to top surface and outer to inner surface of casting as shown in Figure 2.13a and Figure 2.13b, respectively. However, no such pattern was observed for ilmenite and SiC reinforced composites. This was attributed to presence of porosity and occurrence of interfacial reaction.

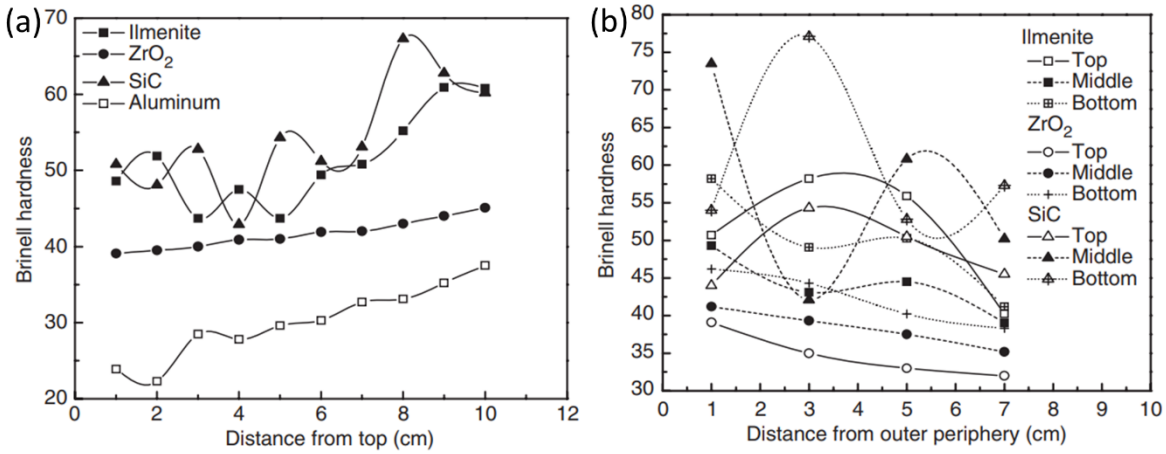

Figure 2.13 Variation of hardness from (a) top to bottom and (b) outer periphery to inner for ilmenite, SiC, and zirconia reinforced AMCs [121].

The measurement of density showed maximum reduction in density for zirconia reinforced AMCs which was followed by SiC and ilmenite reinforced AMCs. The variation in density of AMCs was attributed to the difference in porosity and mismatch in density of matrix with reinforced particles.

Rasidhar *et al.* [122] in **2013** investigated the microstructural and mechanical properties of stir cast AMCs. Pure aluminium was used as matrix whereas ilmenite was used as reinforcement. Ilmenite particles were added in different weight percentage of 1 to 5 wt.% with a step size of 1 wt.%.

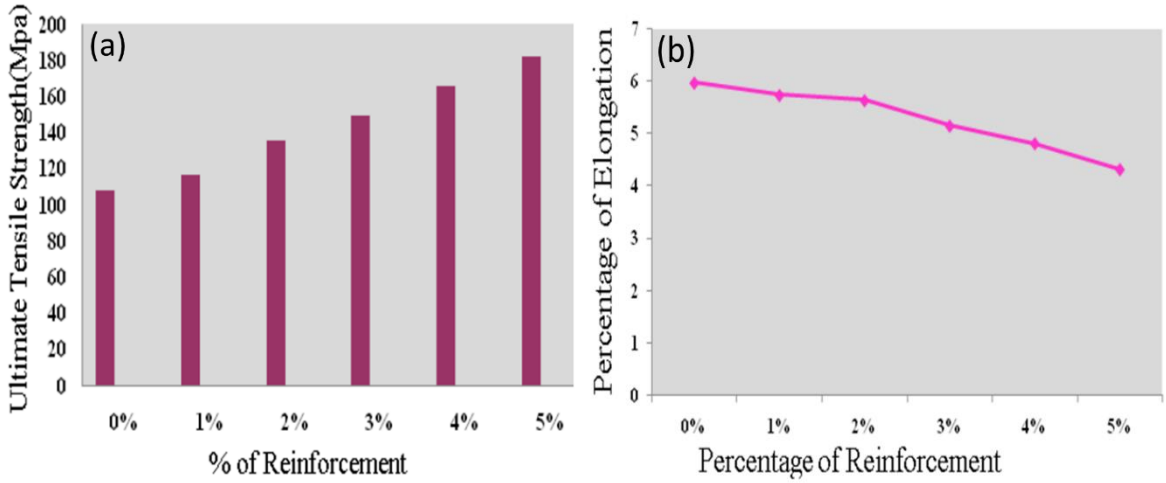

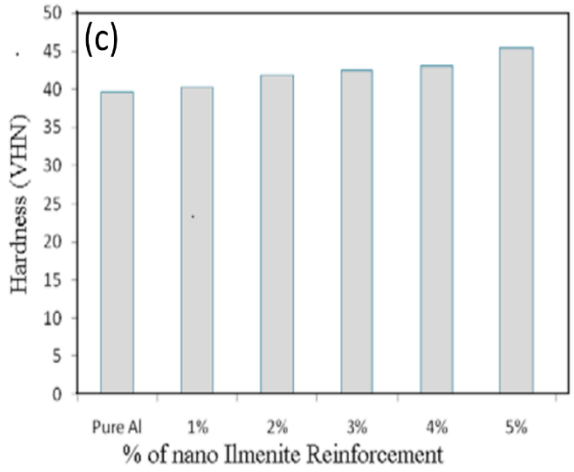

Figure 2.14 Effect of weight percentage of ilmenite on (a) tensile strength, (b) percentage elongation, and (c) hardness of AMCs [122].

Microstructure analysis revealed uniform dispersion of reinforced particles with some agglomeration. Figure 2.14a, Figure 2.14b, and Figure 2.14c presents the variation of tensile strength, percentage elongation, and hardness with respect to change in weight percentage of ilmenite particles. Tensile strength and hardness of Al-ilmenite composite showed an increasing trend with rise in reinforcement level (as shown in Figure 2.14a and Figure 2.14c). The improvement in tensile strength was attributed to presence of hard phase and effective transfer of load from matrix to ilmenite particles. However, the enhancement in hardness was ascribed to increase in resistance to motion of dislocations and presence of hard ilmenite particles. Further, a decrement in ductility of AMCs was observed with increase in concentration of particles from 0 to 5 wt.% (as shown in Figure 2.14b).

Rasidhar *et al.* [123] in **2013** studied the mechanical properties of ilmenite based aluminium matrix nanocomposites. 99.7% pure aluminium was used as matrix whereas crystalline iron titanium oxide was used as reinforcement. Stir casting technique was used to incorporate 1–5 wt.% (with a step size of 1 wt.%) of ilmenite particles in pure Al. Minimum particle size used for ilmenite was 58 nm which was obtained by ball milling set-up. Uniform dispersion of ilmenite particles in Al was revealed by SEM images. Addition of $FeTiO_3$ particles showed significant improvement in hardness of composites as shown in Figure 2.15 due to dispersion hardening effect caused by ilmenite. After 3 wt.% of ilmenite, decrement in hardness values was observed. On the other hand, increase in amount of reinforcement resulted in increase of density due to high density of ilmenite as compared to Al.

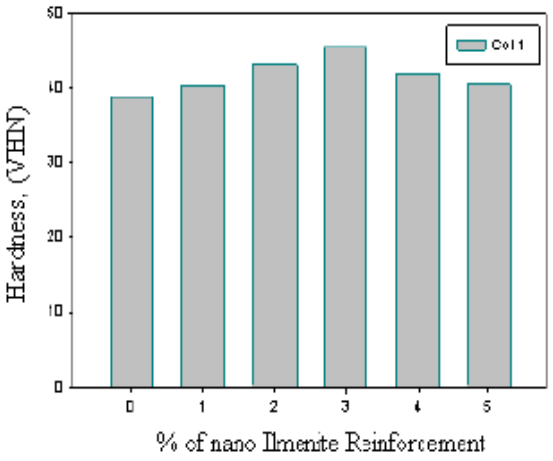

Figure 2.15 Variation of hardness with the percentage of reinforcement [123].

Rasidhar *et al.* [124] in **2015** investigated the microstructural and mechanical properties of Al-ilmenite nanocomposites. Stir casting process was used to add $FeTiO_3$ particles in the molten pool of IE-07 graded aluminium used as matrix. To enhance the wettability of nanoparticles, 0.5 wt.% Mg was added in the molten metal. Reinforced particles were added in the range of 1–5 wt.% and with an increment of 1 wt.%. Microstructural analysis revealed uniform dispersion of ilmenite particles in the matrix. Increase in density, ultimate tensile strength, and compressive strength was observed with increase in content of ilmenite in the matrix. Out of all, composite with 3 wt.% of reinforcement showed better properties. The presence of nano particles, refinement of grain structure of matrix and formation of secondary phase $FeAl_3$ led to improvement in mechanical properties because these secondary phase acted as barrier to the movement of dislocation within the matrix and exhibited greater resistance to applied load. Hence, composite with 3 wt.% of ilmenite showed maximum of 22% improvement in compressive properties. Beyond 3 wt.%, higher degree defects, formation of agglomeration and micro-porosity were observed which degraded the properties of composites.

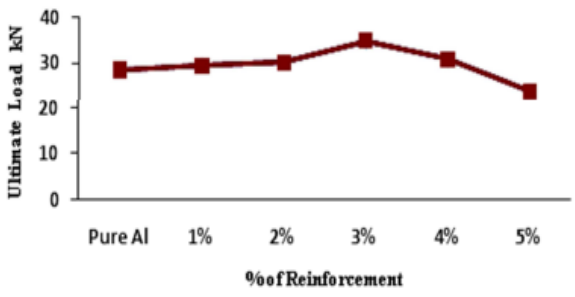

Figure 2.16 Variation in ultimate tensile strength with weight percentage of ilmenite [124].

Analysis of fractured surface from tensile test showed presence of dimples with varying size which justified the ductile nature of nanocomposites. A maximum of 19% improvement in tensile strength of composite reinforced with 3 wt.% of ilmenite was observed as shown in Figure 2.16.

Elwan *et al.* [83] in **2020** studied the influence of number of deformation cycles and volume fraction of ilmenite on the mechanical properties of Al1050 aluminium alloy. The composites were fabricated by using the accumulative roll bonding (ARB) process. In this process, the volume percentage of ilmenite particles varied from 2 to 8 vol.% with a step size of 2 vol.% and ARB process was repeated for seven cycles. With increase in number of cycles, the layer formed by aluminium and ilmenite particles showed an increasing trend. This led to dispersion of ilmenite particles from interface to bulk of aluminium alloy layer and removed all the discontinuity present at the interfaces. After seven cycles of ARB, ilmenite particles were observed to be uniformly distributed in the Al1050 alloy. This was attributed to the fracturing of clusters of ilmenite particles under the action of high deformability. The breaking of clusters of reinforced particles allowed the matrix to come in-between the ilmenite particles. The repeatability of this process allowed uniform distribution of ilmenite particles in Al1050 alloy. The tensile strength of AMCs was dependent on three factors viz. cold working, grain refinement, and the reinforced particles. With increase in ARB cycles and reinforcement level, the tensile strength of fabricated AMCs showed an increasing trend as shown in Figure 2.17a. This was attributed to increase in uniformity of reinforced particles and cold work rate of composites.

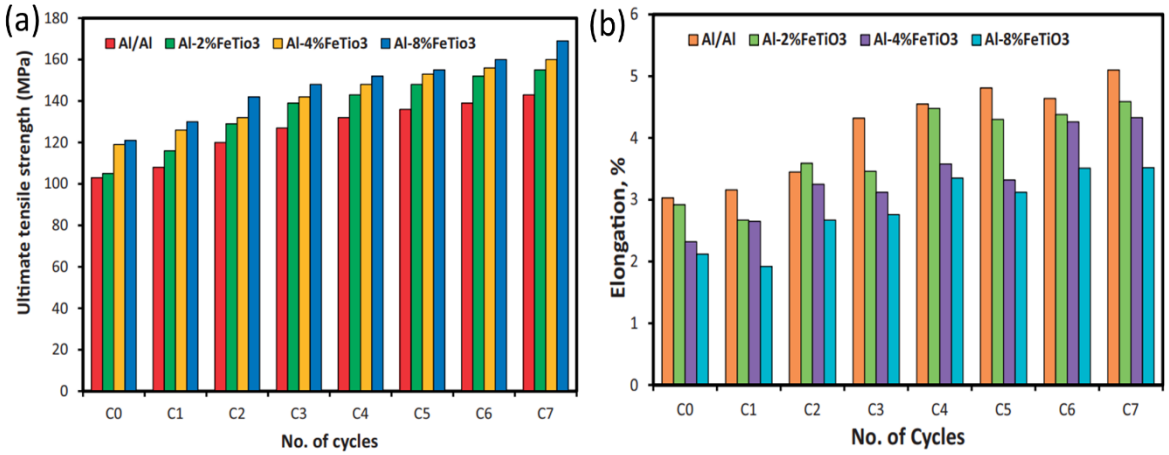

Figure 2.17 Effect of number of cycles and volume fraction on (a) tensile strength and (b) elongation of Al1050-ilmenite composites [83].

Further, the increase in reinforcement level resulted in rise of dislocation density and reduction in grain size. Both these parameters acted as strengthening mechanisms for enhancing the tensile properties of AMCs. After zero cycle, the tensile strength of un-processed Al1050 alloy, ARB processed Al1050 alloy, and ARB processed Al1050-8 vol.% ilmenite composite was 40 MPa, 103 MPa, and 121 MPa respectively. These values of tensile strength increased to 143 MPa for ARB processed Al1050 alloy and 169 MPa for ARB processed Al1050-8 vol.% ilmenite composite after performing the seventh cycle of ARB. The elongation of Al-ilmenite composite showed a decreasing trend with change in reinforcement level from 0 to 8 vol%. However, the increase in number of ARB cycles resulted in enhancement of elongation as shown in Figure 2.17b. The increase in ARB cycles helped in reducing the porosity, provided good interfacial bonding and increase the uniformity of reinforced particles. All these parameters helped in increasing the elongation of base alloy and its composites. On the other hand, the presence of ilmenite particles resulted in accumulation of strain with in the alloy which caused reduction in elongation for AMCs.

(c) Hybrid AMCs reinforced with two different types of synthetic ceramic particles

The following section presents literature review on hybrid AMCs containing a combination of two different synthetic ceramic particles as reinforcement.

Ahlatci *et al.* [105] in **2006** investigated the wear behaviour of Al/(Al_2O_3+SiC) hybrid composites by varying the amount of Mg in the matrix. Composites were made by adding 37 vol.% of Al_2O_3 and 25 vol.% of SiC. Correspondingly, Mg content in matrix was varied till 8 wt.%. Pressure infiltration technique was used to fabricate aluminium matrix hybrid composites. XRD analysis revealed presence of Al_4C_3 and Si phases in both types of matrices. However, an additional precipitate of Mg_2Si was observed in Al-8% Mg matrix. Addition of Mg in hybrid composites resulted in improvement of matrix hardness and compressive strength. Moreover, decrement in porosity and impact toughness was also observed. Microstructure analysis showed presence of porosity around the reinforced particles. Porosity was mainly present near Al_2O_3 particles. However, the increase in wt.% of Mg resulted in increase of wettability of reinforced particles and/or decrease in threshold pressure for infiltration process. This helped in reducing the porosity for hybrid composites. The increase in hardness of composites with addition of Mg was attributed to solid solution hardening of matrix and precipitation of intermetallics i.e. Mg_2Si. Further, Al-Mg alloy composites showed 60% higher value of compressive strength and 70% lower value of impact toughness than pure

Al composite as shown in Figure 2.18a and Figure 2.18b, respectively. This signified that the impact toughness of composites was mainly affected by the matrix hardening and helped in overcoming the effect of porosity.

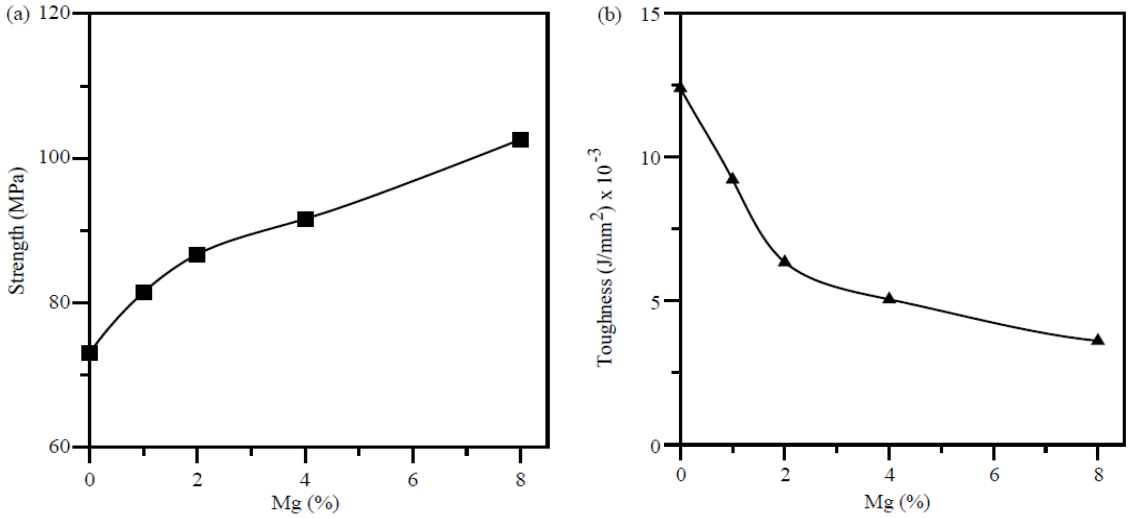

Figure 2.18 Variation of (a) maximum compression strength, and (b) impact toughness with Mg content of the matrix [105].

Composites showed increase in metal-metal and metal-abrasive wear resistance with increase in Mg content. However, increase in testing temperature resulted in decline of abrasive resistance. Worn surface analysis showed formation of iron rich layer during metal-metal wear test whereas for abrasive wear, it showed presence of grooves formed due to abrasive grains. Al-Mg alloy composite showed abrupt increase in wear rate above 200 ℃ in comparison to pure Al composite.

Uthayakumar *et al.* [38] in **2013** examined the dry sliding wear behaviour of stir cast hybrid AMCs reinforced with 5 wt.% of SiC (average particles size: 10 µm) and 5 wt.% of B_4C (average particles size: 65 µm) particles. Metallurgical study of composites showed uniform distribution of reinforced particles in the aluminium matrix. Wear performance of composites were evaluated using pin-on-disc tribometer. Wear tests were performed by varying the sliding speed and applied load over a range of 1–5 m/s and 20–100 N respectively. Figure 2.19a and Figure 2.19c show the effect of sliding velocity and applied load on wear rate of AMCs respectively. However, the variation of coefficient of friction with respect to sliding velocity and applied load is shown by Figure 2.19b and Figure 2.19d, respectively. Wear test revealed that beyond 60 N load and 4 m/s sliding speed, composite showed an increasing trend in wear rate and coefficient of friction as shown in Figure 2.19. Reduction in coefficient of friction till 60 N load was observed due to formation of boron oxide rich tribo-layer. At lower sliding

speeds (below 4 m/s), rate of formation of tribo-layer was more as compared to samples tearing which got reversed at higher sliding speeds and increased wear rate. Also, increase in heat generation during sliding resulted in softening of composite pin.

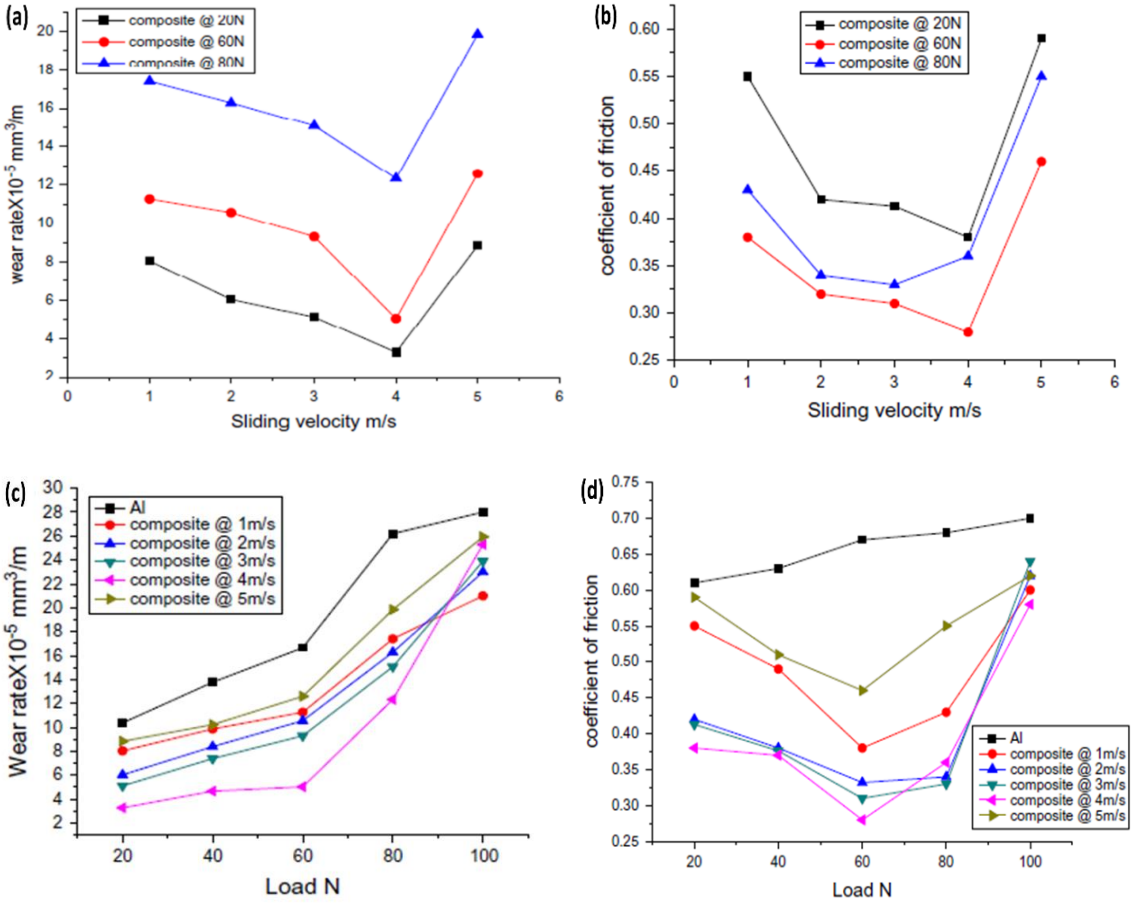

Figure 2.19 Effect of sliding velocity on (a) wear rate, and (b) coefficient of friction, and effect of load on (c) wear rate, and (d) coefficient of friction [38].

Tribo-layer formed was a mixture of pulled-out particles and oxides of both, the composite pin and the counter surface material. This layer had a low shear strength which prevented direct metal-to-metal contact and reduced the wear rate at low applied load and sliding speed conditions. At higher load conditions, protruded reinforcement led to tearing of tribo-layer, and increased the localized stresses causing larger wear debris. This also led to three body abrasion condition by the pulled out reinforced particles. Focused ion beam study on subsurface deformation showed increase in deformation with increase in applied load. For sliding speed range of 1–4 m/s, wear mechanism changed from mild abrasion to severe abrasion with change in load range from 20–60 N to 80–100 N. However, at higher load and sliding speed conditions, melt wear was also observed due to generation of high order of localized stress.

Kumaran and Uthayakumar [125] in **2014** analyzed the effect of applied load and sliding velocity on wear properties of AA6351 alloy composites. The stir casting process was used to add 5 wt.% of SiC and 5 wt.% of B_4C particles in AA6351 aluminium alloy. The wear process parameters were varied from 20–100 N and 1–5 m/s. When applied load and sliding speed was varied from 20–60 N and 1–3 m/s, the rise in wear rate was less significant as shown in Figure 2.20. This was attributed to addition of hard ceramic particles and formation of boron oxide thick layer on the mating surfaces. The formation of tribo layer helped in reduction of wear rate by acting as a third body component between the counter surfaces. When applied load and sliding speed were increased beyond 60 N and 3 m/s, a sharp increase in wear rate was observed as shown in Figure 2.20a and Figure 2.20b, respectively. This was ascribed to rise in surface temperature which decreased the stability of tribo-layer and exposed the sliding surface to steel disc for increasing the wear rate.

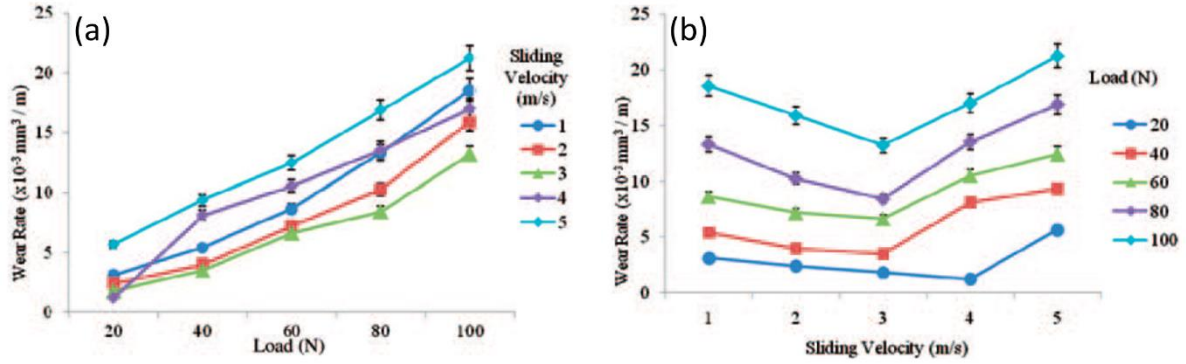

Figure 2.20 Effect of (a) applied load and (b) sliding velocity on wear rate of hybrid AMCs [125].

For coefficient of friction, the increase in applied load and sliding velocity till 60 N and 3 m/s showed a decreasing trend. This was attributed to formation of strong interfacial bonding by ceramic particles which resulted in effective transfer of load from matrix to reinforced particles. Due to effective transfer of load, a reduction in deformation of composite was observed which caused a reduction in COF values. Further, the increase in COF for rise in applied load and sliding speed beyond optimum value was ascribed to pulling out of reinforced particles from sliding surface. SEM images of worn surface revealed presence of shallow grooves and craters at low load conditions. With increase in applied load from 60–80 N and sliding velocity from 1–5 m/s, severe abrasion was observed on the sliding surface. This signified that entrapment of hard ceramic particles led to abrasive action on sliding surfaces. The increase in load beyond 80 N showed a transition in wear mechanism from abrasive to delamination wear.

Show *et al.* [126] in **2014** analyzed the effect of single (Al_2O_3) and dual (Al_2O_3+SiC) reinforcement on dry sliding wear characteristics of 6351 aluminium alloy. Stir casting process was used to fabricate both types of composites. The reinforcement level was kept at a volume percentage of 4 vol.%. However, the dual reinforced 6351 aluminium composite was made by mixing SiC and Al_2O_3 particles in equal proportions. The particle size used for SiC and Al_2O_3 was 25±6 µm and 10±3 µm respectively. The addition of hard SiC (28 GPa) and Al_2O_3 (18 GPa) particles in 6351 Al alloy resulted in high hardness in both, single and dual reinforced AMCs. Highest hardness value was shown by SiC+Al_2O_3 reinforced AMCs which was followed by Al_2O_3 reinforced AMCs and 6351 Al alloy as given in Table 2.5.

Table 2.5 Hardness of 6351 Al alloy and its composites [126].

Composite of samples	Hardness (HV)
6351 Al alloy	55±0.17
6351 Al alloy+4 vol.% of Al_2O_3	59±0.78
6351 Al alloy+2 vol.% of Al_2O_3+2 vol.% of SiC	61±1.89

The increase in applied load from 19.6 N to 63.8 N led to rise in wear rate of AMCs. Highest reduction in wear rate was observed for 6351 Al-2 vol.% SiC-2 vol.% Al_2O_3 composite. At low load conditions, the resistance to wear rate of base alloy was provided by the hard reinforced particles. However, the increase in applied load to 63.8 N led to breakdown of reinforced particle clusters which resulted in rise of wear rate for AMCs. In comparison to base alloy, the reduction in wear rate at higher load conditions was attributed to formation of tribo-oxide layer by rise in temperature due to frictional heat. Further, the analysis of 6351 Al alloy composite with Al_2O_3 particles signified that reinforced particles acted as nucleation site for oxidation.

Muley *et al.* [127] in **2015 s**tudied the effect of nano-hybrid reinforcement on mechanical and tribological properties of LM6 Al based stir cast composites. Nano-particles of SiC/Al_2O_3 were mixed in equal ratio and added as 0.5, 1.0, 1.5, and 2 wt.%. The reinforced particles were observed to be uniformly distributed in the LM6 alloy. However, the high surface energy of particles led to negligible amount of agglomeration. Figure 2.21 presents the graphs of microhardness, ultimate tensile strength (UTS), and wear loss. Microhardness of composites increased with increase in reinforcement level as shown in Figure 2.21a. Further, there was increase in residual stresses due to mismatch of thermal expansion between matrix and reinforcement resulting in higher dislocation density and increased hardness.

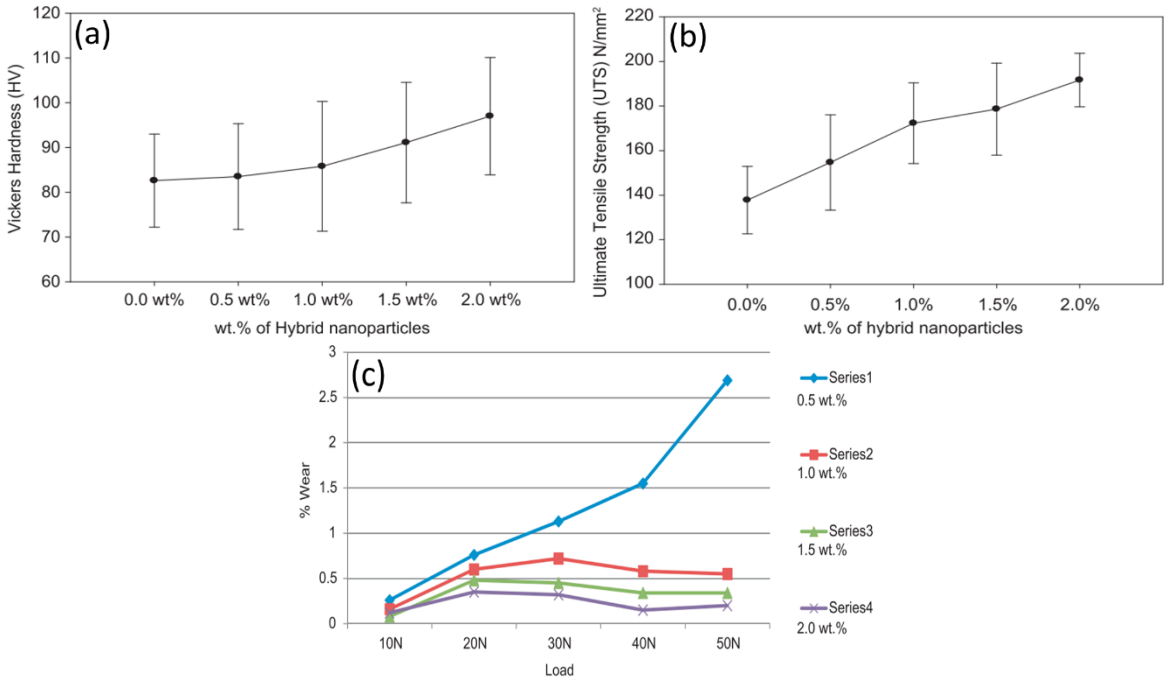

Figure 2.21 (a) Hardness, (b) ultimate tensile strength, and (c) wear loss of hybrid composites [127].

The hardness of composites increased from 84 HV to 98 HV with rise in reinforcement level to 2 wt.%. UTS showed increasing trend due to effective load transfer from matrix to the better bonded and uniformly distributed reinforcement. For 2 wt.% reinforcement, UTS value increased from 138 N/mm^2 (of base alloy) to 193 N/mm^2 as shown in Figure 2.21b. However, the increase in applied load led to rise in wear loss for all compositions of composites as shown in Figure 2.21c. The addition of SiC particles were responsible for reduction in flow of material and resulted in formation of SiO_2 on sliding surfaces which created a lubricity effect. Moreover, SiC particles promoted formation of iron rich (Fe_3O_4) layer on sliding surfaces which resulted in lower wear loss. The addition of Al_2O_3 improved hardness and strength of composites. Out of both the reinforcements, SiC particles were more effective than Al_2O_3 particles due to their high hardness and better wettability.

Singh and Goyal [128] in **2016** studied the dry sliding wear characteristics of T6 heat treated AA6982 alloy reinforced with SiC and B_4C particles. Response surface methodology (RSM) was used to optimize the wear parameters such as reinforcement level (0 to 20 wt.%), sliding speed (0.6 to 3 m/s), load (14.71 to 73.55 N) and sliding distance (400 to 2000 m). The stir casting process was used to incorporate the combination of SiC and B_4C in 5 to 20 wt.%; with a step size of 5 wt.%. Both the reinforced particles were mixed in equal weight percentage at a particular reinforcement level. SEM micrographs revealed uniform distribution of reinforced particles whereas some agglomeration of particles were observed with increase in

concentration of particles. Further, the formation of precipitates of intermetallic (Mg_2Si) was also observed for all the composites. Till 15 wt.% of reinforcement level, hardness of composites increased from 101 HV to 113 HV due to presence of hard ceramic particles. However, addition of 20 wt.% of SiC and B_4C resulted in hardness of 111 HV (Table 2.6). This was attributed to agglomeration of reinforced particles.

Table 2.6 Micro-hardness of hybrid AMCs at different weight percentage [128].

Sample composition	HV 1	HV 2	HV 3	HV average
AA6082-T6 alloy	100	102	101	101
AA6082-T6-2.5 wt.% SiC-2.5 wt.% B_4C	104	103	105	104
AA6082-T6-5 wt.% SiC-5 wt.% B_4C	107	108	111	109
AA6082-T6-7.5 wt.% SiC-7.5 wt.% B_4C	112	113	115	113
AA6082-T6-10 wt.% SiC-10 wt.% B_4C	111	110	111	111

The wear rate of hybrid composites decreased with increment in reinforcement level and sliding speed. This was attributed to rise in hardness of composites and reduction in damage caused by trapped debris between sliding surfaces. At higher sliding speeds, the mechanical strength of counter surfaces enhanced due to rise in shear rate and simultaneously reduced the contact time between the sliding surfaces. The increase in applied load and sliding distance showed higher value of wear rates. This was attributed to increment in contact stresses and interaction of counter surfaces. RSM analysis revealed the sequence of factors influencing the wear rate as sliding distance, sliding speed, load, and reinforcement level. However, the only interaction of load and sliding distance was considered as effective in influencing the wear rate of AMCs. The error in predicted values from the equation given by RSM analysis and experimental value was observed in the range of 3 to 7%.

Ekka *et al.* [129] in **2016** investigated the effect of different combinations of cenosphere, SiC and Al_2O_3 particles on the wear characteristics of Al7075 aluminium alloy composites. In each combination of reinforcement (viz. cenosphere+SiC, cenosphere+Al_2O_3, and SiC+Al_2O_3), individual reinforced particles were added in 4 wt.%. Uniform dispersion of reinforced particles was obtained by using stir casting process. Taguchi analysis was performed by varying the combination of reinforcement, load (35, 55, and 75 N), and sliding speed (1.5, 2.25, and 3 m/s). From ANOVA analysis, applied load (B) showed an influence of 53.86% on wear rate of composite which was followed by 16.69% for different combination of reinforcements (A) and 9.99% for interaction of both the factors. Sliding speed (C) showed a negligible effect on the wear rate of hybrid composites. For coefficient of friction (COF), the contribution value for applied load was 15.13% whereas other factors showed negligible effect. The interaction of combination of reinforcement and applied load showed a contribution of 19.97% whereas

an influence of 28.68% was obtained for interaction of applied load and sliding speed. The wear rate of composites showed increasing trend with rise in applied load. This was attributed to rise in plastic deformation and delamination wear of sliding surfaces. In contrast to this, the increment in sliding speed and the combination of SiC-cenosphere showed reduction in wear rate values. This was ascribed to reduction in contact time between the sliding surfaces. COF showed reduction in values with rise in applied load and sliding speed. This was attributed to formation of mechanical mixed layer which converted two body wear to three body wear. Regression and ANN model was used to predict the values of wear rate and coefficient of friction. The error in predicted value of wear rate and coefficient of friction was observed to be lesser for ANN model in comparison of regression analysis as shown in Figure 2.22a and Figure 2.22b.

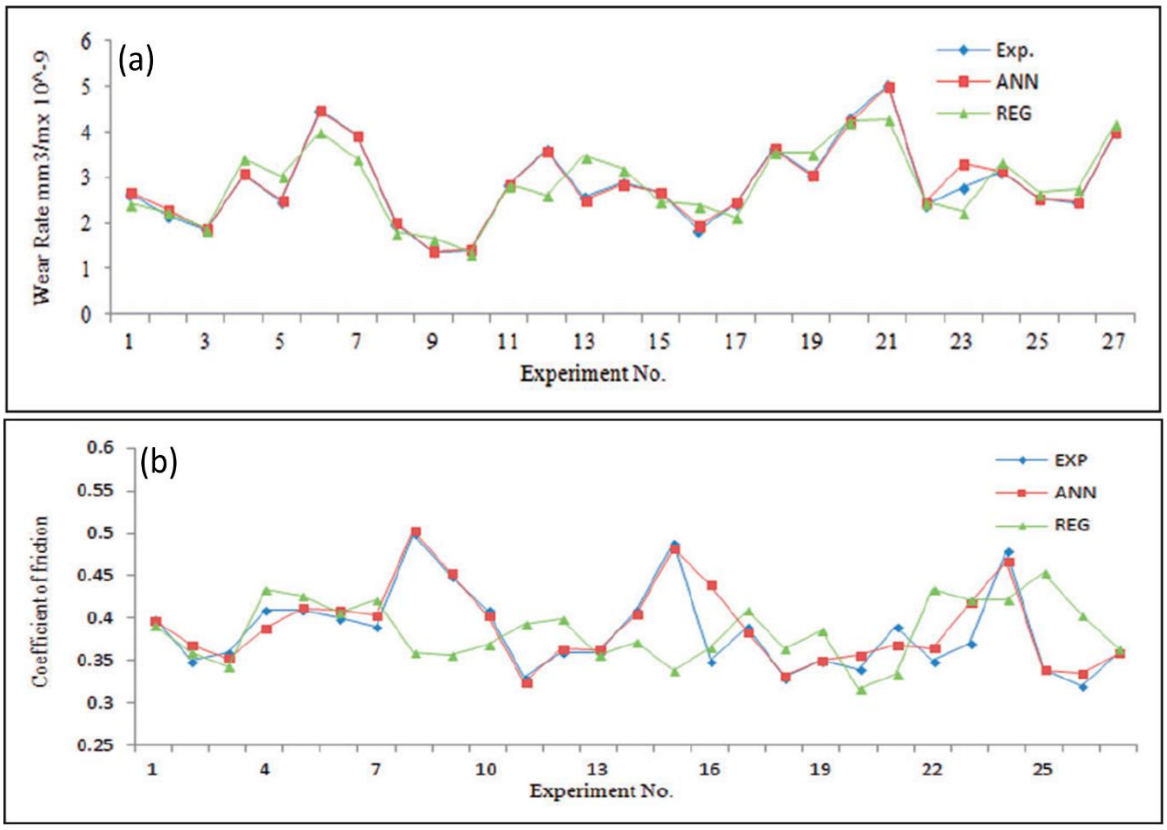

Figure 2.22 Comparison of (a) wear rate and (b) coefficient of friction values obtained from experiment, ANN model, and regression model [129].

Ghasali *et al.* [106] in **2017** fabricated aluminium matrix composites (AMCs) by using different heating methods. Pure aluminium and 1056 aluminium powder were used as matrix whereas SiC and TiC particles were used as reinforcement. Composites were made by adding 15 wt.% of SiC and 7 wt.% of TiC in two different matrix material i.e. pure aluminium and 1056 aluminium powder. Samples of size 5×5×25 mm^3 were made by applying pressure of 240

MPa on powder mixture of matrix and reinforcement. Further, samples were sintered at 650 ℃ and 750 ℃ for 1 hour and without soaking time. Heat rate of sintering process was varied by using two different furnaces i.e. conventional and microwave furnace. In conventional furnace, composites were heated at a rate of 10 ℃/min whereas in microwave furnace, it was 60 ℃/min. XRD analysis showed the presence of aluminium along with crystalline phase of SiC and TiC for both the matrix i.e. pure Al and 1056 Al. Figure 2.23a and Figure 2.23b show the XRD pattern of 1056 Al and pure aluminium obtained after the sintering process.

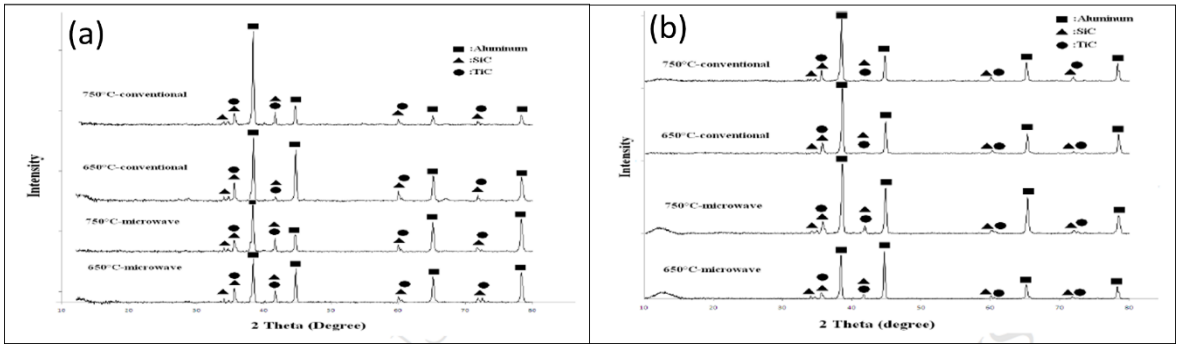

Figure 2.23 XRD patterns of sintered samples with (a) 1056 aluminium and (b) pure aluminium as matrix [106].

After sintering at 750 ℃ in microwave furnace, composites formed by Al-1056 powder showed higher values of relative density, bending strength and microhardness i.e. 96.32±0.3, 340±14 MPa and 192±10 Vickers. SEM analysis revealed uniform distribution of reinforced particles in both the matrix under conventional and microwave heating methods.

Das *et al.* [130] in **2018** studied the effect of sliding speed, normal load, and sliding distance on the wear properties of stir-cast AA6061 hybrid AMCs. The composites were fabricated in two different combinations of hybrid A (0.5 wt.% SiC and 1.5 wt.% B_4C) and hybrid B (1.5 wt.% SiC and 1.5 wt.% B_4C). Testing parameters for dry sliding wear test were varied in three levels viz. sliding distance (1000, 1500, and 2000 m), sliding speed (100, 300, and 500 rpm) and normal load (10, 20, and 30 N). For all samples, the track diameter was maintained at 240 mm. Wear rate of composites showed increasing trend with rise in normal load and sliding speed as shown in Figure 2.24a–d and Figure 2.24e–h, respectively. This was attributed to softening of sliding surfaces due to rise in surface temperature. In addition to this, the increase in sliding distance and weight percentage of SiC particles led to reduction in wear rate as shown in Figure 2.24. The increase in concentration of SiC particles prevented the exposure of matrix material to counter surface which helped in enhancing the wear resistance of composites. Further, the increase in sliding distance led to formation of mechanically diversified layer on sliding surfaces. This reduced the stress acting on the composite surface which led to decrease

in plastic deformation and wear rate of composites. Coefficient of friction showed reduction in values with rise in normal load and sliding speed. This was attributed to reduction in area of contact by matrix material which affected the rise in temperature of sliding surfaces.

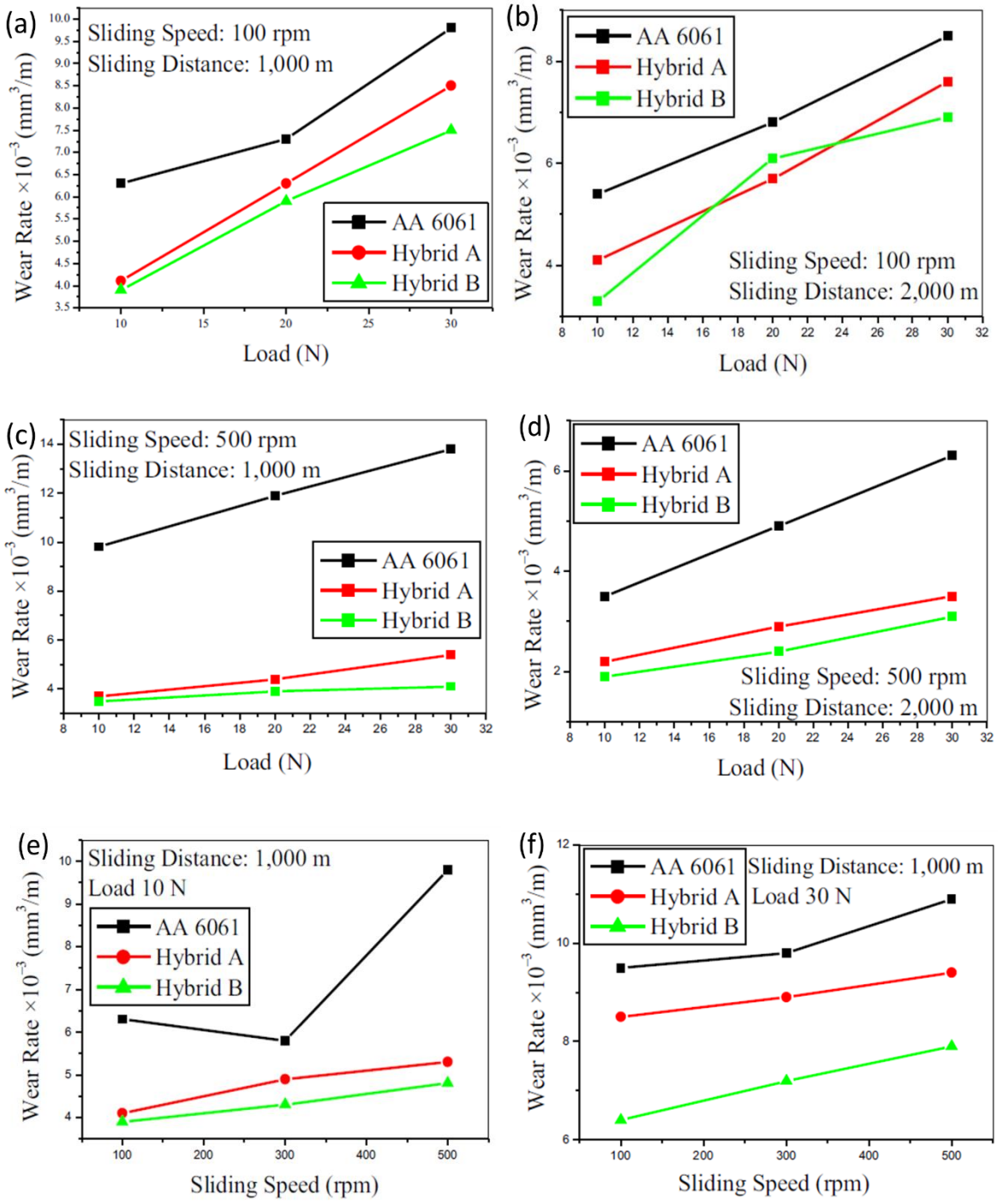

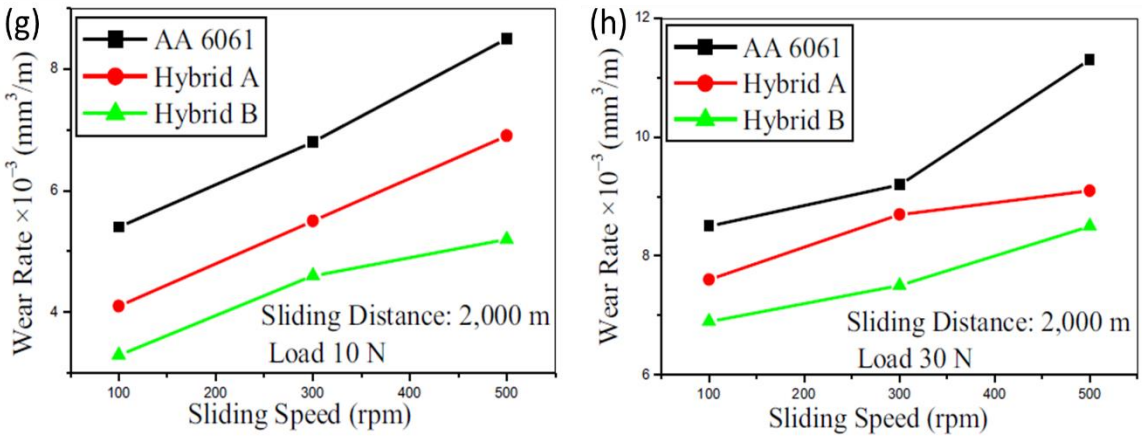

Figure 2.24 Variation in wear rate of hybrid AMCs as a function of normal load for different combination of sliding distance and sliding speed i.e. (a) 100 rpm & 1000 m, (b) 100 rpm & 2000 m, (c) 500 rpm & 1000 m, (d) 500 rpm & 2000 m. Variation in wear rate of hybrid AMCs as a function of sliding speed for different combination of sliding distance and normal load i.e. (a) 10 N & 1000 m, (b) 30 N & 1000 m, (c) 10 N & 2000 m, (d) 30 N & 2000 m [130].

The Taguchi analysis of wear rate revealed that sliding speed was the most influential factor which was followed by normal load and sliding distance. This sequence was followed by both the composites i.e. hybrid A and hybrid B. In case of coefficient of friction, normal load was found to be the most influential factor for hybrid A composites whereas, sliding speed was most significant factor for hybrid B composites.

Sethi *et al.* [107] in **2019** studied the thermal and mechanical properties of yttrium tungstate ($Y_2W_3O_{12}$)-aluminium nitride (AlN) reinforced AMCs. Composites were prepared by following the processes of high energy ball milling, compaction, sintering and forging. Mixing of both the reinforcements was done in such a way that one reinforcement was added in 30 wt.% whereas other reinforcement was added in range of 0–15 wt.% (step size: 5 wt.%). Forged composites showed higher relative density as compared to sintered composites. Forged composites showed relative density of 90% which was ascribed to better diffusion of metal during forging process. Hybrid composites showed improved hardness due to uniform dispersion of particles, high hardness of each filler, difference in CTE of matrix and reinforcement, and elastic modulus mismatch. The variation of compressive strength and yield strength for change in weight percentage of $Y_2W_3O_{12}$ and AlN is shown in Figure 2.25. Improvement in compressive strength was additionally influenced by the effectiveness of load transfer from soft matrix to hard reinforced particles. When 5, 10 and 15 wt.% of AlN particles were added in 30 wt.% of $Y_2W_3O_{12}$ composites, then improvement of 29%, 37% and 43%, respectively in compressive strength was observed as shown in Figure 2.25a. Thermal strain

analysis revealed that on increase in weight percentage of reinforcement, work hardening capacity of Al matrix increased. Work hardening of Al matrix occurred mainly at the interfacial region of matrix and particles. This resulted in reduction of residual strain present in the composites.

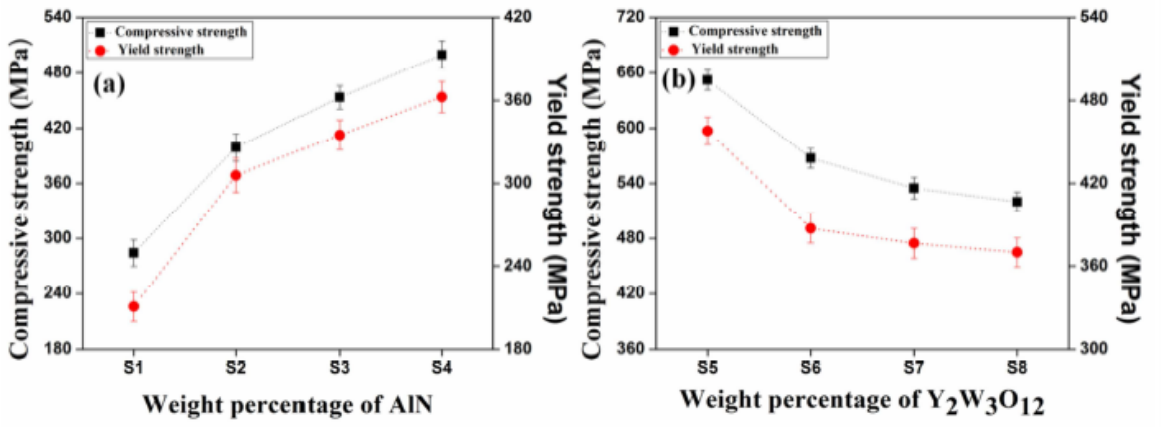

Figure 2.25 Compressive strength of (a) 30 wt.% $Y_2W_3O_{12}$ composite with S_1 = 0 wt.%, S_2 = 5wt.%, S_3 = 10 wt.%, S_4 = 15 wt.% of AlN particles and (b) 30 wt.% of AlN composite with S_5 = 0 wt.%, S_6 = 5wt.%, S_7 = 10 wt.%, S_8 = 15 wt.% $Y_2W_3O_{12}$ [107].

During thermal strain test, no phase transformation was observed which meant that hybrid composites were thermally and dimensionally stable. Composites showed increase in thermal conductivity with increase in AlN reinforcement level. AlN particles possess higher thermal conductivity as compared to $Y_2W_3O_{12}$ particles. However, the increase in phonon scattering at high temperatures led to reduction in thermal conductivity. At constant weight percentage of $Y_2W_3O_{12}$, the increase in wt.% of AlN led to rise in hardness, compressive strength and thermal conductivity. In contrast, a reduction in thermal conductivity values were observed. On the other hand, the increase in wt.% of $Y_2W_3O_{12}$ at fixed amount of AlN resulted in reduction of compressive strength (Figure 2.25b), thermal conductivity and coefficient of thermal expansion (CTE) whereas an increase in hardness value was observed.

Fenghong *et al.* [131] in **2019** studied the mechanical and wear properties of stir-cast AMCs. Al6061 was used as the base material whereas SiC and WC were used as the reinforcement. The average particle size used for SiC and WC was 125 µm and 3 µm respectively. The reinforcement particles were added in 5, 7.5, and 10 wt.%. Microstructural analysis revealed uniform dispersion of reinforced particles. SEM showed that reinforced particles were mainly present at grain boundary cavity. At interfacial sites, precipitates of Mg_2Si and undissolved Al6 (Fe, Mn) in aluminium solid solution were observed. Increase in hardness of composites was observed due to presence of stiffer and strong reinforcement i.e. SiC and WC in the matrix.

Addition of both reinforcements i.e. SiC and WC in matrix showed significant improvement in compressive strength, tensile strength, and wear resistance.

Table 2.7 Wear analysis of Al6061/SiC/WC composites [131].

Sample	Applied load (N)	Initial weight in "g"	Final weight in "g"
Al6061 + 5%SiC+5%WC	20	3.905	3.789
	10	4.322	4.302
Al6061 + 7.5%SiC+7.5%WC	20	3.856	3.645
	10	4.234	4.105
Al6061 + 10%SiC+10%WC	20	3.756	3.648
	10	4.120	4.082

The increase in tensile strength and yield strength of composites was attributed to strong interfacial bonding between matrix and reinforcement. On comparison with base alloy, 38% improvement in tensile strength and 30.76% improvement in yield strength was observed. However, 86% decrease in percentage elongation was observed. This was due to reduction in elastic deformation. For compressive strength, reinforcements helped in restricting the material flow and crack propagation. Table 2.7 shows wear analysis of hybrid composites. With increase in applied load and sliding distance, temperature at the point of contact between sliding surfaces increased due to rise in frictional force. This described the cause for increase in variation of wear w.r.t time under high load conditions.

Suresh *et al.* [132] in **2019** investigated the effect of Al_2O_3 and SiC particles reinforcement on the mechanical and tribological properties of Al 7075 aluminium alloy. Besides this, magnesium was also added in the composites to enhance the wettability of reinforced particles. The composites were fabricated by using stir casting process. The mixing of reinforced particles was done by adding the same amount of weight percentage i.e. 1, 2, 3, and 4 wt.% respectively whereas magnesium particles were added in 1 wt.%. The particle size used for SiC and Al_2O_3 was 50 nm and 20–30 nm respectively.

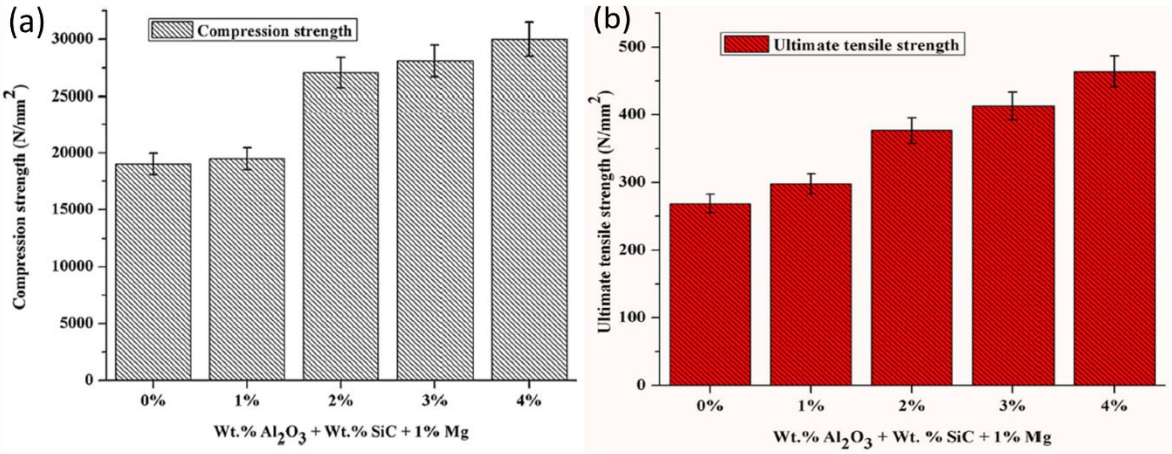

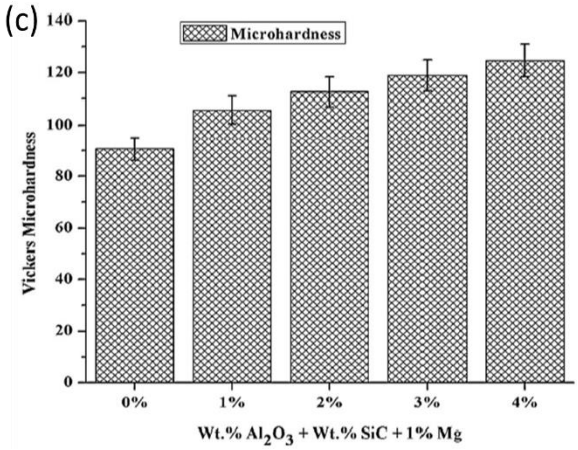

Figure 2.26 Effect of hybrid reinforcement on (a) compressive strength, (b) tensile strength, and (c) hardness on Al7075 alloy [132].

SEM image of polished surface of AMCs showed uniform distribution of reinforced particles. The addition of Mg particles restricted the formation of Al_4C_3 at the interface regions and the formation of oxides at the surface of particles prevented the occurrence of chemical reaction with matrix alloy. The tensile strength of base alloy increased from 269 MPa to 463 MPa when reinforced particles were added in 4 wt.% as shown in Figure 2.26b. Similarly, compressive strength and hardness showed an increasing trend with rise in concentration of reinforced particles as shown in Figure 2.26a and Figure 2.26c, respectively. The highest reduction in wear rate and friction coefficient was obtained for Al7075/4 wt.% SiC/4 wt.% Al_2O_3 composites. Increase in applied load showed rise in wear rate of hybrid composites. The improvement in wear rate of AMCs was attributed to enhancement in hardness of base alloy and reduction in physical contact of matrix with the counter surface.

Am *et al.* [133] in **2019** analyzed the dry sliding wear characteristics of SiC and Al_2O_3 reinforced hybrid AMCs. The wear characteristics of stir-cast Al7075-SiC-B_4C composites were compared with T6 heat treated Al7075-SiC-B_4C composites. T6 heat treatment was performed by water quenching the samples heated at 465 ℃ for 2 hours. Further, these samples were kept at a temperature of 120 ℃ for 5 hours and allowed to cool in atmospheric conditions. The reinforced particles were added in three different weight percentages of 10, 20 and 30 wt.% in which SiC and B_4C particles were mixed in equal proportions. The wear rate of composites were analyzed by varying the sliding distance, reinforcement level, and normal load. With increase in sliding distance and normal load, wear rate showed an increasing trend. This was attributed to softening of sliding surfaces due to rise in surface temperature which increased the plastic deformation and wear loss of sliding surfaces. On the other hand, the T6 heat treatment and particles addition led to reduction of wear loss for hybrid composites. This was

ascribed to lubricity effect shown by reinforced particles. At different applied load conditions, the wear rate of hybrid composites was influenced by formation of mechanical mixed layer (MML) on sliding surfaces. The thickness of MML and rise in surface temperature was less at low load conditions. With rise in applied load, both the parameters showed an increasing trend. For Al7075-15 wt.% SiC- 15 wt.% B_4C composite, the rise in temperature was so significant that MML was unable to protect the composite surface. This led to rise in wear rate with increase in reinforcement level from 20 wt.% to 30 wt.%. SEM analysis of worn surfaces revealed formation of wide and shallow grooves for as-cast hybrid composites. The grooves transformed to small and fine grooves when T6 heat treatment was performed on composites.

Hillary *et al.* [134] in **2020** examined the tribological properties of SiC and TiB_2 reinforced Al6061 aluminium alloy composites. Varying amounts of TiB_2 particles (2, 4, 6, 8, and 10 wt.%) and constant amount of SiC particles (5 wt.%) were incorporated in Al6061 alloy using stir casting. Wear test was performed by varying the applied load from 10 to 40 N, sliding distance from 500 to 2000 m, and sliding velocity from 1.04 to 2.61 m/s. For all the composites, the rise in applied load led to increase in wear rate values. Besides this, a reduction in wear rate values was observed due to increase in concentration of TiB_2 particles. During interaction of sliding surfaces, the asperities of soft matrix (Al6061 alloy) made adhesion joints by cold welding with the hard counter surface. These adhesion joints broke and increased the material removal rate from sliding surfaces. Further, the increase in applied load led to rise in surface temperature and helped in work hardening of sliding surfaces. Both the factors helped in reducing the wear rate of composites by formation of oxides and mechanical mixed layer on sliding surfaces. However, the rise in surface temperature beyond critical point led to severity of delamination wear. The change in sliding distance from 500 m to 2000 m and sliding velocity from 1.04 m/s to 2.61 m/s resulted in rise of wear rate values for all the composites. This was attributed to reduction in stability of mechanically mixed layer. With increase in concentration of TiB_2, applied load, and sliding distance, coefficient of friction (COF) showed a decreasing trend. This was ascribed to reduction in adhesion joints and formation of iron oxides which acted as a lubricant agent. However, a rise in COF was observed with increase in sliding speed from 1.04 to 2.61 m/s. This was attributed to entrapment of fragmented lubricant layer between the sliding surfaces which acted as abrasive particles to enhance the COF of composites. The SEM analysis of worn surface revealed presence of smooth and fine grooves which corresponded to mild wear for Al6061+5 wt.% SiC +10 wt.% TiB_2 composites.

Pranavi *et al.* [135] in **2022** investigated the mechanical and tribological properties of Al5059-Al_2O_3-B_4C hybrid AMCs. The mixture of reinforced particles were added in weight percentage of 5 (SP1), 10 (SP2) and 15 (SP1) wt.% by using stir casting. Mixing of B_4C and Al_2O_3 particles was done in equal proportions. Hardness of hybrid composites increased with rise in reinforcement level from 5 to 15 wt.%. This was attributed to formation of strong interfacial bonding by reinforced particles with matrix and the high hardness of Al_2O_3 particles. In addition to this, reinforced particles were also responsible for reduction in dislocation movement generated by indenter of hardness tester. SP3 composite showed an improvement of 23.2% and 37.5% in tensile strength and elongation in comparison to base alloy. The effective transfer of load from matrix to reinforced particles was responsible for enhancement in tensile strength and elongation of hybrid composites. SEM images of fractured surface revealed presence of voids and ridges at lower concentration of reinforced particles. These features were presented due to insufficient distribution of particles. However, an improvement in distribution and bonding of reinforced particles with rise in reinforcement level led to improvement in strength of composites.

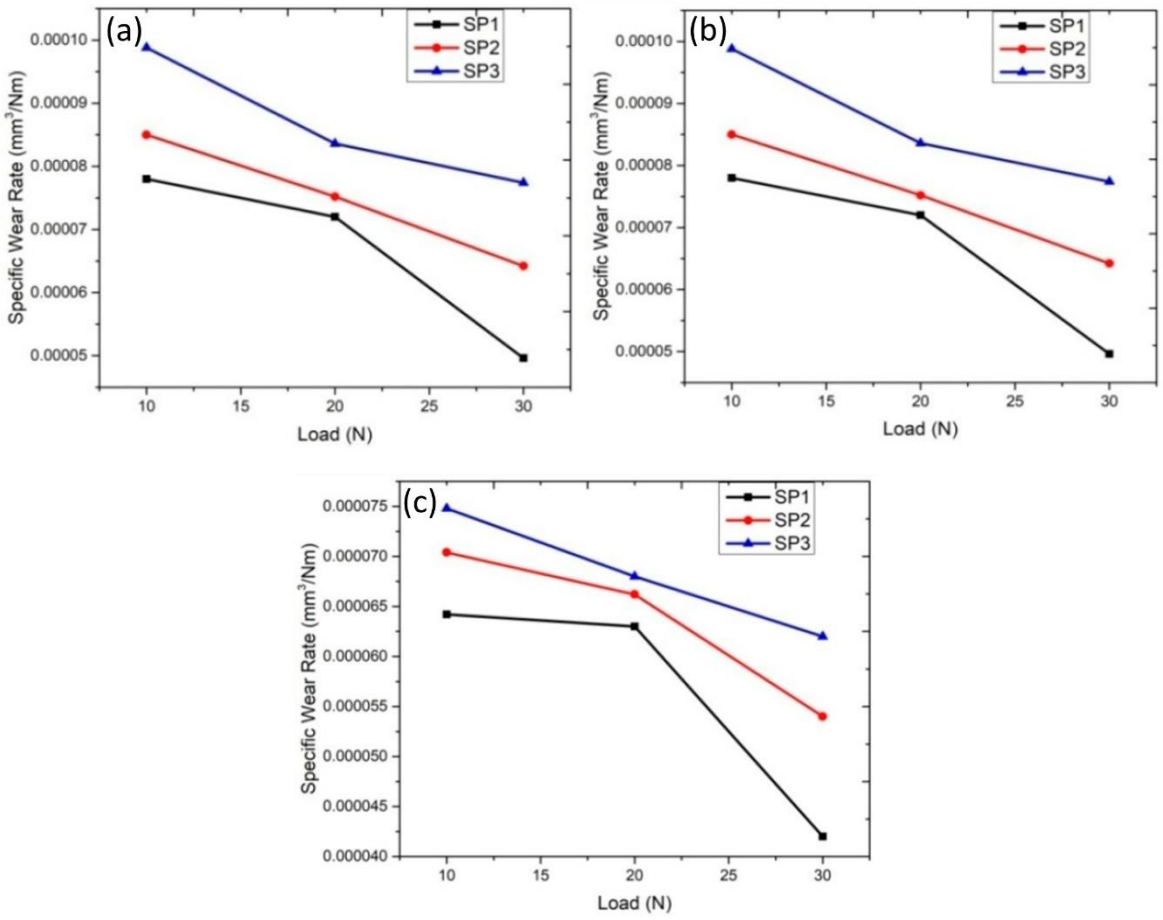

Figure 2.27 Change in wear rate of AMCs w.r.t load at (a) 500 rpm, (b) 600 rpm, and (c) 700 rpm [135].

The tribological properties of composites were studied by varying the sliding speed, applied load, and reinforcement level as shown in Figure 2.27. Figure 2.27a, Figure 2.27b, and Figure 2.27c represent the effect of applied load on specific wear rate of AMC at a sliding speed of 500 rpm, 600 rpm, and 700 rpm, respectively. The rise in reinforcement level showed a reduction in specific wear rate (SWR). In contrast, SWR showed increasing trend with change in applied load from 10 to 30 N and sliding speed from 500 rpm to 700 rpm. In context of reinforcement level, the reduction in SWR was ascribed to addition of hard ceramic particles and rise in hardness of base alloy by reinforced particles. These factors reduced the destruction of sliding surface under the action of applied load. Further, the increase in applied load and sliding speed led to increase in shear force acting between sliding surfaces which resulted in higher loss of material from counter surfaces. Coefficient of friction (COF) showed decreasing trend with rise in reinforcement level and applied load. However, the increase in sliding speed led to increment in COF value for hybrid composites. The variation in COF values was ascribed to reduction in exposure of base alloy to the counter surface due to addition of reinforced particles. Besides this, the increment in hardness of composite also affected the COF of composites.

(d) Hybrid AMCs reinforced with a combination of synthetic ceramic particles and mineral particles

This section discusses the literature available on AMCs and their properties reinforced with a combination of synthetic ceramic particles and minerals particles.

Das *et al.* [136] in **2009** studied the abrasive wear behavior of Al-Cu alloy reinforced with a combination of reinforcements of zircon and silicon carbide particles. The average particle size used for silicon carbide and zircon was 65 µm. However, an additional average particle size of 135 µm was used for zircon. The addition of silicon carbide and zircon particles in Al-Cu alloy was done using stir casting. Microstructure analysis revealed uniform distribution of reinforced particles. Further, decrease in particle size of zircon (from 135 µm to 65 µm) and the proportion of zircon particles led to rise in hardness of hybrid Al-Cu alloy composites. For all sliding distances, the wear rate of hybrid composites was superior to the monolithic alloy. Hybrid composite with smaller particles size of silicon carbide and zircon showed highest reduction in wear rate of Al-Cu alloy. This was attributed to the high hardness of composites, which decreases the penetration depth of counter surface. The variation of wear rate of hybrid composite in reference to sliding distance was found to be negligible when compared to variation that occurred in Al-Cu alloy. This was ascribed to the increase in dislocation density

caused by mismatch in coefficient of thermal expansion between matrix and reinforcement. The study of wear track revealed the presence of ploughing marks which attributed to the occurrence of abrasive type of wear mode.

Sharma *et al.* [104] in **2012** analyzed the combined effect of two particle reinforcement (silicon carbide and zircon) on the microstructure and wear resistance of LM13 aluminium alloy based AMCs fabricated by two-step stir casting process. LM13 alloy was melted at 750 ℃ and stirred at 630 rpm. Pre-heated (450 ℃) mixture of particles (zircon + SiC) was added to the molten mass. The particle size of both sands was in the range of 20−32 µm. After mixing, the slurry was allowed to solidify at room temperature. After solidification, the mixture was again re-melted and stirred for 12–15 min. Different proportions used for mixing zircon sand and SiC for 15 wt.% was 1:0 (composite A), 1:3 (composite B), 1:1 (composite C), 3:1 (composite D), and 0:1 (composite E). The dendritic morphology present in the base alloy was modified in the presence of reinforced particles. These dendrites were refined due to increase in restrictions and nucleation rate by reinforced particles. The increase in percentage of SiC particles resulted in highest refinement and change in morphology to globular.

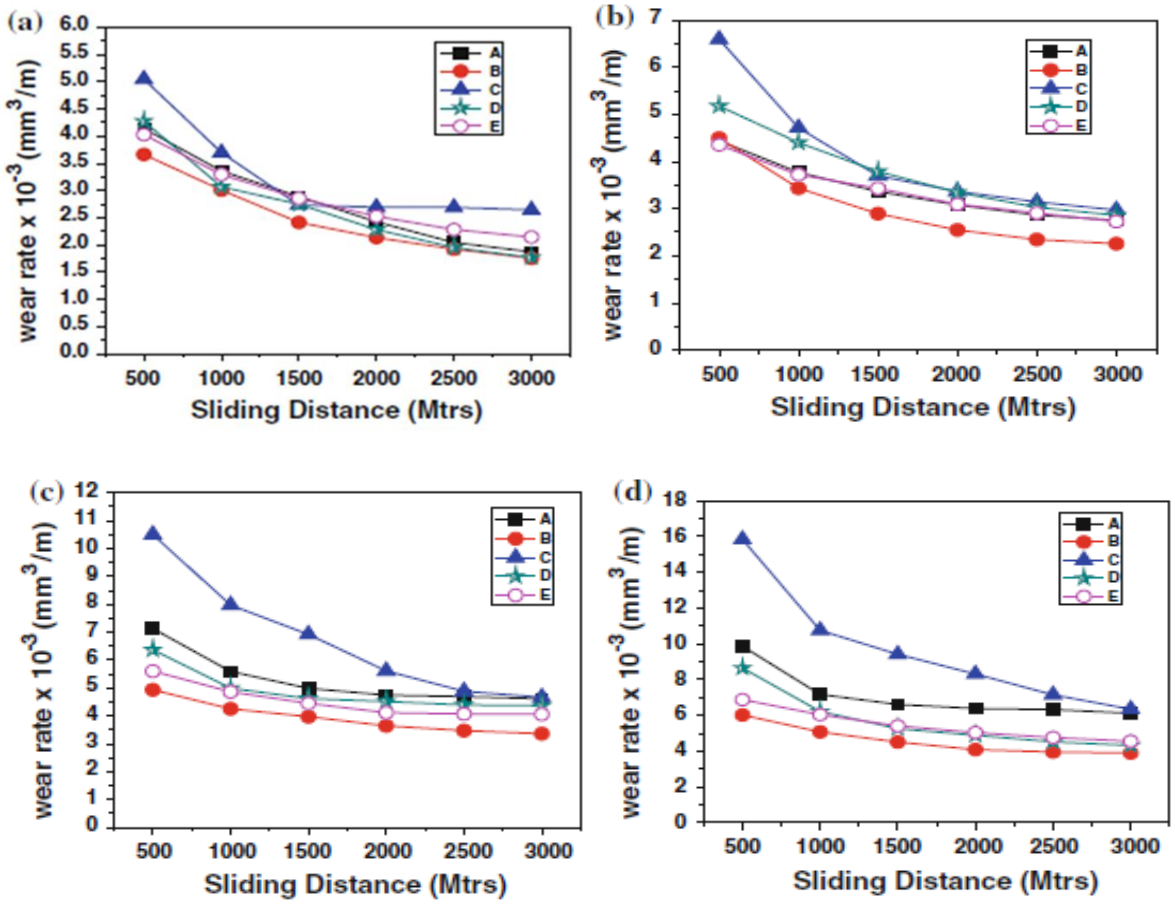

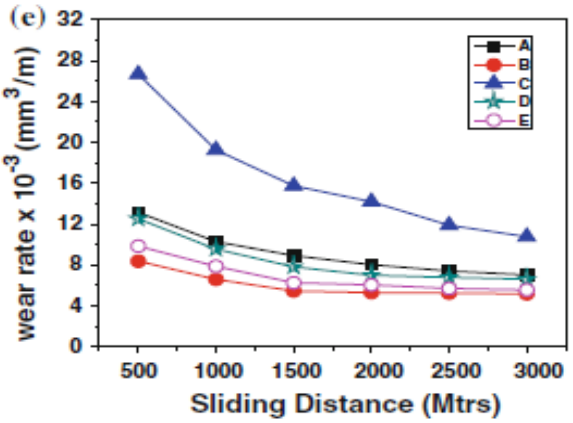

Figure 2.28 Wear rate of different composites at a sliding distance of 0–3000 m and applied load of (a) 1 kg, (b) 2 kg, (c) 3 kg, (d) 4 kg, and (e) 5 kg [104].

Microhardness taken at interfacial region revealed that zircon sand particles formed strong interfacial bonding with the matrix material. Dual particle reinforcement enhanced wear resistance of base alloy as compared to single particle reinforcement for any given proportion. The combination of 75% SiC and 25% zircon reinforced composite yielded better wear resistance as compared to other combinations at each applied load condition as shown in Figure 2.28a–e. SEM images revealed that delamination mechanism was mainly responsible for wear at high loads.

Rajmohan *et al.* [137] in **2013** investigated the effect of silicon carbide and mica on mechanical and tribological properties of Al356 aluminium alloy composites. The average particle size used for silicon carbide and mica was 25 µm and 45 µm respectively. Stir casting was used to fabricate AMCs by adding a fixed amount of SiC (10% in mass fraction) and varying the mica content from 0–6%. Further, ANOVA analysis was performed by selecting three levels of sliding distance (0.314, 0.942, and 1.57 m/s), load (9.81, 29.43, and 49.05 N), and mass fraction of mica (0, 3, and 6%). Further, the increase in sliding velocity led to reduction in wear loss. This was attributed to the oxidation of sliding surfaces due to rise in interfacial temperature. The oxide layer formed helped in separating the sliding surfaces, and its low shear strength was responsible for the reduction in coefficient of friction values. Further, ANOVA analysis revealed that wear loss was mainly influenced by applied load which was followed by mass fraction of mica.

Kumar *et al.* [79] in **2013** studied the tribological properties of LM13 based AMCs reinforced with dual reinforced particles. Different combinations of two ceramic sand particles (zircon and SiC; particle size: 20–32 µm) were used in the ratio of 1:3, 1:1 and 3:1 (total wt.%: 15 wt.% only). Hybrid composites were compared individually with only zircon reinforced and

SiC particle reinforced composites. Two-step stir casting process was used for the fabrication of composites. Microstructural analysis showed uniform dispersion of reinforced particles in the matrix. Further, increase in proportion of SiC particles in comparison of $ZrSiO_4$ particles led to higher refinement of eutectic silicon and morphology of eutectic silicon changed to globular. LM13 alloy with 3.75 wt.% of $ZrSiO_4$ and 11.25 wt.% of SiC showed superior wear characteristics as compared to other composites. With increase in temperature, a linear increase in wear was observed at both the applied load conditions i.e. 1 kg and 5 kg as shown in Figure 2.29a and Figure 2.29 b, respectively. After 200 ℃, transition in wear from mild to serve condition was observed due to thermal softening of composites causing plastic deformation of samples as shown in Figure 2.29.

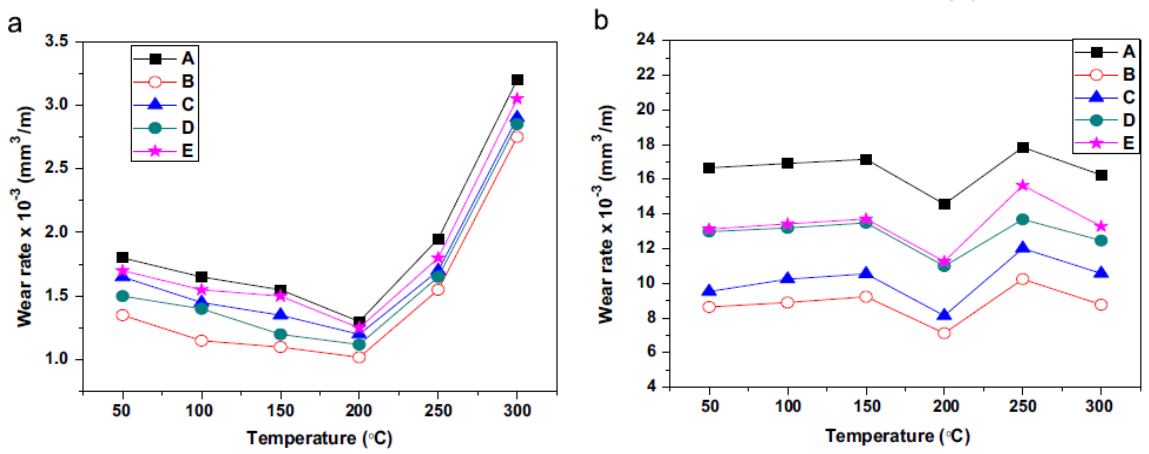

Figure 2.29 Wear rate against temperature of composites with (a) 1 kg load and (b) 5 kg [79].

At low temperature (till 200 ℃) and low applied load (1 kg), adhesive wear was responsible for removal of material whereas at higher temperatures (above 200 ℃) and applied load (5 kg), delamination was responsible for wear of composites. At higher temperatures and applied loads, decrease in wear rate was attributed to formation of oxide glazing layer on sliding components. These layers helped in preventing the metal-to-metal contact between counter surfaces.

Patel *et al.* [138] in **2014** studied the effect of SiC and $ZrSiO_4$ (zircon) particle reinforcement on microstructure/mechanical properties of ADC-12 aluminium alloy. SiC and $ZrSiO_4$ particles were reinforced with different wt.% combination of A (9+3), B (6+6) and C (3+9) wt.% respectively in ADC-12 alloy stir cast composites. Table 2.8 shows the properties obtained in various composites.

Table 2.8 Variation of microhardness (HV) and compressive strength (N/mm^2) [138].

Composite	Particles (HV)	Interface (HV)	Matrix (HV)	Ultimate tensile strength (N/mm^2)
A	228.03	121.38	73.06	150.283
B	165.10	109.81	61.43	157.806
C	180.43	111.91	63.98	112.202

The dendrites of ADC-12 alloy got affected by addition of reinforced particles. These particles acted as a barrier to the growth of dendrites and helped in refinement of microstructure of base alloy. SiC particles were responsible for greater refinement of microstructure of the two reinforcements. Further, the combination B (50% SiC and 50% zircon) yielded the best tensile strength. This was attributed to different roles played by individual reinforcements. SiC was helpful in refining the eutectic silicon with blunted and globular morphological features whereas zirconium silicate provided good interfacial bonding strength and microhardness (Table 2.8).

Elango *et al.* [41] in **2014** investigated the dry sliding wear behaviour of LM25 alloy stir cast composites reinforced with SiC (25 µm) and TiO_2 (50 µm) particles. The melting of LM25 alloy was done at 825 ℃, followed by addition of pre-heated mixture of particles (SiC + TiO_2). Pre-heating of particles was done at 500 ℃ for different combinations of reinforced particles as (7.5% SiC + 2.5% TiO_2) and (2.5% SiC + 7.5% TiO_2). Finally, the molten mass was poured into a pre-heated steel mould and cooled in the air. The variation in content of reinforced particles in LM25 alloy led to a reduction in wear rate, as shown in Figure 2.30. However, the wear rate increased with change in applied load from 29.43 N to 49.05 N and sliding distance from 0 to 628 m as shown in Figure 2.30a–c. The wear rate of LM25+2.5% SiC+7.5% TiO_2 composite was superior to LM25+2.5% SiC+7.5% TiO_2 composite and base alloy. This was attributed to high hardness and lubricity effect shown by TiO_2 particles.

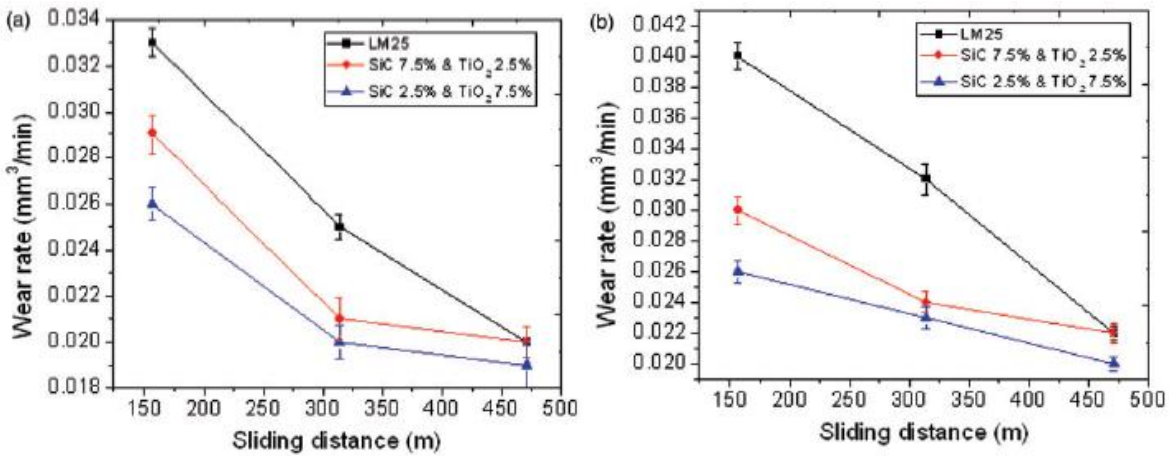

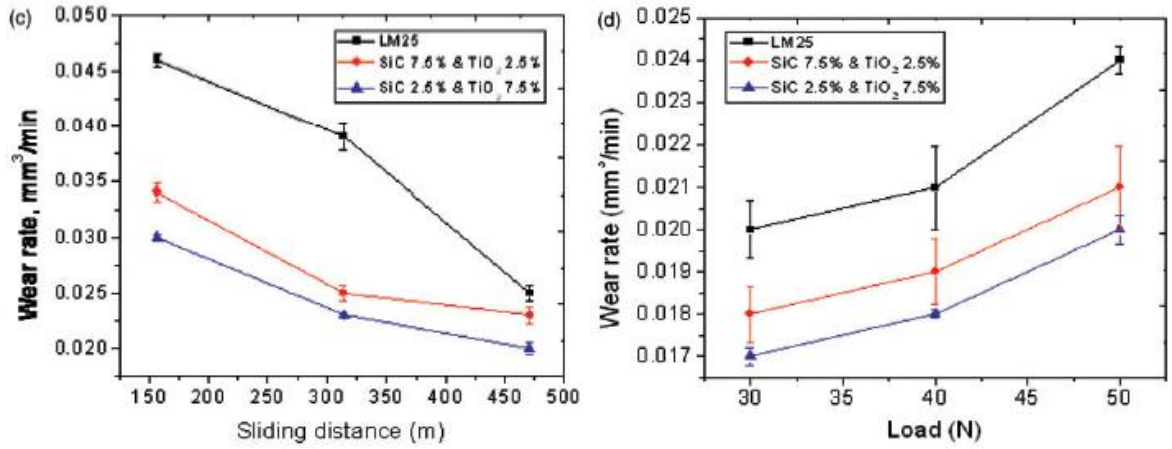

Figure 2.30 Wear rate of LM25 alloy and its composites at applied loads of a) 29.43 N, b) 39.24 N, and c) 49.05 N. d) Variation of wear rate at a sliding distance of 628 m with respect to change in applied load for base alloy and hybrid composites [41].

With increase in load, there was a faster change in wear regime from mild to severe in case of base alloy as compared to composites (Figure 2.30d). COF of composites decreased with increase in content of TiO_2 particles and applied load. Addition of TiO_2 showed lubricating property. SEM images of worn surfaces revealed that abrasive wear was responsible for the wear of composites.

Abbass and Fouad [92] in **2015** studied the effect of reinforcement of Al_2O_3 (50 nm) and TiO_2 (30 nm) nanoparticles on wear characteristics of Al-12 wt.% Si matrix hybrid AMCs prepared by powder metallurgy.

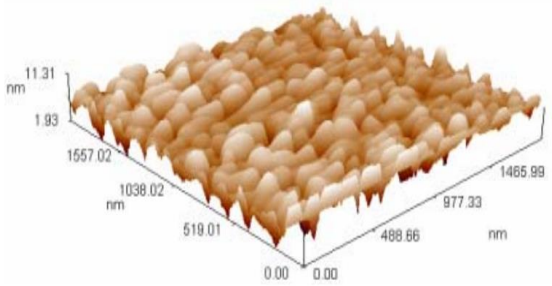

Figure 2.31 AFM image of Al-12 wt.% Si alloy ball milled with 4 wt.% of (Al_2O_3+TiO_2) reinforced particle [92].

A mixture of equal proportion of reinforced particles was added in weight percentage of 2 to 6 wt.% with a step size of 2 wt.%. Uniform mixing of reinforced particles in matrix was obtained by using ball milling process. For this, the ball to powder ratio was kept at 20:1. Atomic force microscopy (AFM) of ball milled powder was used to determine the average particle size of powder as shown in Figure 2.31. The average particle size was observed to be 100.69 nm. The density and hardness of composites increased with rise in reinforcement level. For composite

with 6 wt.% of (Al_2O_3+TiO_2), hardness and density values increased from 87 to 135 kg/mm^2 and 2.6079 to 2.8325 g/cm^3 respectively. Hybrid composites showed lower wear rate than the base alloy at any given load/sliding time because of increased hardness and interfacial bonding between reinforcement and matrix. Wear behaviour of base alloy/nanocomposites showed similar pattern with three regions (i) mild wear which occurred between loads of 5−7.5 N, (ii) transition wear which was observed between loads of 7.5−10 N, and (iii) severe wear which occurred at higher loads of 12.5 N. The hybrid nanocomposites at 6 wt.% level provided highest hardness and best wear resistance.

Kumar and Rajadurai [78] in **2016** studied the influence of rutile (TiO_2) reinforcement on microhardness and wear characteristics of Al-based hybrid composites. TiO_2 (0%, 4%, 8%, 12%; mass fraction) was blended to Al-15% SiC composites through powder metallurgy process (average grain size of SiC and rutile particles: 44−45 μm). For uniform mixing of powder, planetary mixer with 12 mm diameter steel ball was used. For effective bonding of reinforcement with matrix, it was preheated to 200 ℃ before cold compaction at 800 MPa. The sintering process was done at 650 ℃ for 2 h and then cooled in furnace for 8 h. Inclusion and increase of mass fraction of rutile increased the density and microhardness of hybrid composites (Figure 2.32).

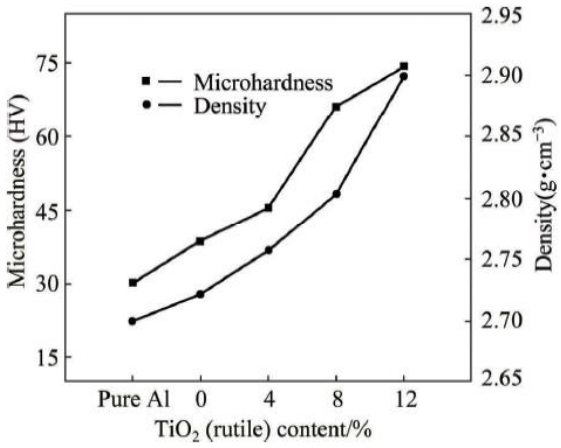

Figure 2.32 Density and micro-hardness of Al−15%SiC− x% TiO_2 composites with varying content of TiO_2 [78].

Hybrid composites revealed better wear resistance than the Al-SiC composites and the base matrix. Al-15% SiC reinforced with 12% TiO_2 showed highest wear resistance. This reduction in wear rate was ascribed to the increase in resistance to plastic flow of sliding surfaces. The decrement in plastic flow was obtained due to presence of hard rutile particles and the formation of strong interfacial bonding. SEM images revealed that delamination and adhesive

wear were the predominant wear mechanisms. XRD patterns of wear debris revealed presence of minimum oxide phases, specifically for composites reinforced with 12% TiO_2. Minimum oxide phases indicated prevention of micro-machining of particles by the reinforcement phase and less plastic deformation of the material, leading to lower wear loss.

Tirth [91] in **2018** studied the dry sliding wear behaviour of 2218 Al alloy-$Al_2O_3(TiO_2)$ hybrid composites. AA2218-Al_2O_3 (TiO_2) composites were synthesized by stirring 2, 5, and 7 wt.% of 1:2 mixture of Al_2O_3 (alumina):TiO_2 (rutile) powders in molten AA2218 alloy which was followed by T6 heat treatment. Particle reinforcement to alloy increased the density, hardness, but also porosity. Microstructure examination showed that particle distribution was uniform in the composites with 2 and 5 wt.% of particles. Agglomeration of particles was observed in 7 wt.% composites. Volume loss in wear increased linearly with sliding distance in all composites. Wear rate of composites increased linearly with increasing load but decreased with particle addition. Dominant wear mechanism appeared to be purely adhesive in matrix alloy and it transformed to adhesive-abrasive (3 body) in AMCs. Wear regime changed from mild to severe with increase in load. Delamination was responsible for removal of metallic chunks and chips in alloy. Presence of particles resisted delamination for certain time period resulting decreased wear rate but then yielded to ploughing/shear forces.

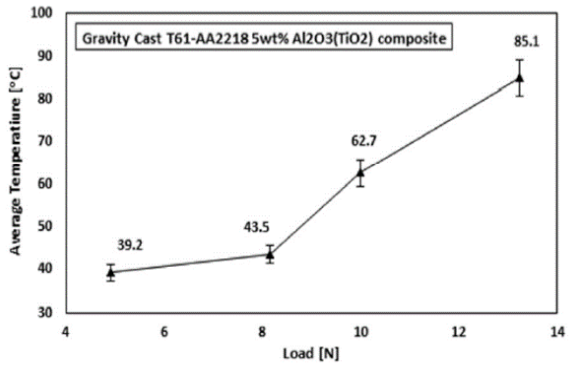

Figure 2.33 Average rise in temperature with respect to applied load for T6 heat treated AA2218-5 wt.% $Al_2O_3(TiO_2)$ composite [91].

Transfer layer formation was initiated by compaction of wear debris along wear track, which then spread around to cover the track significantly along the sliding surface. This caused intermittent decrease in wear rate and reduction of COF in composites. Fe content in worn-out surfaces (detected in EDAX) increased with particle addition, even though wear rate of composites decreased due to increase in wear of counterface yielding Fe at the pin-counterface interface. Maximum temperature rise was recorded as 85.1 ℃ at 13.24 N in 5 wt.% composite which was quite less considering dry sliding wear conditions (Figure 2.33). Increased porosity

content in hybrid composites could be the reason for reduced COF. For 7 wt.% composite, COF increased probably due to ploughing out of large number of coarser Al_2O_3 particles that were segregated and loosely bonded to the matrix. COF fluctuated with load and its lowest value was estimated at 10 N. This variation was attributed to formation of transfer layer, presence of porosity etc.

Arif *et al.* [139] in **2018** studied the wear properties of pure aluminium reinforced with micro SiC (37 µm) and nano zirconia (30–50 nm) particles. Full factorial design of experiments was used to analyze the effect of sliding distance, applied load, and weight percentage of zirconia on wear behaviour of AMCs. Further, analysis of variance (ANOVA) and artificial neural network (ANN) were used to investigate the percentage contribution and role of individual process parameters on tribological behavior of AMCs. Powder metallurgy process was used to incorporate different weight percentages of zirconia (0, 3, 6, and 9 wt.%) in pure aluminium by keeping the weight percentage of SiC fixed at 5 wt.%. The wear tests were performed at three levels of sliding distances (300 m, 600 m, and 900 m) and two levels of applied load (20 N and 30 N). The analysis of full factorial and ANOVA revealed that wear behaviour was mainly influenced by the sliding distance which was followed by weight percentage of zirconia and applied load conditions. The percentage contribution for these factors was 79.47%, 10.35%, and 6.7% respectively. The variation in experimental and predicated value of wear loss from ANN model is shown in Figure 2.34.

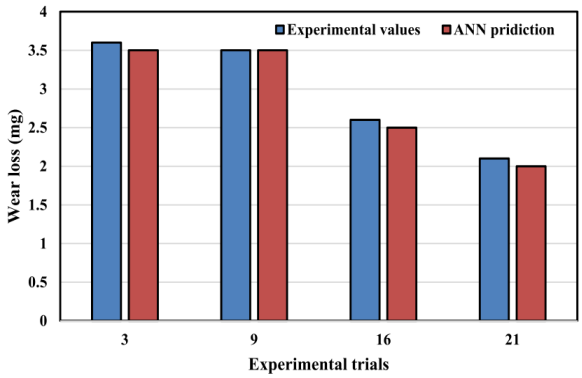

Figure 2.34 Comparison of experimental wear loss and predicted wear loss from ANN [139].

The prediction of wear loss values by ANN was done by feeding the 4-10-1 topology of forward back propagation neural network. This model gave the mean absolute error of 0.0041 at hidden layer of 10 nodes.

Palanikumar *et al.* [140] in **2019** compared the wear and friction behaviour of stir-cast Al6061 +mica+B_4C composites with Al6061+B_4C composites and Al6061 aluminium alloy. The

fabricated composites were designated as BXMY, where X and Y represented the weight percentage of B_4C and mica respectively. Figure 2.35a, Figure 2.35b, and Figure 2.35c present the effect of sliding distance on wear rate of AMCs at an applied load of 10 N, 20 N, and 30 N, respectively. However, the effect of applied load on wear rate for different AMCs is shown by Figure 2.35d. The increase in weight percentage of B_4C particles from 4 to 12 wt.% led to reduction in wear rate of boron carbide reinforced AMCs. At 12 wt.% of B_4C, AMC showed an improvement of 84.7% over the base alloy. The addition of mica particles along with B_4C particles decreased the value of wear rate as shown in Figure 2.35a–d. This was ascribed to the lubricity effect shown by mica particles and protection provided by boron carbide to base alloy.

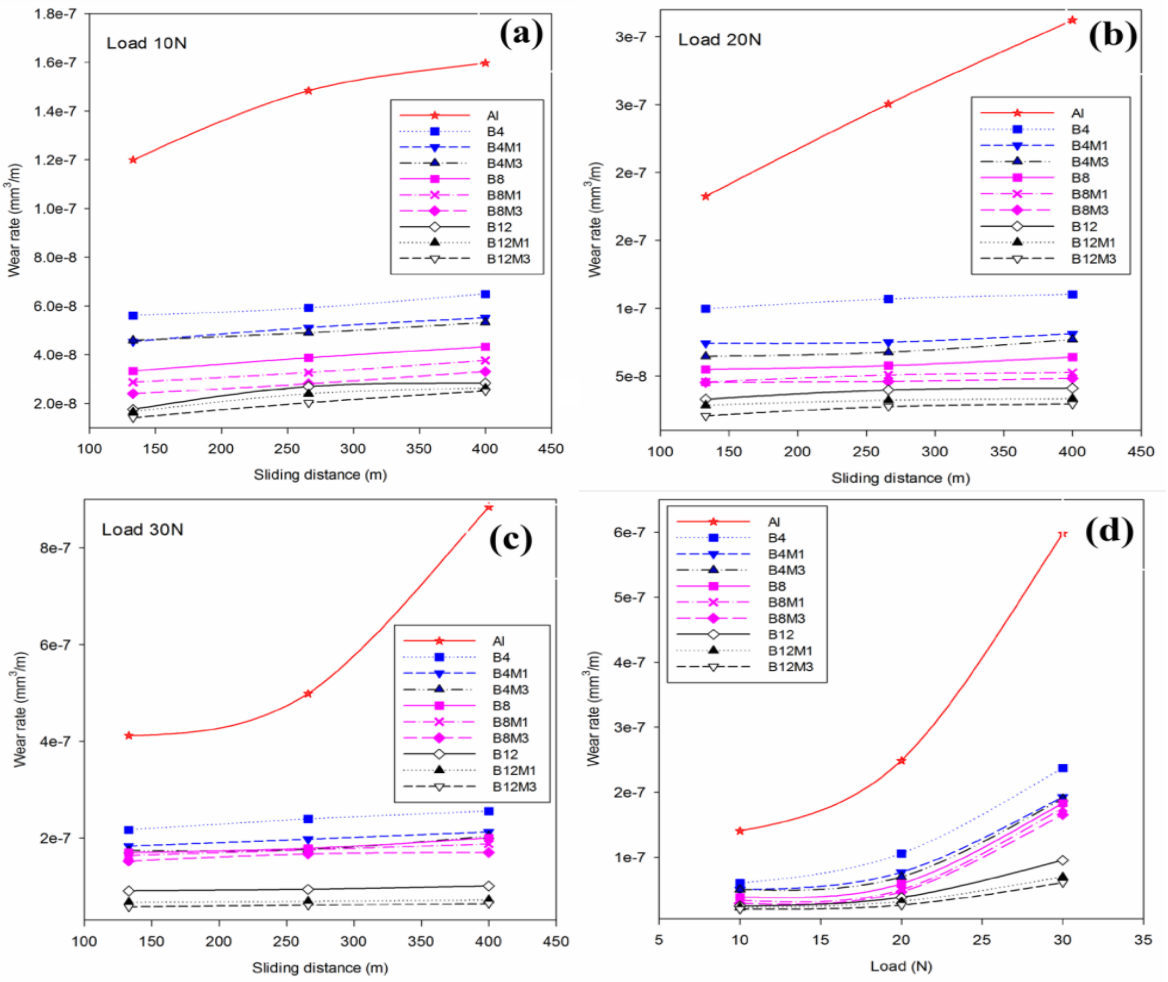

Figure 2.35 Effect of sliding distance on wear rate of hybrid composites at (a) 9.81 N, (b) 20 N, and (c) 30 N. (d) Variation of wear rate concerning different applied load conditions [140].

Compared to B12 composite, B12M3 composite showed a reduction of 36% in wear rate at an applied load of 30 N (Figure 2.35c). With increase in weight percentage of both the reinforcements and applied load, friction coefficient values showed a decreasing trend. The wear track analysis of B12 composites revealed formation of a compact layer. This compact

layer was formed due to crushing of plastically deformed wear debris trapped between the sliding surfaces. Besides this, micro-cracks, gap zones, and pits were also observed on the wear track. The presence of these features increased the roughness value of wear track. For B8 composite, the roughness value was 78.1417 nm as observed from atomic force microscope (AFM). However, the addition of mica particles in B8M3 composite led to a reduction of roughness value from 78.1417 to 41.7518 nm. This was attributed to the filling of microcracks by mica particles.

Sharma *et al.* [141] in **2021** investigated the mechanical and tribological properties of stir-cast hybrid AMCs. Al-Mg-Si-T6 aluminium was used as the matrix, whereas silicon carbide and muscovite particles were used as reinforcements. Silicon carbide with a particle size of 6 µm was added in a fixed amount of 5 wt.%. However, the particle size and reinforcement level used for muscovite were 28 µm and 2–4 wt.% (with a step size of 1 wt.%) respectively. Till 3 wt.% of muscovite, an increase in hardness and tensile strength values was observed whereas toughness and flexural load for bending showed highest value at 2 wt.% of muscovite. For Al-SiC (5 wt.%)-muscovite (3 wt.%) composite, the values of hardness, tensile strength, yield strength, and percentage elongation were 48.88 BHN, 117.85 MPa, 109.40 MPa, and 5.32% respectively. Further, the flexural load and impact strength showed the highest value of 3.99 kN and 8.78 J when muscovite was added in 2 wt.%.

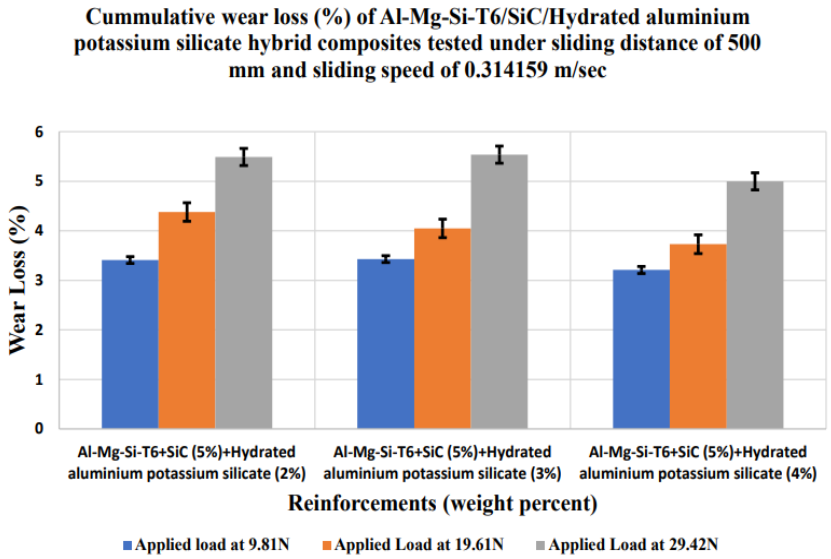

Figure 2.36 Wear loss of hybrid AMCs at different applied load conditions and weight percentage of muscovite [141].

The micro-scratch test on hybrid composites revealed the increase in traction force and abrasive friction coefficient with rise in content of muscovite. This was ascribed to reduction in

adhesion, patching, and scraping of sliding surfaces by hard SiC and muscovite particles. Moreover, the wear rate of hybrid composites showed decreasing trend with rise in weight percentage of muscovite, whereas the change in applied load from 9.81 N to 29.42 N showed an increase in wear loss for all the samples as shown in Figure 2.36. SEM analysis of worn surfaces revealed the change in mechanism from abrasive to delamination wear with increase in applied load. In addition to this, the presence of wavy marks on sliding surface indicated the formation of thin oxide layer. This oxide layer was formed due to the generation of frictional heat by relative motion of sliding surfaces.

Kishore *et al.* [142] in **2021** analyzed the mechanical and tribological properties of alumina and mica reinforced aluminium matrix composites. Stir casting process was used to disperse the reinforced particles in Al7075 aluminium alloy. The mixture of reinforced particles were obtained by varying the weight percentage of mica from 1–3 wt.% and adding the alumina particles in 3 wt.%. Table 2.9 represents the hardness, impact strength, wear loss, and friction coefficient values for different hybrid composites. With increase in concentration of mica, wear rate and friction coefficient showed reduction in values. However, hardness values showed an increasing trend with negligible changes in impact strength of AMCs.

Table 2.9 Mechanical and tribological properties of Al7075/Al_2O_3/mica composites [142].

Composition of composite	Hardness (BHN)	Impact strength (J)	Wear loss (μm) at load of 40 N, sliding speed of 3.35 m/s, and sliding distance of 400 m.	Friction coefficient
Al7075/3% Al_2O_3/1% mica	52	8	423	0.35
Al7075/3% Al_2O_3/2% mica	72	7	231	0.32
Al7075/3% Al_2O_3/3% mica	77	8	169	0.31

Ahamad *et al.* [143] in **2021** investigated the wear behaviour of Al6351 alloy reinforced with Al_2O_3 and TiO_2 particles. Besides this, the wear characteristics were optimized by using the ANOVA and TOPSIS analysis. Stir casting process incorporated the reinforced particles in equal proportions, and the weight percentage varied from 2.5–10 wt.%. Vickers hardness of hybrid composites increased from 49 to 79 HV with rise in reinforcement level from 0 to 10 wt.%. This was ascribed to reduction in plastic deformation and increase in strength of composite by formation of strong matrix-reinforcement bonding. The increase in applied load resulted in rise of wear rate for hybrid composites. In contrast, a reduction in wear rate was observed with increment in weight percentage of reinforced particles as shown in Figure 2.37. At lower load conditions (5 N and 10 N), adhesion wear was responsible for removal of

material from sliding surfaces. However, a transition in mechanism from adhesion to abrasive wear was observed with change in applied load to 20 N and 25 N.

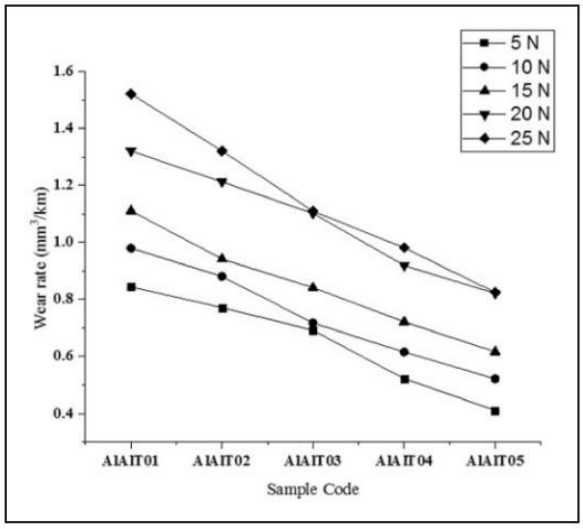

Figure 2.37 Wear rate of hybrid composites at different applied load conditions [143].

The addition of reinforced particles restricted the plastic deformation of matrix material under the action of applied load. ANOVA analysis revealed that reinforcement level and applied load significantly affected the wear rate of hybrid composites. On the other hand, TOPSIS analysis ranked Al-10 wt.% Al_2O_3-10 wt.% TiO_2 composite at the top of other composites. This signified the attainment of highest wear resistance in comparison to other compositions of composites. SEM images of wear track revealed that adhesive wear mechanism was dominant at lower weight percentage of reinforced particles. In contrast, abrasive wear mechanism was observed at high reinforcement level of particles.

Hariharan *et al.* [144] in **2022** investigated the effect of different combinations of SiC and MoS_2 on mechanical and tribological properties of LM24 alloy AMCs. The composites were fabricated using stir casting process in which MoS_2 particles were added in 1 wt.% whereas SiC particles were added in 3, 6, and 9 wt.%. SEM micrographs of composites revealed uniform distribution of reinforced particles. The mechanical properties of fabricated AMCs showed an increasing trend with rise in reinforcement level as shown in Figure 2.38. Figure 2.38a, Figure 2.38b, Figure 2.38c, Figure 2.38d, and Figure 2.38e show the variation of tensile strength, compressive strength, hardness, impact strength, and flexural strength, respectively. The reason for enhancement in hardness, tensile strength, impact strength, compressive strength, and flexural strength was the refinement of microstructure and effect of transfer of load from matrix to reinforced particles. The fracture analysis of tensile samples of AMCs revealed occurrence

of less number of voids and condensed microcracks in comparison to base alloy. This signified that AMCs failed due to a brittle fracture.

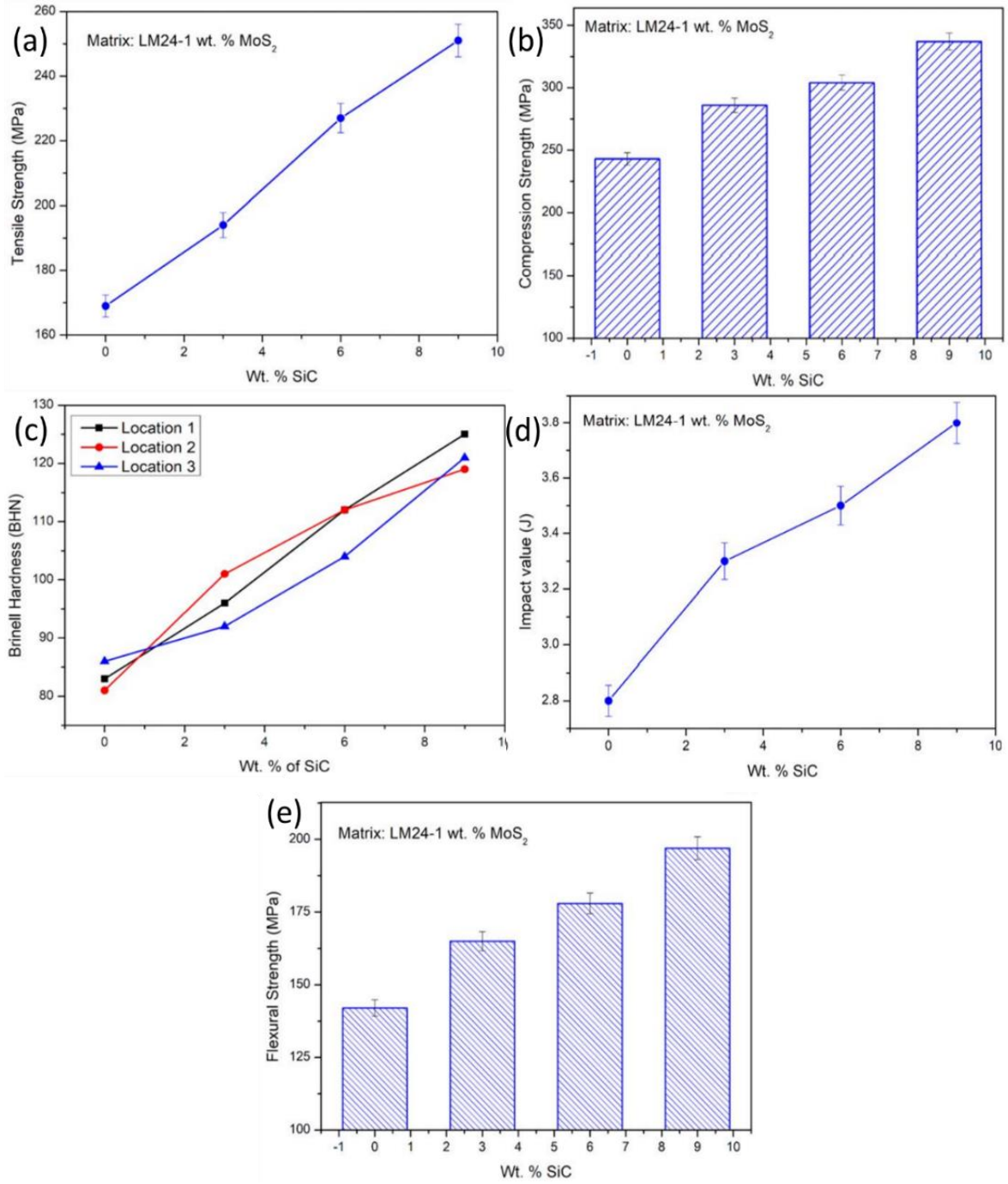

Figure 2.38 (a) Tensile strength, (b) compressive strength, (c) hardness, (d) impact strength, and (e) flexural strength of LM24/SiC/MoS_2 composites [144].

The wear rate of LM24/SiC/MoS_2 composites decreased with increment in concentration of reinforced particles. Further, ANOVA and gray relational analysis revealed that wear rate was mainly influenced by applied load followed by sliding velocity and sliding distance. SEM micrographs of worn surfaces revealed that reinforced particles were helpful in restricting the

plastic deformation and movement of dislocation density. This helped in reducing the wear rate of LM24 alloy on addition of mixture of SiC and MoS_2 particles.

2.3. Summary of the literature

- The combination of synthetic ceramic particles and mineral particles was used as reinforcement by various research groups to fabricate AMCs. For synthetic ceramics, SiC and Al_2O_3 particles were mainly used as reinforcement whereas zircon, rutile, mica, and muscovite were used as mineral particles. In case of combination of two different synthetic ceramic particles as reinforcement, authors have mainly used SiC, Al_2O_3, TiC, TiB_2, and B_4C particles in combination.
- The properties obtained by different combinations of reinforcements viz. 'synthetic + mineral' and 'mineral + mineral' (dual particle reinforced AMCs or hybrid AMCs) showed better wear and mechanical properties in comparison to individually reinforced AMCs (single particle reinforced AMCs). The particle size used for reinforcement mainly lied in the range of 20–65 μm. Based on the particle size, reinforcement level was varied from 2–12 wt.%.
- Different authors have processed hybrid composites by (a) selecting different particle size for both the reinforcements, (b) varying the mixing proportion of both the reinforcements, or (c) varying the amount of one reinforcement and keeping the other constant.
- Hybrid composites showed high hardness, high ultimate tensile strength, high compressive strength and low coefficient of friction which was attributed to better bonding and uniform distribution of reinforced particles.
- Some researchers studied the effect of high temperature on wear behaviour of hybrid and single particle reinforced AMCs. The addition of reinforced particles led to increase in working range of the base alloy. Further, an improvement in transition temperature was also observed for AMCs. At transition temperature, wear rate showed a sharp increase in the values.
- To improve wettability of B_4C, various authors added titanium, magnesium, strontium and K_2TiF_6 flux with the reinforced particles. Addition of these elements as flux resulted in formation of reaction layer on surface of B_4C particles which had great affinity for the molten melt of Al due to metallic-metallic interaction between them. The reaction product formed from flux included TiC and TiB_2.

- Composites reinforced with B_4C particles showed an increase in wear resistance with increase in its weight percentage. On the other hand, a decrease in coefficient of friction was observed. Authors reported that decrease in COF was attributed to higher load carrying capacity of reinforced particles and formation of MML.

2.4. Gaps in the existing literature

Several studies have been conducted to evaluate the wear characteristics of AMCs reinforced with ceramic particle reinforcements (viz. 'only synthetic ceramic particles', 'only mineral particles', 'combination of synthetic ceramic and synthetic ceramic particles', and 'combination of synthetic ceramic and mineral particles'). However, the following limitations provide further scope of research in the field of composites.

- For the hybrid composites containing a combination of synthetic ceramic particles and mineral particles, rutile mineral particles have been mostly used. No work has been reported on the several other combinations like 'B_4C + $FeTiO_3$' to investigate the wear characteristics of hybrid AMCs.
- In most of the reported work, the reinforcement particle size used in hybrid AMCs is in the range of 20–65 μm. The effect of variation in reinforcement particle size on wear characteristics/properties of hybrid AMCs has not been evaluated by researchers.
- Limited work has been reported on the effect of variation in proportion of constituent particles added as reinforcement in the hybrid composites. There is a need to study the properties of hybrid composites by varying the mixing ratio of different categories of reinforced particles.
- For hybrid composites, limited work on high-temperature wear studies has been reported. There is a need to evaluate the impact of operating temperature on the wear characteristics and to observe the transition in wear mode (from mild to severe and vice versa).
- Heat treatment has a significant effect on tribological and mechanical properties of AMCs. However, limited work is reported on effect of heat treatment on hybrid aluminium matrix composites (e.g. T4 and T6 heat treatments).
- Aluminium alloys have high electrical and thermal properties which can be used for effective dissipation of heat generated from the system. However, the decrease in strength at high temperatures restricts the use of aluminium alloys. The use of ceramic particle as reinforcement provides thermal stability and strength at high temperatures. Thus, there is

a need to explore the thermal and electrical properties of AMCs reinforced with ceramic particles.

The next chapter presents the design of the study used in the present research work.

Chapter 3
DESIGN OF THE STUDY

Overview

This chapter discusses the objectives and key issues of the present research. The 'materials and methods' section of the chapter provides details of starting materials, the processing methodology to prepare composites, and the designations used for the various AMCs. Machines and equipment used in the present research and their details are also included in this chapter. The details of various characterization techniques and different mechanical tests performed on the developed composites are also described in this chapter.

3.1. Objectives of the present research

The main objective of the present research work was to develop economical and light-weight AMCs reinforced with a combination of mineral and synthetic ceramic particles for improved wear characteristics under room as well as elevated temperature conditions. It was envisaged that these newly developed hybrid AMCs may provide a good substitute for commercial materials used for brake rotors, disc rotors, bearing cages etc. An automobile grade aluminium alloy was taken as the matrix material and ceramic particles were taken as the reinforcement. Two different types of reinforcements were used viz. (i) a naturally occurring mineral, and (b) a synthetic ceramic. Both, single particle reinforced composites (containing only one type of reinforcement) and hybrid composites (containing two different types of reinforcements) were processed. The effect of change in reinforcement particle size, weight fraction of reinforcement, and mixing proportions for a given reinforcement level on the microstructure, coefficient of friction values, and dry sliding wear characteristics of resulting AMCs were investigated.

The following were the objectives undertaken in the present work:

I. To fabricate AMCs containing B_4C ceramic particles and ilmenite mineral particles as reinforcement(s). LM13 aluminium alloy was taken as the matrix material. Composites were prepared through stir casting route. Different particle size range (i. 20–32 μm, and ii. 106–125 μm.) and weight fractions (0–15 wt.%; step size of 5 wt.%) of reinforcement were used to prepare AMCs. For hybrid AMCs, the mixing weight proportions of reinforcement were 1:3, 1:1, and 3:1 for a given reinforcement level.

II. To evaluate the structure and hardness of the processed AMCs through optical microscopy, SEM-EDS, X-ray diffraction and nano-hardness tester to establish the structure-property relationship.

III. To analyze the dry sliding wear behaviour and COF values of fabricated AMCs at room temperature and also at elevated temperature conditions (100–300 ℃; step size of 100 ℃). Wear behaviour was evaluated under operating loads of 9.8–49.0 N for sliding distance in the range of 0–3000 m. The sliding velocity during wear test was kept constant at 1.6 m/s.

3.2. Materials and methods

3.2.1 Starting materials

AMCs were processed using LM13 alloy (an aluminium-silicon alloy) as the matrix material (base alloy). The base alloy was supplied by ‘Emmes Metals Private Limited’, India. Boron

carbide, B_4C (a synthetic ceramic) and ilmenite, $FeTiO_3$ (a naturally occurring mineral) were selected as particle reinforcements. Boron carbide and ilmenite particles were procured from 'Parshwamani Metals', India and 'Rare Earths Limited', India respectively. The chemical composition of LM13 alloy, ilmenite, and boron carbide is presented in Table 3.1.

Table 3.1 Chemical composition of matrix material and reinforced particles.

Element (wt.%)	Cu	Mg	Si	Fe	Mn	Ni	Zn	Pb	Sn	Ti	B	C	O	Al
LM13 alloy	1.5	0.4	12.0	0.4	0.4	1.0	0.2	0.1	0.1	0.2	-	-	-	83.7
Ilmenite	-	-	-	15.37	-	-	-	-	-	36.93	-	-	47.70	-
B_4C	-	-	-	-	-	-	-	-	-	-	67.37	32.63	-	-

LM13 alloy is a commonly used material for making engine components. LM13 alloy possesses good fluidity, high strength, and low thermal-expansion coefficient. These properties are sustained even under elevated temperature conditions [145–147].

B_4C is a widely utilized reinforcement material for AMCs because of its low density (20–40% lighter than other ceramic particles), high hardness (third hardest material after diamond and cubic boron nitride), high impact resistance, and high wear resistance [84]. Further, Ilmenite is a low-cost mineral which is abundantly available in the coastal regions of Odisha, Kerala, Andhra Pradesh, and Tamil Nadu of the Indian subcontinent. Ilmenite has high hardness and low thermal conductivity. It has high chemical stability at elevated temperatures and is used as an anti-corrosion pigment [82,83]. Table 3.2 presents the values for different properties of boron carbide and ilmenite particles.

Table 3.2 Properties of B_4C and ilmenite [80,148–151].

Property	Boron Carbide (B_4C)	Ilmenite ($FeTiO_3$)
Density	2.52 g/cm^3	4.72 g/cm^3
Hardness	9.49 Mohs	5.5 Mohs
Thermal conductivity	30 W/mK	1.49 W/mK
Coefficient of thermal expansion	3.20×10^{-6} K^{-1}	27.90×10^{-6} K^{-1}
Melting point	2450 ℃	1050 ℃

Table 3.3 presents the chemical composition of grey cast iron, the commercially used material for brake rotor applications. The wear rate of the cast iron was compared with the composites developed in the present research.

Table 3.3 Chemical composition of commercially used brake rotor material [152].

Element (wt.%)	Mn	Sn	Fe	C	Cr	P	S	Cu	Ti	Si
Commercial brake rotor (i.e. grey cast iron)	0.51	0.061	92.84	3.54	0.034	0.054	0.1	0.69	0.012	2.15

3.2.2 *Processing of AMCs*

Stir casting process was used for processing of AMCs. In the stir casting process, an electric furnace was used to melt the matrix material (LM13 alloy) at 700 ℃. After melting, the molten alloy was stirred at 625 rpm for 10 min using a graphite stirrer to generate a vortex in the melt. Pre-heated ceramic particles (450 ℃, 15 min) were added to the vortex of the molten pool using a funnel attached to the stirrer. During addition of ceramic particles to the molten pool, the stirrer speed was reduced to 250 rpm. After the addition of the particles, the speed of stirrer was again increased to 650 rpm and continued for next 10 minutes. Finally, the melt was poured into a cast iron mould ($12\times12\times4$ cm^3) and was allowed to cool to room temperature. The billets obtained after the casting were cut into the shape of cylindrical pins for various tests and characterization of AMCs. Figure 3.1 presents the sequence of processing steps of the stir casting route used for developing the AMCs.

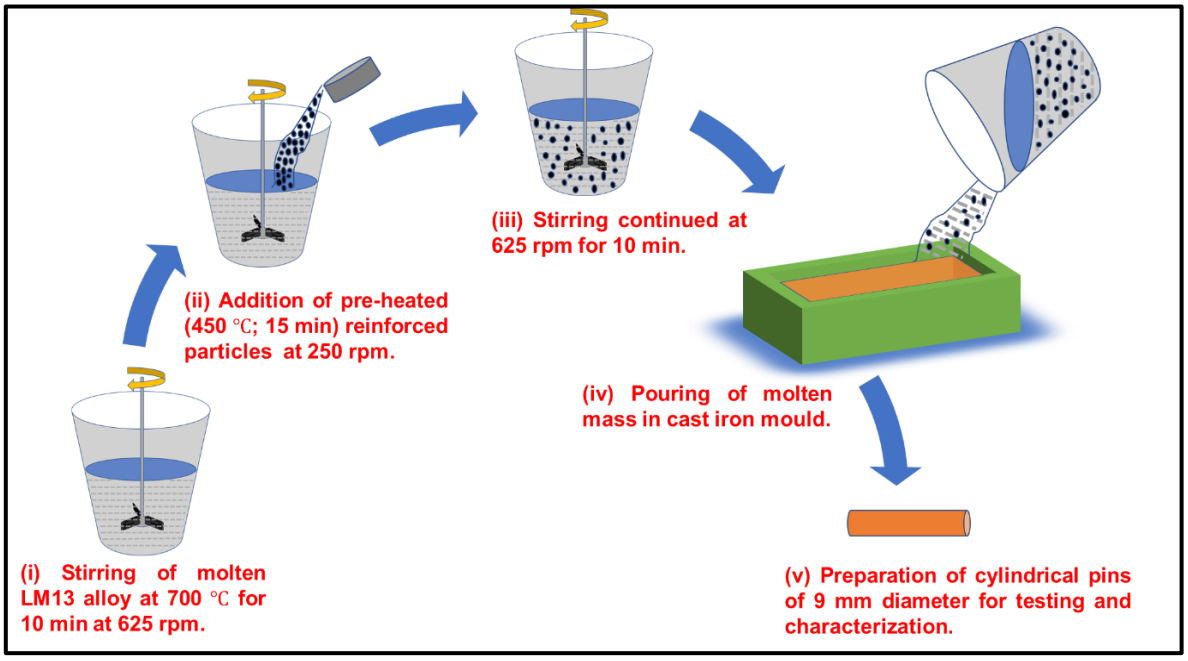

Figure 3.1 Schematic diagram of the stir casting process used for processing of AMCs.

In the present research, three main types of AMCs were processed. These include (i) single particle reinforced AMCs containing only B_4C ceramic particles, (ii) single particle reinforced AMCs containing only ilmenite mineral particles, and (iii) dual particle reinforced hybrid AMCs containing both, B_4C as well as ilmenite particles. For each of these AMCs, two types of particle sizes (coarse: 106–125 µm; fine: 20–32 µm) were used. Further, for the hybrid AMCs, for any reinforcement level (wt.%), the two types of particles were mixed in the weight proportion of 1:3, 1:1, and 3:1. After processing, specimens were prepared for characterization and wear testing.

The designations used for various AMCs processed in the present research are presented in Table 3.4. The initial part of designations containing the numerals '5', '10', and '15' signify the reinforcement level (wt.%) as 5, 10, and 15 wt.% respectively. The intermediate part of designations containing the letters 'F' and 'C' signify the particle size of reinforced particles as 'fine' or 'coarse' respectively. The latter part of designations containing the letters 'IR', 'BR', or 'BI' signify ilmenite reinforced, boron carbide reinforced, and boron carbide-ilmenite (hybrid) reinforced composites respectively. Further, for the hybrid AMCs, the affixes, '13', '11', and '31' added at the end of the designation signified the weight ratio of boron carbide to ilmenite particles reinforced in the hybrid AMCs as 1:3, 1:1, and 3:1 respectively.

Table 3.4 Terminology used for various AMCs.

Total weight percentage of reinforced particles in the AMC (wt.%)	**Mixing proportion of boron carbide and ilmenite particles (X:Y)***	**Designation used for fabricated AMC with particle size in the range of**	
		'Fine' (20-32 µm)	***'Coarse' (106-125 µm)***
0	-	LM13 alloy	
5	1:0	5FBR	5CBR
	0:1	5FIR	5CIR
	1:3	5FBI-13	5CBI-13
	1:1	5FBI-11	5CBI-11
	3:1	5FBI-31	5CBI-31
10	1:0	10FBR	10CBR
	0:1	10FIR	10CIR
	1:3	10FBI-13	10CBI-13
	1:1	10FBI-11	10CBI-11
	3:1	10FBI-31	10CBI-31
15	1:0	15FBR	15CBR
	0:1	15FIR	15CIR
	1:3	15FBI-13	15CBI-13
	1:1	15FBI-11	15CBI-11
	3:1	15FBI-31	15CBI-31

*** X:Y, where X represents wt.% of B_4C particles and Y represents wt.% of ilmenite particles**.

3.2.3 Machines and equipment

Details of various machines/equipment used in the present research are discussed as follows:

(i) Power hacksaw

The billets of the as-received LM13 base alloy were large in size. These were cut into smaller pieces using a power hacksaw machine (Make: Tansi, HMT, Bengaluru). For each casting, the weight of each piece was kept in the range of 1.0–1.2 Kg. Figure 3.2 presents the power hacksaw machine used in the present work.

Figure 3.2 Power hacksaw machine (Courtesy: Thapar Institute of Engineering & Technology, Patiala).

(ii) Ball milling process

The as-received boron carbide and ilmenite particles had size in the range of 120–150 µm and 200–300 µm respectively. Ball milling process was used to reduce the particle size. Figure 3.3 presents the schematic of ball milling set-up.

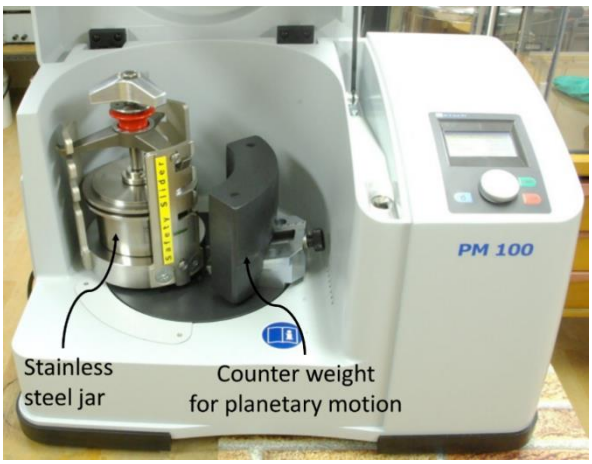

Figure 3.3 Ball milling apparatus (Courtesy: Thapar Institute of Engineering & Technology, Patiala).

The ball milling set-up (Make: PM100, Retsch, Germany) mainly comprised of a stainless steel milling jar of capacity 250 ml containing stainless steel balls of diameter 12 mm. The powder whose particle size was to be reduced was put in the milling jar. The weight ratio of steel balls to powder was kept in the ratio of 10:1. The rotational speed of the milling jar was kept as 283 rpm. During the milling process, the milling jar was provided with planetary motion for 8 h. This made the steel balls to collide against each other which reduced the particle size of the powder contained in the milling jar along with the stainless steel balls. After ball milling of the as-received particles, the particles sizes were reduced and were obtained into two different categories viz. ‘Fine’ (20–32 µm) and ‘Coarse’ (106–125 µm).

(iii) Sieve shaker

Sieve shaker set-up (Make: AS200, Retsch, Germany) was used to separate the ball milled powder into different particle sizes. For this, the ball milled powder was allowed to pass through various sieves having different mesh sizes viz. 125 µm, 106 µm, 75 µm, 50 µm, 32 µm, and 20 µm. The top-most sieve of the sieve shaker having a mesh size of 125 µm was loaded with 200 g of ball milled powder. The stack of sieves were arranged in decreasing order of mesh sizes and was allowed to shake at an amplitude of 2 mm for 4–6 h. The particles retained in the sieves of 20 µm and 106 µm size were considered to have particle size range of 20–32 µm and 106–125 µm respectively. Figure 3.4 presents the photograph of sieve shaker set-up used in the present work.

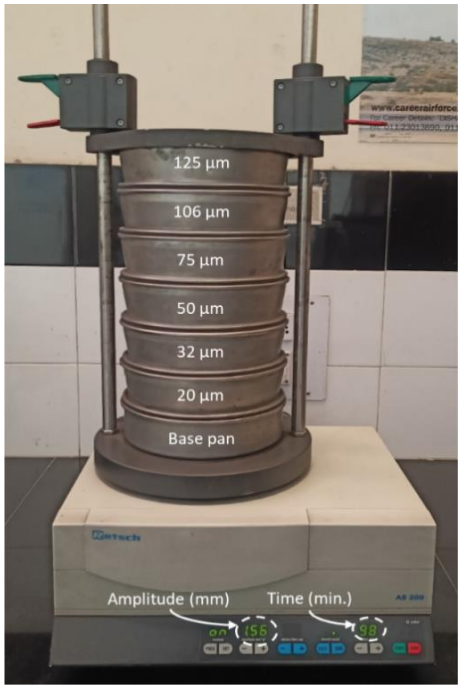

Figure 3.4 Sieve shaker set-up (Courtesy: Thapar Institute of Engineering & Technology, Patiala).

(iv) Stir casting set-up

Stir casting set-up consists of an electric furnace to melt the alloy in a graphite crucible. Besides this, there was an electric motor attached to a three blade stirrer to rotate it at variable speed. A funnel was attached to the stirrer for the addition of particles to be reinforced. After the stir casting process was complete, forging tongs were used to pour the molten mass into a rectangular mold of cast iron. Figure 3.5 presents the schematic of stir casting set-up, the vortex generated by the stirrer in the molten pool, and the solidified billet in the rectangular mold.

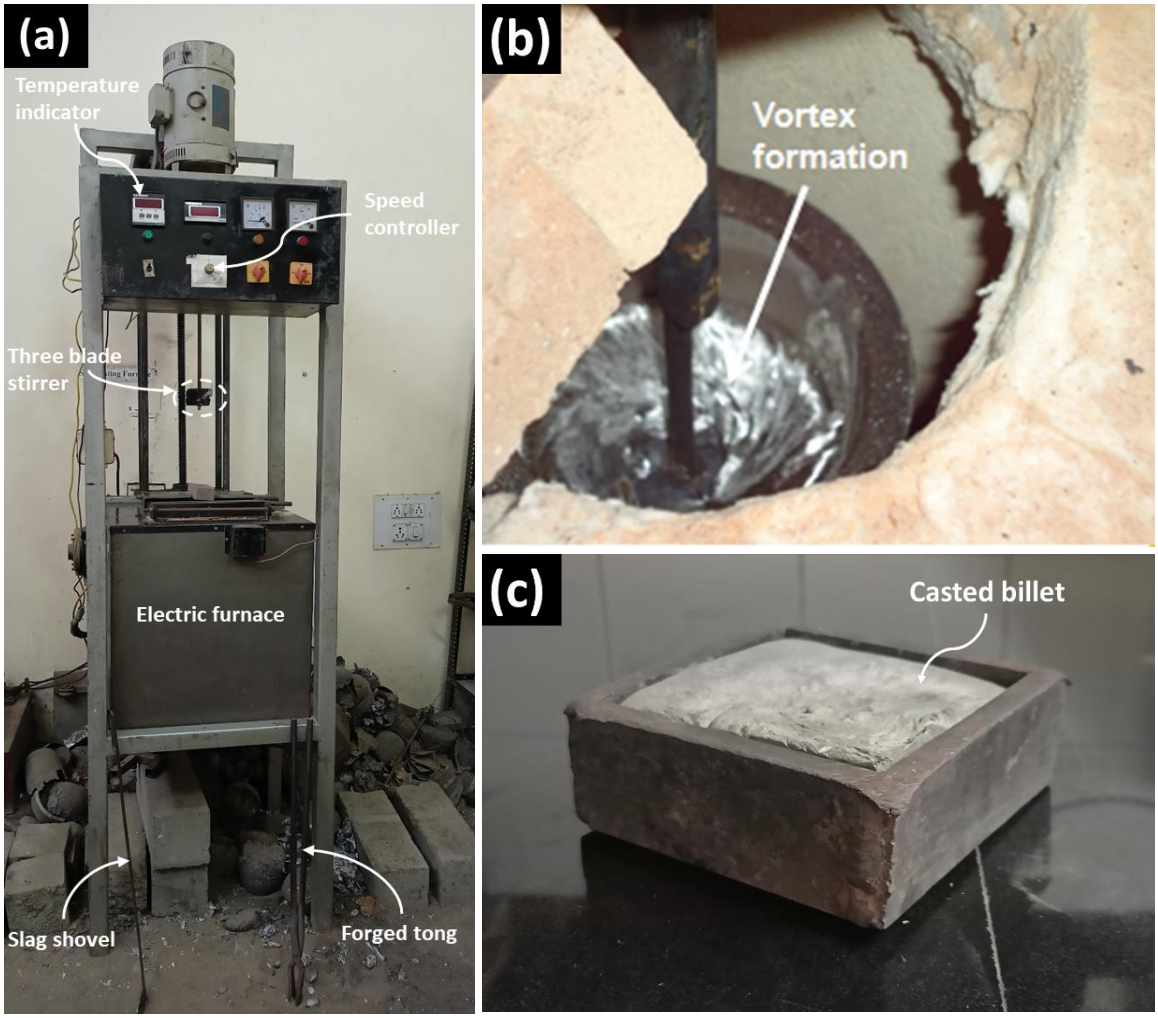

Figure 3.5 (a) Stir casting set-up, (b) vortex generated by the three blade stirrer, and (c) solidified billet after the casting process (Courtesy: Thapar Institute of Engineering and Technology, Patiala).

(v) Muffle furnace

Muffle furnace was used to preheat a specific amount of ceramic particles in a graphite crucible (this specific amount of particles was equal to the reinforcement level of particles in weight percentage in a given composite formulation). Preheating of particles was done at 450 ℃ for 15 min to eliminate volatile substances. These preheated ceramic particles were added into the molten pool of base alloy. Preheating also increased the surface energy of particles which was attributed to enhance the wettability of these reinforced particles by the molten aluminium alloy. Figure 3.6 shows the muffle furnace used in the present research.

Figure 3.6 Muffle furnace (Courtesy: Thapar Institute of Engineering and Technology, Patiala).

(vi) Precision cutter

A diamond cutter (Make: Sample Cutter for Pod Unit, Ducom Instruments, Bangalore, India) was used to cut the casted AMCs for obtaining specimens required for characterization (optical microscopy, SEM microscopy, X-ray diffraction etc.). To obtain the specimen, the casted material was mounted on the steel vice. The material was placed in a position relative to the cutting wheel using a micrometer screw. Cutting was done by lowering the material over the cutter using a dead weight mechanism so that uniform load acted during cutting. Figure 3.7 illustrates the precision cutter utilized in the present work.

Figure 3.7 Precision cutter (Courtesy: Thapar Institute of Engineering and Technology, Patiala).

(vii) Metallography

For microstructural analysis, the prepared samples of composites were polished using the standard metallurgical procedure to get a mirror finish on their surface. Initially, the samples were flattened and polished using emery sheets (grades used in the sequence are: 200, 400, 800, 1000 and 2500 grit size). Next, velvet cloth polishing was performed on a disc polisher

(Make: MetaServ 3000, Buehler Binghamton, New York) using diamond paste. The mirror finished surface obtained was analyzed under an optical microscope (Make: Eclipse MA-100, Nikon Instruments, Tokyo, Japan) equipped with a digital camera and image analysis software. The disc polisher and the optical microscope used in this research are shown in Figure 3.8.

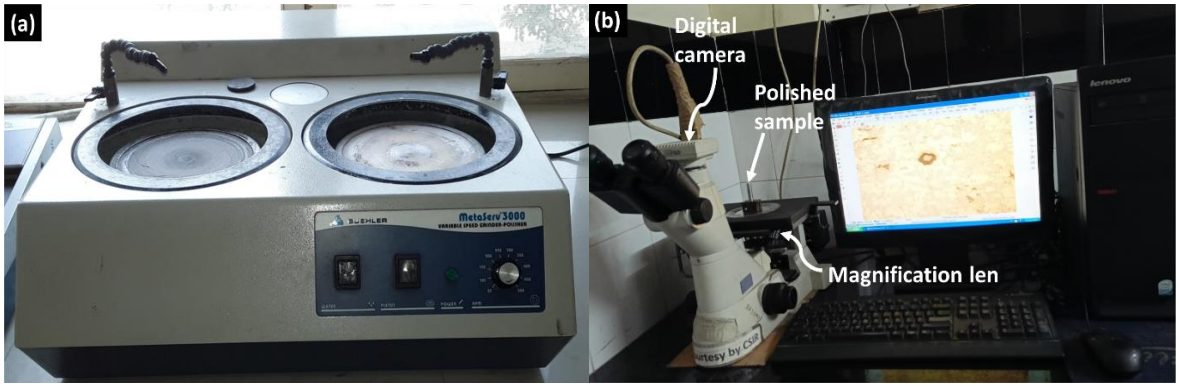

Figure 3.8 (a) Disc polisher and (b) optical microscope (Courtesy: Thapar Institute of Engineering and Technology, Patiala).

(viii) X-ray diffractometer

To determine the phases present in the processed AMCs, diffraction patterns were recorded using an X-ray diffractometer (Make: SmartLab SE, Rigaku, Japan) with $Cu_{K\alpha}$ radiation (λ =1.54 Å). The diffraction of monochromatic $Cu_{K\alpha}$ radiation was done at a scanning speed of 0.02 degrees/second and the scanning range (2θ) was varied from 20°−90°. The database of 'International Centre for Diffraction Data (ICDD)' was used to identify different phases present in the AMCs. Figure 3.9 shows the X-ray diffraction set-up.

Figure 3.9 X-ray diffraction set-up (Courtesy: Thapar Institute of Engineering and Technology, Patiala).

(ix) Nano-hardness tester

Nano-hardness testing of the base alloy and various AMCs was done using the nano-hardness testing facility (Make: TI 950 Tribo-Indenter, Hysitron Incorporation, Minneapolis, US). Nano-hardness measurement was done by taking a minimum of ten indentations per phase at 1000 μN with a dwell time of 5 s. Figure 3.10 shows the nano-hardness tester utilized in the present research.

Figure 3.10 Nano-hardness tester (Courtesy: Indian Institute of Technology, Ropar).

(x) Micro-hardness tester

Vickers micro-hardness tester (Make: Mitutoyo MVK-HO, Japan) was used to measure the micro-hardness of AMCs. A square based pyramid diamond indenter with 136° face angle between opposite faces was used to apply a load of 1000 kg for a dwell time of 15 s. For every sample, a total of five readings were taken for obtaining the hardness values. Vickers microhardness tester used in the research work is shown in Figure 3.11.

(xi) Dilatometer

Thermal analysis of AMCs was done using a dilatometer (Make: STA 449 F3 Jupiter, NETZSCH, Germany). For this, thermal strain values and coefficient of thermal expansion (CTE) values were obtained. Cylindrical samples having dimensions of 6×6×4 mm^3 were used for the purpose. For thermal analysis, temperature of chamber was increased in the range of 50–300 ℃ at a heating rate of 5 ℃/min and change in length of sample (ΔL) was recorded with respect to rise in temperature. Change in length (ΔL) divided by original length (L) of sample provided the thermal strain of AMCs. Further, considering 'ΔT' as the change in operating temperature, CTE value was obtained as given in Equation 3.1. The dilatometer set-up used in the present work is shown in Figure 3.12.

$$CTE = \frac{\Delta L}{L * \Delta T} \quad \text{..... (3.1)}$$

Figure 3.11 Vickers microhardness tester (Courtesy: Thapar Institute of Engineering and Technology, Patiala).

Figure 3.12 Dilatometer apparatus (Courtesy: Thapar Institute of Engineering and Technology, Patiala).

(xii) Wear testing

Wear tests were performed on a wear testing machine (Make: Wear and Friction Monitor TR-20 CH-400, Ducom Instruments, Bangalore, India) under dry sliding conditions, both for ambient and high temperature conditions (100 ℃, 200 ℃, and 300 ℃). The wear set-up, its control panel, and a test pin of the composites developed in the present research are shown in Figure 3.13. High temperature wear tests were performed in a closed container attached to three electric heaters (to reach operating temperatures till 400 ℃). The container temperature was monitored using thermocouples. Applied load was varied as 9.8 N, 29.4 N, and 49.0 N. For

each wear test, sliding distance was varied from 0–3000 m and sliding speed was selected as 1.6 m/s.

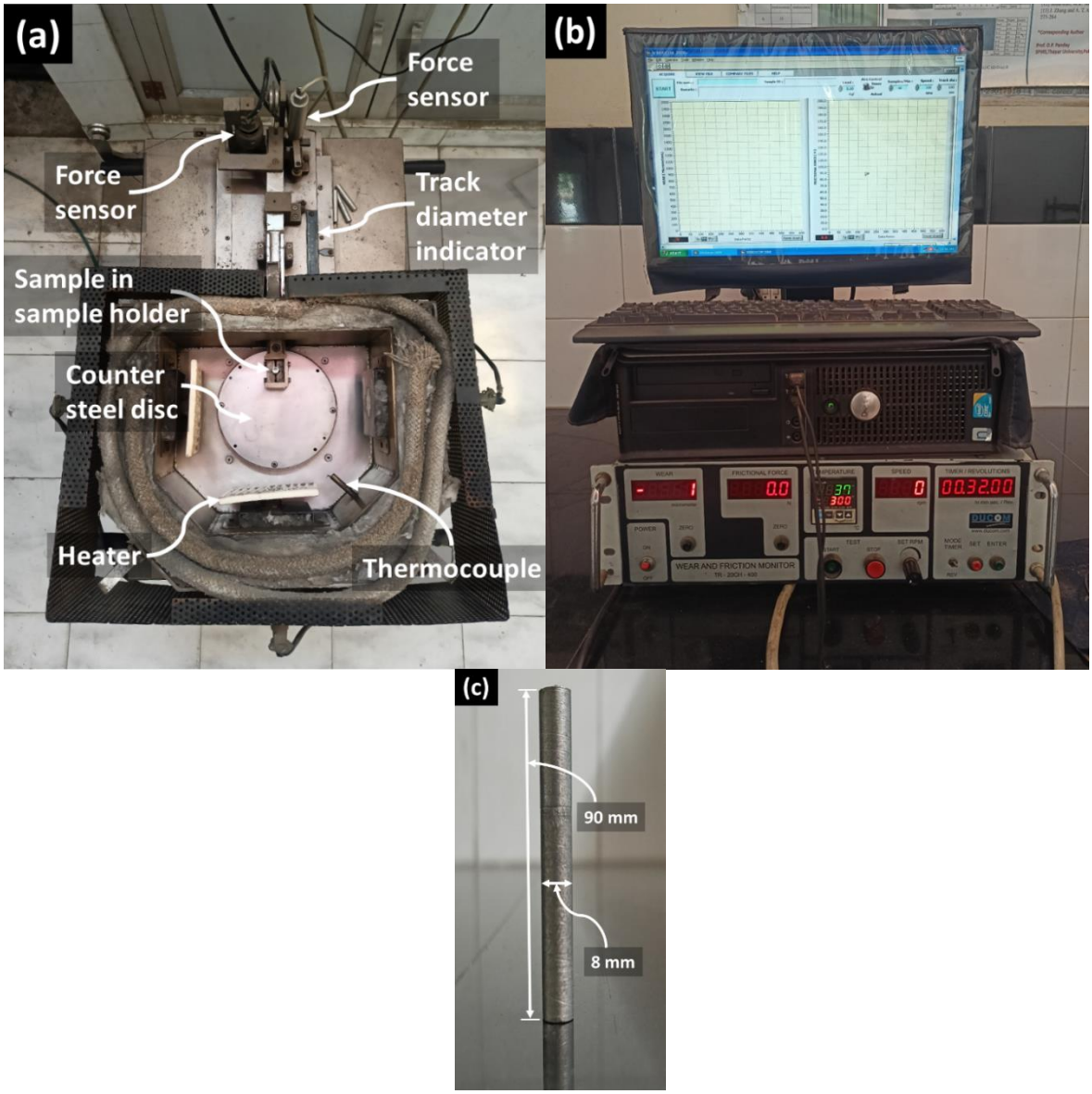

Figure 3.13 (a) Pin-on-disc set-up, (b) control panel of pin-on-disc set-up, and (c) wear sample as per ASTM G99 standard (Courtesy: Thapar Institute of Engineering and Technology, Patiala).

Loss in height (h_l) of cylindrical pins due to relative sliding between counter surfaces (cylindrical pins obtained from the processed composites and the steel disc of the wear test set-up) was measured using LVDT sensors attached to the pin-on-disc set-up. Using this height loss (h_l), the total volume loss (V_l) was calculated. Finally, wear rate was calculated as per Equation 3.2 by determining volume loss (V_l) and sliding distance (d_s).

$$WR = \frac{\pi * d^2 * h_l}{4 * d_s} \quad \text{..... (3.2)}$$

For the wear test, cylindrical pins of 9 mm diameter (as per ASTM G99 standard) were prepared from the casted billets of processed AMCs. The length of pins were kept in the range of 90–100 mm. All samples (base alloy and various AMCs) were tested against a steel disc (EN31 die steel having hardness of 63 HRC).

Further, frictional force values were also obtained from the wear test data. The frictional force values divided by the applied load provided values of coefficient of friction. Frictional force values were measured using the load sensor attached to the pin-on-disc set-up.

(xiii) Surface roughness tester

Surface roughness tester (Make: SJ-400, Mitutoyo model, Germany) was used to determine the roughness of sliding surface obtained after the wear test performed at a particular testing condition. The roughness tester uses the stylus method of measurement, has profile resolution of 12 nm and measures roughness up to 100 µm. Trace length and cut-off length of 1.25 mm and 0.25 mm respectively were used. For every sample, a total of four readings were taken for obtaining the roughness values. Surface roughness tester used in the research work is shown in Figure 3.14.

Figure 3.14 Surface roughness tester (Courtesy: Metrology Lab, Thapar Institute of Engineering and Technology, Patiala).

(xiv) SEM-EDS set-up

Figure 3.15 shows the SEM set-up used in the present research. Scanning electron microscope attached with EDS facility was used to analyze the microstructure and the chemical composition of different phases. The purity of the ceramic powders (boron carbide particles and ilmenite particles) and also their average particles size after the ball milling process was checked through SEM-EDS analysis. Further, wear tracks and wear debris obtained after the wear test of various AMCs were analyzed using micrographs obtained through SEM set-up

(Make: JSM-6510LV, JOEL Ltd., Tokyo, Japan). SEM micrographs were used to ascertain the mechanisms involved in the materials removal process due to wear under different applied load conditions. Further, SEM with EDS (Make: INCA 51-ADD 0076, Oxford Instruments, Abingdon, United Kingdom) was used to determine the other significant changes occurring during the wear test. Examples of such changes include occurrence of oxidation of the pin surface, materials loss from the counter surface etc.

Figure 3.15 SEM set-up (Courtesy: SAI LAB, Thapar Institute of Engineering and Technology, Patiala).

The next chapter presents and discusses the results related to the mechanical testing and characterization of base alloy and single particle reinforced AMCs at room as well as high temperature conditions.

Chapter 4
RESULTS AND DISCUSSION
(Characterization and testing of single particle reinforced AMCs)

Overview

This chapter presents the results and discussion pertaining to the characterization and testing of single particle reinforced AMCs. The purity of the two reinforcements (ilmenite and boron carbide) and their particle size distribution were checked and confirmed through SEM-EDS analysis. XRD analysis was conducted to determine the constituents of base alloy and various AMCs. The effect of reinforcement of boron carbide and ilmenite particles and their content on the microstructure of LM13 base alloy was investigated. The variation observed in microstructure of AMCs with variation in weight percentage and particles size of reinforcement has been reported in this chapter. Similarly, the effect of reinforcement level and particle size on coefficient of thermal expansion, hardness, wear, and coefficient of friction values of various AMCs has been monitored and presented here. The friction and wear characteristics of AMCs were studied at room and high operating temperatures. Finally, SEM-EDS analysis was performed on the wear-track and wear-debris obtained after each wear test to determine the type of wear mechanisms responsible for removal of material due to wear under different operating conditions.

4.1. SEM-EDS analysis of ball milled powder

The as-received boron carbide and ilmenite particles had size in the range of 120–150 µm and 200–300 µm respectively. Ball milling process was used to reduce the particle size. After ball milling, the powder was sieved and segregated into two different categories viz. 'Fine' (20–32 µm) and 'Coarse' (106–125 µm). Figure 4.1 presents the SEM-EDS micrographs of boron carbide and ilmenite powders considered in the two categories of 'fine' and 'coarse' particle size ranges. EDS analysis of boron carbide particles showed presence of boron and carbon (Figure 4.1a−b) whereas iron, titanium and oxygen were observed for ilmenite particles (Figure 4.1c−d). Further, the atomic percentage given by EDS was used to determine the chemical formula for each reinforcement. For boron carbide, the derived chemical formula was $B_{3.23–3.25}C$ which can be considered equivalent to B_4C. On the other hand, the derived chemical formula for ilmenite was $FeTi_{1.32–1.56}O_{3.29–3.36}$ which is equivalent to $FeTiO_3$.The above mentioned observations and results signified that the as-received particles were of high purity and also no change in phase occurred during the ball milling process.

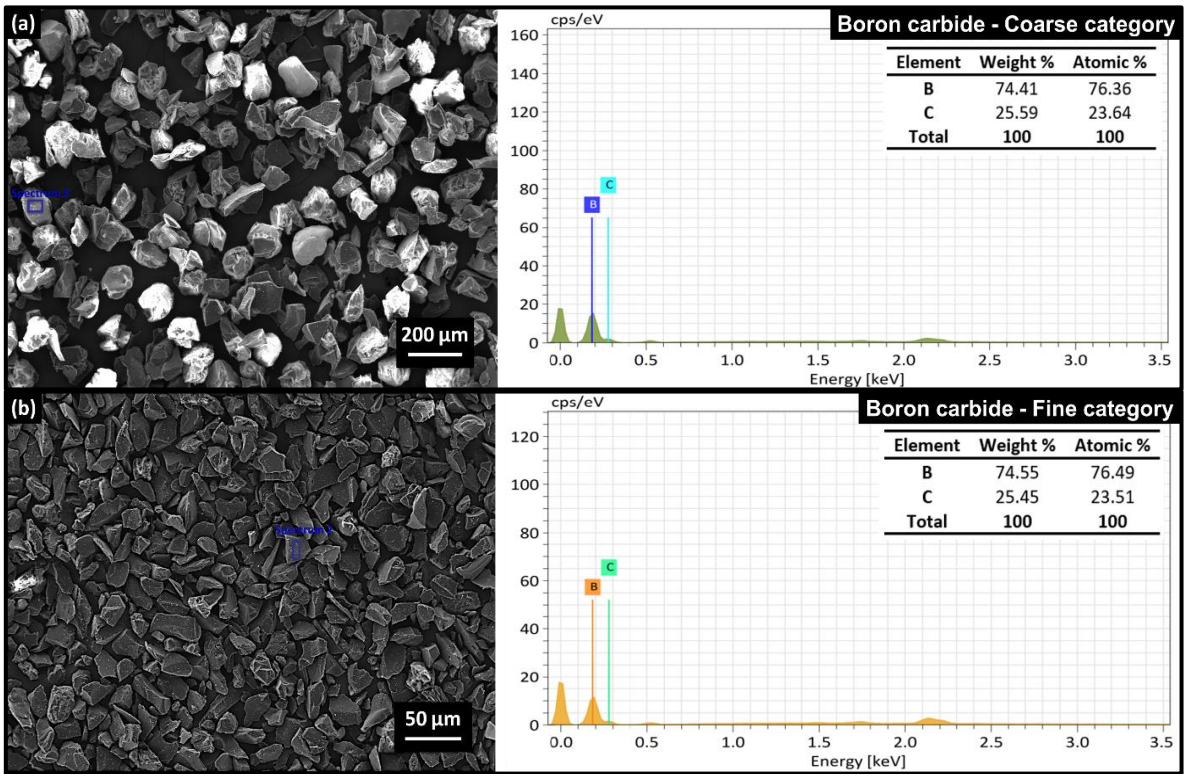

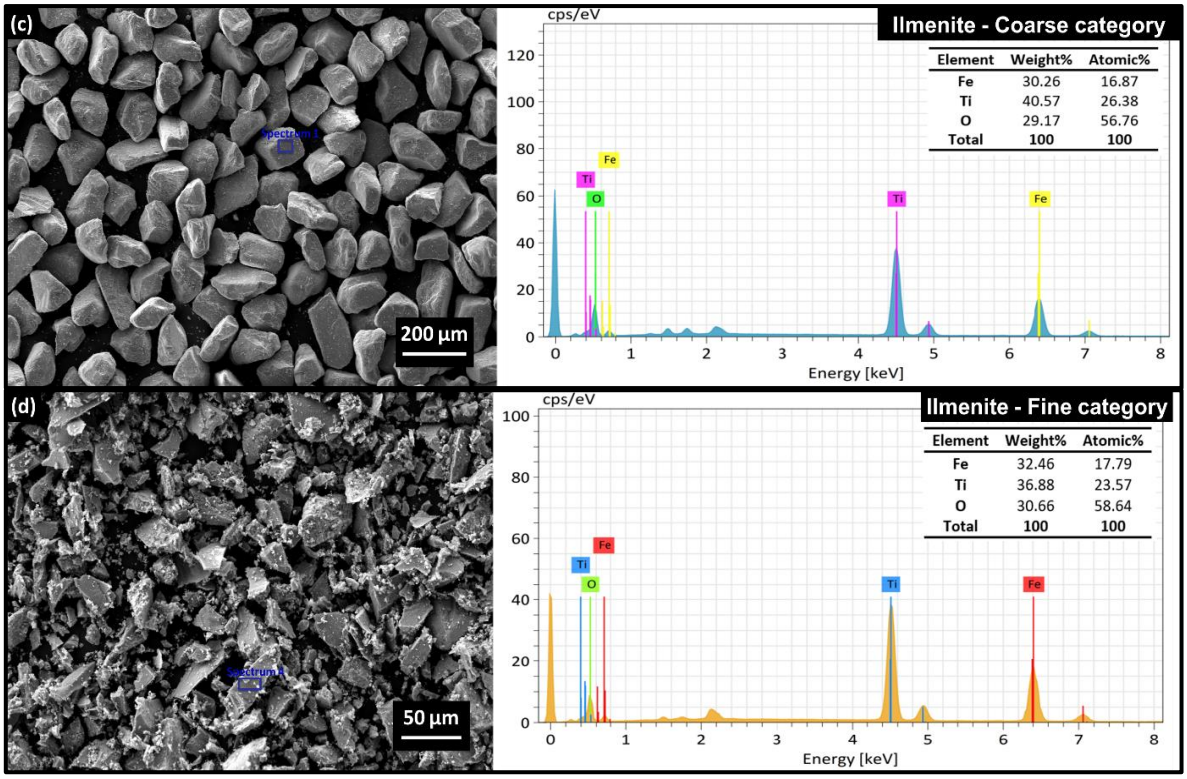

Figure 4.1 SEM-EDS of (a) boron carbide particles – coarse category, (b) boron carbide particles – fine category, (c) ilmenite particles – coarse category, and (d) ilmenite particles – coarse category.

Figure 4.2 presents the particle size distribution for boron carbide and ilmenite particles considered in the two categories of 'fine' and 'coarse' particle size ranges. For 'fine' category, the average particle size was observed as 25.52±3.48 µm and 25.24±2.85 µm for boron carbide and ilmenite respectively. Further, for the 'coarse' category, the average particle size was obtained as 115.64±5.70 µm and 116.60±5.72 µm for boron carbide and ilmenite respectively.

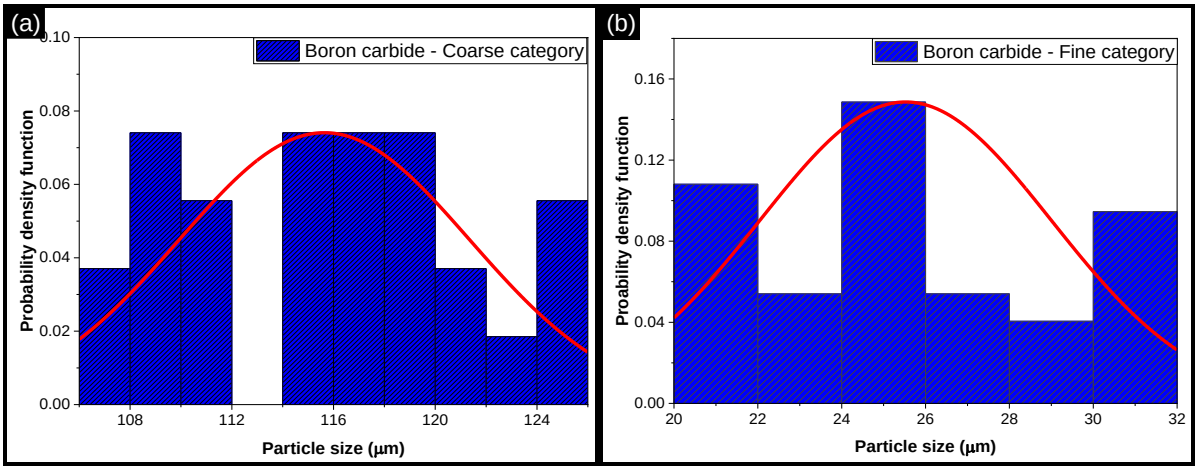

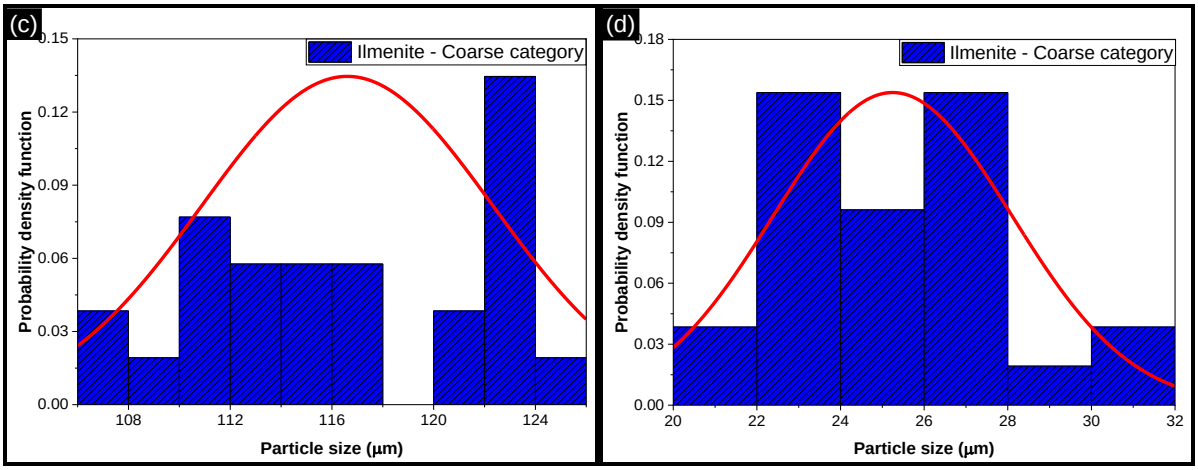

Figure 4.2 Particle size distribution of (a) boron carbide particles - coarse category, (b) boron carbide particles - fine category, (c) ilmenite particles - coarse category, and (d) ilmenite particles - fine category.

4.2. XRD analysis

This section presents the results of XRD analysis conducted to determine the constituents of base alloy and various AMCs.

4.2.1 LM13 alloy

Figure 4.3 presents the XRD profile of as-cast LM13 alloy. XRD pattern showed peaks of aluminium and silicon which were the main constituents of matrix.

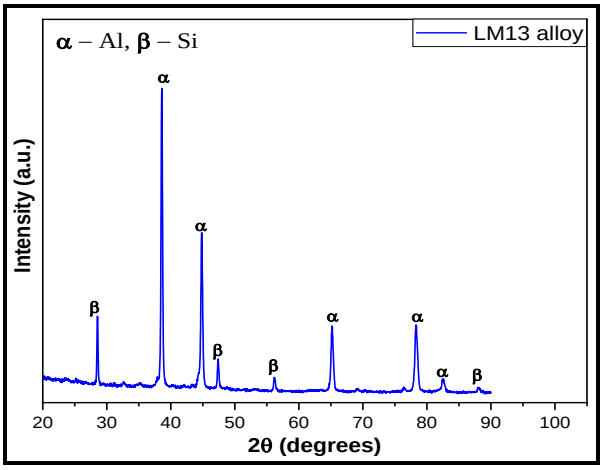

Figure 4.3 X-ray diffraction profile of as-received LM13 alloy.

4.2.2 Single particle reinforced composites containing coarse particles

XRD patterns of single particle reinforced AMCs containing maximum reinforcement (15 wt.%) of 'coarse' particles (i.e. '15CBR' composite and '15CIR' composite) are presented in Figure 4.4a–b.

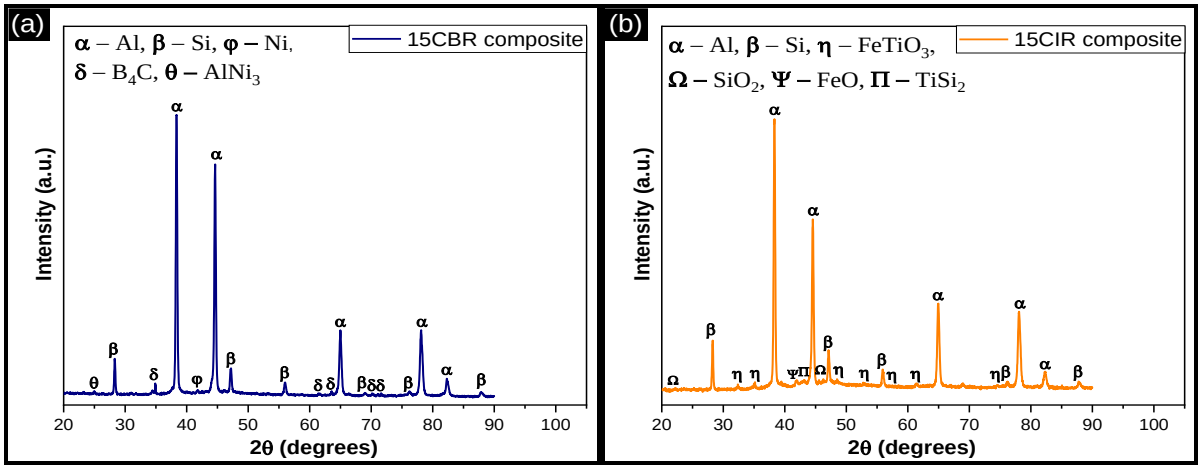

Figure 4.4 X-ray diffraction profile of (a) '15CBR' and (b) '15CIR' composites.

XRD patterns of both the composites showed peaks of aluminium (Al) and silicon (Si) which correspond to the matrix material (LM13 alloy). Further, several other peaks (additional peaks) were observed which indicated presence of reinforced particles, formation of intermetallic compounds, and/or occurrence of interfacial reaction products. Boron carbide particles reinforced '15CBR' composite showed additional peaks indicating the presence of boron carbide (B_4C), nickel (Ni), and aluminium-nickel ($AlNi_3$) phases. Further, ilmenite particles reinforced '15CIR' composite showed additional peaks indicating presence of ilmenite ($FeTiO_3$), silicon oxide (SiO_2), iron oxide (FeO), and titanium-silicon ($TiSi_2$) phases. Aluminium-nickel phase in 'CBR' composites signified the formation of intermetallic compounds (this phase was absent in ilmenite based '15CIR' composite). In case of 'CIR' composites, the presence of silicon oxide, iron oxide, and titanium-silicon phases signified formation of interfacial products through reaction between reinforced particles (ilmenite) and the matrix material (silicon of the base alloy). The interfacial reaction can be described as Equation 4.1 [80].

$$3Si + FeTiO_3 \rightarrow FeO + SiO_2 + TiSi_2 \quad \ldots\ldots\ldots\ldots\ldots\ldots (4.1)$$

It is reported that occurrence of interfacial reaction on reinforced particles results in better wetting behaviour [46,153,154]. So, formation of interfacial products on ilmenite particles based 'CIR' composites may result in formation of relatively stronger interfacial bonding in 'CIR' composites. No such interfacial reaction was observed for boron carbide based 'CBR' composites.

XRD diffractograms also provided data from which the average crystallite size and crystallinity of base alloy and composites was determined. Table 4.1 presents the average crystallite size and crystallinity values obtained from X-ray analysis for the base alloy and composites.

Table 4.1 Crystallinity and crystallite size of base alloy, '15CIR' composite, and '15CBR' composite.

Base alloy/AMC	Crystallinity (%)	Average crystallite size (nm)
LM13 alloy	30	65.74
'15CIR' composite	55	45.56
'15CBR' composite	63	41.60

It was observed that addition of reinforced particles to the base alloy increased the crystallinity and reduced the crystallite size of AMCs. Increase in crystallinity signifies an increase in the nucleation rate of new crystals. This increase in nucleation rate causes formation of crystallites of smaller sizes i.e. decrease in the average crystallite size [21]. During the solidification process in AMCs, the reinforced particles provide hindrance to the growth of crystals of the base alloy. This hindrance restricts the crystal growth and promotes refining of the crystal size of base alloy. Also, the hard reinforced particles create a pining effect which splits the existing crystals into multiple crystals [155]. For these reasons addition of reinforced particles reduced the average crystallite size in AMCs as compared to the base alloy.

Further, '15CBR' composite showed relatively higher crystallinity and lower crystallite size than '15CIR' composite. This was attributed to lower density and high inherent hardness of boron carbide as compared to ilmenite as given in Table 3.2. Because of the lower density of boron carbide, relatively higher number of reinforced particles were present in '15CBR' composite than '15CIR' composite which provided higher crystallinity and lower average crystallite size to boron carbide based '15CBR' composite.

4.2.3 Single particle reinforced composites containing fine particles

Figure 4.5a–b presents the XRD patterns of single particle reinforced AMCs containing maximum reinforcement (15 wt.%) of 'fine' particles (i.e. '15FBR' composite and '15FIR' composite). Indexing of the XRD patterns revealed three categories of peaks: (i) peaks related to the matrix (Al, Si, and Ni), (ii) peaks related to the reinforced particles (ilmenite and boron carbide), and (iii) peaks related to the interfacial compounds (SiO_2, FeO, and $TiSi_2$). As discussed in Section 4.2.2, similar peaks were also observed in '15CBR' composite and '15CIR' composite containing coarse particles. However, due to differences in the particle size of reinforced particles from 'coarse' to 'fine', there were differences in the values of crystallite size and crystallinity for the two types of AMCs.

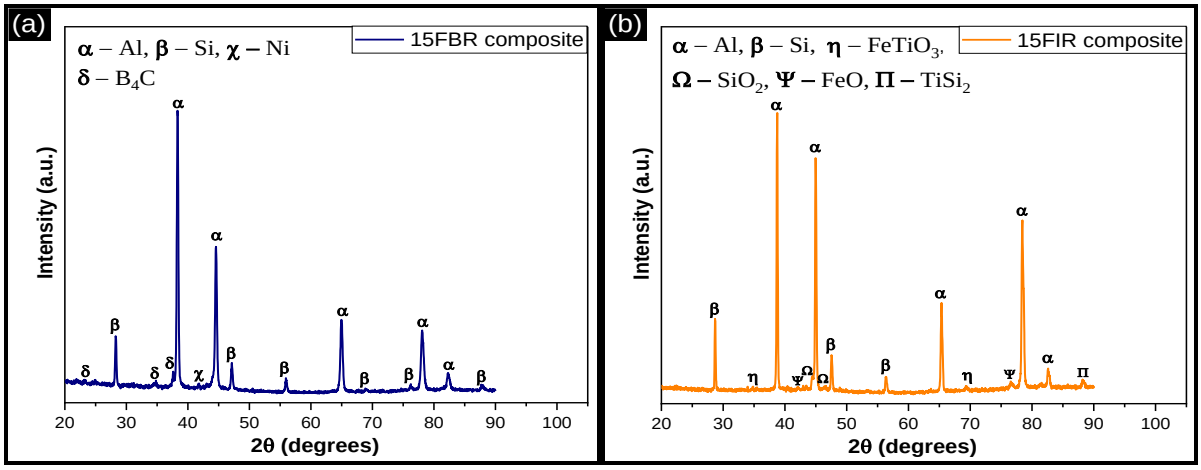

Figure 4.5 X-ray diffraction profile of (a) '15FBR' and (b) '15FIR' composites.

For a given type of AMC ('CBR' or 'FBR') at a given reinforcement level, a decrease in average crystallite size was observed with decrease in particle size of reinforced particles. The reduction in average crystallite size was ascribed to restriction in diffusion of molten alloy by the reinforced particles. This increased the nucleation rate of new crystals [156]. The presence of relatively higher number of particles at a given reinforcement level for composites containing 'fine' particles also led to higher pinning effect and thus lower crystallite size. Table 4.2 presents the values of crystallite size and crystallinity for '15FIR' and '15FBR' composites.

Table 4.2 Crystallinity and crystallite size of base alloy, '15FIR' composite, and '15FBR' composite.

Base alloy/AMC	Crystallinity (%)	Average crystallite size (nm)
LM13 alloy	30	65.74
'15FIR' composite	52	40.97
'15FBR' composite	58	32.62

4.3. Optical microscopy

4.3.1 LM13 alloy

Optical micrographs of LM13 alloy showed presence of two main regions viz. (i) primary α-Al (proeutectic Al), and (ii) eutectic mixture of Al and Si as shown in Figure 4.6. During casting, initially the primary α-Al nucleates in the molten mass. As the temperature decreases, the amount of primary α-Al increases and it grows in the form of dendrites. On reaching the temperature of around 577 ℃, eutectic mixture of Al-Si nucleates in the molten mass around the dendrites of α-Al, as shown in Figure 4.6a [146,157]. In the present work, it was observed that the Si phase present in the as-cast LM13 alloy was flaky in shape (Figure 4.6b).

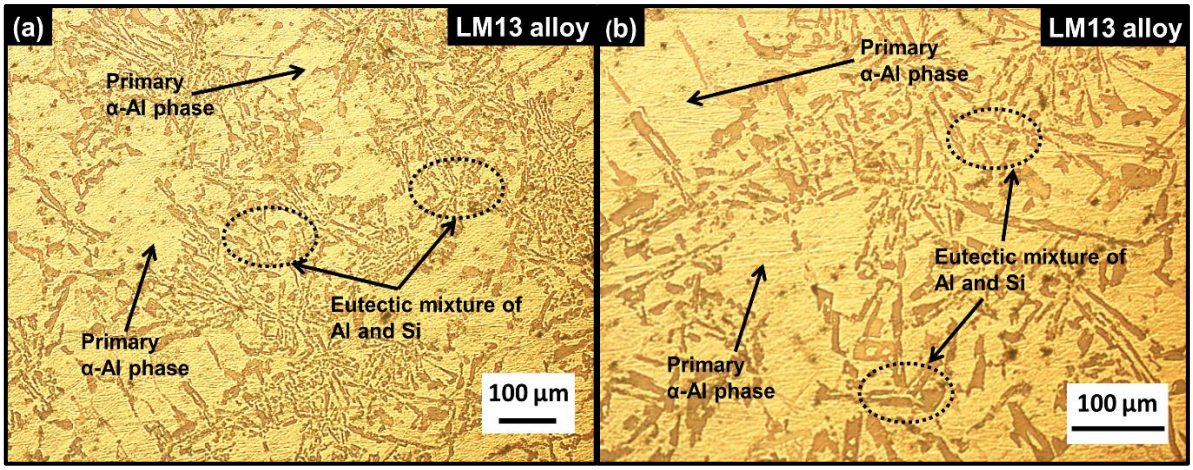

Figure 4.6 Optical micrographs of LM13 alloy at different magnifications of (a) 100X and (b) 200X.

4.3.2 Single particle reinforced composites containing coarse particles

Figure 4.7 presents the optical micrographs of single particle reinforced AMCs containing 'coarse' particles at various reinforcement levels.

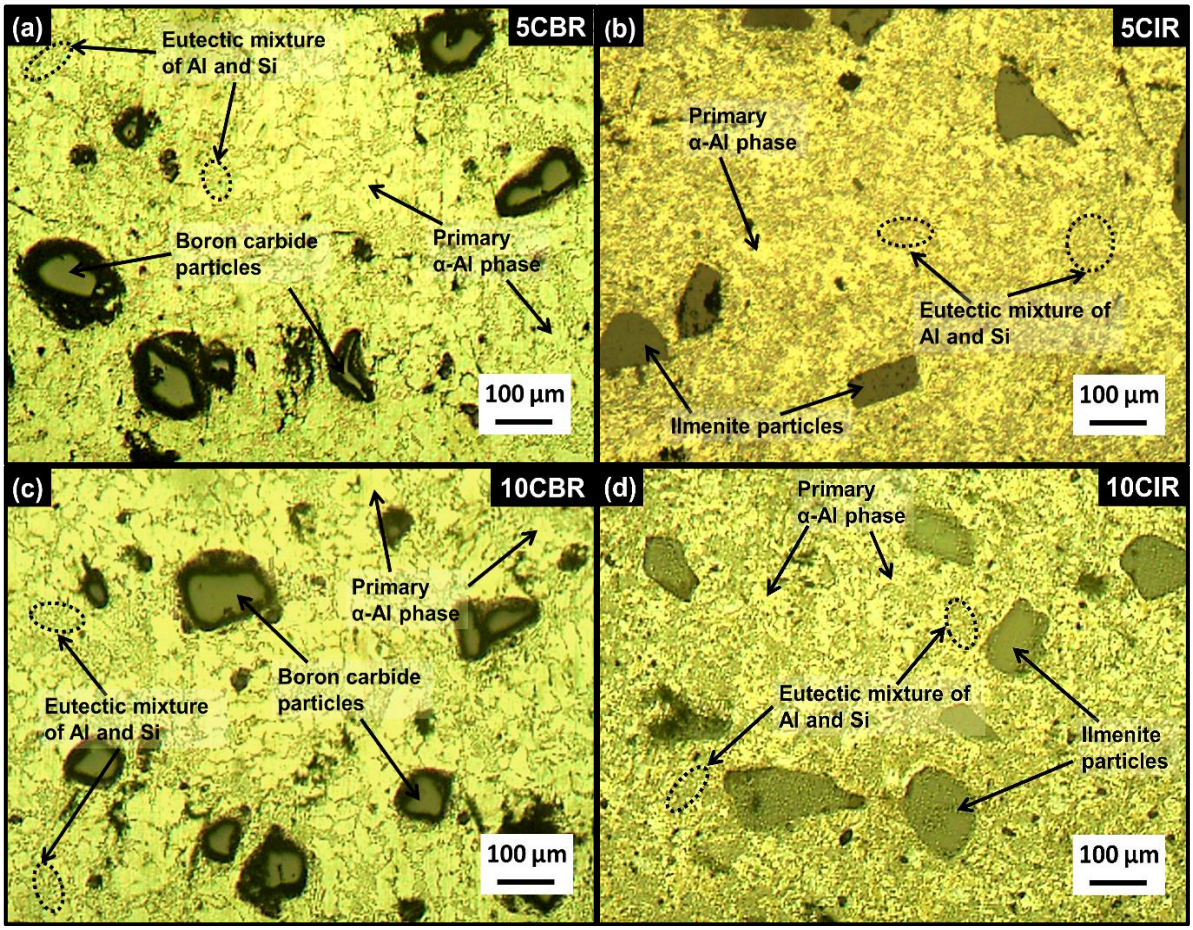

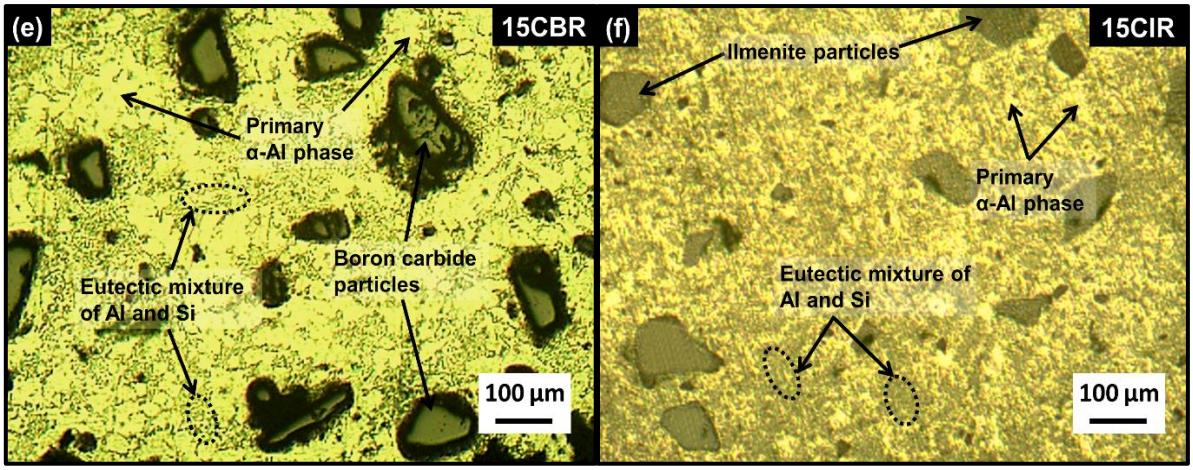

Figure 4.7 Optical micrographs of (a) '5CBR' composite, (b) '5CIR' composite, (c) '10CBR' composite, (d) '10CIR' composite, (e) '15CBR' composite, and (f) '15CIR' composite at a magnification of 100X.

The micrographs revealed that for both types of composites ('CBR' and 'CIR' composites), the reinforced particles are nearly uniformly distributed in the matrix. A large proportion of reinforced particles were observed in the vicinity of eutectic silicon. Further, it was observed that the flake like eutectic silicon morphology present in the base alloy changed to nearly globular type in the processed AMCs. This change in silicon morphology from flake like to globular was more prominent in boron carbide based 'CBR' composites.

The microstructure obtained in metal matrix composites depends on (i) the difference in thermal conductivities of reinforced particles and base alloy (matrix material), and (ii) the distance between two adjacent reinforced particles in the metal matrix [18,158,159]. Due to variation in thermal conductivity of matrix and reinforced particles, there exists a thermal gradient near the reinforced particles. The thermal conductivity values of boron carbide, ilmenite, and LM13 alloy are 30 W/mK, 1.49 W/mK, and 166 W/mK respectively [160,161]. During processing of the composites, the reinforced particles create a temperature difference within the molten mass due to their low thermal conductivity and heat dissipation capability as compared to LM13 alloy. Molten mass around the reinforced particles remains at a higher temperature causing nucleation of primary Al at a distance from the reinforced particles [18,159,162]. Further, with increase in reinforcement level, the distance between adjacent reinforced particles decreases. This decreases the growth of primary Al nuclei. On reaching the eutectic temperature, the molten matter around the particles starts solidifying which results in nucleation of eutectic mixture. For this reason, in the present research, the reinforced particles were surrounded by eutectic mixture as shown in Figure 4.8 for '15CBR' and '15CIR' composites. The reinforced particles also provided hindrance for the growth of constituent

phases present in the processed AMCs. This hindrance helped in refining the grain size of primary Al and also of eutectic silicon (Figure 4.8).

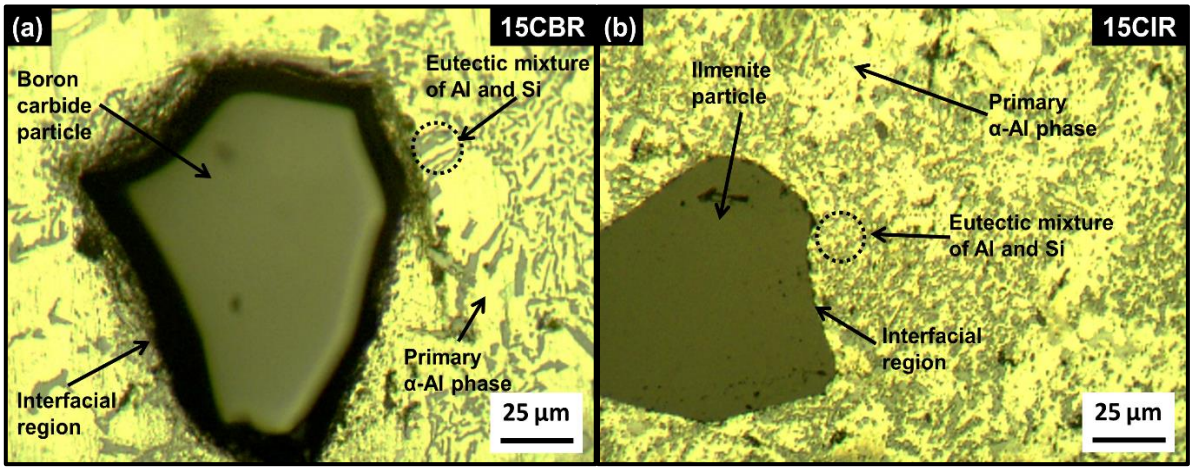

Figure 4.8 Optical micrographs of (a) '15CBR' and (b) '15CIR' composites at magnification of 500X showing interfacial region and different phases present in the AMCs.

4.3.3 Single particle reinforced composites containing fine particles

Figure 4.9 presents the optical micrographs of single particle reinforced AMCs containing 'fine' particles at various reinforcement levels. It was observed that boron carbide and ilmenite particles were uniformly dispersed in matrix in the processed AMCs. Further, eutectic silicon was observed to be present in the locality of reinforced ceramic particles. The segregation of alloying elements (present in the matrix material; here, Si) around the reinforced particles is influenced by surface energy of interface between the alloying elements and the reinforcement. It is reported that high segregation of alloying element around the reinforced particles occurs when surface energy is low [163]. Thus the accumulation of eutectic silicon around the ceramic particles in processed AMCs was due to lower surface energy of silicon-ceramic particle interface as compared to aluminium-ceramic particle interface.

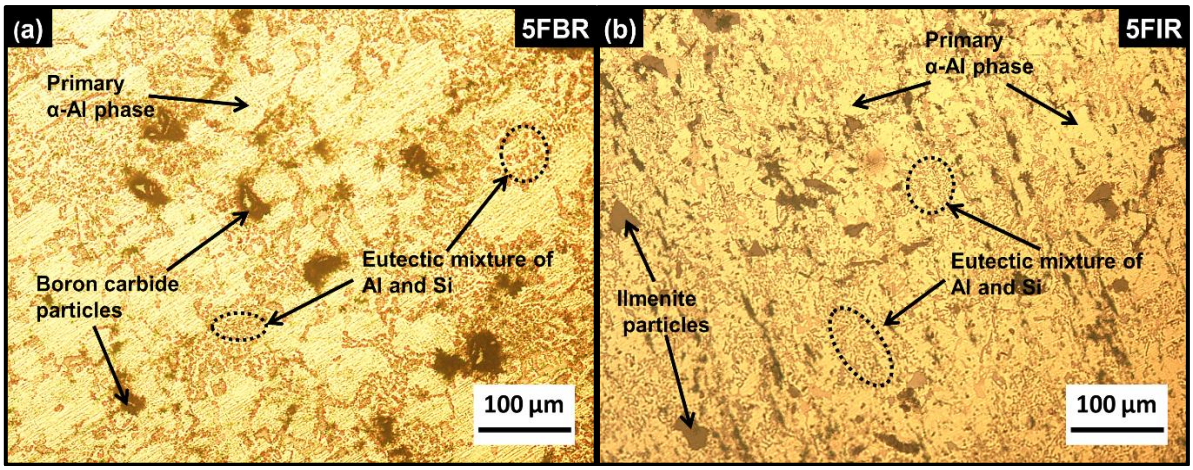

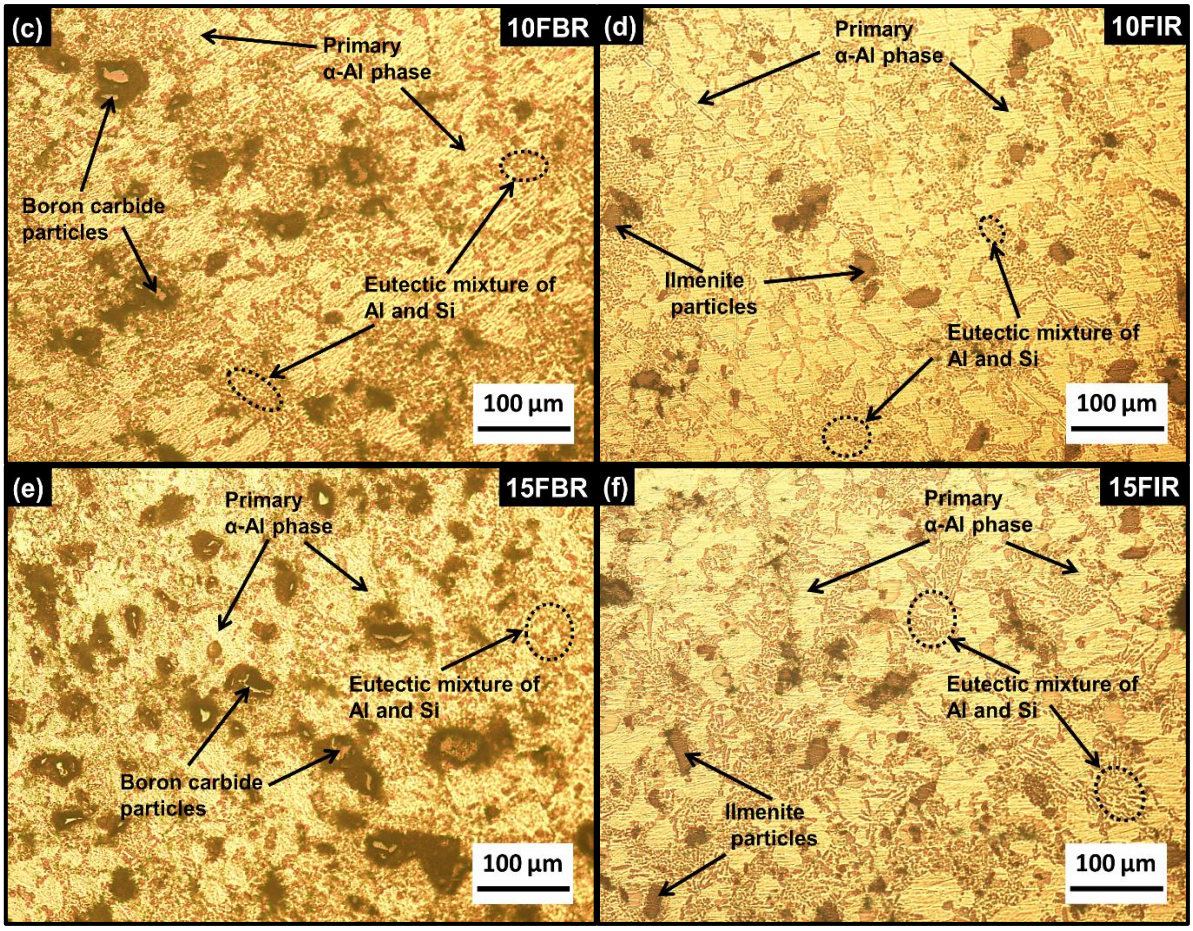

Figure 4.9 Optical micrographs of (a) '5FBR' composite, (b) '5FIR' composite, (c) '10FBR' composite, (d) '10FIR' composite, (e) '15FBR' composite, and (f) '15FIR' composite at 200X**.**

Figure 4.10 presents the optical micrographs of single particle reinforced AMCs containing maximum reinforcement (15 wt.%) of 'fine' and 'coarse' particles (i.e. '15CBR', '15CIR', '15FBR', and '15FIR' composites) at a magnification of 500X. These higher magnification images were used to compare the changes in grain size and morphology of silicon (present in the processed AMCs) due to the addition of 'coarse' and 'fine' category of reinforced particles. It was noted that with increase in reinforcement level in AMCs, the flake like silicon morphology changed to equiaxed structure and grain size of eutectic silicon decreased. Grain size refinement and change in morphology were more prominent in boron carbide based 'FBR' composites.

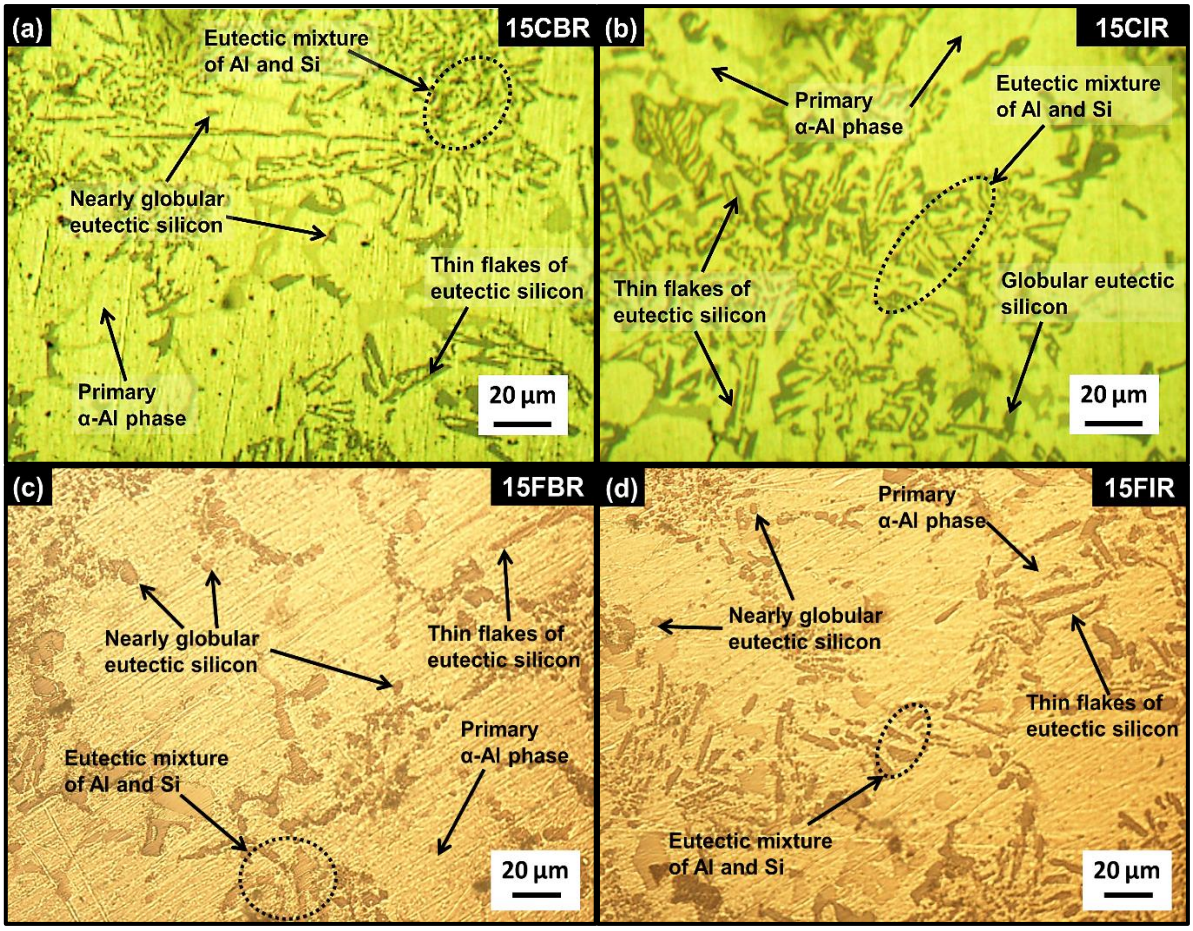

Figure 4.10 Optical micrographs showing change in size and morphology of silicon for (a) '15CBR' composite, (b) '15CIR' composite, (c) '15FBR' composite, and (d) '15FIR' composite at 500X.

The grain size distribution of eutectic silicon present in boron carbide based 'BR' composites and ilmenite based 'IR' composites was obtained using an integrated software with the optical microscope and is presented in Figure 4.11. For a given particle size category of reinforced particles, relatively finer grain size of eutectic silicon was obtained for 'BR' composites as compared to 'IR' composites and base alloy. Further, for a given type of AMC ('BR' composite or 'IR' composite), relatively finer grain size of eutectic silicon was obtained for 'fine' category of reinforced particles. The above mentioned observations were attributed to change in distance between the adjacent reinforced particles due to changes in reinforcement type and particle size category. Reinforcement type with lower density and particle size category with finer size results in larger number of reinforced particles in AMCs at a given reinforcement level and thus decreases the distance between adjacent reinforced particles. This decrease in distance results in restriction to growth of grains resulting in finer grains with globular morphology for eutectic silicon. Now, for the two types of AMCs, boron carbide particles have lower density. Thus, for a given particle size category of reinforced particles, relatively finer grain size of

eutectic silicon was obtained for 'BR' composites. Further, for the two types of particle size categories, fine category has more number of particles at a given reinforcement level. Thus, for a given type of AMC ('BR' or 'IR' composite), relatively finer grain size of eutectic silicon was obtained for AMC reinforced with 'fine' particles.

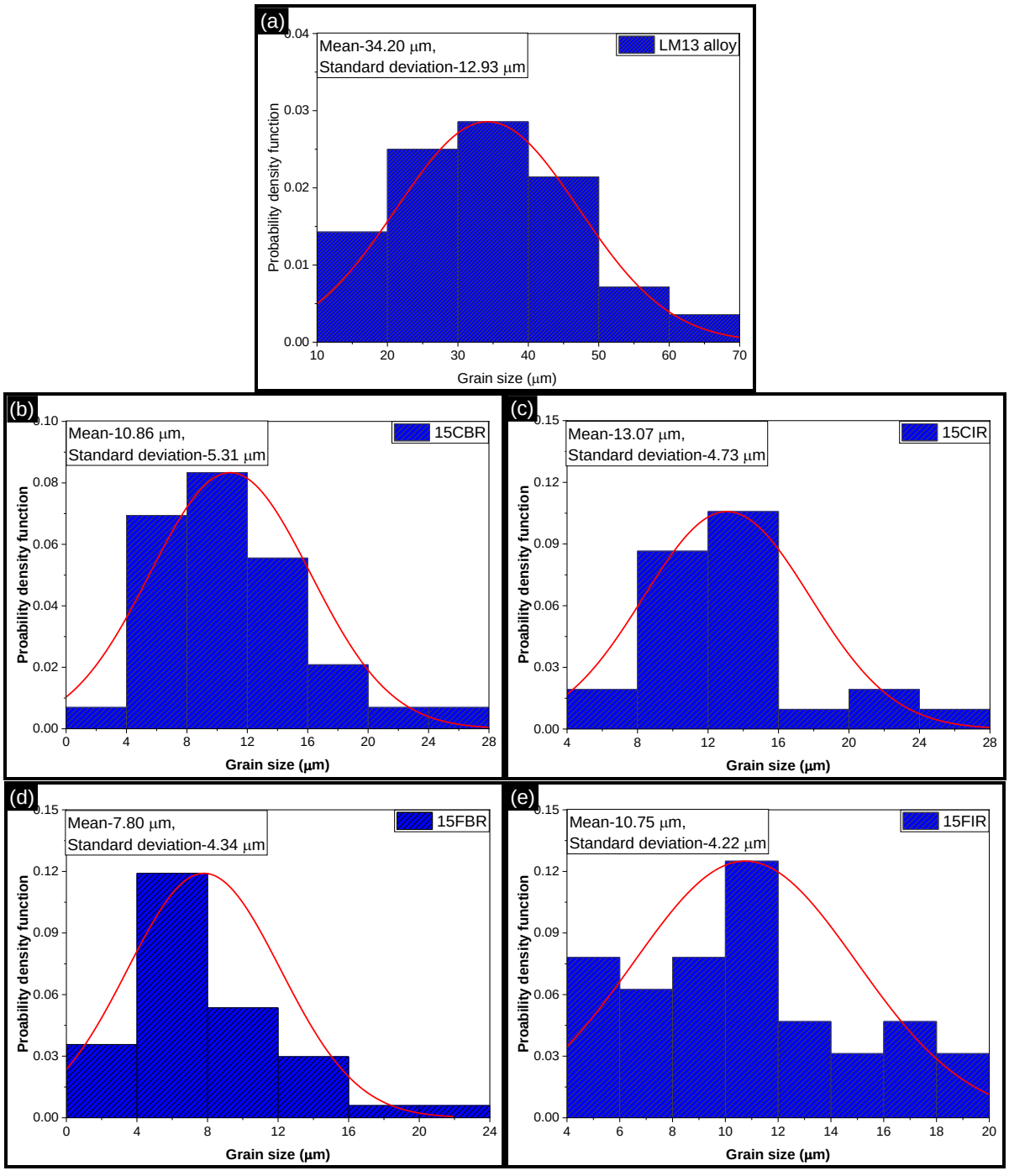

Figure 4.11 Grain size distribution of eutectic silicon in (a) LM13 alloy, (b) '15CBR' composite, (c) '15CIR' composite, (d) '15FBR' composite, and (e) '15FIR' composite.

4.4. Hardness analysis

4.4.1 Single particle reinforced composites containing coarse particles

Table 4.3 provides the hardness values for single particle reinforced AMCs containing 'coarse 'particles of boron carbide and ilmenite (i.e. 'CBR' and 'CIR' composites). Hardness of the base alloy was determined as 96.11±5.42 HV. AMCs showed higher hardness values than the base alloy. For any given reinforcement level, both types of AMCs showed comparable values of hardness with boron carbide based AMCs showing slightly higher values. During hardness testing, the indentation obtained on the specimen's surface under the effect of load results in localized plastic deformation of the material. For the unreinforced base alloy, the indenter caused a high degree of localized plastic deformation in the absence of particle reinforcement. However, during hardness testing of AMCs, there was a decrease in localized plastic deformation due to the presence of the hard ceramic particle reinforcement. Further, for a given type of AMC, hardness showed increase with increase in reinforcement level. This was a result of the reduced inter-particle distance causing resistance to plastic deformation [164].

Table 4.3 Vickers hardness values for 'BR' and 'IR' composites reinforced with coarse particles.

Reinforcement level in AMCs (wt.%)	Vickers hardness value (HV) for AMCs reinforced with	
	boron carbide (B_4C)	ilmenite ($FeTiO_3$)
	'CBR' composites	'CIR' composites
5	110.33±4.43	103.44±5.17
10	120.93±8.46	111.18±6.67
15	129.42±5.18	120.63±4.82

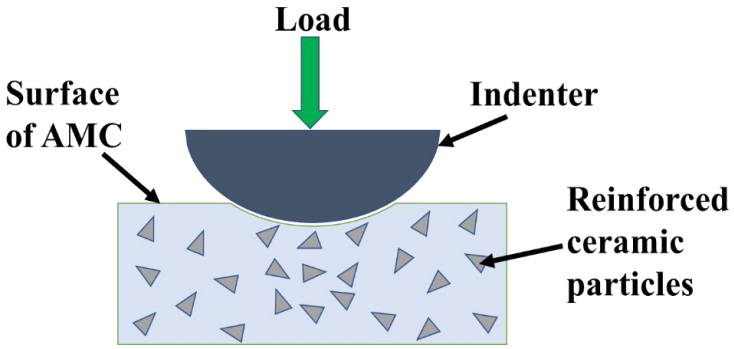

Figure 4.12 Particle concentration near indenter in AMCs during hardness testing.

During hardness testing, the compressive force allows the material to flow downwards in the vertical direction. This vertical flow of material causes the reinforced particles to concentrate beneath the indenter as shown in Figure 4.12. This increase in concentration of particles below the indenter leads to transfer of load from the matrix to the reinforced particles. Also, plastic deformation of the matrix material decreases with decrease in inter-particle distance [165]. The

pattern of plastic deformation in the unreinforced base alloy is uniform, as there is no reinforcement. However, the presence of reinforced particles in composites fragments the field of plastic deformation. This fragmentation corresponds to non-deformability of reinforced particles and causes an increase in resistance to plastic deformation of matrix material [165]. Due to these reasons, hardness of AMCs shows a rising trend with increase in reinforcement level. Further, these factors also depend on the number of particles present in the AMC at a given reinforcement level. This aspect has a direct correlation with density of particles at a given reinforcement level. Due to high number of particles in 'BR' composites at particular reinforcement level, the field of plastic deformation is highly fragmented which causes higher restriction to plastic deformation of the matrix. For this reason, at a given reinforcement level, boron carbide particles based 'CBR' composites showed higher hardness than ilmenite reinforced 'CIR' composites.

4.4.2 Single particle reinforced composites containing fine particles

Table 4.4 provides the hardness values for single particle reinforced AMCs containing 'fine' particles of boron carbide and ilmenite (i.e. 'FBR' and 'FIR' composites). Again, for any given reinforcement level, both types of AMCs showed comparable values of hardness with boron carbide based 'BR' composites showing slightly higher values. Also, for a given type of AMC at a given reinforcement level, hardness values were higher for AMC containing 'fine' particles (compared to 'coarse' particles; comparing values in Table 4.3 and Table 4.4). For these reasons, '15FBR' composite showed the highest hardness. XRD results (Table 4.2) had also shown relatively lower crystallite size for '15FBR' composite confirming its higher hardness compared to '15FIR' composite.

Table 4.4 Vickers hardness values for 'BR' and 'IR' composites reinforced with fine particles.

Reinforcement level in AMCs (wt.%)	Vickers hardness value (HV) for AMCs reinforced with	
	boron carbide (B_4C)	ilmenite ($FeTiO_3$)
	'FBR' composites	'FIR' composites
5	117.92±4.12	106.46±4.37
10	123.89±5.38	115.20±5.28
15	135.59±3.71	129.53±6.87

The reasons for improved hardness of AMCs over the base alloy were already discussed for 'CBR' and 'CIR' composites in Section 4.4.1. The same reasons hold good for 'FBR' and 'FIR' composites also. Further, hardness of AMCs is also influenced by mismatch in the coefficient of thermal expansion (CTE) values of reinforcement and matrix [13,19]. CTE values for LM13 alloy, B_4C particles, and $FeTiO_3$ particles are 20.29×10^{-6} K^{-1}, 3.20×10^{-6} K^{-1}

and 27.90×10^{-6} K^{-1} respectively [45,166,167]. Due to the high mismatch in CTE values of matrix and reinforcement, the dislocation density in AMCs increases which also resulted in higher hardness of AMCs [13].

4.5. Coefficient of thermal expansion (CTE)

4.5.1 Single particle reinforced composites containing coarse particles

Figure 4.13 presents the 'thermal strain versus operating temperature' and 'CTE versus operating temperature' graphs for base alloy and various AMCs (reinforced with coarse particles). Operating temperature was varied in the range of 50–300 ℃. Experimentally, CTE values were calculated as per Equation 3.1.

For the base alloy (here, LM13 alloy), CTE value is mainly affected by restriction provided by secondary phase (here, eutectic silicon) to the expansion of primary phase (here, aluminium). This restriction to expansion of aluminium depends upon the specific area of contact between aluminium and silicon [168]. From microstructural analysis, high grain size of silicon (34.20 µm; Figure 4.11a) in LM13 alloy was observed which signified its low specific area of contact with aluminium. This relatively low specific area of contact attributed to lower restriction by silicon to expansion of aluminium resulting in increasing trend in CTE values with operating temperature.

For a given AMC composition present at a given operating temperature, the thermal strain and CTE values (for change in temperature from ambient conditions to the given operating temperature) were lower as compared to those of the base alloy. Further, for a given operating temperature, the CTE values of AMCs decreased with increase in reinforcement levels (Figure 4.13d and Figure 4.13f). The results showed that addition of reinforced particles to LM13 alloy decreased the CTE of resulting AMCs. This signified that addition of ceramic particles is an effective method to tailor the CTE value of LM13 alloy. '15CBR' and '15CIR' composites showed maximum reduction in the average CTE values (37.58% and 48.51% respectively over the base alloy for change in temperature from ambient conditions to 300 ℃). During heating of AMCs, the presence of reinforced particles restricted the expansion of matrix material due to difference in CTE values of matrix and reinforced particles. This restriction to the expansion of matrix material caused decrease in CTE of AMCs [18]. It may be noted that the relatively lower average CTE value obtained for 'CIR' composites (48.51% decrease compared to base alloy) indicated higher interfacial bonding strength of matrix-reinforcement in 'CIR' composites as compared to 'CBR' composites [23,169].

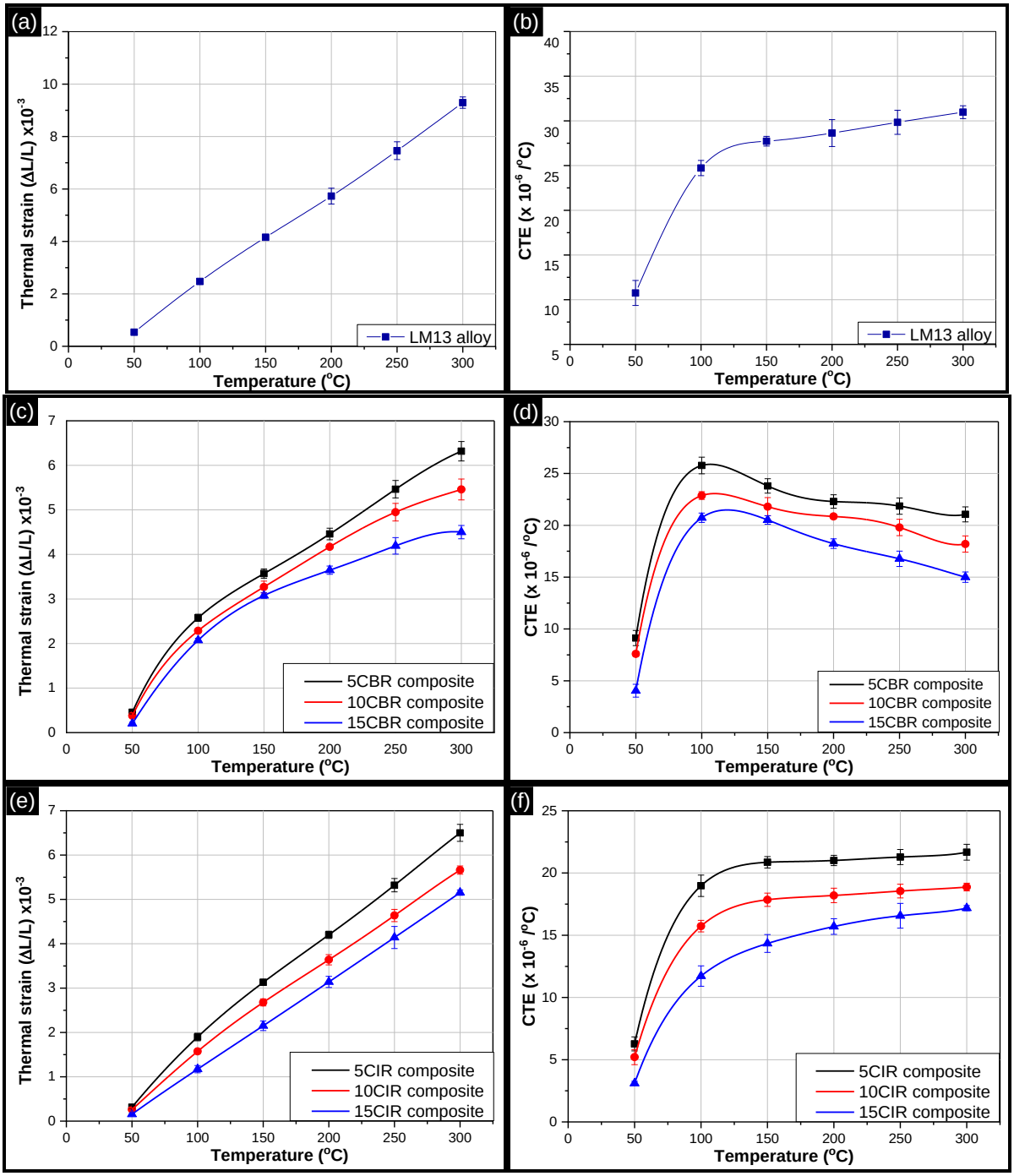

Figure 4.13 Variation in thermal strain and CTE values as a function of operating temperature for (a & b) LM13 base alloy, (c & d) 'CBR' composites, and (e & f) 'CIR' composites.

For increase in temperature in the range of 50−100 ℃, the CTE values of AMCs increased (for both types of AMCs viz. 'CBR' and 'CIR' composites). However, with further rise in temperature in the range of 100–300 ℃, the trend observed in CTE values as a function of operating temperature was different for the two types of AMCs. In this temperature range (100–300 ℃), 'CBR' composites showed a decreasing trend in CTE values whereas 'CIR' composites continued to show an increasing trend with increase in temperature. Generally, with

increase in operating temperature, the thermal strain increases which results in increase in CTE values of AMCs. In the present research, this general behaviour was displayed by the base alloy and also by 'CIR' composites. However, for 'CBR' composites, the decreasing trend in CTE values with increase in temperature in the range of 100−300 ℃ was a typical behaviour reported in literature also [170,171]. It is reported in literature that an increase in solid solubility of silicon in aluminium shows a negative effect on thermal expansion of AMCs [170,171]. This factor (Si solubility factor) also resulted in decrease in CTE values of 'CBR' composites with increase in temperature in the high temperature regime (100−300 ℃). In the context of Si solubility factor, the results indicated that presence of ilmenite in 'CIR' composites, suppressed the Si solubility factor, and so, these AMCs continued to show increase in CTE values with increase in temperature (for the entire range, 50−300 ℃). XRD analysis of '15CIR' composite (Section 4.2.2) had shown occurrence of interfacial reaction between silicon and ilmenite particles (Equation 4.1). This signified high affinity of ilmenite particles towards silicon present in the LM13 base alloy and was a possible reason restricting the solubility of silicon in aluminium in '15CIR' composite. However, no such interfacial reaction was observed in the case of '15CBR' composites. This signified that there was no restriction to solubility of Si in Al. This resulted in increase in solid solubility of silicon in aluminium with rise in temperature and hence a decreasing trend in CTE values in 'CBR' composites.

4.5.2 Single particle reinforced composites containing fine particles

Figure 4.14 presents the 'thermal strain versus operating temperature' and 'CTE versus operating temperature' graphs for base alloy and various AMCs (reinforced with fine particles). The trends observed in thermal strain and CTE values of AMCs reinforced with fine particles were the same as were observed for AMCs with coarse particles. For both types of AMCs ('FBR' and 'FIR' composites), thermal strain values continuously increased with increase in temperature for the entire range of 50–300 ℃ (Figure 4.14a and Figure 4.14c). With regards to CTE values, for increase in temperature in the range of 50−100 ℃, the CTE values of AMCs increased for both types of AMCs. However, with further rise in temperature in the range of 100–300 ℃, the trend observed in CTE values as a function of operating temperature was different for the two types of AMCs. In this temperature range (100–300 ℃), 'FBR' composites showed a decreasing trend whereas 'FIR' composites continued to show an increasing trend with increase in temperature (Figure 4.14b and Figure 4.14d). The reasons for this trend were the same as were reported in the last section for AMCs with coarse particles.

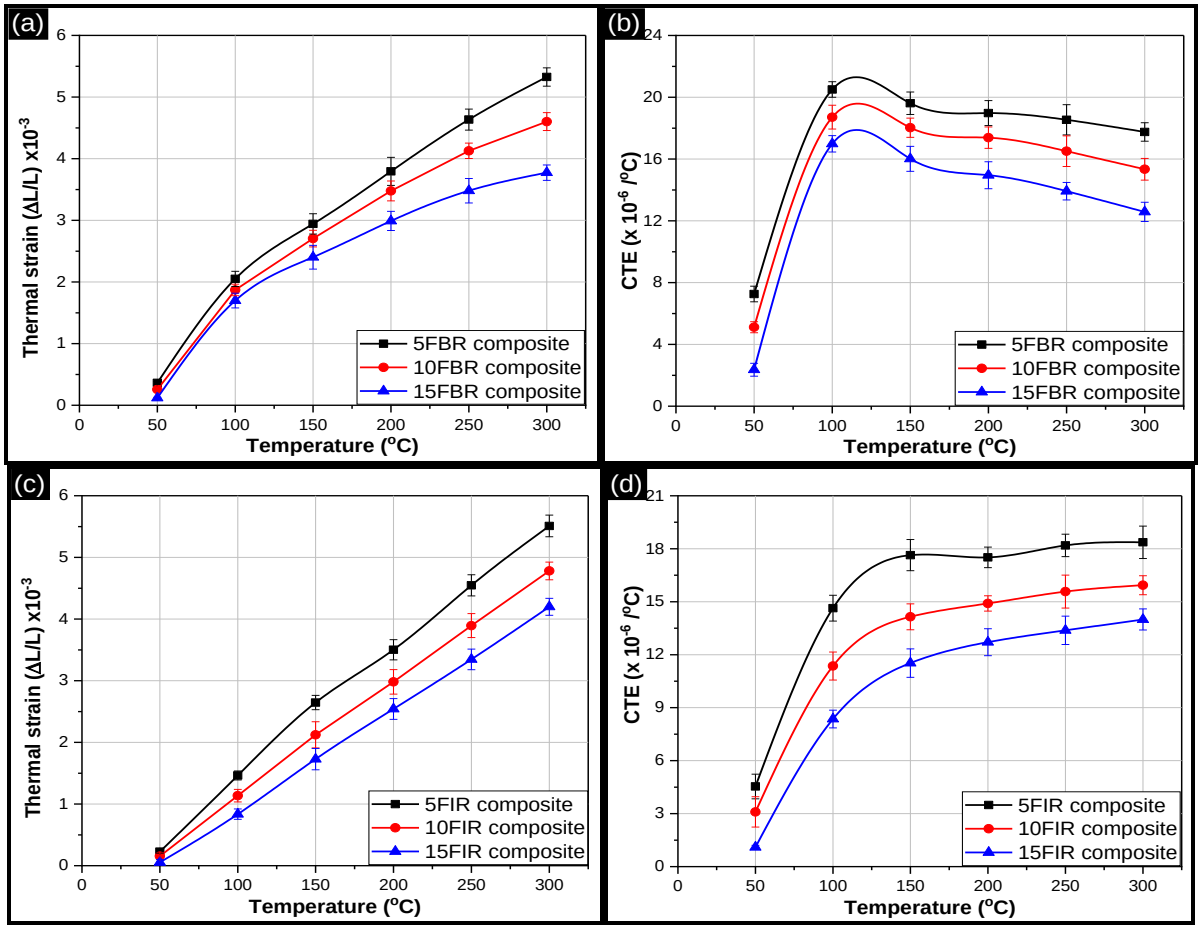

Figure 4.14 Variation in thermal strain and CTE values as a function of operating temperature for (a & b) 'FBR' composites and (c & d) 'FIR' composites.

Further, thermal strain and CTE values of 'FBR' and 'FIR' composites as a function of reinforcement level showed the same trends as were observed for AMCs with coarse particles. Thus, for a given operating temperature, any increase in the reinforcement level caused a decrease in thermal strain and CTE values. Finally, it was noted that for a given type of AMC at a given reinforcement level, with change in particle size from 'coarse' to 'fine' led to decrease in thermal strain and CTE values. '15FBR' and '15FIR' composites showed a reduction of 49.67% and 60.02% respectively in average CTE value over the base alloy. These improvements in CTE values of AMCs containing fine particles were attributed to the presence of relatively higher matrix-reinforcement interfacial area. During rise in temperature, this higher interfacial area between matrix and reinforced particles provides restriction to the expansion of matrix material. This results in generation of higher dislocation motions around the interfacial region, pinning of dislocations etc. [172]. These factors resulted in lower CTE values of AMCs reinforced with fine particles.

4.6. Wear rate behaviour under room temperature conditions

4.6.1 Single particle reinforced composites containing coarse particles

Figure 4.15 presents the wear rate behaviour of base alloy and various AMCs (containing coarse particles) as a function of sliding distance under different applied loads at room temperature conditions. The wear graphs showed three distinct wear regions based on the sliding distance: (i) region showing sharp increase in wear rate for sliding distance in the range of 0–500 m, (ii) region showing sharp decrease in wear rate for sliding distance in the range 500–1500 m, and (iii) region showing no significant change in wear rate for sliding distance in the range of 1500–3000 m.

During the initial stage of sliding, asperities of pin and disc surface make contact with each other as both have different surface roughness values [13]. For pin, the roughness value (R_a) was 0.31±0.01 µm and for the counter disc, it was 0.24±0.02 µm. Under the action of applied load, these asperities deformed plastically and got fractured which led to rise in wear rate for sliding distance (in the range of 0–500 m). Next, the fractured asperities resulted in formation of wear debris which either got trapped between the sliding surfaces or moved out of the system [5,13]. The stress acting on the sliding surface (i.e. worn surface of pin) and the entrapped debris due to the applied load led to strain hardening [13,58]. This strain hardening of pin was mainly responsible for decrease in wear rate in the sliding range of 500–1500 m. With further increase in sliding distance, a hard mechanical mixed layer (MML) was formed between the pin and disc surfaces due to entrapment of wear debris and the phenomenon of strain hardening [5]. MML or tribo-layer contains worn out materials coming from matrix material, counter surface material, reinforced particles, and their respective oxides. The presence of higher oxide content was due to oxidation during friction between both the contact surfaces [173,174].

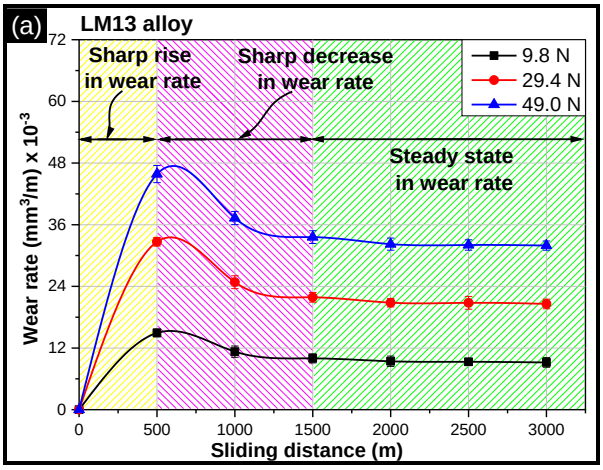

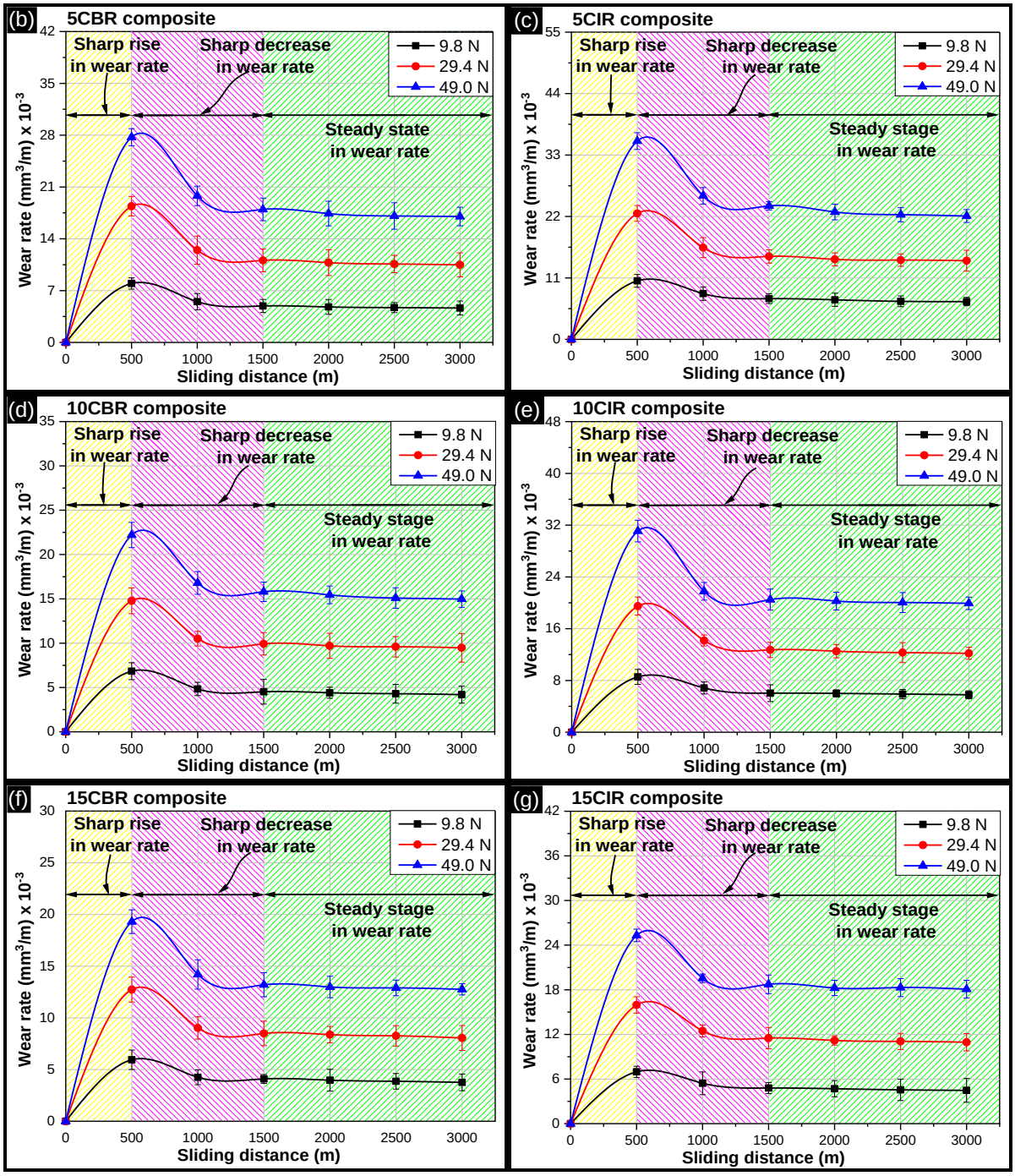

Figure 4.15 Wear rate as a function of sliding distance under various loads for (a) LM13 alloy, and different AMCs viz. (b) '5CBR', (c) '5CIR', (d) '10CBR', (e) '10CIR', (f) '15CBR', and (g) '15CIR'.

Chen and Alpas [175] provided relationship for the maximum temperature (T_{max}) obtained at the worn surface given as Equation 4.2.

$$T_{max} = T_o + a \times F^{\frac{1}{4}} \times v^{\frac{1}{2}} \quad \ldots\ldots\ldots\ldots\ldots\ldots\ldots\ldots\ldots\ldots \quad (4.2)$$

Where, 'F' is the applied load, 'v' is the sliding velocity, and 'T_o' & 'a' are constants. The values of 'T_0' and 'a' depend on values of F and v. If $\left(F^{\frac{1}{4}} \times v^{\frac{1}{2}}\right)$ is less than 2.8, 'T_0' and 'a' are equal to 290 K and 15.1 respectively. Otherwise, the values are -191 K and 210.5 respectively. For sliding speed of 1.6 m/s, the predicted maximum temperature attained under various applied loads is shown in Table 4.5. Such high temperatures attained on the worn surface contribute towards formation of an oxide film on the pin surface. This oxidation of the sliding surface (formation of oxide film on the pin surface) and the formation of mechanically mixed layer result in attainment of steady-state wear rate behaviour [58].

Table 4.5 Maximum temperature predicted at the pin surface under different applied loads.

Sliding velocity (m/s)	Applied load (N)	T_o (K)	a	Maximum temperature at the sliding pin surface (K)
1.6	9.8	290	15.1	324
1.6	29.4	-191	210.5	429
1.6	49.0	-191	210.5	513

Wear graphs of LM13 alloy, 'CBR' composites, and 'CIR' composites showed higher wear rates at higher applied loads for a given composition-sliding distance condition (as shown in Figure 4.15). During the initial conditions of sliding, plastic deformation and fracturing of material occurs and micro-cracks are developed beneath the contact surface. As the sliding distance increases, propagation and convergence of these micro-cracks lead to removal of material [58,174]. At relatively higher loads, this mechanism dominates and delays the work hardening of sliding pin surface, leading to higher wear rates. Further, in case of steady-state wear regime, increase in applied load affects the oxidation of worn surfaces and MML [18,175]. Higher applied load results in higher temperature at worn surfaces and higher oxidation rates of material. This results in formation of a protective layer of oxides on the worn surface, preventing further wear [175]. However, higher loads also affect the stability of MML. At higher loads, generation of micro-cracks is higher causing removal of material from MML [176]. The overall effect is the increase in wear rate at higher applied loads. AMCs (both 'CBR' and 'CIR') showed lower wear rate than the base alloy for any applied load-sliding distance condition. Further, drop in wear rate of AMCs was observed with increase in content of reinforced particles. During sliding, dislocations are generated on the worn pin surface and their movement is blocked by the reinforced ceramic particles (secondary particles). This restriction by the reinforced particles results in piling up of dislocations around the particles. The entrapment of dislocations around the secondary particles leads to increase in strain

hardening and resistance to plastic deformation, thus lowering the wear rate of AMCs compared to the base alloy [173].

Table 4.6 summarizes the improvements obtained in wear rate of processed AMCs over the base alloy. For a given reinforcement level and applied load-sliding distance condition, 'CBR' composites showed superior wear characteristics than 'CIR' composites.

Table 4.6 Percentage decrease in wear rate of AMCs containing coarse particles over the base alloy.

S.No.	Applied load (N)	Percentage decrease in wear rate of AMC compared to the base alloy (%)					
		'CIR' composites			'CBR' composites		
		'5CIR'	'10CIR'	'15CIR'	'5CBR'	'10CBR'	'15CBR'
1.	9.8	30	43	53	47	54	60
2.	29.4	31	40	51	44	55	61
3.	49.0	23	32	45	40	52	58

Boron carbide particles have higher hardness (9.3 Mohs) in comparison to ilmenite particles (5.0–6.0 Mohs) [42,148]. At a particular reinforcement level, the low density of boron carbide (2.52 g/cm^3) leads to reinforcement of higher number of particles as compared to ilmenite particles (4.72 g/cm^3). Hence, in case of 'CBR' composites, the entrapment of dislocations is higher which corresponds to high strain hardening [173]. Also, MML is more stable in 'CBR' composites because of their relatively higher hardness. In case of 'CIR' composites, the maximum temperature (predicted using Equation 4.2) is attained much early as compared to 'CBR' composites. This is attributed to the lower thermal conductivity of ilmenite (1.49 W/m K) in comparison to boron carbide (30 W/m K) [160,161]. Thus, the heat generated due to friction is dissipated to a lesser extent in 'CIR' composites causing relatively higher temperature at the pin surface. This results in early formation of oxide layer, and thus, prevents wear of 'CIR' composites. Also, as stated earlier, interfacial bonding formed by ilmenite particles was relatively stronger than the boron carbide particles. Thus, it may be noted that both types of AMCs significantly improved the wear rate behaviour over the base alloy (wear reduction was higher for 'CBR' composites); however, the factors and reasons through which these improvements were obtained in the two types of composites were very different.

4.6.2 Single particle reinforced composites containing fine particles

Figure 4.16 presents the wear rate behaviour of base alloy and various AMCs (containing fine particles) as a function of sliding distance under different applied loads for room temperature conditions.

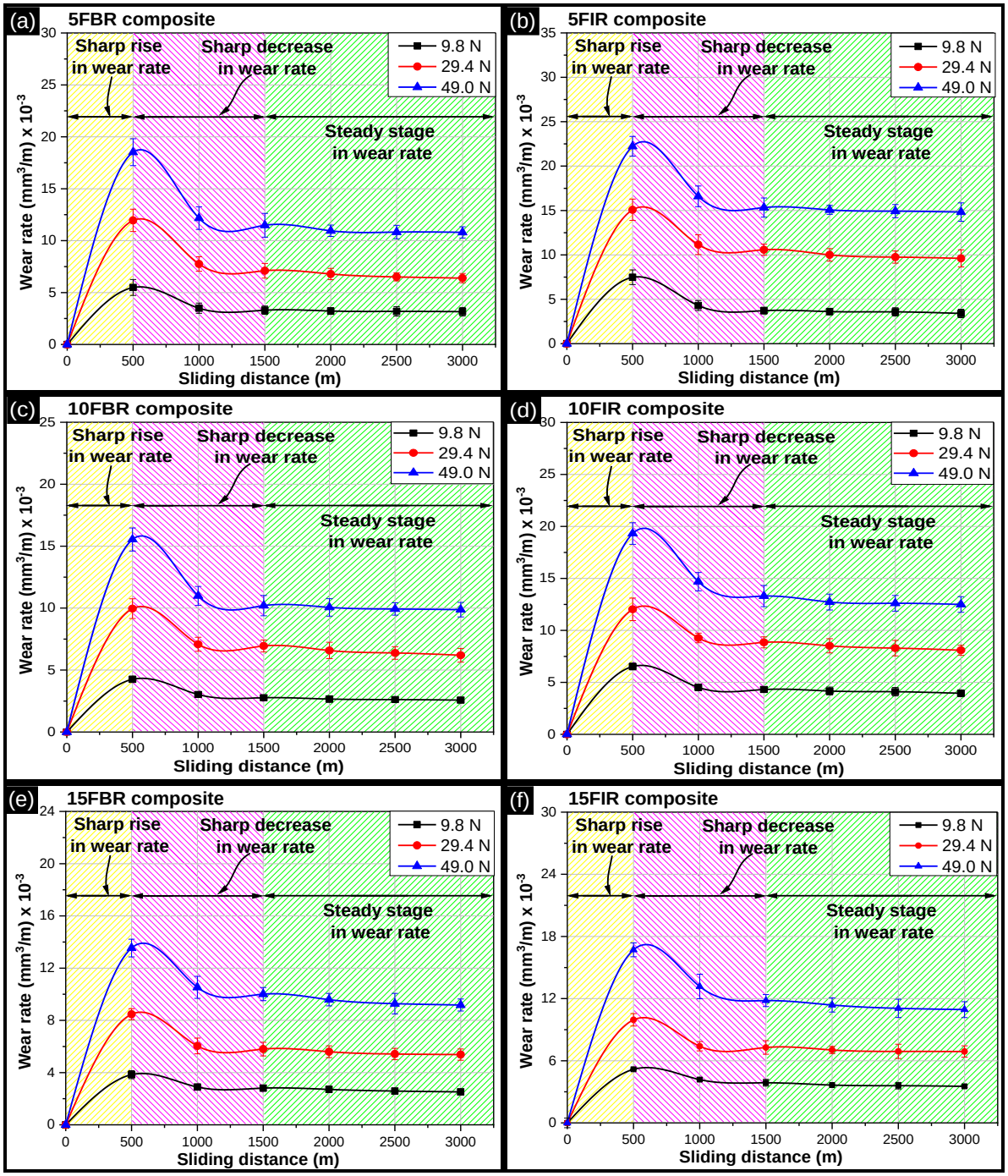

Figure 4.16 Wear rate as a function of sliding distance under various loads for (a) '5FBR' composite, (b) '5FIR' composite, (c) '10FBR' composite, (d) '10FIR' composite, (e) '15FBR' composite, and (f) '15FIR' composite.

With rise in load, a rise in wear rate for all AMCs was observed for a given composition-sliding distance condition. Under applied load, the sliding surfaces experience plastic deformation, fracturing of asperities, and development of micro-cracks beneath the contact surface. With increase in sliding distance, the generated micro-cracks propagate and converge causing removal of material [58,174]. The increase in applied load, accelerates the mechanism of crack

initiation and propagation. Moreover, it also delays the work hardening of materials resulting in higher wear rate [18,175]. Higher applied loads also result in higher temperature at the worn surfaces and higher oxidation rate of materials as the sliding distance reaches the steady-state region. This results in formation of a protective oxide layer on the worn surface which also helps in preventing the wear rate of samples [175]. However, higher loads also affect the stability of MML. At higher loads, generation of micro-cracks is higher causing removal of material from the MML [176]. The overall effect is an increase in wear rate at higher applied loads. The results also showed that at a particular applied load, wear rate decreased with rise in weight percentage of reinforcement. This decrease in wear rate was attributed to presence of hard ceramic particles which restrict the plastic deformation of matrix and also cause work hardening of the pin surface [177,178]. Both parameters (resistance to plastic deformation and work hardening) depend on number of particles present in the composites. With increase in number of particles, the resistance to plastic deformation and the work hardening effect increases. So, wear rate decreased with increase in reinforcement levels at a given load. For the same reasons, the addition of low density (along with high hardness) boron carbide particles in 'CBR' composites resulted in higher decrease in wear rate than 'FIR' composites for a given reinforcement level-applied load condition. The reduction in wear rate (maximum wear rate at sliding distance of 500 mm) of 'FIR' and 'FBR' composites over the base alloy is shown in Table 4.7.

Table 4.7 Percentage decrease in wear rate of AMCs containing fine particles over the base alloy.

S. No.	Applied load (N)	Percentage decrease in wear rate of AMC compared to the base alloy (%)					
		'FIR' composite			'FBR' composite		
		'5FIR'	'10FIR'	'15FIR'	'5FBR'	'10FBR'	'15FBR'
1.	9.8	50	56	65	63	72	74
2.	29.4	54	63	70	63	70	74
3.	49.0	52	58	64	60	66	70

Comparing the wear results of AMCs containing coarse particles ('CIR' and 'CBR' composites) against those containing fine particles ('FIR' and 'FBR' composites), it was observed that reduction in particle size of the reinforced particles resulted in more decrease in the wear rate of composites. It is well reported that when a composite material is sliding against a counter surface under the action of an applied load, the reinforced particles get pulled out from the sliding surfaces. For 'CBR' and 'CIR' composites, since the particle size is relatively larger, the removal of particles allowed larger area of base alloy to come in contact with the counter surface as compared to 'FBR' and 'FIR' composites. Also, with relatively larger

particle size, the number of particles present on the sliding surface (compared to finer particles for a given reinforcement level) were lesser. These are the main reasons for higher deformation of the base alloy and higher wear rates of 'CBR' and 'CIR' composites.

4.7. Coefficient of friction under room temperature conditions

4.7.1 Single particle reinforced composites containing coarse particles

Figure 4.17 presents the coefficient of friction (COF) values under room temperature conditions for base alloy and various AMCs (containing 'coarse' particles) as a function of applied load over the entire sliding distance. It was observed that reinforcement of ceramic particles to the matrix material reduced the COF of resulting AMCs over the base alloy for all applied load conditions. At a given applied load condition for a given type of AMC, increase in reinforcement level resulted in a decrease in COF values. Further, for a given reinforcement level for a given type of AMC, an increase in applied load led to increase in COF values. Further, at a given reinforcement level-applied load condition, ilmenite based 'CIR' composites showed relatively lower COF values than the boron carbide based 'CBR' composites.

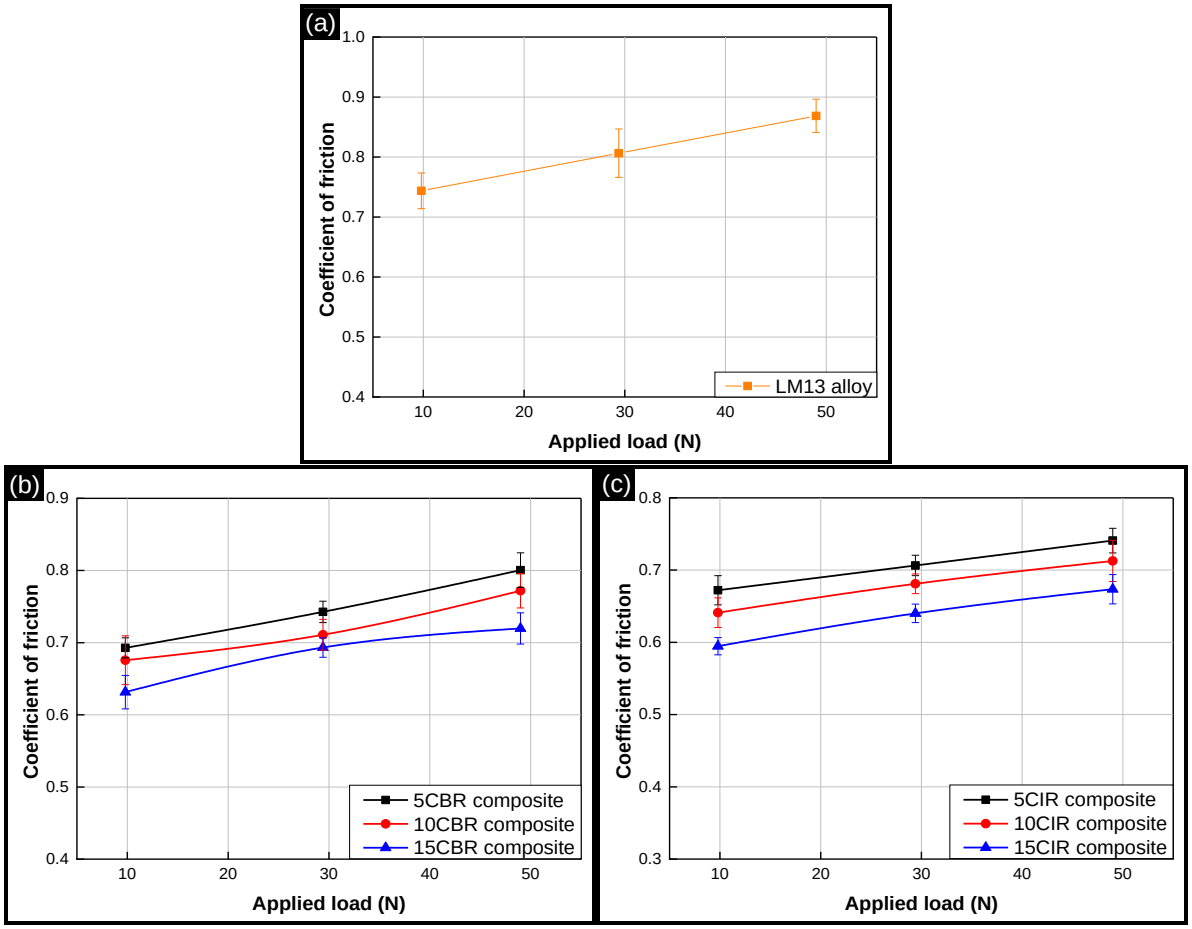

Figure 4.17 Coefficient of friction values for (a) LM13 base alloy, (b) 'CBR' composites, and (c) 'CIR' composites as a function of applied load.

The decrease in COF values on addition of reinforced particles was attributed to (i) reduction in the area of contact of the matrix phase with the counter surface due to presence of reinforced particles, and (ii) higher strength of interfacial bond formed between matrix and reinforced particles [18,179]. The incorporation of reinforced particles in the matrix decreased the actual area of contact of matrix material (composite pin) with the counter surface (steel disc). As a result, the indent caused by asperities of counter surface into the composite pin surface was relatively less. So the force required to shear the sliding surface was also less which reduced the COF of AMCs [18,180]. COF values also depend on the interfacial bond formed between matrix and reinforcement in AMCs [181]. This is because during sliding wear, the pulling out of reinforced particles from the matrix depends on the strength of interfacial bond. If the interfacial bond is weak, there is easy pulling out of particles which exposes the matrix material more to the steel disc. This increases the depth of indent caused by the steel asperities and results in higher COF value [179,181]. The attainment of lower COF values by AMCs (over the base alloy) signified the formation of good interfacial bonding of matrix and reinforced particles. For particular applied load and reinforcement level, the lowest COF value was obtained for '15CIR' composite followed by '15CBR' composite and LM13 alloy. This signified that the strength of interfacial bonding plays an important role in affecting the COF values of AMCs as ilmenite based 'CIR' composites had relatively higher interfacial bond strength. The increase in COF values with increase in applied load was attributed to the increase in plastic deformation of sliding surfaces under the effect of higher loads resulting in increased COF values.

4.7.2 Single particle reinforced composites containing fine particles

Figure 4.18 presents the coefficient of friction (COF) values under room temperature conditions for various AMCs (containing 'fine' particles) as a function of applied load. It was observed that reinforcement of ceramic particles to the matrix material reduced the COF of resulting AMCs over the base alloy for all applied load conditions. At a given applied load condition for a given type of AMC, increase in reinforcement level resulted in a decrease in COF values. Further, for a given reinforcement level for a given type of AMC, an increase in applied load led to increase in COF values. Further, at a given reinforcement level-applied load condition, ilmenite based 'FIR' composites showed relatively lower COF values than the boron carbide based 'FBR' composites.

The reasons for the trends observed in COF values of AMCs containing coarse particles have been discussed in Section 4.7.1. The same reasons hold good for AMCs containing fine particles also i.e. 'FBR' and 'FIR' composites.

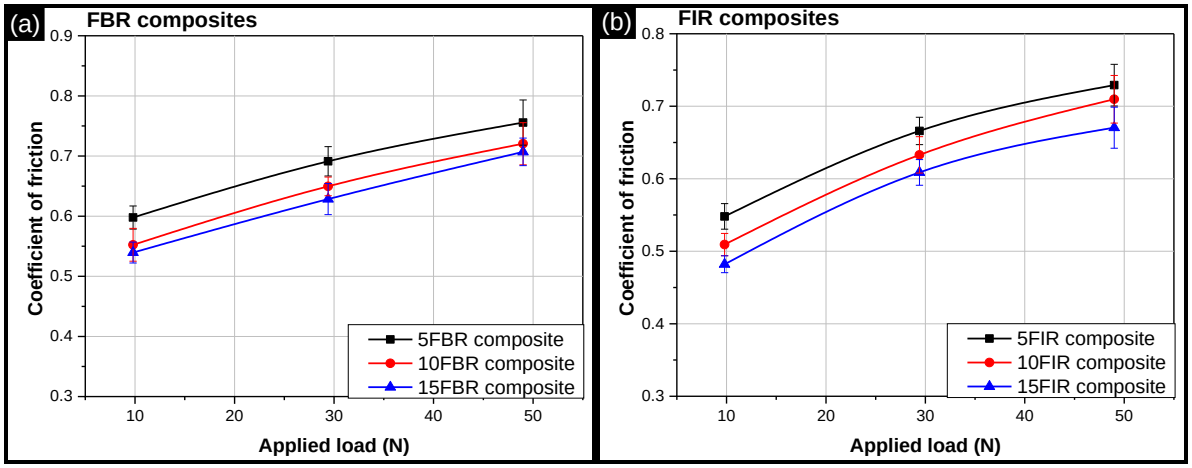

Figure 4.18 Coefficient of friction values for (a) 'FBR' composites, and (b) 'FIR' composites as a function of applied load.

For a given type of AMC at a given reinforcement level, COF values of AMCs decreased with change in particle size from 'coarse' to 'fine'. This is because for AMCs reinforced with relatively fine particles, the depth of penetration into the pin surface by the counter steel surface during sliding is lesser (for a given applied load-reinforcement level condition). With decrease in penetration depth, the force required to plough the sliding surface was also reduced. This led to decrease in frictional force which corresponded to reduction in COF of AMCs containing fine particles (compared to those containing coarse particles).

4.8. Wear-tracks and debris under room temperature conditions

4.8.1 Single particle reinforced composites containing coarse particles

Figure 4.19 presents the SEM micrographs of wear-tracks of AMCs containing maximum reinforcement level of 'coarse' particles (i.e. '15CBR' and '15CIR' composites) tested under different load conditions. Worn-out surface of AMCs showed presence of delaminated area, grooves, and some trapped debris. There was relatively more surface damage observed for ilmenite based '15CIR' composite. The greater surface damage in 'CIR' composites was attributed to the presence of relatively larger number of micro-cracks and lesser stability of MML. Presence of grooves on the wear-tracks signified entrapment of wear-debris. The entrapment of wear particles resulted in three body abrasive wear which ploughed the worn surface by the hard wear-debris [80].

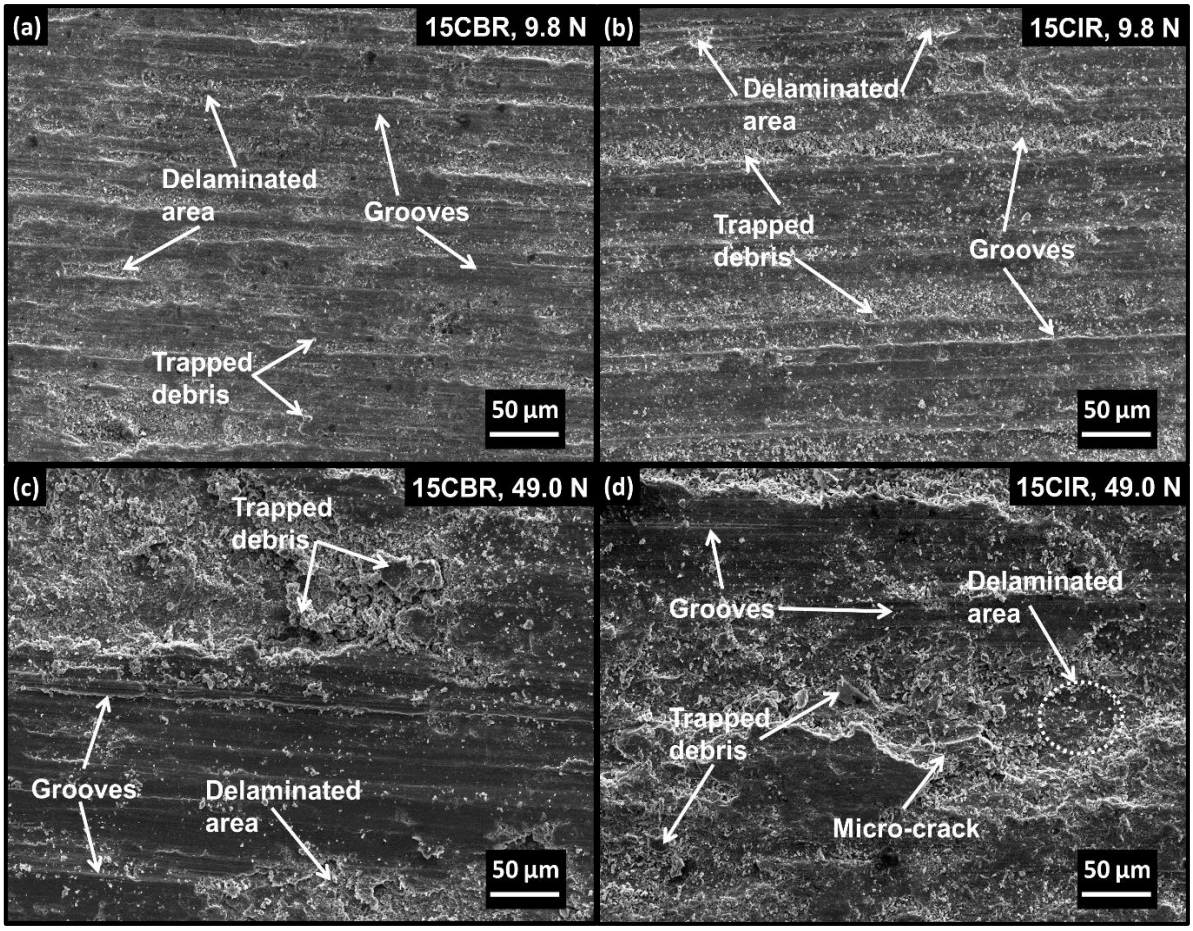

Figure 4.19 SEM images of wear-tracks of (a) '15CBR' at 9.8 N, (b) '15CIR' at 9.8 N, (c) '15CBR' at 49.0 N, and (d) '15CIR' at 49.0 N.

Figure 4.20 presents the SEM micrographs of wear-debris of AMCs containing maximum reinforcement level of 'coarse' particles (i.e. '15CBR' and '15CIR' composites) tested under different load conditions. The apparent size of wear-debris for '15CBR' composite was higher than '15CIR' composite indicating relatively higher number of micro-cracks in '15CIR' composite. Thus, higher number of micro-cracks in '15CIR' composite resulted in relatively higher wear rate. Formation of flake-like debris justified the removal of material by micro-cracks as explained earlier. Micro-cuts/thread-like debris were obtained due to the abrasive action caused by trapped particles. Fractured-debris were obtained due to the rupturing of entrapped particles under applied load. Finally, the EDS analysis at different points revealed the formation of oxides on the debris which signified the rise in temperature of the pin surface due to continuous sliding under applied load (as shown in Figure 4.22).

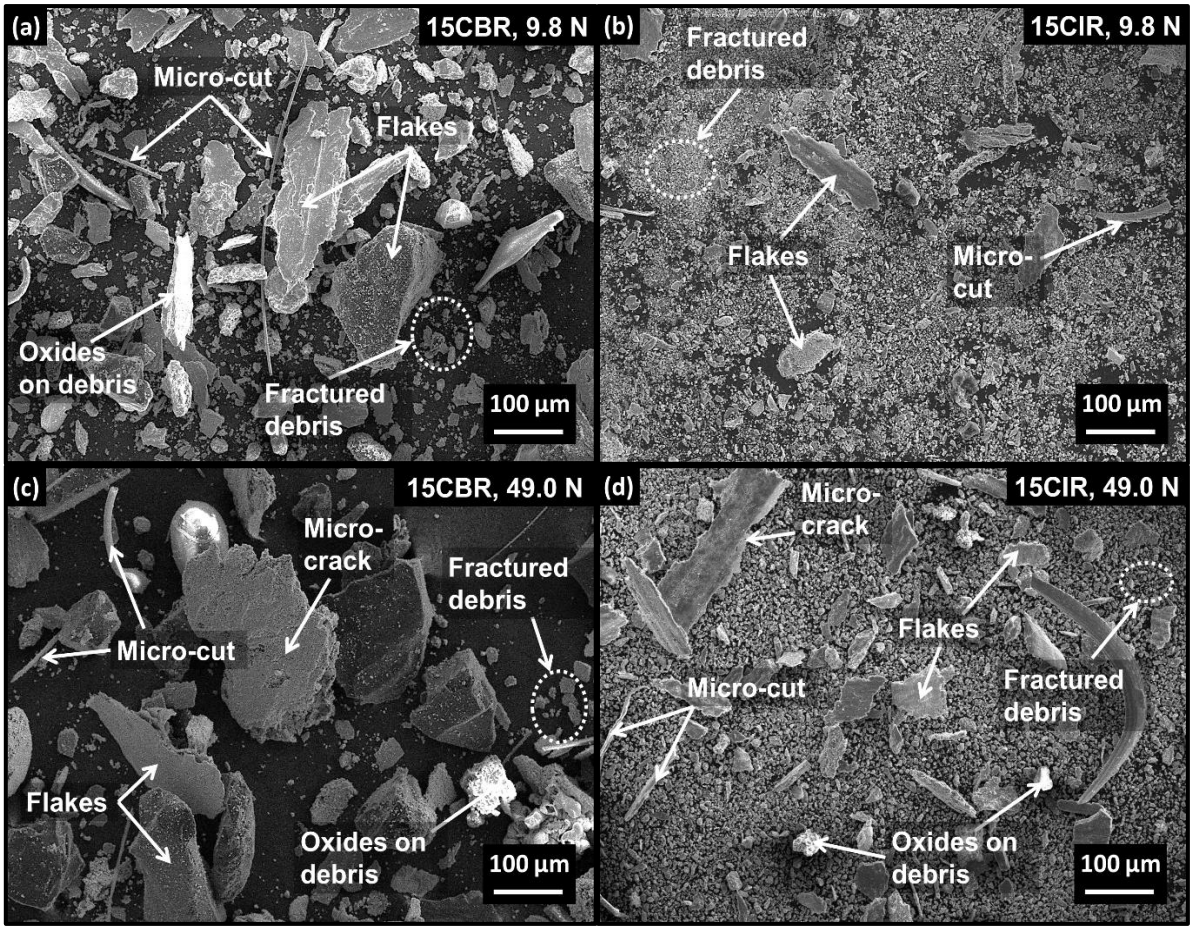

Figure 4.20 SEM images of wear-debris for (a) '15CBR' at 9.8 N, (b) '15CIR' at 9.8 N, (c) '15CBR' at 49.0 N, and (d) '15CIR' at 49.0 N.

SEM-EDS results pertaining to wear-tracks and wear-debris at an applied load of 9.8 N and 49.0 N for AMCs containing coarse particles i.e. '15CBR' and '15CIR' composites is presented in Figure 4.21 and Figure 4.22 respectively.

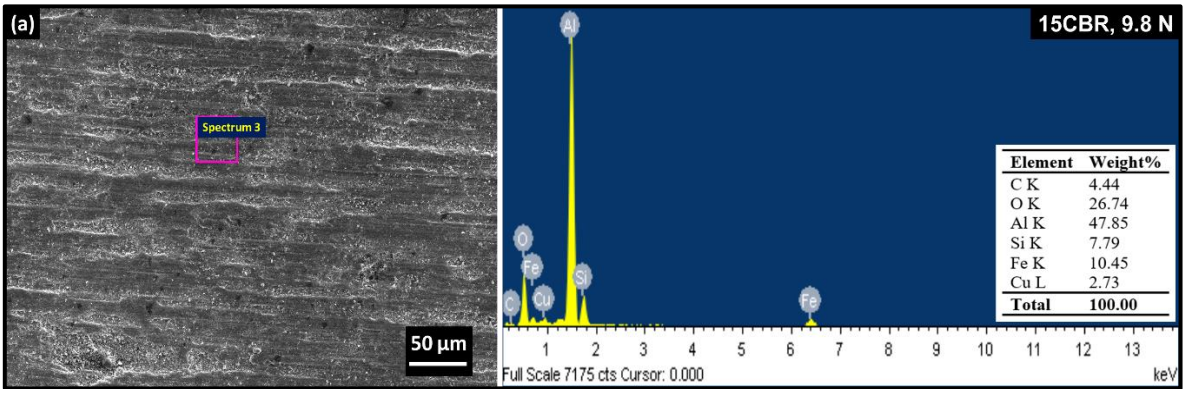

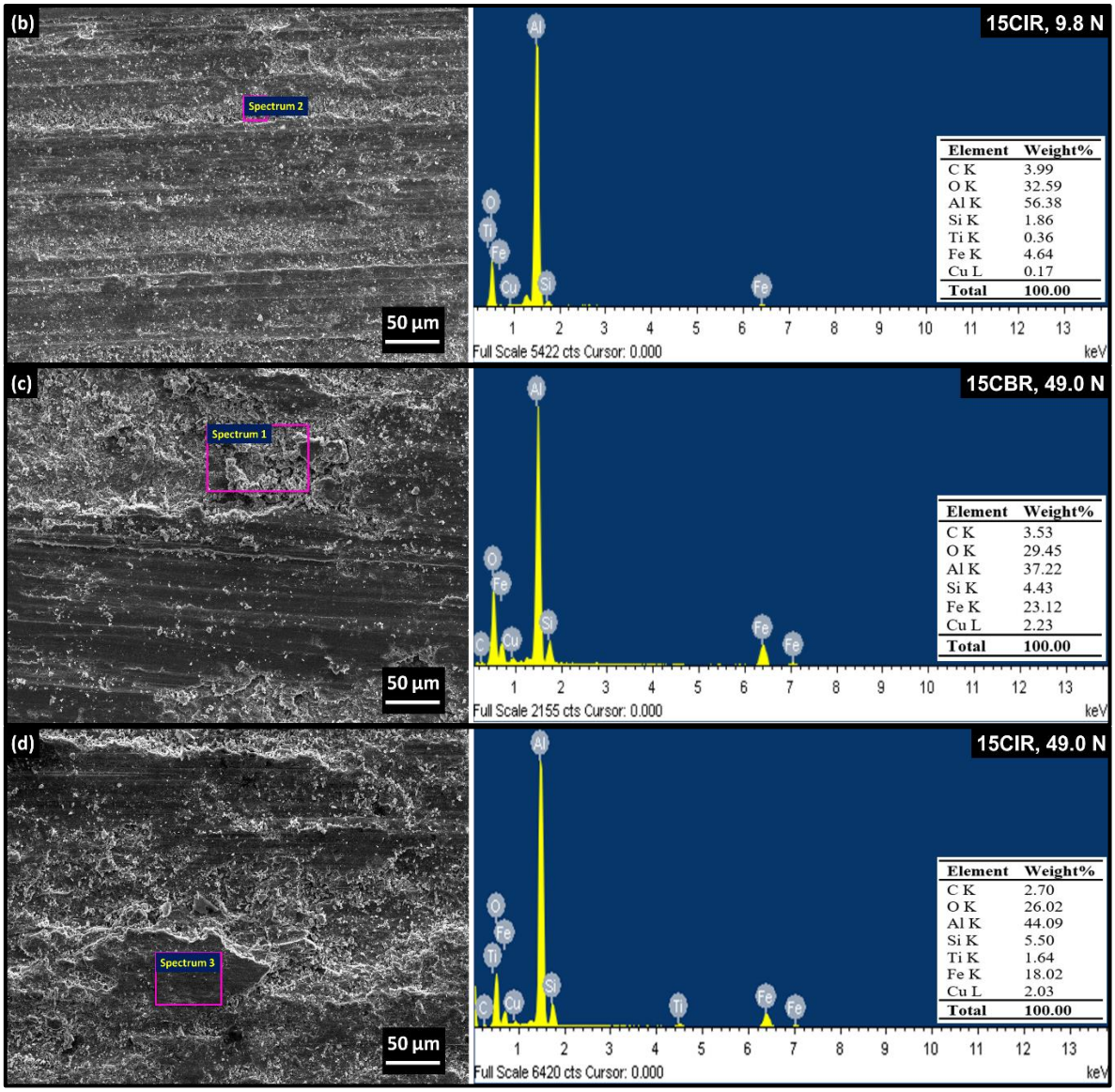

Figure 4.21 SEM-EDS of wear-tracks of (a) '15CBR' at 9.8 N, (b) '15CIR' at 9.8 N, (c) '15CBR' at 49.0 N, and (d) '15CIR' at 49.0 N.

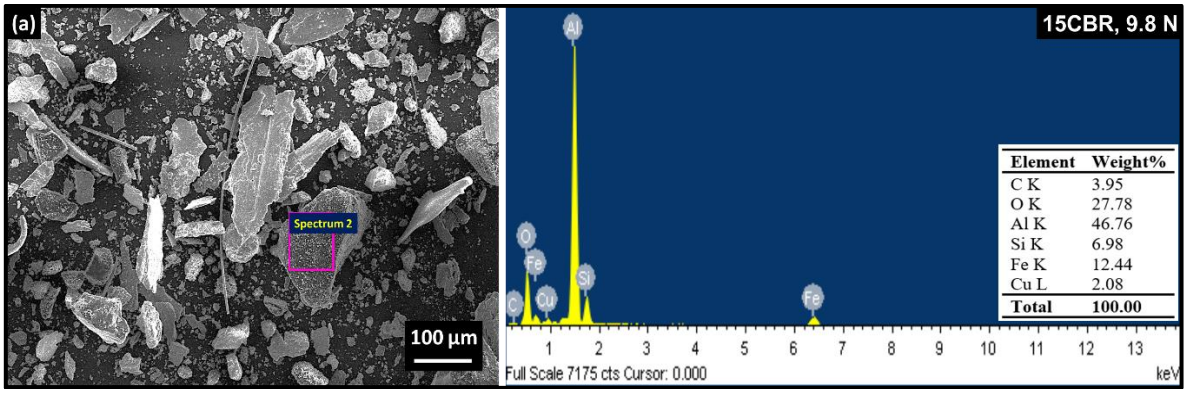

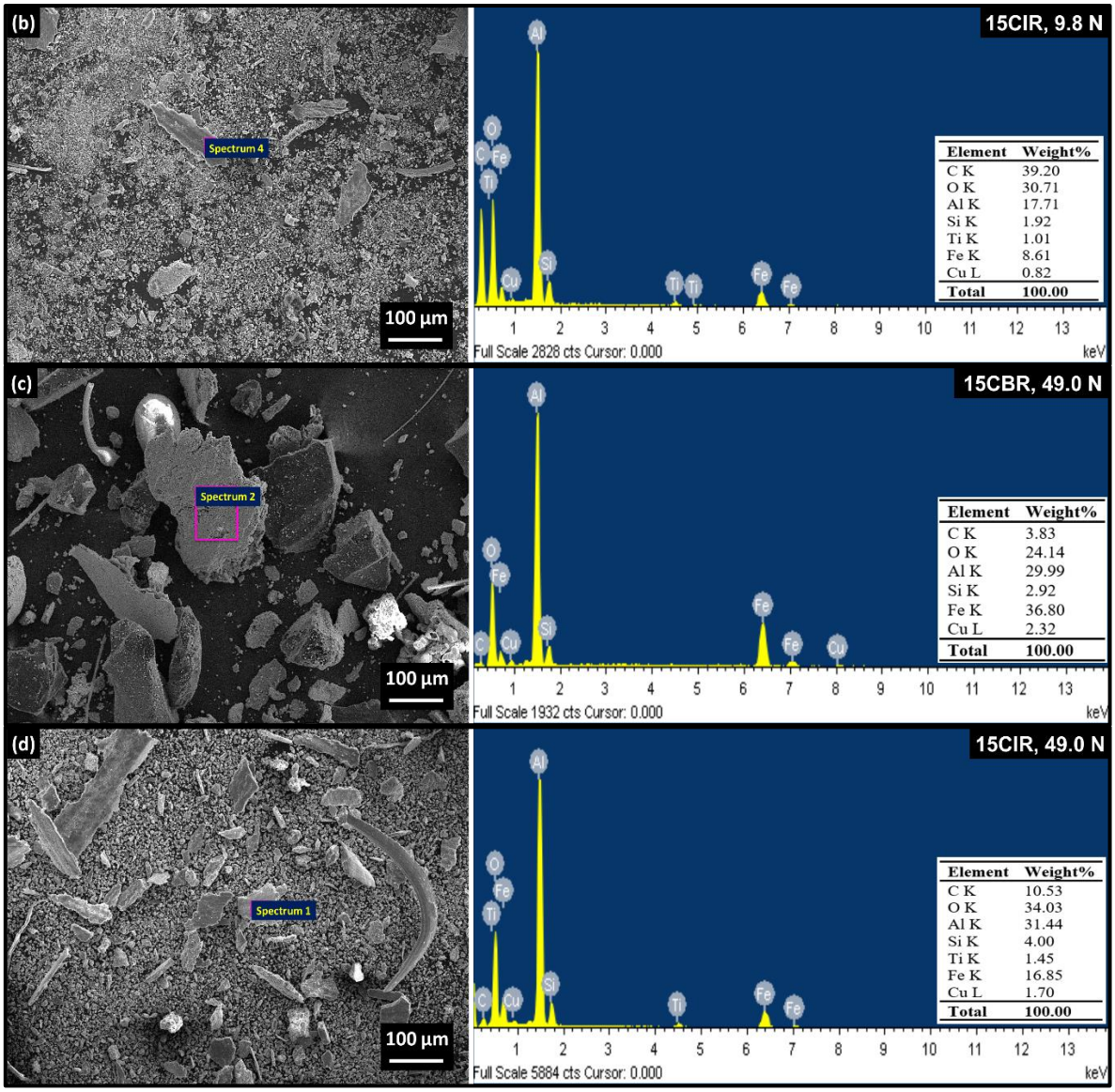

Figure 4.22 SEM-EDS of wear-debris for (a) '15CBR' at 9.8 N, (b) '15CIR' at 9.8 N, (c) '15CBR' at 49.0 N, and (d) '15CIR' at 49.0 N.

EDS analysis of wear-tracks and wear-debris of '15CBR' composite under both the load conditions showed presence of aluminium, silicon, oxygen, iron, carbon, and copper as shown in Figure 4.21a, Figure 4.21c, Figure 4.22a, and Figure 4.22c. Similarly, EDS analysis of '15CIR' composite under both the load conditions showed presence of aluminium, silicon, oxygen, iron, carbon, copper, and titanium on wear-tracks as well as on wear-debris as shown in Figure 4.21b, Figure 4.21d, Figure 4.22b, and Figure 4.22d. Interestingly, boron was not observed in 'CBR' composites, may be due to the low atomic number of boron which makes it difficult to be detected in EDS analysis. The net amount of oxygen present on the wear-track of '15CIR' composite (calculated after deducting the amount of oxygen present in ilmenite) at 49.0 N was 21.10 wt.% (Figure 4.21d) which was lower than the '15CBR' composite (29.45

wt.%; Figure 4.21c). This signified that the MML (which is a mixture of oxide particles) formed on the surface of 'CBR' composites was relatively more stable. On the other hand, the relatively high amount of oxygen on wear-debris of '15CIR' composite at 49.0 N (net percentage of oxygen present was calculated as 29.68 wt.% after deducting the amount present in ilmenite; Figure 4.22d) in comparison to '15CBR' composite (24.14 wt.%; Figure 4.22c) justified the high oxidation rate in 'CIR' composites. Further, for both types of AMCs under both the load conditions, the presence of significant amount of iron and carbon on wear-tracks revealed the transfer of material from the counter-disc also. This transfer of material was higher in '15CBR' composite (under both load conditions) which again signified the formation of more stable MML on the worn surface of 'CBR' composites.

4.8.2 Single particle reinforced composites containing fine particles

SEM images of wear-tracks obtained for AMCs containing maximum reinforcement level of 'fine' particles (i.e. '15FBR' and '15FIR' composites) at different applied loads are presented in Figure 4.23. Figure 4.23a and Figure 4.23b show the worn surface of '15FBR' and '15FIR' composites at an applied load of 9.8 N respectively. Both surfaces showed presence of grooves along with some craters signifying the wear mode to be abrasive. In the initial stages of wear, sliding surface of pin and the steel disc (counter-surface) made asperities to asperities contact. As the sliding continued, fracture of asperities led to formation of abrasive particles which got trapped between the two sliding surfaces. These abrasive particles consisted of materials of reinforcement, base alloy, and steel disc which caused ploughing action on the pin surface [180,182]. SEM images of wear-tracks of '15FBR' and '15FIR' composites at an applied load of 49.0 N are presented in Figure 4.23c and Figure 4.23d respectively. Here, wear of sliding surface occurred due to crack generation/crack merging which resulted in development of delaminated craters [23,38]. In addition to this, presence of relatively smaller craters on '15FBR' composite surface was attributed to greater protection of this '15FBR' pin surface by MML. Due to high hardness of '15FBR' composite as discussed in Section 4.4.2, the load acting on the MML was also sustained by the underlying hard AMC surface which also enhanced the stability of MML formed.

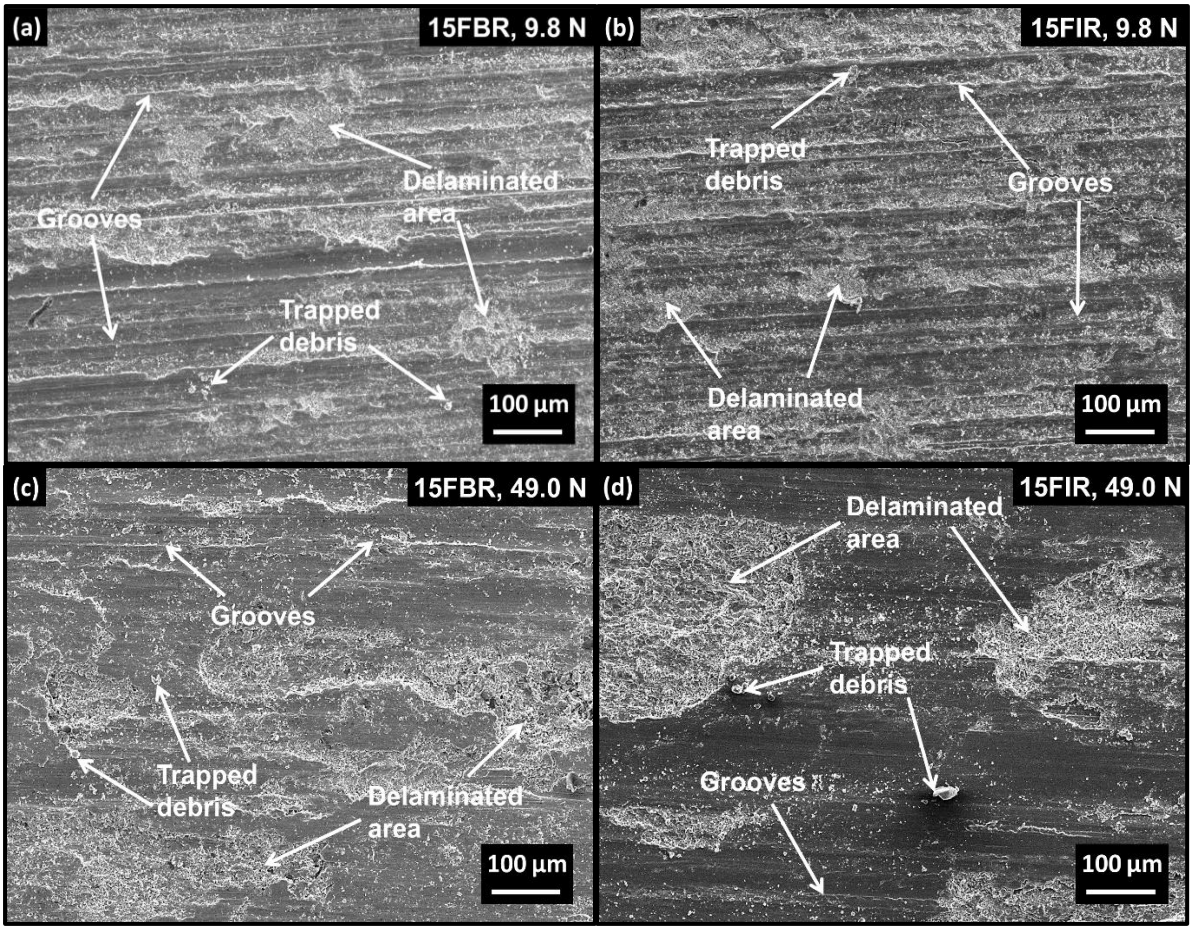

Figure 4.23 SEM micrographs of wear-tracks of (a) '15FBR' at 9.8 N, (b) '15FIR' at 9.8 N, (c) '15FBR' at 49.0 N, and (d) '15FIR' at 49.0 N.

SEM images of wear-debris of AMCs containing maximum reinforcement of 'fine' particles ('15FBR' and '15FIR' composites) at an applied load of 9.8 N and 49.0 N respectively are shown in Figure 4.24. It was observed that debris mainly consisted of plate like structure. At low loads, the formation of flake-like debris was attributed to shearing of wedge formed due to ploughing of the sliding surface [18]. With increase in applied load, there was a rise in the size of debris which was attributed to the generation of micro-cracks and their subsequent convergence as shown in Figure 4.24c–d. The formation of molten debris represented significant rise in the temperature of sliding surfaces (i.e. the composite pin and the counter-surface steel disc). Under the action of applied load and temperature, some of the trapped debris were observed in the form of molten debris [23]. Micro-cut type and thread-like debris were observed due to the abrasive action of debris trapped between the counter surfaces. Fractured-debris were observed due to the breakage of trapped debris under the action of applied load. Also, oxides on the debris were identified by analyzing the EDS results which showed presence of additional oxygen signifying formation of various oxides.

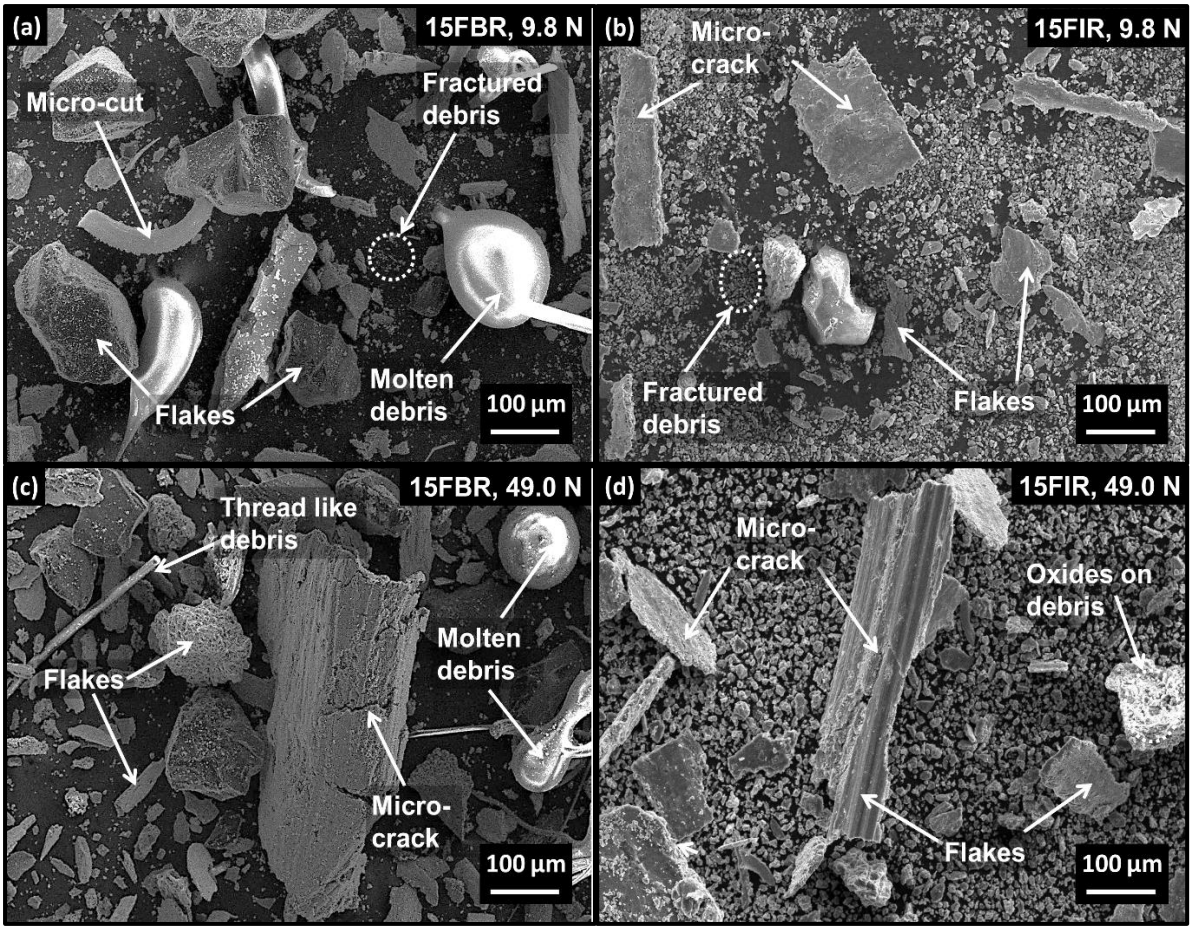

Figure 4.24 SEM micrographs of wear-debris of (a) '15FBR' at 9.8 N, (b) '15FIR' at 9.8 N, (c) '15FBR' at 49.0 N, and (d) '15FIR' at 49.0 N.

Figure 4.25 and Figure 4.26 present the EDS spectrum of wear-track and wear-debris at different applied loads for AMCs containing 'fine' particles ('15FBR' and '15FIR' composites respectively).

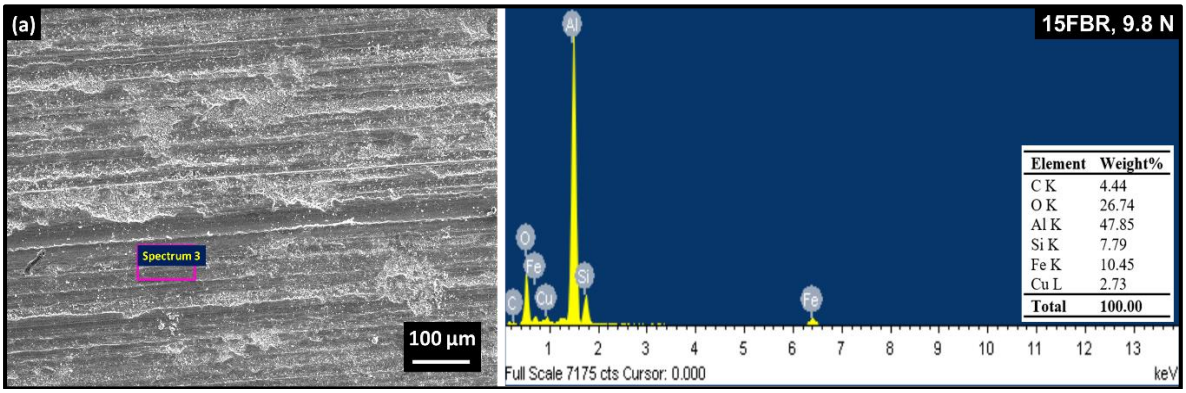

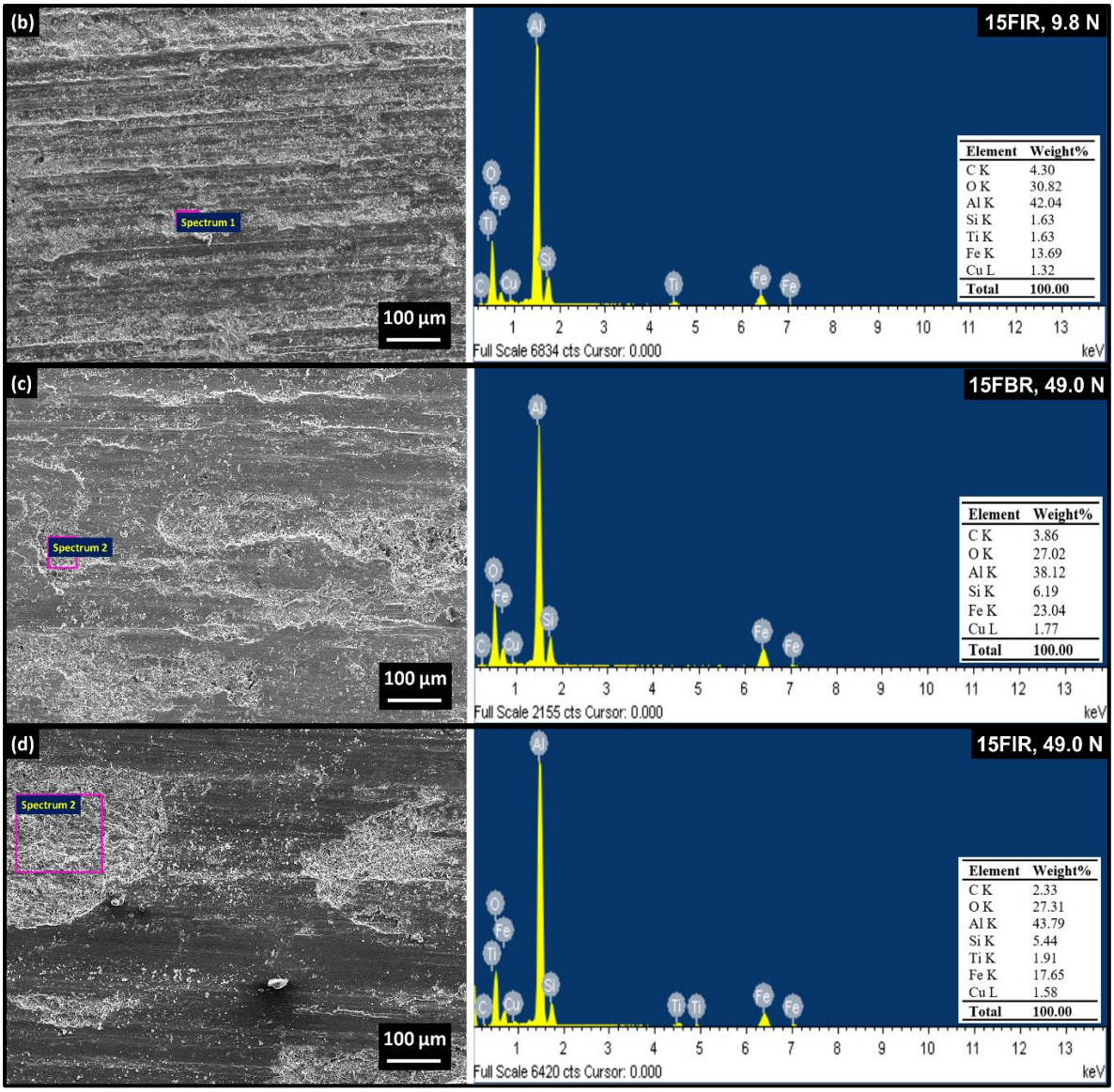

Figure 4.25 SEM-EDS of wear surface for (a) '15FBR' at 9.8 N, (b) '15FIR' at 9.8 N, (c) '15FBR' at 49.0 N, and (d) '15FIR' at 49.0 N.

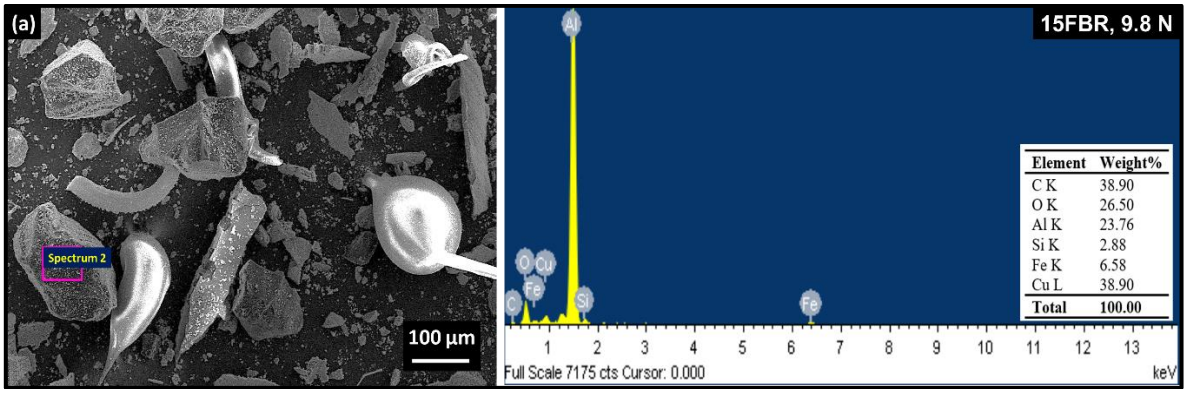

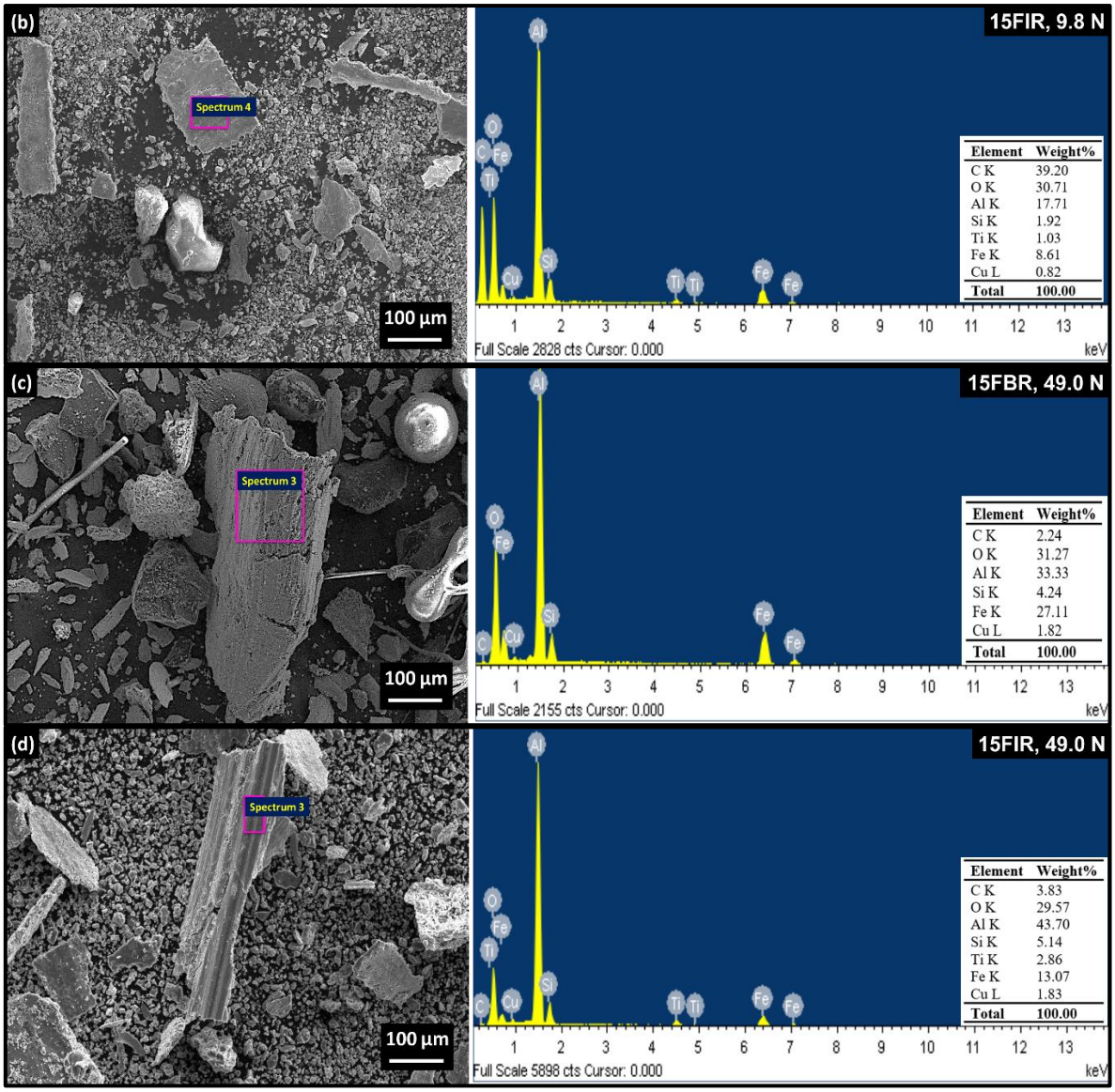

Figure 4.26 SEM-EDS of wear debris for (a) '15FBR' at 9.8 N, (b) '15FIR' at 9.8 N, (c) '15FBR' at 49.0 N, and (d) '15FIR' at 49.0 N.

For the wear-track of '15FIR' composite, the amount of oxygen and iron coming from ilmenite were deducted to obtain the net weight percentage of iron and oxygen constituents on the sliding surface. The revised weight percentage of (iron, oxygen) present on the sliding surface at 9.8 N and 49.0 N load was obtained as (9.78 wt.%, 24.63 wt.%) and (16.86 wt.%, 24.84 wt.%) respectively. For wear-debris of '15FIR' composite, the amount of iron and oxygen as obtained was (8.18 wt.% & 29.38 wt.%) and (11.89 wt.% & 25.88 wt.%), respectively. For wear-track, an increase in the contents of iron, carbon, and oxygen was observed with rise in applied load. This increase in amount of iron and carbon on the worn surface corresponded to transfer of material from the steel disc to the pin surface. Further, an increase in the oxygen content corresponded to oxidation of the worn surface due to rise in temperature during sliding

wear. Transfer of material and oxidation signified formation of tribo-layer (MML) on the sliding surface. Further, the relative stability of tribo-layer in the two types of AMCs was determined by EDS analysis of wear-track. Higher content of iron, carbon, and oxygen on the wear-track of '15FBR' composite (in comparison of '15FIR' composite) signified higher stability of MML in '15FBR' composite under both the applied load conditions.

4.9. Wear rate behaviour under high temperature conditions

4.9.1 Single particle reinforced composites containing coarse particles

Figure 4.27 presents the average steady-state wear rate behaviour of base alloy and various AMCs (containing coarse particles) as a function of operating temperature for various applied load conditions. For obtaining the average steady-state wear rate at a given temperature, the wear rates obtained in the sliding distance range of 1500–3000 m were considered. Several earlier studies have also reported attainment of steady-state wear in the sliding distance range of 1500–3000 m for ceramic particle reinforced AMCs [13,23].

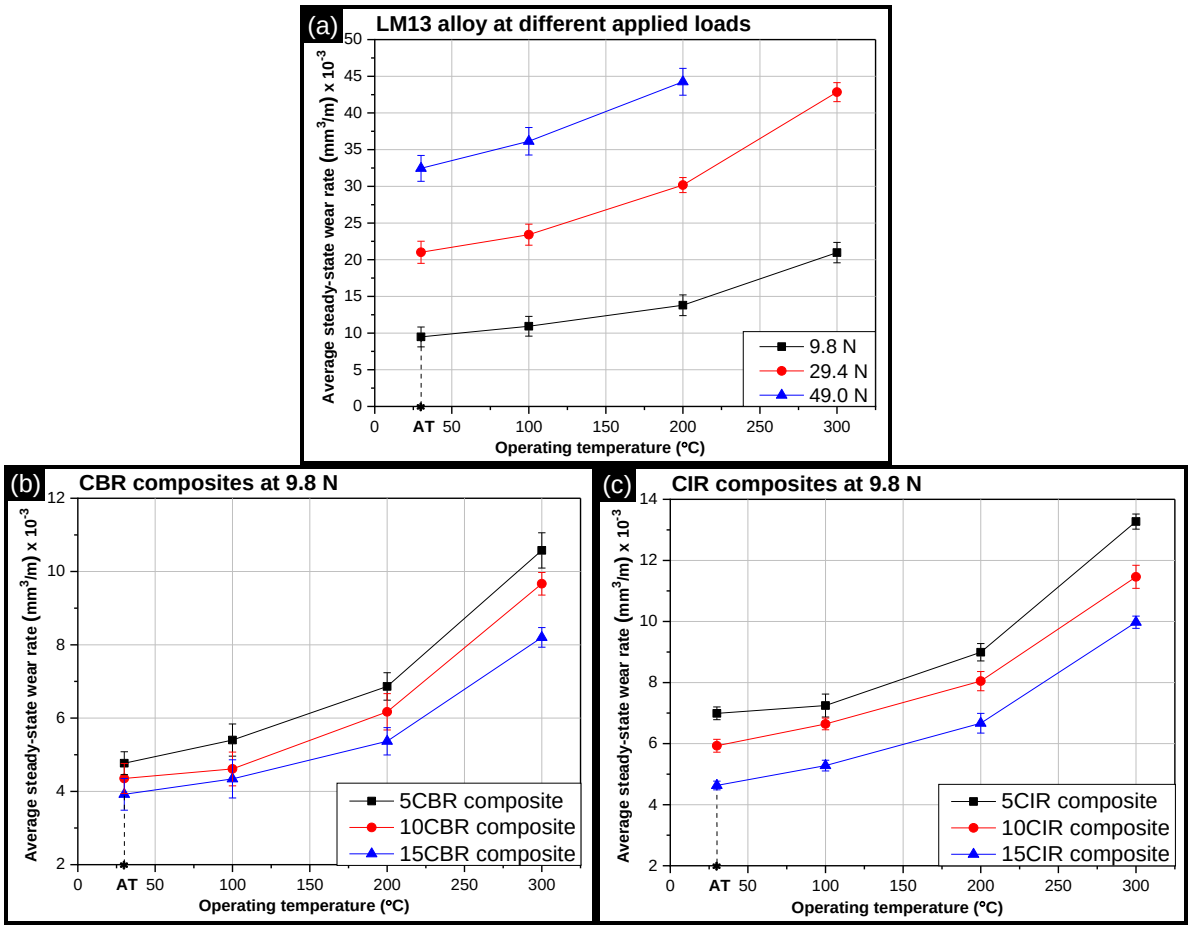

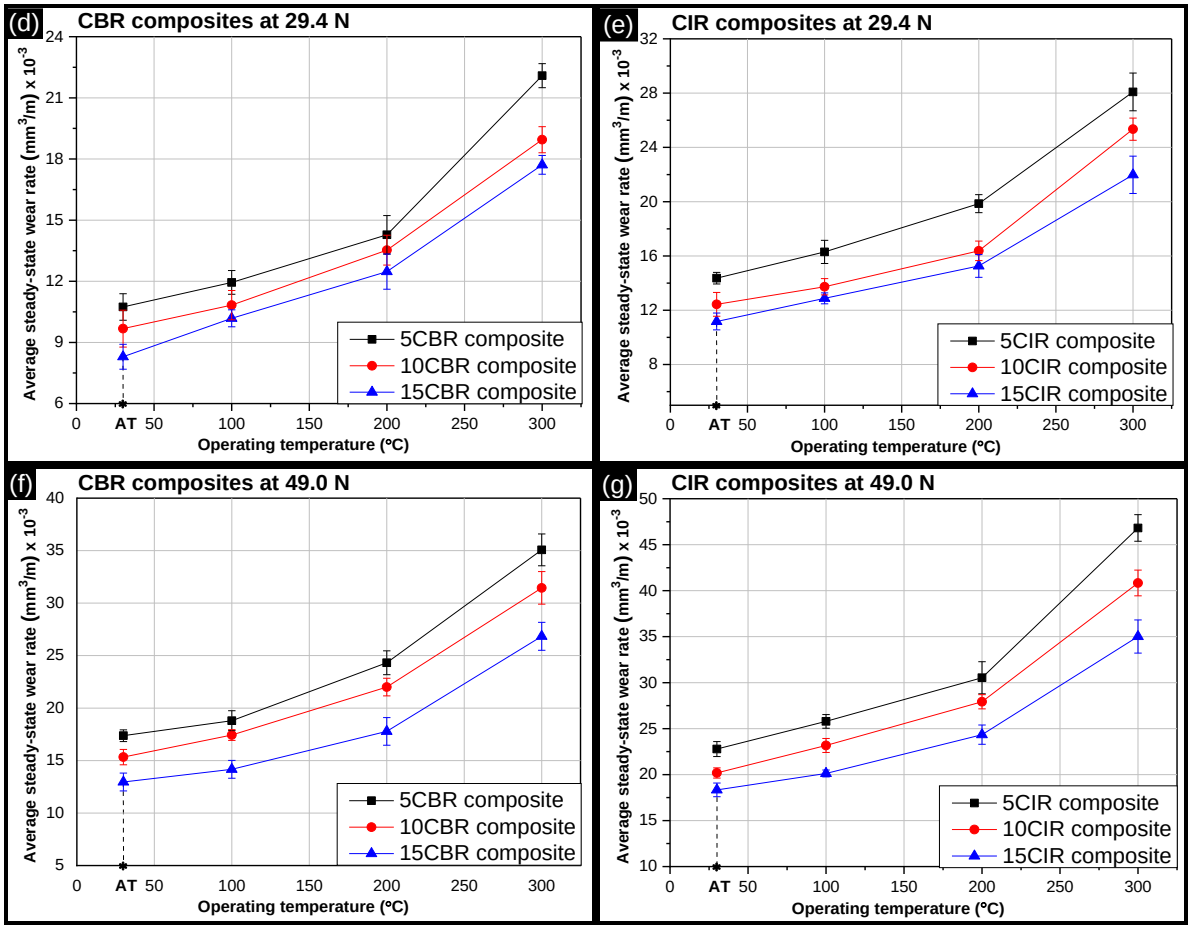

Figure 4.27 Variation in average steady-state wear rate with operating temperature for (a) LM13 alloy at different applied loads, (b) 'CBR' composites at 9.8 N load, (c) 'CIR' composites at 9.8 N load, (d) 'CBR' composites at 29.4 N load, (e) 'CIR' composites at 29.4 N load, (f) 'CBR' composites at 49.0 N load, and (g) 'CIR' composites at 49.0 N load. 'AT' represents ambient temperature conditions.

Figure 4.27a presents the average wear rate values of base alloy at various operating temperature-applied load conditions. For all applied load conditions, wear rate increased with increase in operating temperature for the entire range of temperature, AT to 300℃. Higher applied load-operating temperature resulted in rupturing of the oxide layer and thermal softening of pin causing increase in wear rate. For the high load-temperature condition of 49.0 N-300 ℃, excessive wear of base alloy pin occurred. Wear rate of base alloy could not be determined for these extreme conditions as the height loss in composite pin could not be measured beyond sliding distance of 1850 m (due to excessive wear, the pin suffered extensive height loss to an extent that the measuring sensor reached its upper limit, and thus, the height loss could not be obtained).

Figure 4.27b–g present the average wear rate for various AMCs as a function of operating temperature for various reinforcement levels at a given applied load. Similar to the trend observed for LM13 alloy, for all applied load conditions, a continuous rise in wear rate was

seen for AMCs with increase in operating temperature (for the entire range, AT to 300 ℃). However, the following differences were noted: (i) for any applied load-operating temperature condition, AMCs showed lower average steady-state wear rate in comparison to base alloy, (ii) for any applied load-operating temperature condition, average wear rate of AMCs reduced with rise in reinforcement level and finally (iv) compared to the base alloy which showed complete wear at 1850 m for the extreme condition of 49.0 N-300 ℃, the AMCs were able to withstand this extreme condition. High temperature wear behaviour of AMCs is influenced by hardness and oxidation rate of matrix material which varies according to temperature conditions [180,182]. For a given applied load-reinforcement level condition, an increase in operating temperature results in a decrease in hardness of matrix material/AMCs. This decrease in hardness is attributed to increase in grain size of matrix material with increase in temperature. When hardness value decreases beyond a critical level, the sustainability of protective oxide layer on the sliding surface decreases, and the surface gets exposed to the hard steel disc [77,183]. These are the reasons for sudden rise in wear rate of AMCs beyond the transition temperature (i.e. 200 ℃). The incorporation of ceramic particles in LM13 alloy resulted in lesser decrease in hardness value for a given rise in operating temperature. This is because presence of ceramic particles creates a pinning effect which restricts the grain growth of matrix material. Hence, the growth in grain size of AMCs is less in comparison to that in base alloy. For these reasons, the operating temperature required to reduce the hardness and sustainability of oxide layer was higher in case of AMCs [184].

Table 4.8 presents the percentage decrease in average steady-state wear rate of AMCs containing 'coarse' particles ('CBR' and 'CIR' composites) over the LM13 alloy at operating temperature of 200 ℃ (mild-to-severe transition temperature).

Table 4.8 Percentage decrease in average steady-state wear rate of AMCs over base alloy at mild-to-severe transition temperature.

S. No.	Applied load (N)	Percentage reduction in average steady-state wear rate of a given AMC over LM13 alloy at 200 ℃ (%)					
		'CIR' composites			'CBR' composites		
		'5CIR'	'10CIR'	'15CIR'	'5CBR'	'10CBR'	'15CBR'
1.	9.8	35	42	**52**	50	55	**61**
2.	29.4	34	46	49	53	55	59
3.	49.0	31	37	45	45	50	60

Maximum reduction in wear rate for AMCs was shown by '15CBR' composite (61% reduction over base alloy at 9.8 N load condition) and '15CIR' composite (52% reduction over base alloy at 9.8 N). Reinforcement of ceramic particles to the matrix material resulted in refinement of

grains, both of primary Al and eutectic Si present in the matrix material. This provided increased grain boundary area in AMCs and resulted in better restriction to movement of cracks generated during the sliding wear [185]. The restriction to propagation of cracks reduced the tendency for convergence of cracks. This resulted in removal of material at a slower rate. Further, as discussed earlier, the reinforced particles also reduced the CTE of resulting AMCs causing reduced wear rates. With increase in temperature, the expansion of matrix material was restricted by the reinforced boron carbide particles and ilmenite particles. This enhanced the dimensional stability and slackened the softening of matrix at high temperature conditions (Figure 4.13). This increase in dimensional stability and reduced softening of matrix in AMCs helped in decreasing the transfer of material from pin surface to steel counter surface [23]. Hence, the lower CTE of AMCs at high temperatures (compared to base alloy) resulted in lower wear rates of AMCs over base alloy. Further, during wear testing, sliding surfaces experienced rise in temperature due to the frictional force. Due to lower thermal conductivity of reinforced particles, especially ilmenite (thermal conductivity of ilmenite: 1.49 W/mK), a high temperature zone got created at the contact surfaces which led to establishment of an oxide layer on the sliding composite pin surface. This oxide layer prevented direct metal-to-metal contact which helped in reducing the wear rates of AMCs [160,161,186]. For all these reasons (grain refinement, lower CTE value, and lower thermal conductivity), the average steady-state wear rate continuously reduced with increase in reinforcement level in AMCs for a given applied load-operating temperature condition. The attainment of lowest wear rate by '15CBR' composite at a given high operating temperature was attributed to the high thermal conductivity and low density of its reinforcement i.e. B_4C particles. The reasons for this are same as discussed in Section 4.6.1.

Figure 4.28 presents the derivative of wear rate with respect to operating temperature for AMCs containing maximum reinforcement level of 'coarse' particle ('15CBR' and '15CIR' composites) over the entire range of operating temperature (AT−300 ℃). For any given value of derivative of wear rate w.r.t. operating temperature, the wear rate behaviour of both the AMCs is comparable and is extremely superior as compared to the base alloy. For example, in Figure 4.28a, at a derivative value of 0.025 $mm^3m^{-1}℃^{-1}$ at 9.8 N, '15CIR' and '15CBR' can operate till high temperatures of about 215 ℃ (corresponding to point 'b') and 255 ℃ (corresponding to point 'c') respectively, whereas the base alloy specimen can operate till a relatively low temperature of about 105 ℃ only (corresponding to point 'a'). Based on this analysis, it was observed that both types of AMCs can work nearly in the same operating

temperature when wear rate is an important consideration. 'CBRs' were observed to be slightly superior to 'CIRs' in terms of resistance provided to wear rate. However, it may be noted that the naturally occurring mineral of ilmenite used in 'CIRs' is very cost-effective (price of boron carbide particles used in 'CBRs' is about 25 times more than the price of ilmenite used in 'CIRs').

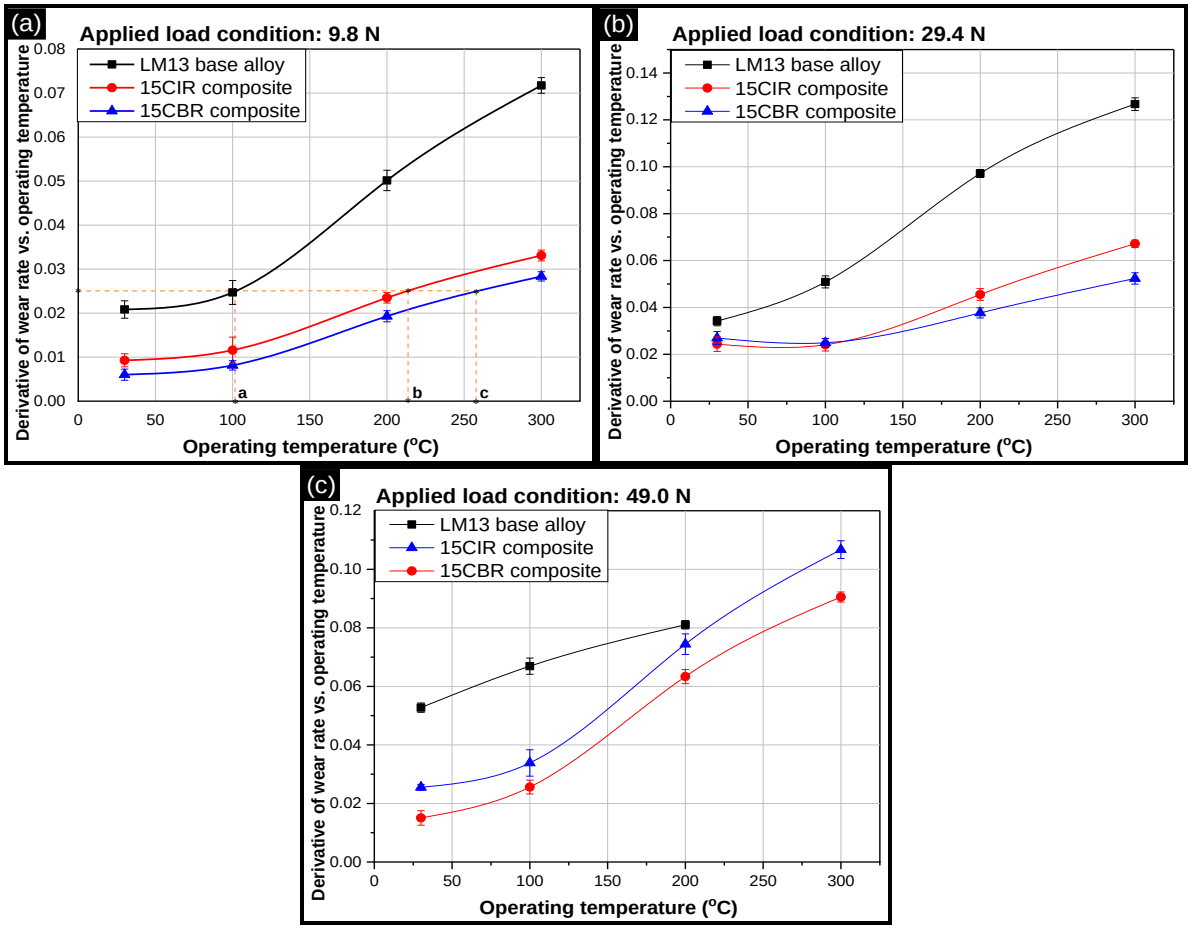

Figure 4.28 Derivative of wear rate versus operating temperature as a function of operating temperature at an applied load of (a) 9.8 N, (b) 29.4 N, and (c) 49.0 N for LM13 base alloy, '15CBR' composite and '15CIR' composite.

4.9.2 Single particle reinforced composites containing fine particles

Figure 4.29 presents the average steady-state wear rate behaviour of various AMCs (containing fine particles) as a function of operating temperature for various applied load conditions. All samples showed a rise in wear rate with increase in temperature under any given load condition. Increase in applied load at a particular operating temperature-reinforcement level condition led to increase in wear rate. For a given type of AMC at a given reinforcement level, a rapid rise in the average steady-state wear rate was detected when testing was done at operating temperature of 200 ℃. This temperature was noted as the transition temperature where sharp

rise in wear rate of samples was detected. At a particular operating temperature, reinforcement level, and applied load, lowest wear rate was shown by 'FBR' composites, followed by 'FIR' composites, and then the LM13 alloy. Further, for each type of AMC (ilmenite reinforced or boron carbide reinforced), decrease in wear rate was observed with rise in reinforcement level at a particular applied load-operating temperature condition.

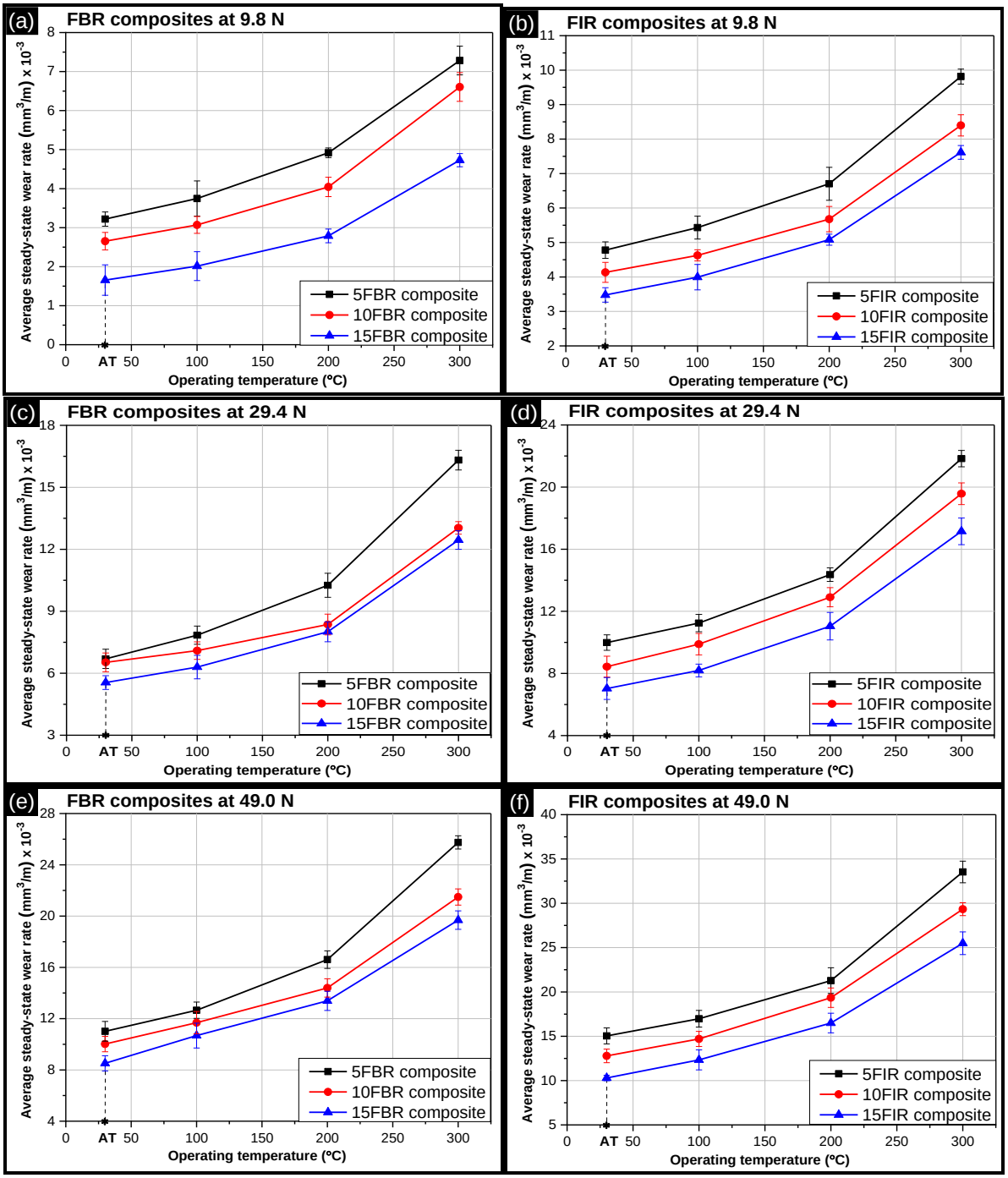

Figure 4.29 Variation in average steady-state wear rate with operating temperature for (a) 'FBR' composites at 9.8 N applied load, (b) 'FIR' composites at 9.8 N applied load, (c) 'FBR' composites at 29.4 N applied load, (d) 'FBR' composites at 29.4 N applied load, (e) 'FBR' composites at 49.0 N applied load, and (f) 'FIR' composites at 49.0 N applied load. 'AT' represents ambient temperature conditions.

In Section 4.9.1, the reasons for the trends observed in high temperature wear behaviour of AMCs with coarse particles were covered. The same reasons hold good for AMCs containing 'fine' particles ('FBR' and 'FIR' composites). The differences obtained in the wear rate in these AMCs containing 'fine' particles from those containing 'coarse' particles are discussed ahead. Table 4.9 presents the percentage decrease in average steady-state wear rate of AMCs containing 'fine' particles ('FBR' and 'FIR' composites) over the LM13 alloy at operating temperature of 200 ℃ (mild-to-severe transition temperature).

Further, for a given type of AMC at a given reinforcement level and at a given operating temperature-applied load condition, the change in particle size from 'coarse' to 'fine' resulted in lower wear rate of AMCs. This behaviour was attributed to the relatively lower CTE and grain size of 'fine' particle reinforced AMCs when compared to 'coarse' particle reinforced AMCs (already discussed in Section 4.3.3 and Section 4.5.2). The relatively lower CTE of 'fine' particles reinforced AMCs provides them with higher dimensional stability. This results in relatively less softening of 'FBR' and 'FIR' composites at a given high temperature compared to their coarse particle counterparts. Also, the addition of fine particles led to relatively higher refinement of the matrix material in 'FBR' and 'FIR' composites. This increased the resistance to propagation of cracks generated during the sliding wear. These reasons resulted in lower wear rate for 'fine' particle reinforced AMCs (compared to those containing coarse particles).

Table 4.9 Percentage decrease in average steady-state wear rate of AMCs over base alloy at mild-to-severe transition temperature.

S. No.	Applied load (N)	Percentage reduction in average steady-state wear rate of a given AMC over LM13 alloy at 200 ℃ (%)					
		'FIR' composites			'FBR' composites		
		'5FIR'	'10FIR'	'15FIR'	'5FBR'	'10FBR'	'15FBR'
1.	9.8	51	59	63	64	71	80
2.	29.4	68	71	**75**	77	81	**82**
3.	49.0	29	36	45	45	52	56

Figure 4.30 presents the derivative of wear rate with respect to operating temperature for LM13 base alloy and various AMCs containing maximum reinforcement level of 'fine' particles ('15FBR' and '15FIR' composite) over the entire range of operating temperature (AT to 300 ℃).

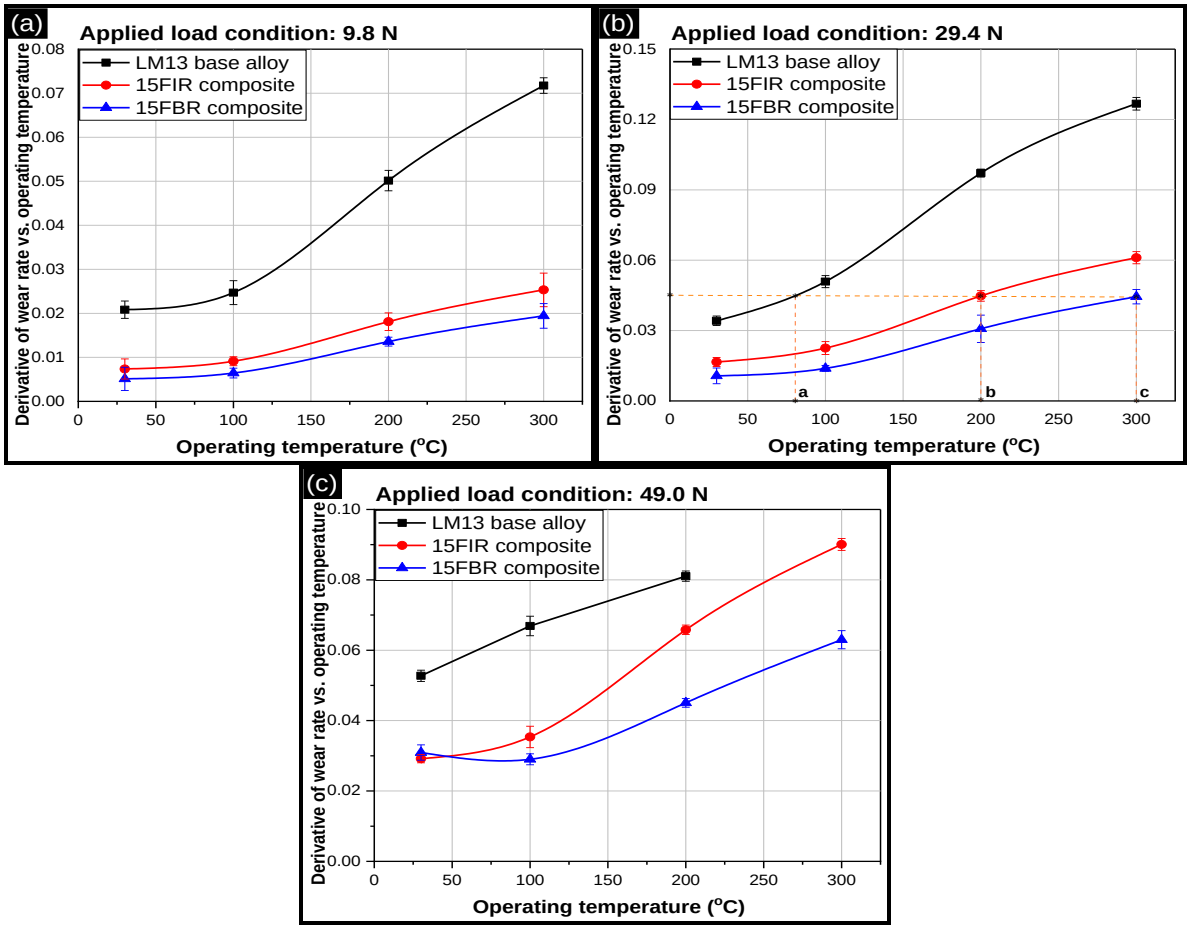

Figure 4.30 Derivative of wear rate versus operating temperature as a function of operating temperature at an applied load of (a) 9.8 N, (b) 29.4 N, and (c) 49.0 N for the LM13 base alloy, '15FBR' composite and '15FIR' composite.

These graphs signified the working range of temperature of base alloy and various AMCs at particular value of wear rate. For different applied load conditions, the working temperature range of AMCs was higher than that of LM13 alloy due to the addition of ceramic reinforcement in AMCs. At a derivative value of 0.045 $mm^3m^{-1}{}^{o}C^{-1}$ at 29.4 N, the maximum working temperature of LM13 alloy was obtained as 80 ℃. However, this maximum working temperature was 200 ℃ and 300 ℃ respectively for ilmenite and boron carbide reinforced AMCs.

4.10. Coefficient of friction under high temperature conditions

4.10.1 Single particle reinforced composites containing coarse particles

Figure 4.31 presents the coefficient of friction values of base alloy and various AMCs (containing coarse particles) as a function of operating temperature for various applied load conditions. For any applied load-operating temperature condition, increase in reinforcement

level resulted in decrease in COF values. Further, increase in applied load and/or operating temperature for a given AMC at a given reinforcement level led to increase in COF for all the samples.

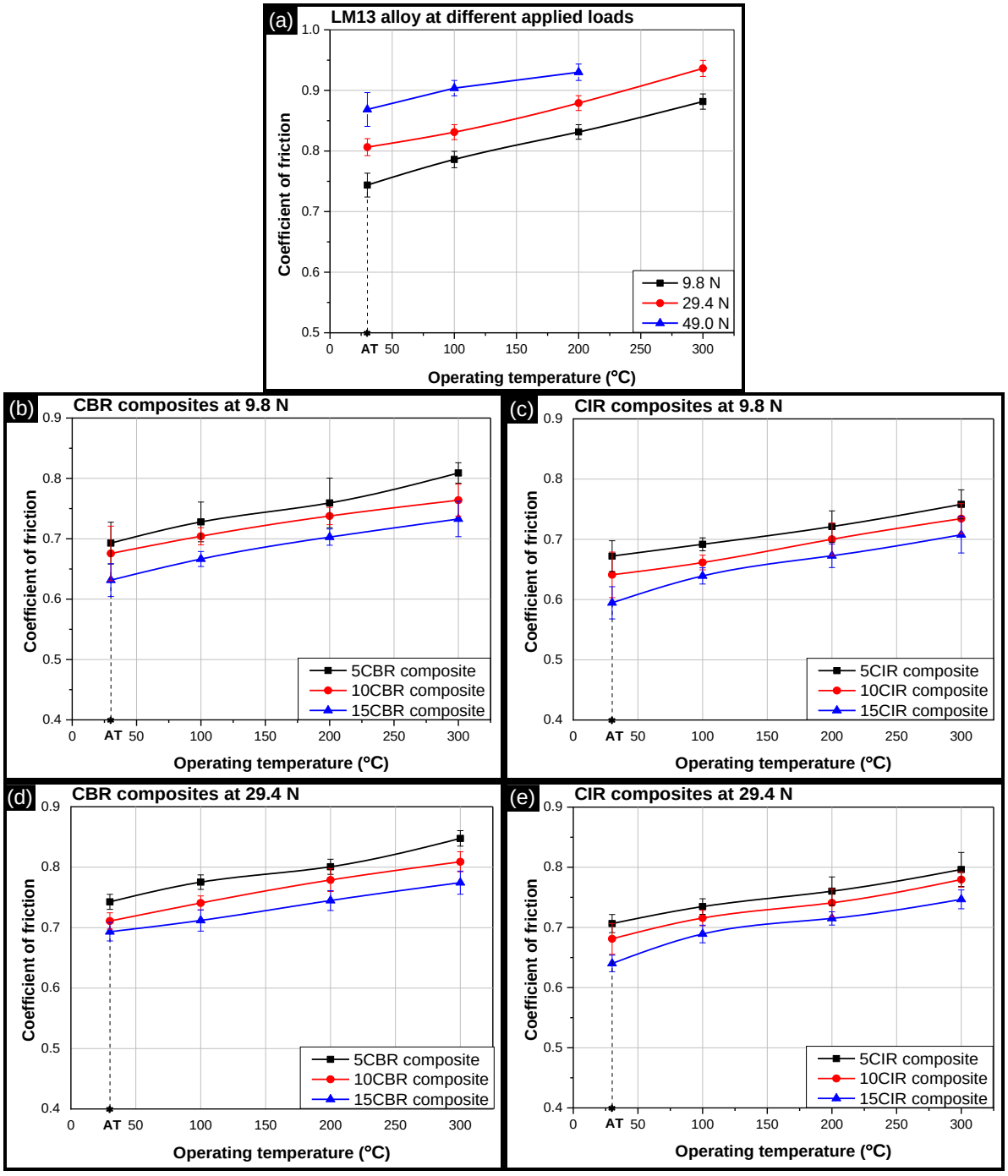

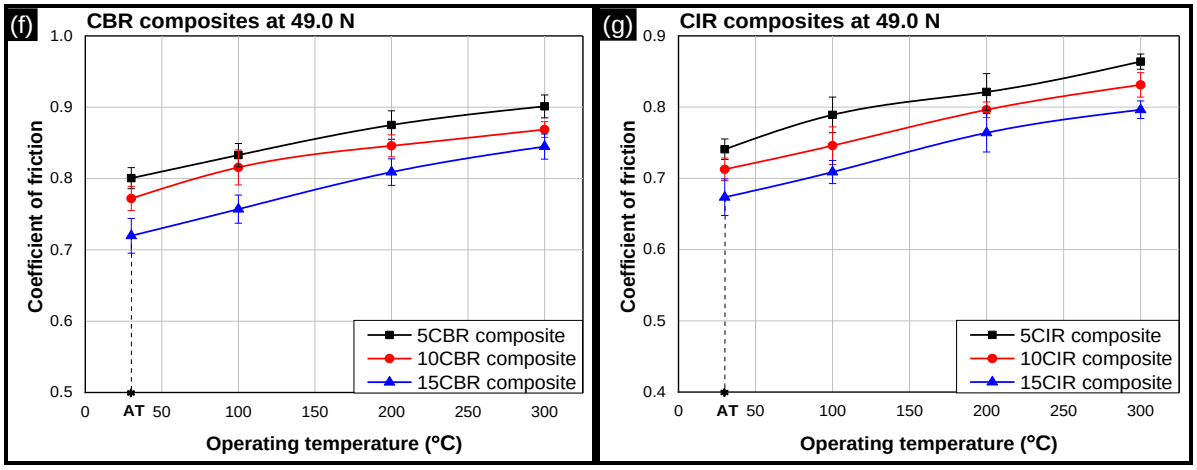

Figure 4.31 Variation in COF values with operating temperature for (a) LM13 alloy at different applied loads, (b) 'CBR' composites at 9.8 N load, (c) 'CIR' composites at 9.8 N load, (d) 'CBR' composites at 29.4 N load, (e) 'CIR' composites at 29.4 N load, (f) 'CBR' composites at 49.0 N load, and (g) 'CIR' composites at 49.0 N load. 'AT' represents the ambient temperature conditions.

Increase in applied load and/or operating temperature caused increase in softening of sliding surfaces and also instability of the oxide layer [77,180]. Increase in softening of pin surface resulted in higher penetration of asperities of counter steel disc into the sliding pin. Further, the reduction in stability of oxide layer exposed the matrix material to the counter steel disc. On account of these factors, increase in COF values was observed with increase in applied load and operating temperature. On addition of reinforced particles, a decrement in thermal softening and penetration depth of asperities of steel disc resulted in lower COF values of AMCs [18,180]. At a particular testing condition and reinforcement level, 'CIR' composites showed lower COF values in comparison of 'CBR' composites. This was attributed to the strong interfacial bonding made of ilmenite particles with matrix in 'CIR' composites.

4.10.2 Single particle reinforced composites containing fine particles

Figure 4.32 presents the coefficient of friction values of various AMCs (containing fine particles) as a function of operating temperature for various applied load conditions. For any applied load-operating temperature condition, increase in reinforcement level resulted in decrease in COF values. Further, increase in applied load and/or operating temperature for a given AMC at a given reinforcement level led to increase in COF for all the samples.

The trends observed for COF values of AMCs containing 'fine' particles ('FBR' and 'FIR' composites) were similar to the trends observed in AMCs containing 'coarse' particles ('CBR' and 'CIR' composites). Thus, the reasons for change in COF of AMCs containing 'fine' particles were the same (as discussed in Section 4.10.1).

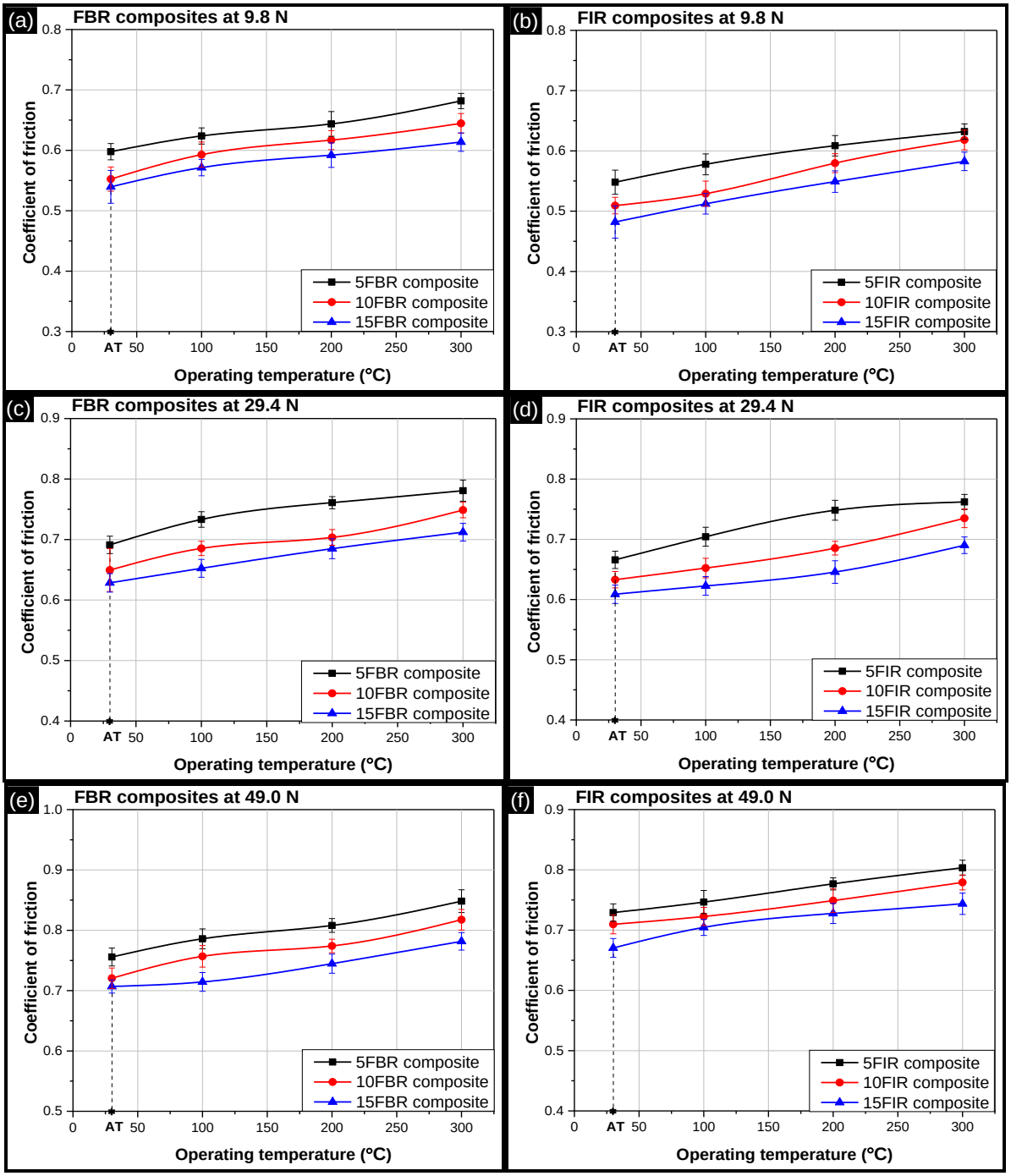

Figure 4.32 Variation in COF values versus operating temperature for (a) 'FBR' composites at 9.8 N load, (b) 'FIR' composites at 9.8 N load, (c) 'FBR' composites at 29.4 N load, (d) 'FIR' composites at 29.4 N load, (e) 'FBR' composites at 49.0 N load, and (f) 'FIR' composites at 49.0 N load. 'AT' represents the ambient temperature conditions.

Finally, for a given type of AMC at a given reinforcement level and at a given operating temperature-applied load condition, the change in particle size from 'coarse' to 'fine' resulted in lower COF values of AMCs. This behaviour was attributed to the relatively lower penetration depth of counter steel into sliding surface of AMCs (already discussed in Section 4.7.2).

4.11. Wear-tracks and debris under high temperature conditions

4.11.1 Single particle reinforced composites containing coarse particles

Figure 4.33 presents the wear-track of AMCs containing maximum reinforcement level of 'coarse' particles ('15CBR' and '15CIR' composites) at an operating temperature of 200 ℃ and various applied load conditions.

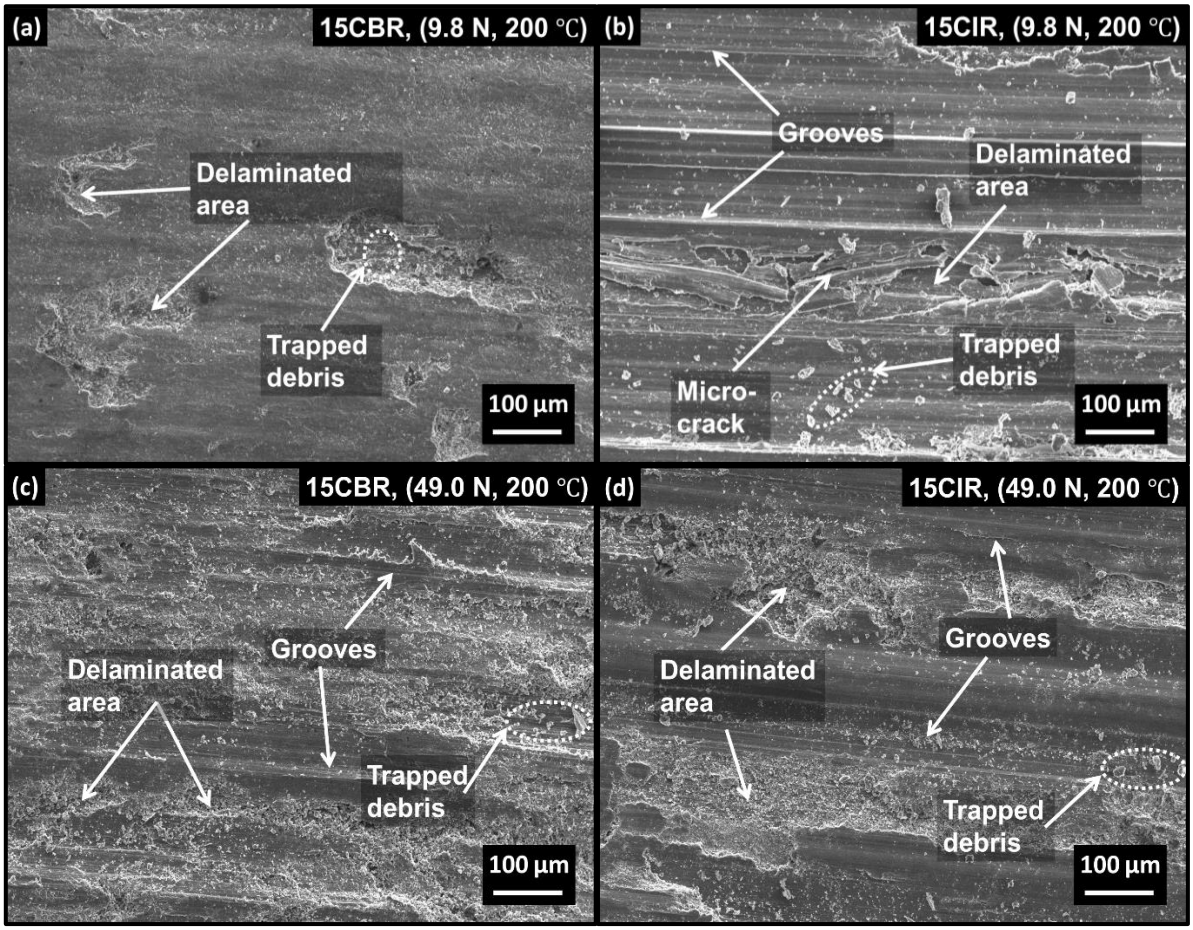

Figure 4.33 SEM images of wear-track at an operating temperature of 200 ℃ for (a) '15CBR' at 9.8 N, (b) '15CIR' at 9.8 N, (c) '15CBR' at 49.0 N, and (d) '15CIR' at 49.0 N.

Wear-track obtained after wear test for 'CBR' and 'CIR' composites comprised of three different constituent regions viz. ploughing region, delamination region, and mechanical mixed layer. Wear-tracks of '15CBR' and '15CIR' are shown in Figure 4.33a and Figure 4.33b respectively for the operating condition of 200 ℃-9.8 N. Both types of AMCs showed presence of abrasive grooves on the sliding surface (i.e. ploughing region). This signified the entrapment of fractured asperities between the counter-surfaces (pin and steel disc) which acted as abrasive particles for ploughing the sliding surface. Grooves observed were slightly shallower for '15CBR' when compared to '15CIR' composite. This was attributed to microstructure refinement in 'CBRs' which had resulted in better hardness.

Figure 4.34 presents the EDS analysis of wear-tracks of AMCs containing maximum reinforcement level of 'coarse' particles ('15CBR' and '15CIR' composites) at the extreme condition of loads (9.8 N and 49.0 N) and the transition temperature of 200 ℃. Figure 4.34a and Figure 4.34b presents the results of EDS analysis of wear-tracks of '15CBR' and '15CIR' composites respectively. In case of '15CIR' composite, the percentage of iron on the sliding surface (wear-tracks) is the sum of iron coming from ilmenite ($FeTiO_3$) and from EN31 steel disc. Similarly, the percentage of oxygen is the sum of oxygen coming from ilmenite and from oxides formed due to rise in temperature as a result of sliding of surfaces. After deducting the amount of oxygen and iron present in ilmenite, the revised value of iron and oxygen present on wear-track was observed to be 0.90 wt.% and 22.15 wt.% at 200 ℃-9.8 N respectively. The existence of iron and carbon contents on the sliding surface signified transfer of material (Fe and C) from the steel disc to the surface of AMC pin. Further, aluminium, silicon, titanium, and oxygen were also observed on the sliding surfaces. Titanium was observed on the worn surface of '15CIR' due to the reinforced ilmenite particles ($FeTiO_3$). Non-traceability of boron on the wear-track of '15CBR' composite was due to the low atomic number of boron. Presence of oxygen on the wear-tracks of both types of AMCs proved that the sliding surfaces got oxidized as a result of applied load and temperature. Higher oxygen (5.34% higher) and iron contents (93% higher) in '15CBR' composite as compared to '15CIR' composite signified presence of more stable mechanical mixed layer (MML) on the surface of boron carbide based 'CBRs' composites.

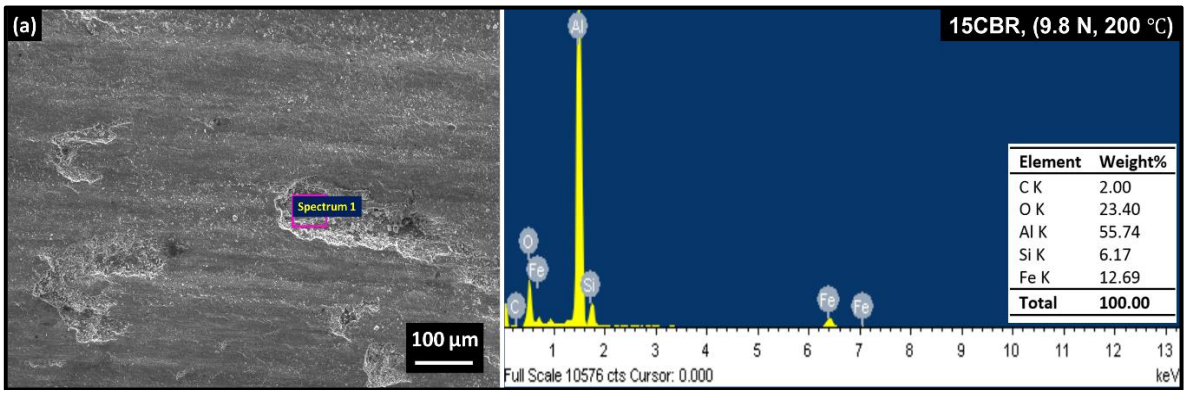

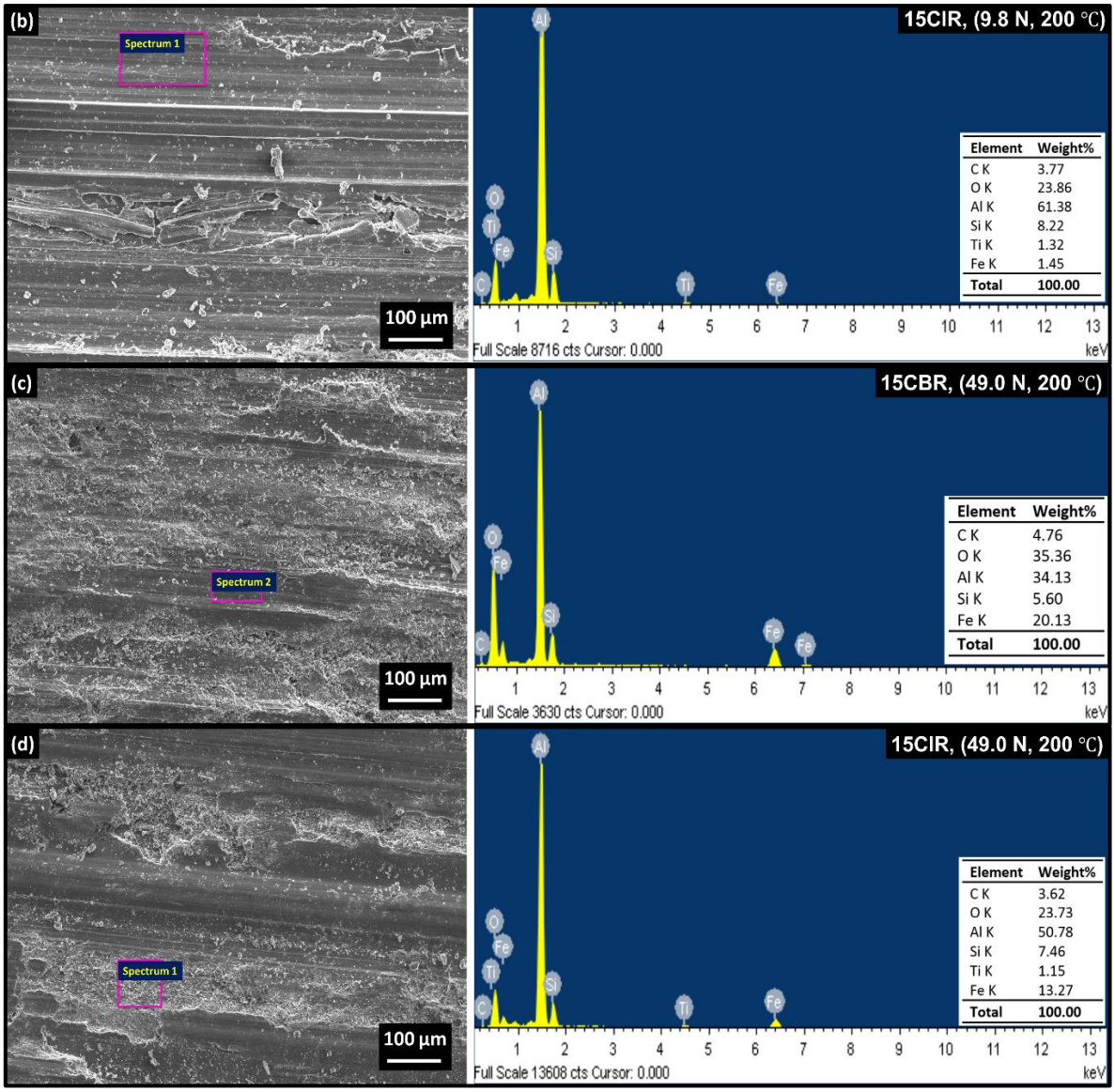

Figure 4.34 SEM-EDS of wear-tracks at an operating temperature of 200 ℃ for (a) '15CBR' at 9.8 N, (b) '15CIR' at 9.8 N, (c) '15CBR' at 49.0 N, and (d) '15CIR' at 49.0 N.

Figure 4.33c and Figure 4.33d present the wear-tracks of '15CBR' and '15CIR' composites under the operating condition of 200 ℃-49.0 N respectively. Both the surfaces showed the presence of craters and abrasive grooves. Presence of craters on the sliding surfaces was attributed to generation and subsequent convergence of cracks under the high applied load-operating temperature conditions. Craters formed due to convergence of cracks at a node resulted in delamination region. Delamination area was relatively more for '15CIR' composite (compare Figure 4.33c and Figure 4.33d). This was attributed to lower restriction to the propagation of cracks generated as a result of applied load. Due to easy propagation of cracks, the tendency of convergence of cracks got increased which resulted in high area of delaminated region in '15CIR' composite.

Figure 4.34c and Figure 4.34d present the EDS analysis of wear-track of AMCs containing maximum reinforcement level of 'coarse' particles ('15CBR' and '15CIR' composites) under the testing condition of 200 ℃-49.0 N. The revised values of iron and oxygen contents (obtained after deducting the values of iron and oxygen contents coming from ilmenite particles) present on the sliding surface of '15CIR' composite were calculated to be 12.79 wt.% and 22.24 wt.% respectively. Thus, the higher amount of iron (57.38% higher than '15CIR' composite) and oxygen (58.99% higher than '15CBR' composite) contents on the wear-track of '15CBR' composite signified formation of more stable MML as compared to '15CIR' composite.

Figure 4.35 and Figure 4.36 present the SEM images and EDS results respectively of wear-debris of AMCs containing maximum weight percentage of 'coarse' particles ('15CBR' and '15CIR' composite) under extreme loads (9.8 N and 49.0 N) and transition temperature (200 ℃).

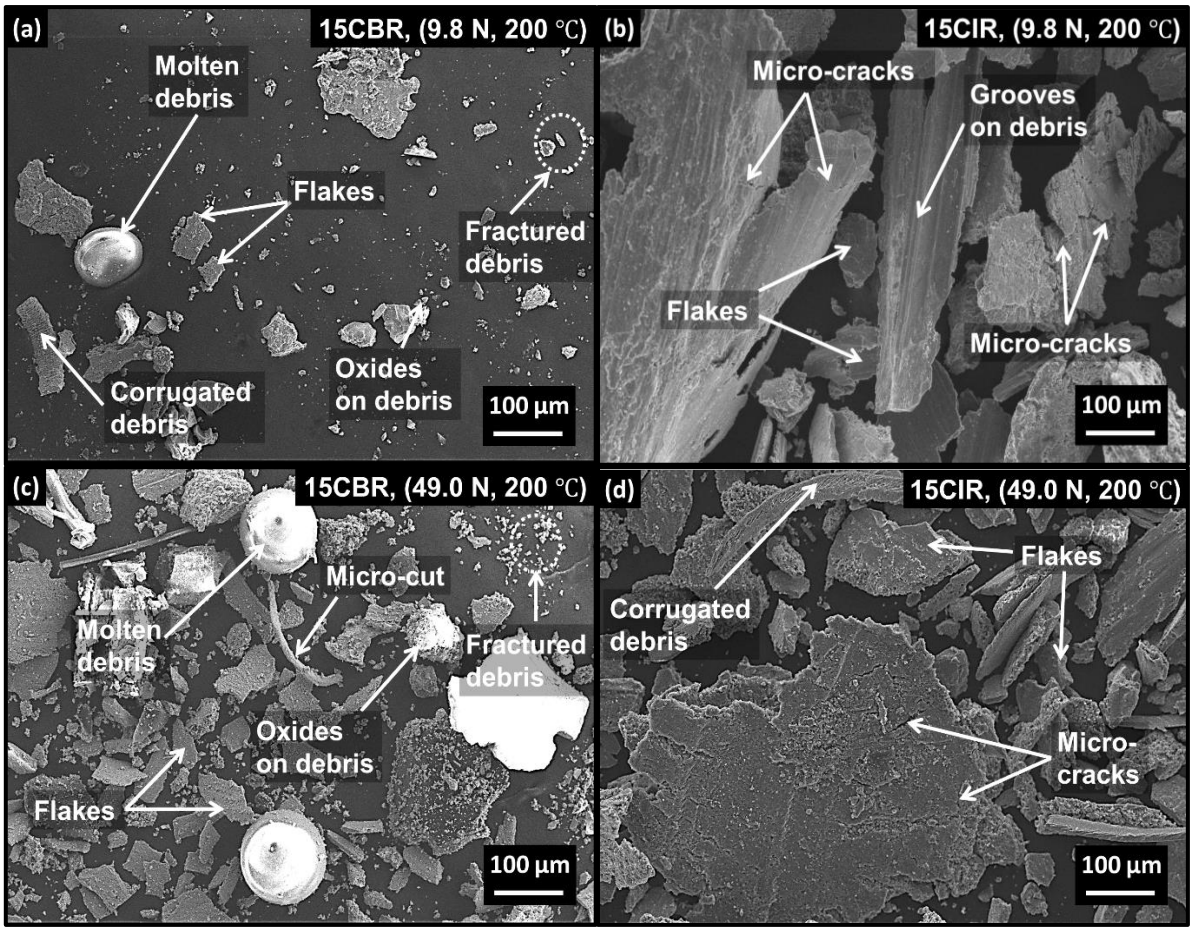

Figure 4.35 SEM images of wear-debris at an operating temperature of 200 ℃ for (a) '15CBR' at 9.8 N, (b) '15CIR' at 9.8 N, (c) '15CBR' at 49.0 N, and (d) '15CIR' at 49.0 N.

Worn-out material of both type of AMCs consisted mainly of flake-like debris. At low loads (9.8 N), the presence of flake-like debris was due to the removal of wedges formed as a result of abrasive wear. This resulted in small sized debris (Figure 4.35a and Figure 4.35b) [18]. For '15CIR' composite, the presence of micro-cracks on flake-like debris was due to the plastic deformation of sliding pin surface under the effect of applied load. The presence of ploughing marks on flakes signified that after the initial abrasive action, the removal of material occurred due to convergence of micro-cracks. For '15CBR', additional features like corrugated debris (due to repetitive stress), molten debris, oxide on debris, and fractured debris (due to applied load conditions) were also observed [23]. The presence of corrugated debris was due to adherence of wear-debris to the sliding surface which subjected them to repetitive action of stresses. Further, formation of molten debris was due to attainment of higher temperature as a result of frictional heat. Another reason stated for formation of molten debris is the fusion of fractured debris to obtain the minimum surface area [187]. Further, the frictional heat was also responsible for formation of oxides on MML which got removed to form oxides on debris. The presence of oxides was confirmed by taking EDS at different points. During sliding of surfaces, some debris get trapped between the pin and disc surface and get fractured under the action of applied load. This resulted in formation of fractured debris. With change in applied load from 9.8 N to 49.0 N for both the composites (i.e. '15CBR' and '15CIR' composites), the size of wear-debris showed an increasing trend (Figure 4.35c and Figure 4.35d). This behaviour was attributed to higher rate of propagation and convergence of micro-cracks generated on the sliding surface. Under high load condition (49.0 N), an additional feature of micro-cut was observed when compared to debris of low load conditions (9.8 N). The generation of micro-cut debris was ascribed to the abrasive action performed by entrapped debris.

Figure 4.36 presents the EDS analysis of wear-debris of AMCs containing maximum reinforcement level of 'coarse' particles at different applied loads at operating temperature of 200 ℃.

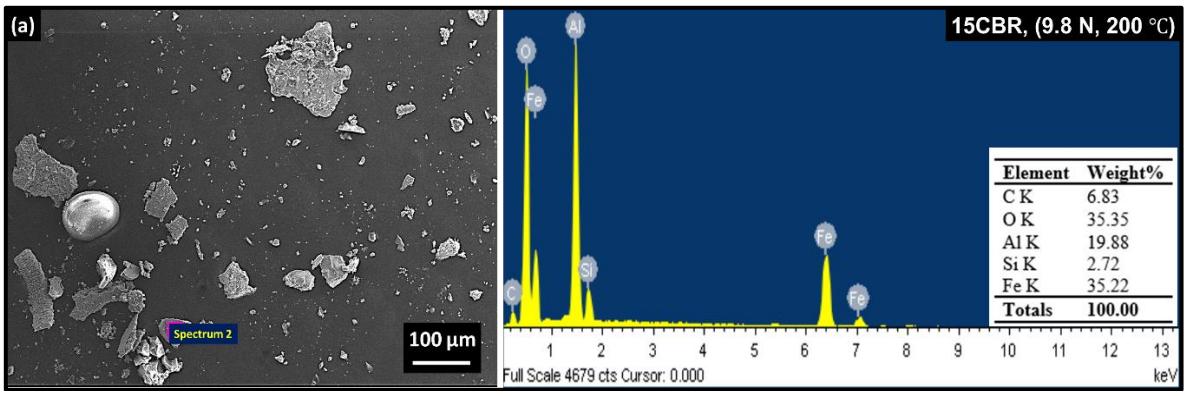

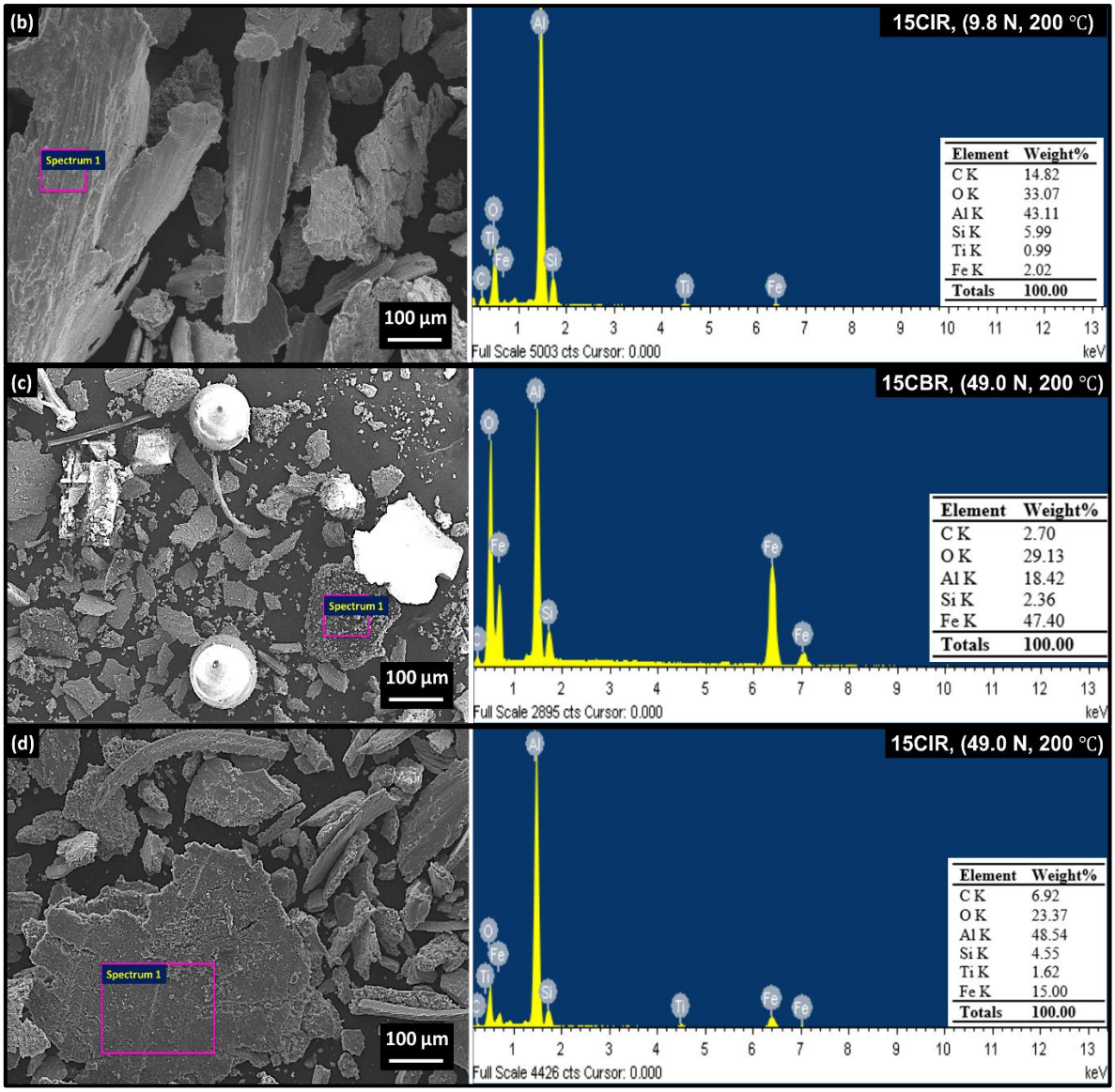

Figure 4.36 SEM-EDS of wear-track at an operating temperature of 200 ℃ for (a) '15CBR' at 9.8 N, (b) '15CIR' at 9.8 N, (c) '15CBR' at 49.0 N, and (d) '15CIR' at 49.0 N.

EDS analysis of wear-debris indicated presence of silicon, aluminium, oxygen, titanium, iron, and carbon. The presence of these elements in debris signified formation/removal of MML during the sliding wear.

4.11.2 Single particle reinforced composites containing fine particles

Figure 4.37 shows the SEM micrographs of wear-tracks obtained for AMCs containing maximum reinforcement level of 'fine' particles (i.e. '15FIR' and '15FBR' composites) at different applied loads and operating temperature of 200 ℃. At all the applied load conditions, wear-tracks of both the composites (i.e. '15FBR' and '15FIR') showed presence of trapped debris and delaminated area. The presence of trapped debris revealed their entrapment between

the counter surfaces which was responsible for formation of MML and grooves on the pin surface. Delaminated area was formed due to generation and convergence of micro-cracks under the action of applied load. With increase in applied load, the tendency of formation and convergence of micro-cracks also increased. Thus, for a particular reinforcement type and reinforcement level, higher delamination area was observed for wear-track obtained at 49.0 N (Figure 4.37c and Figure 4.37d). Similarly, higher delaminated area was observed for '15FIR' composite in comparison to'15FBR' composite at a particular applied load condition. This was attributed to higher number of hard particles present in '15FBR' composite (due to the relatively lower density and higher hardness of boron carbide particles than ilmenite particles) which restricted the propagation of micro-cracks and resulted in lower delaminated area in '15FBR' composite.

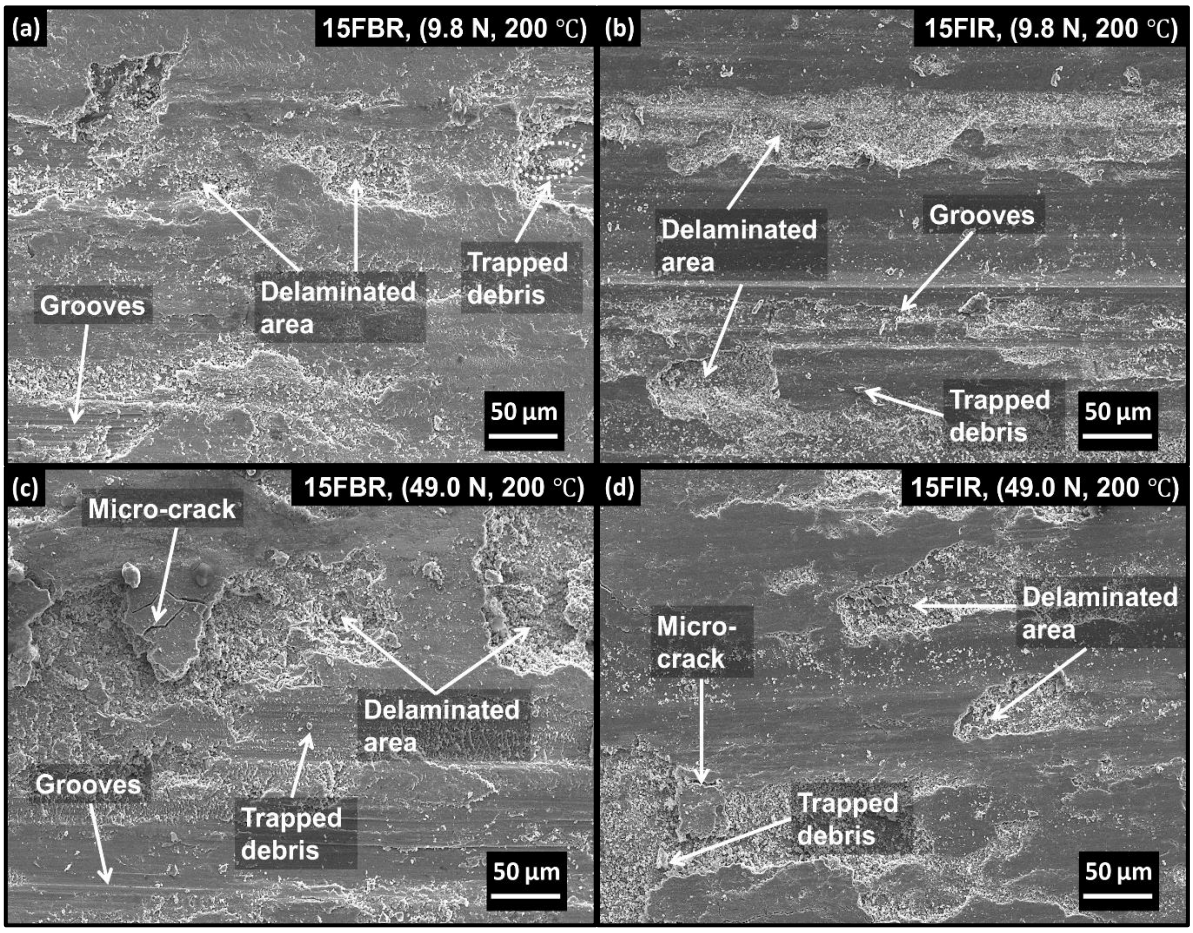

Figure 4.37 SEM images of wear-track at an operating temperature of 200 ℃ for (a) '15FBR' at 9.8 N, (b) '15FIR' at 9.8 N, (c) '15FBR' at 49.0 N, and (d) '15FIR' at 49.0 N.

Figure 4.38 presents the SEM micrographs of wear debris of AMCs containing maximum reinforcement level of 'fine' particles (i.e. '15FBR' and '15FIR' composite) at different applied loads for an operating temperature of 200 ℃. Figure 4.38a and Figure 4.38b show the wear-

debris of ‘15FBR’ and ‘15FIR’ composites respectively at an operating condition of 200 ℃-9.8 N respectively. Both the composites showed presence of flake-like debris. Oxide on debris and fractured debris like features were observed in ‘15FBR’ composite whereas corrugated debris, micro-cracks, and grooves on debris were the main features observed for ‘15FIR’ composite.

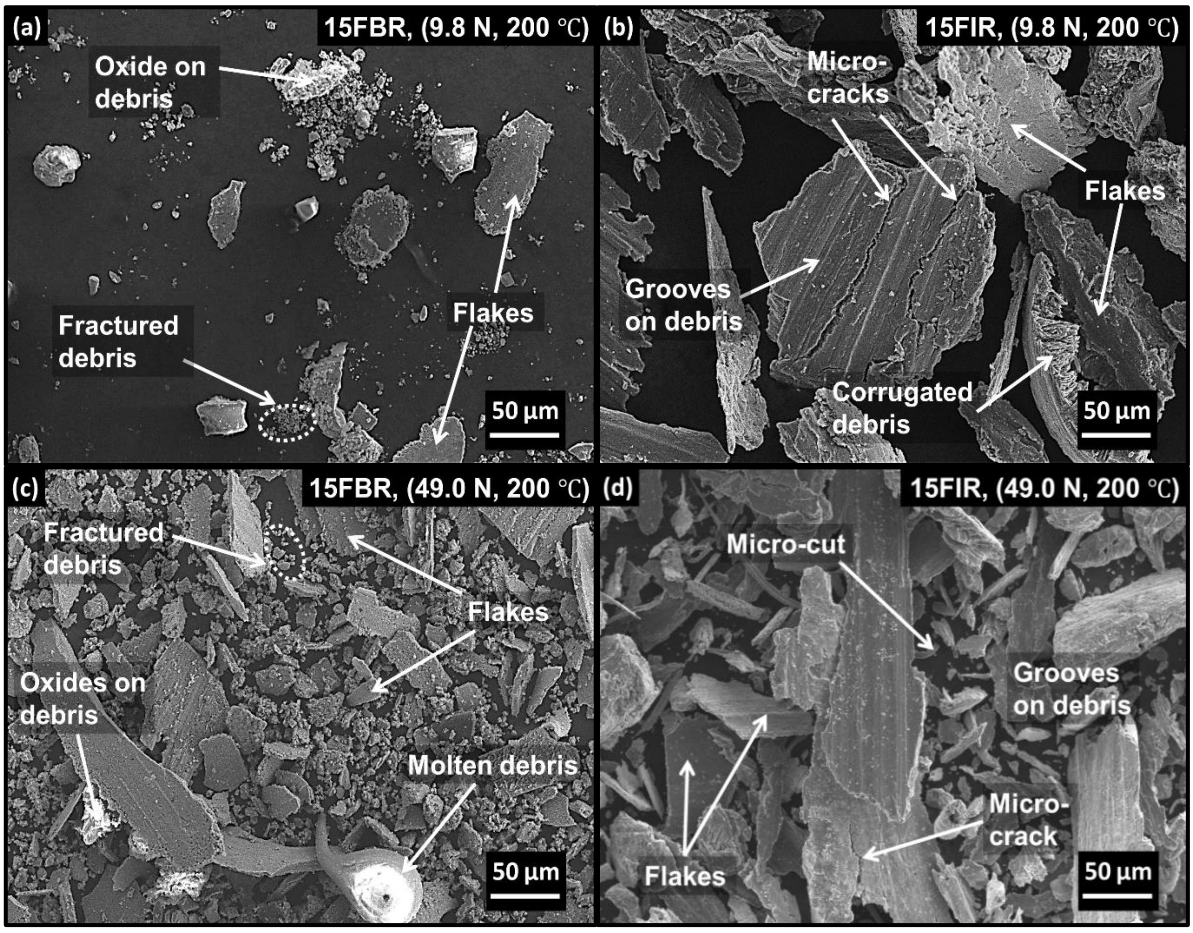

Figure 4.38 SEM images of wear-debris at an operating temperature of 200 ℃ for (a) ‘15FBR’ at 9.8 N, (b) ‘15FIR’ at 9.8 N, (c) ‘15FBR’ at 49.0 N, and (d) ‘15FIR’ at 49.0 N.

Further, the debris obtained for ‘15FBR’ and ‘15FIR’ composites at the testing condition of 200 ℃-49.0 N are shown in Figure 4.38c and Figure 4.38d respectively. In comparison to the low load condition, additional features like ‘molten debris’ and ‘micro-cut’ debris were noted under this high load condition. The reasons for these additional features obtained in debris are already discussed in Section 4.11.1. On comparing the features of debris for ‘15FBR’ and ‘15FIR’ AMCs under various loads, it was observed that wear-debris of ‘15FIR’ showed relatively very large flake size. From this, it was noted that for a given operating temperature, reinforcement level, and applied load, the type of AMC whose wear-debris showed larger flakes had shown relatively higher wear rates.

Figure 4.39 shows the EDS analysis of wear-track obtained for AMCs containing maximum reinforcement level of ‘fine’ particles (i.e. ‘15FBR’ and ‘15FIR’ composites) at an operating temperature of 200 ℃ for the extreme applied loads.

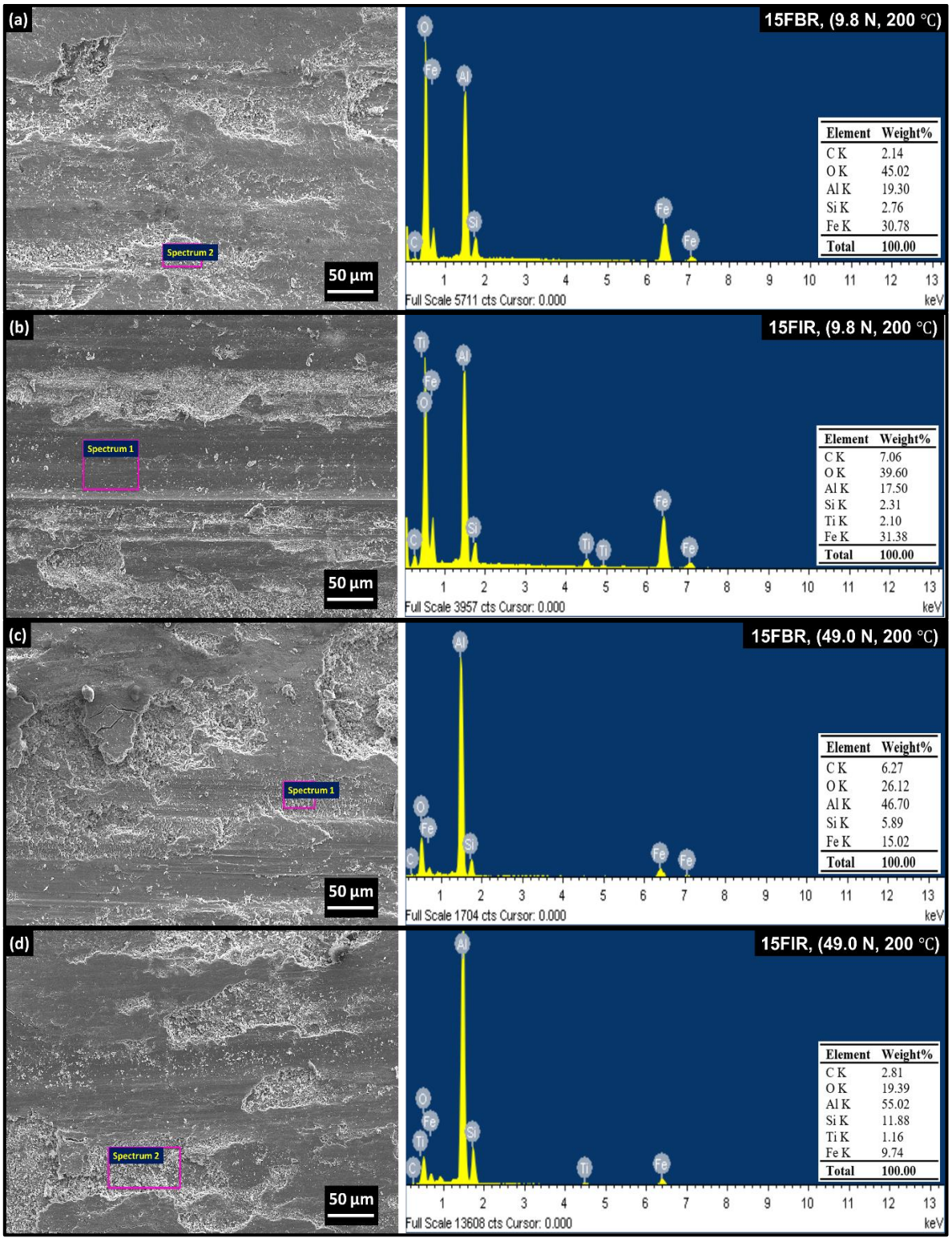

Figure 4.39 SEM-EDS of wear-track at an operating temperature of 200 ℃ for (a) ‘15FBR’ at 9.8 N, (b) ‘15FIR’ at 9.8 N, (c) ‘15FBR’ at 49.0 N, and (d) ‘15FIR’ at 49.0 N.

After deducting the amount of iron and oxygen present in ilmenite, the iron and oxygen contents present on the sliding surface of '15FIR' composite at 200 ℃-9.8 N were calculated as 30.50 wt.% and 36.88 wt.% respectively. For operating condition of 200 ℃-49.0 N, the calculated value of iron and oxygen contents on the wear-track of '15FIR' composite were calculated as 9.25 wt.% and 17.89 wt.% respectively. The presence of iron, carbon, and oxygen on both the sliding surfaces under a particular testing condition signified the transfer of material between the two counter surfaces (i.e. composite pin and steel disc). This transfer of material under the action of applied load and operating temperature led to formation of MML. In case of '15FBR' composite, iron content present on the sliding surface at 200 ℃-9.8 N and 200 ℃-49.0 N was 0.92% and 62.37% higher respectively than that present on the sliding surface of '15FIR' composite. Similarly, oxygen content showed a higher percentage of 22.07% and 46.00% respectively on the sliding surface of '15FBR' composite at 200 ℃-9.8 N and 200 ℃-49.0 N. The presence of higher content of iron and oxygen on the sliding surfaces of '15FBR' composite implied that more stable MML was formed on this composite than the '15FIR' composite.

Figure 4.40 shows the EDS analysis of wear-debris obtained for AMCs containing maximum reinforcement level of 'fine' particles (i.e. '15FBR' and '15FIR' composites) at an operating temperature of 200 ℃ for the extreme applied loads. EDS analysis of wear-debris of '15FIR' composite showed the presence of aluminum, silicon, iron, carbon, oxygen, and titanium for both the testing conditions. Similarly, the wear-debris of '15FBR' composite showed the existence of aluminum, silicon, iron, carbon, and oxygen. The presence of elements from pin and steel disc in wear-debris signified the formation and removal of MML during the sliding wear.

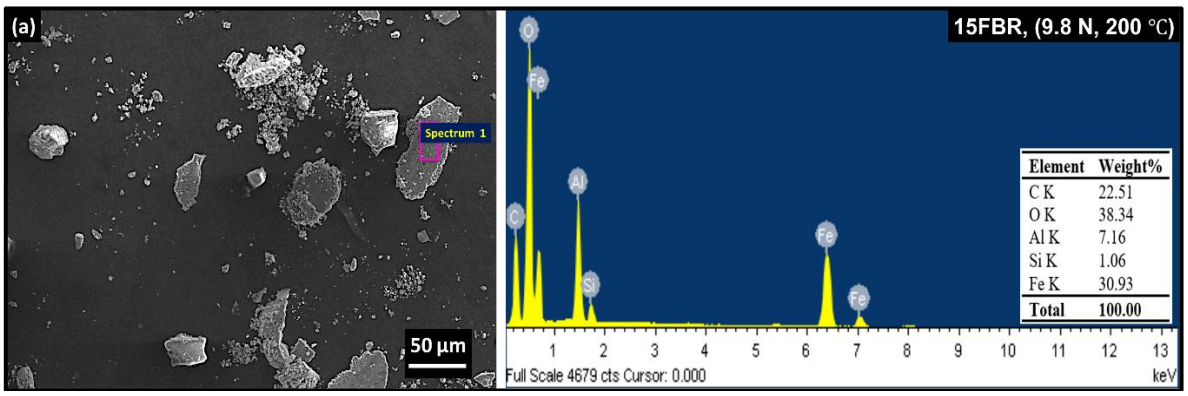

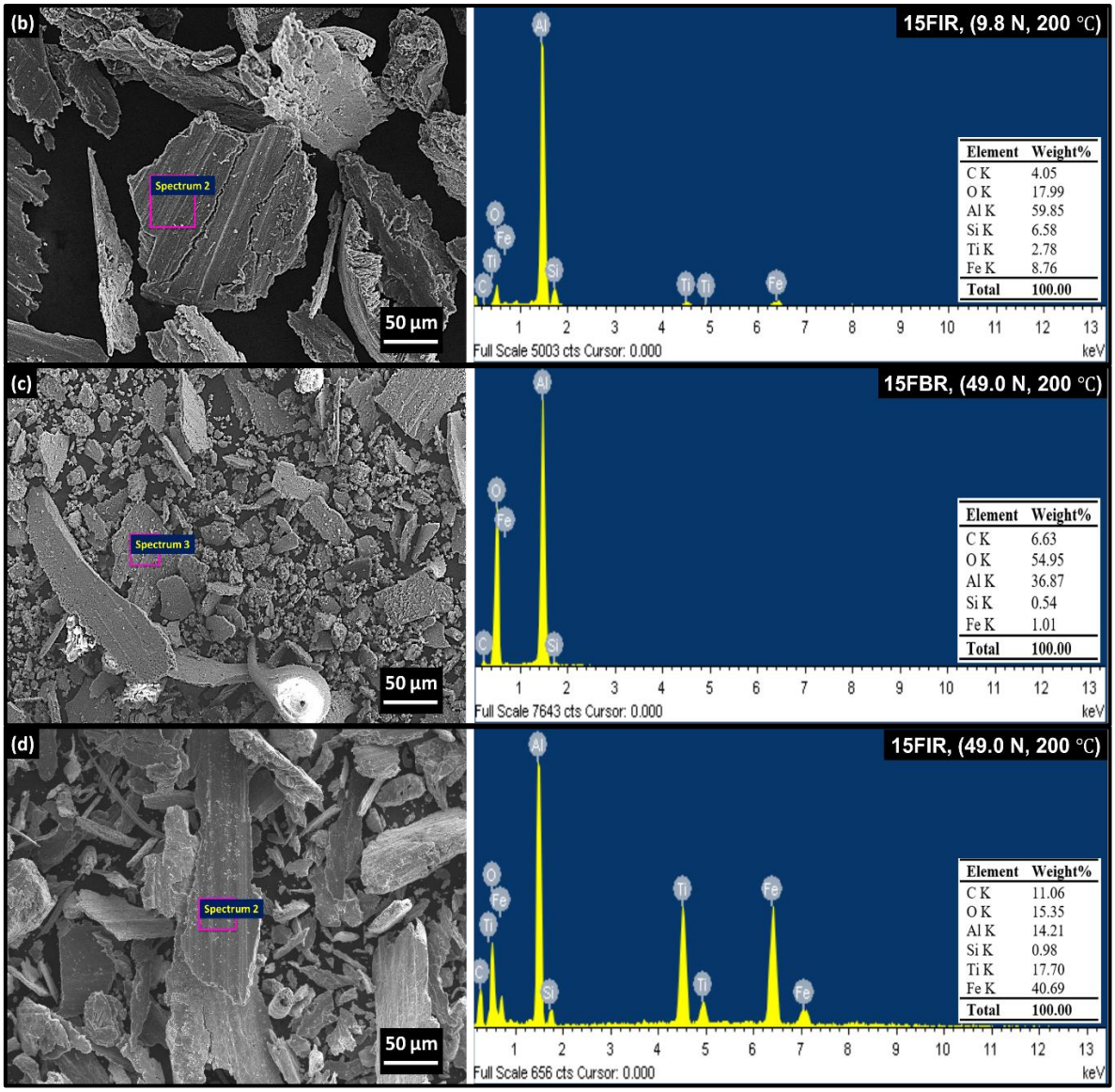

Figure 4.40 SEM-EDS of wear-debris at an operating temperature of 200 ℃ for (a) '15FBR' at 9.8 N, (b) '15FIR' at 9.8 N, (c) '15FBR' at 49.0 N, and (d) '15FIR' at 49.0 N.

The next chapter presents and discusses the results related to the mechanical testing and characterization of dual particle reinforced AMCs under room temperature as well as high temperature conditions.

Chapter 5
RESULTS AND DISCUSSION
(Characterization and testing of dual particle reinforced AMCs)

Overview

This chapter presents the results and discussion pertaining to the characterization and testing of dual particle reinforced AMCs. XRD analysis was conducted to determine the constituents of base alloy and various AMCs. The combined effect of reinforcements (i.e. boron carbide and ilmenite) on the microstructure of LM13 base alloy was investigated. The changes observed in microstructure of hybrid AMCs with variations in weight percentage, mixing proportion, and particles size of reinforcements was investigated. Similarly, the effect of reinforcement level, mixing proportion, and particle size on coefficient of thermal expansion, hardness, wear rate, and coefficient of friction values of various hybrid AMCs was observed. The friction and wear characteristics of hybrid AMCs were investigated, both at room temperature as well as high operating temperature conditions. Finally, SEM-EDS analysis was performed on the wear-track and wear-debris to determine the type of wear mechanisms responsible for removal of material under different operating conditions.

5.1. XRD analysis

5.1.1 Dual particle reinforced composites containing coarse particles

XRD diffraction pattern of dual particle reinforced '15CBI-31' composite containing 'coarse' particles is presented in Figure 5.1. This hybrid composite contained maximum reinforcement level of 15 wt.% with mixing proportion of boron carbide and ilmenite particles in the weight ratio of 3:1. The peaks of 'α' and 'β' seen in the spectra signified the presence of aluminium and silicon constituents of base alloy.

Further, the presence of peaks of 'δ' and 'η' present in the spectra signified the presence of boron carbide and ilmenite reinforcements in matrix material. Some additional peaks of 'ψ', 'Ω', and 'π' represented peaks of iron oxide, silicon oxide, and titanium oxide respectively. The presence of these metal oxides confirmed the occurrence of interfacial reaction between ilmenite and silicon which is presented as Equation 5.1. This chemical reaction benefits the AMCs by improving the interfacial strength [80,153,154].

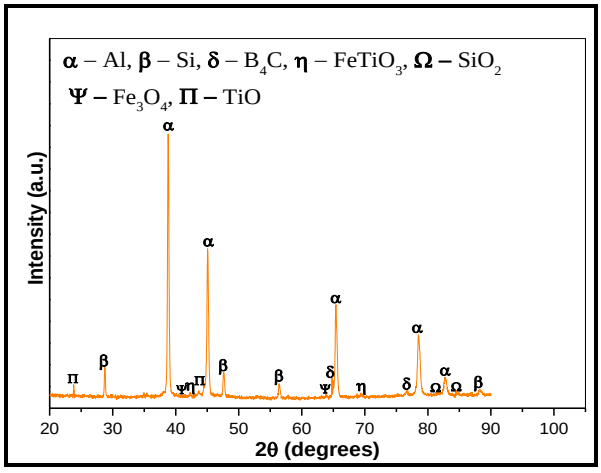

Figure 5.1 XRD diffraction for '15CBI-31' hybrid AMCs.

The formation of interfacial compounds (SiO_2, Fe_3O_4, TiO_2) signified that the surface of reinforced ilmenite particles was completely wetted by the LM13 alloy [13,38]. The increased wettability of ilmenite particles by undergoing the chemical reaction confirmed that a strong interfacial bond was formed between matrix-reinforced particles. Similar observations are reported by other researchers also [46,80].

$$3FeTiO_3 + 3Si \rightarrow Fe_3O_4 + 3SiO_2 + 3TiO \quad \ldots\ldots\ldots\ldots\ldots\ldots\ldots\ldots \quad (5.1)$$

The absence of compounds like Al_4C_3, Al_3BC, and Al_3BC_3 signified that no interfacial reaction occurred between matrix and boron carbides particles [188]. Thus, the wetting of boron carbide by LM13 alloy occurred without any chemical reaction. In literature, it is reported that the

interface formed by chemical reaction provides more interfacial strength [23,80]. Hence, the interface formed by ilmenite particles had more strength in comparison to that of boron carbide particles.

Further, the strength of interfacial bond formed between matrix and reinforced particles can also be characterized by the interfacial energy concept [13,189]. For formation of coherent or partially coherent bonding, the interfacial energy should be low which further depends upon the lattice misfit between matrix and reinforced particles. The calculation of lattice misfit (λ) was done according to the revised Turnbull-Vonnegut equation. In the revised Turnbull-Vonnegut equation, the relative increase in d spacing of reinforced particle (d_r) is calculated with respect to the d-spacing of base alloy (d_b), as given in Equation 5.2. If $\lambda \leq 0.05$ then interface formed has coherent bonding, whereas for $0.05<\lambda\leq 0.25$, partially coherent bond is formed [189]. The values of lattice misfit at different crystal faces of matrix and reinforced particles are shown in Table 5.1.

$$\lambda = \left|\frac{d_r - d_b}{d_b}\right| \quad \text{..... (5.2)}$$

Table 5.1 Possible coherent/partially coherent interfaces of boron carbide and ilmenite particles with eutectic mixture of LM13 alloy in '15CBI-31' composite.

S. No.	Aluminium		Silicon		Boron carbide		Ilmenite		Lattice misfit (λ) of Al and Si with	
	d(Å)	(h,k,l)	d(Å)	(h,k,l)	d(Å)	(h,k,l)	d(Å)	(h,k,l)	B_4C	$FeTiO_3$
1.	2.33	(1,1,1)	-	-	2.30	(1,1,3)	2.24	(1,1,-3)	0.01618	0.03969
2.	2.02	(2,0,0)	-	-	1.89	(0,2,4)	1.87	(0,2,4)	0.06621	0.07412
3.	1.43	(2,2,0)	-	-	1.39	(2,2,0)	1.40	(0,3,3)	0.02247	0.01710
4.	1.22	(3,1,1)	-	-	1.21	(1,1,9)	1.21	(2,1,-8)	0.00799	0.00553
5.	1.16	(2,2,2)	-	-	-	-	1.15	(1,3,4)	-	0.00853
6.	-	-	3.13	(1,1,1)	2.80	(1,1,0)	2.76	(1,0,4)	0.10585	0.11954
7.	-	-	1.91	(2,2,0)	1.89	(0,2,4)	1.87	(0,2,4)	0.01518	0.02352
8.	-	-	1.63	(3,1,1)	1.62	(1,0,7)	1.62	(2,1,-2)	0.00677	0.00619
9.	-	-	1.56	(2,2,2)	1.56	(2,1,4)	1.51	(1,2,-4)	0.00005	0.03589
10.	-	-	1.35	(4,0,0)	1.33	(1,3,1)	1.34	(1,0,10)	0.01514	0.00854
11.	-	-	1.24	(3,3,1)	1.21	(1,1,9)	1.23	(2,2,-3)	0.02772	0.01061
12.	-	-	1.10	(4,2,2)	-	-	1.10	(4,0,1)	-	0.00527

*** d(Å): d spacing in Angstrom and (h, k, l): miller indices**

The reinforced particles were surrounded by eutectic mixture of aluminium and silicon. It can be noted from Table 5.1 that aluminium and boron carbide formed coherent interfacial bonding along the crystal faces of (3,1,1) and (1,1,9) respectively as the value of lattice misfit for the crystal faces was lower than 0.05 and also lower than the other combinations of crystal faces. Similarly, aluminium and ilmenite also formed coherent interfacial bonding along the crystal faces of (3,1,1) and (2,1,-8) respectively as their value of lattice misfit for the crystal faces was lowest and also lower than 0.05. In the context of silicon, the crystal face of (2,2,2) made a

coherent bond with the crystal face of (1,2,-4) of boron carbide. Further, the crystal faces of (4,2,2) and (4,0,1) were responsible for coherent bonding between silicon and ilmenite respectively. Thus, as discussed, the formation of coherent bonding between matrix and reinforced particles signified a strong interfacial bonding. Further, it is well reported in literature that strength of interfacial bonding between matrix-reinforcement is higher for reinforcements which show interfacial reaction [18,80]. The occurrence of interfacial reaction between matrix and ilmenite particles signified formation of relatively stronger interface in ilmenite reinforced AMCs as compared to the boron carbide reinforced counterparts.

5.1.2 Dual particle reinforced composites containing fine particles

XRD diffraction pattern of dual particle reinforced '15FBI-31' composite containing 'fine' particles is presented in Figure 5.2. This hybrid composite contained maximum reinforcement level of 15 wt.% with mixing proportion of boron carbide and ilmenite particles in the weight ratio of 3:1. XRD pattern showed peaks of 'α' and 'β' which corresponded to the main constituents of matrix i.e. aluminium and silicon respectively. Further, the peaks labelled as 'δ' and 'η' in the spectra signified the presence of boron carbide and ilmenite reinforcement in the LM13 alloy respectively. The additional peaks of 'ψ', 'Ω', and 'Π 'revealed the presence of iron oxide, silicon oxide, and titanium oxide respectively. The presence of these metal oxides confirmed the occurrence of interfacial reaction between ilmenite and silicon which is presented in Equation 5.1. However, no such additional peaks of compounds were observed for boron carbide particles.

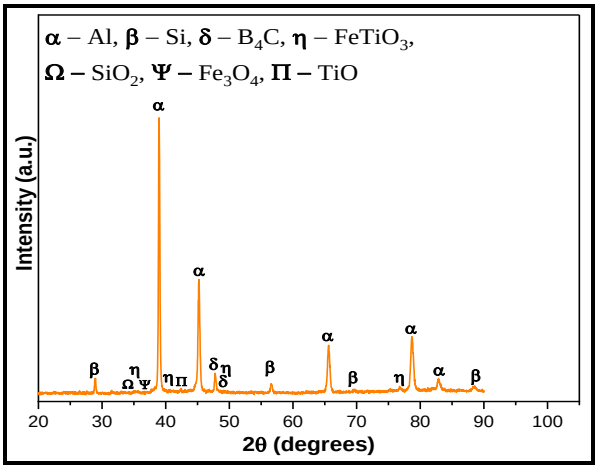

Figure 5.2 XRD diffraction for '15FBI-31' hybrid AMCs.

The observations obtained for '15FBI-31' composite is similar to the '15CBI-31' composite. However, a difference in crystal faces responsible for formation of coherent bonds between

matrix and reinforced particles is observed. This difference is mainly observed for ilmenite particles. Table 5.2 presents the possible crystal faces responsible for making of coherent/partially coherent interfaces between matrix and reinforced particles.

Table 5.2 Possible coherent interfaces of boron carbide and ilmenite particles with eutectic mixture of LM13 alloy in '15FBI-31' composite.

S. No.	Aluminium		Silicon		Boron carbide		Ilmenite		Lattice misfit (λ) of Al and Si with	
	d(Å)	(h,k,l)	d(Å)	(h,k,l)	d(Å)	(h,k,l)	d(Å)	(h,k,l)	B_4C	$FeTiO_3$
1.	2.33	(1,1,1)	-	-	2.30	(1,1,3)	2.32	(0,0,6)	0.01618	0.00827
2.	2.02	(2,0,0)	-	-	1.89	(0,2,4)	1.85	(0,2,4)	0.06621	0.08490
3.	1.43	(2,2,0)	-	-	1.39	(2,2,0)	1.42	(2,1,-5)	0.02247	0.00649
4.	1.22	(3,1,1)	-	-	1.21	(1,1,9)	1.22	(2,2,-3)	0.00799	0.00115
5.	1.16	(2,2,2)	-	-	-	-	1.16	(0,0,12)	-	0.00827
6.	-	-	3.13	(1,1,1)	2.80	(1,1,0)	2.72	(1,0,4)	0.10585	0.13130
7.	-	-	1.91	(2,2,0)	1.89	(0,2,4)	1.85	(0,2,4)	0.01518	0.03488
8.	-	-	1.63	(3,1,1)	1.62	(1,0,7)	1.62	(0,1,8)	0.00677	0.01285
9.	-	-	1.56	(2,2,2)	1.56	(2,1,4)	1.55	(0,0,9)	0.00005	0.01388
10.	-	-	1.35	(4,0,0)	1.33	(1,3,1)	1.33	(1,0,10)	0.01514	0.02331
11.	-	-	1.24	(3,3,1)	1.21	(1,1,9)	1.24	(3,0,6)	0.02772	0.00844
12.	-	-	1.10	(4,2,2)	-	-	1.10	(2,0,11)	-	0.01199

*** d(Å): d spacing in Angstrom and (h,k,l): miller indices**

With respect to lowest lattice misfit value, the crystal faces of (3,1,1) and (1,1,9) were responsible for coherent bonding between aluminium and boron carbide respectively. Similarly, silicon and boron carbide also formed coherent bonding along the crystal faces of (2,1,4) and (2,2,2) respectively. In the context of ilmenite particles, the crystal face of (2,2,-3) made a coherent bond with the crystal face of (3,1,1) of aluminium. Further, the crystal faces of (3,3,1) and (3,0,6) were responsible for coherent bonding between silicon and ilmenite respectively. Thus, as discussed, the formation of coherent bonding and interfacial products were responsible for increase in strength of interface formed between ilmenite and base alloy.

5.2. Optical microscopy

5.2.1 Dual particle reinforced composites containing coarse particles

The optical micrographs of dual particle reinforced AMCs containing 'coarse' particles with different mixing proportions and various reinforcement levels (i.e. 'CBI' composites) are shown in Figure 5.3–5.5.

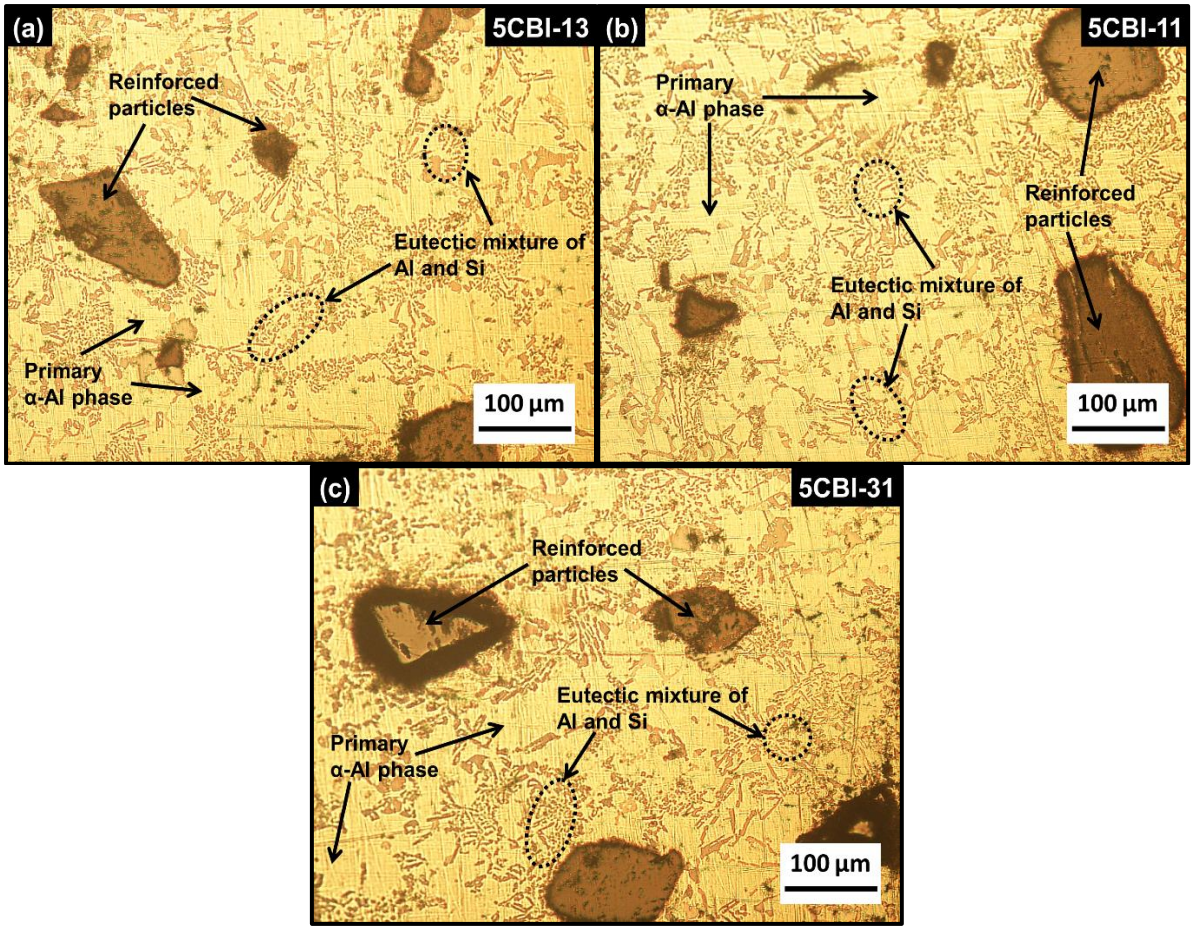

Figure 5.3 Optical micrographs of (a)' 5CBI-13' composite, (b) '5CBI-11' composite, and (c) '5CBI-31' composite at a magnification of 200X.

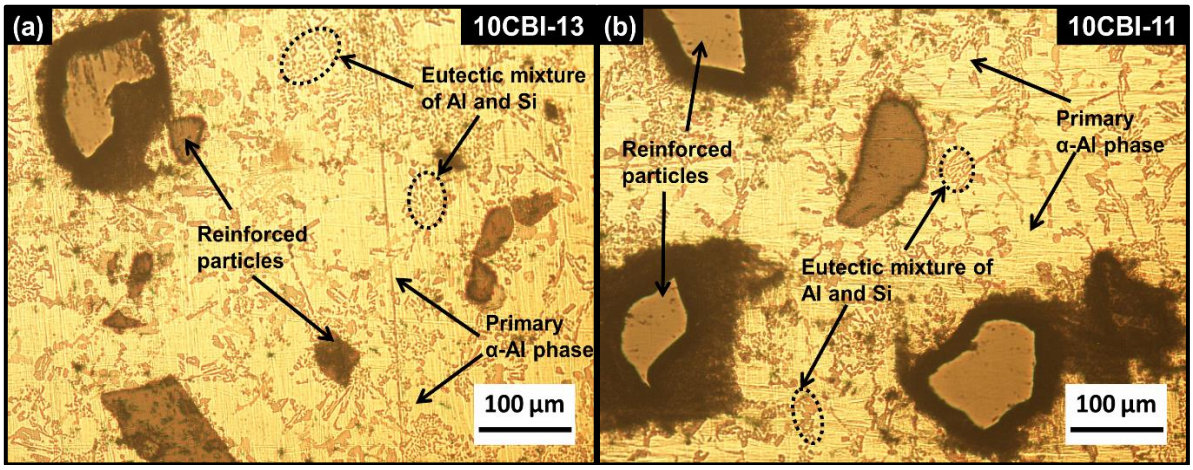

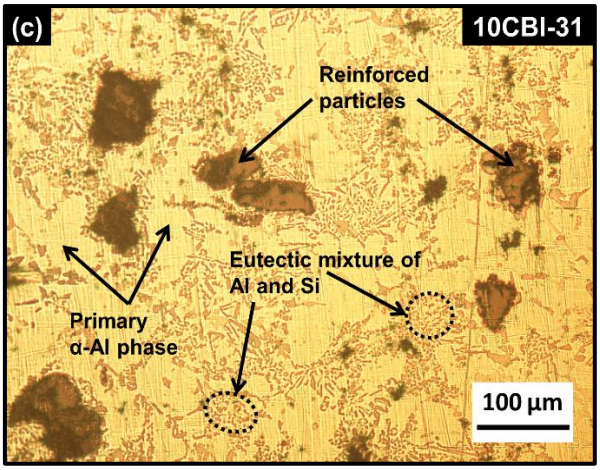

Figure 5.4 Optical micrographs of (a) '10CBI-13' composite, (b) '10CBI-11' composite, and (c) 10CBI-31 composite at a magnification of 200X.

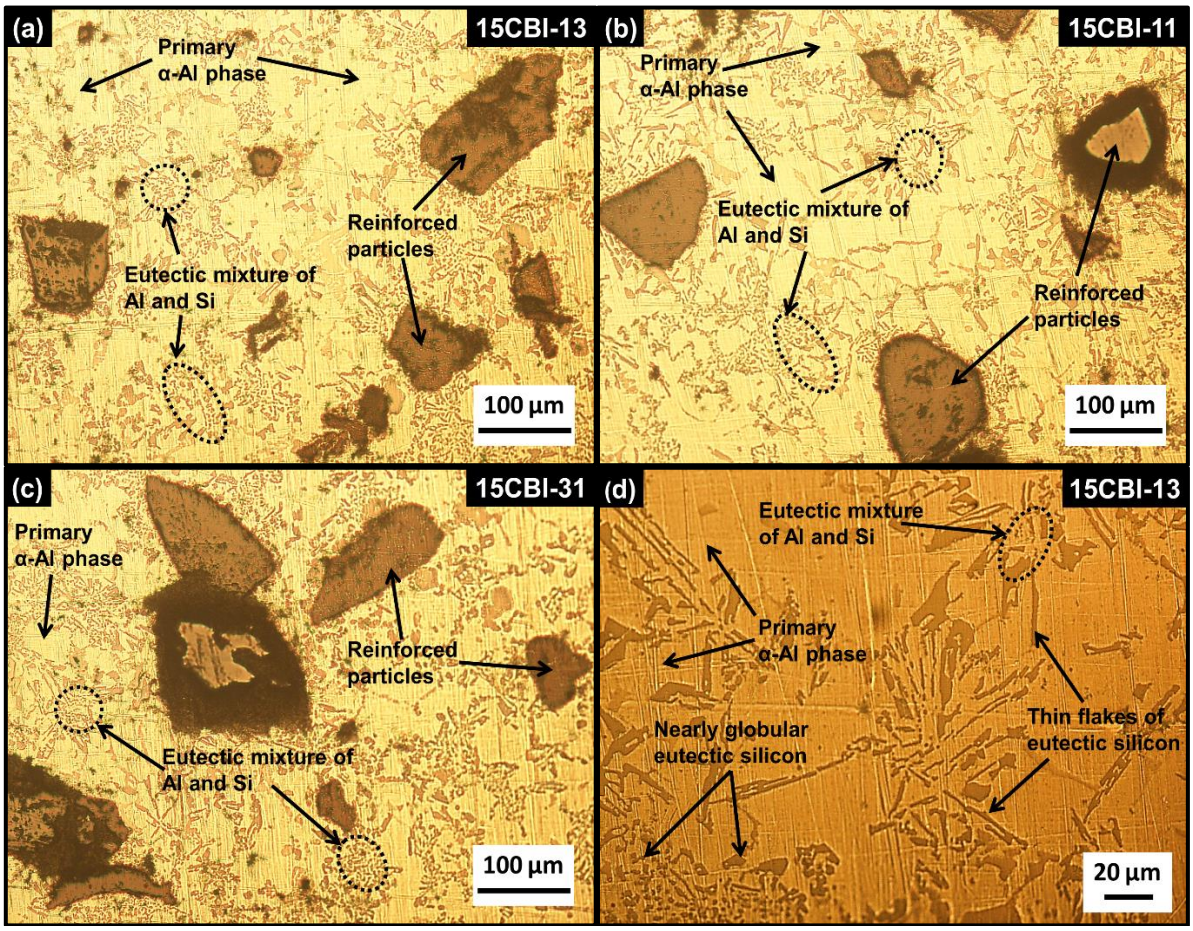

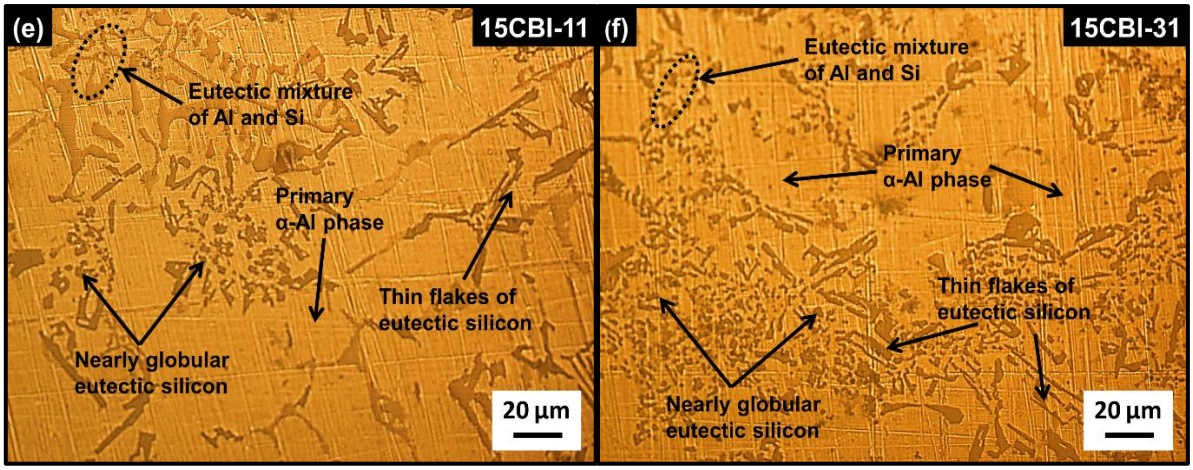

Figure 5.5 Optical micrographs of (a) '15CBI-13' composite, (b) '15CBI-11' composite, and (c) '15CBI-31' composite at a magnification of 200X and optical micrographs showing silicon morphology in (d) '15CBI-13' composite, (e) '15CBI-11' composite, and (f) '15CBI-31' composite at a magnification of 500X.

Figure 5.3a–c, Figure 5.4a–c, and Figure 5.5a–c show the optical micrographs (at 200X) of dual particle reinforced AMCs containing 'coarse' particles with various mixing proportions (i.e. 1:3, 1:1, and 3:1 of the two types of particles) at reinforcement levels of 5 wt.%, 10 wt.% and 15 wt.% respectively. Figure 5.5d–f shows the optical micrographs (at 500X) of AMCs containing 'coarse' particles at maximum reinforcement level and different mixing proportions ('15CBI' composites). The dispersion of reinforced particles in the matrix was observed to be nearly uniform. Reinforced particles led to refinement of eutectic silicon and primary aluminium of the matrix. Increase in reinforcement level at a particular mixing proportion showed further refinement of microstructure. At a particular reinforcement level, the composite with higher concentration of boron carbide particle (i.e. 'CBI-31' composites) showed maximum refinement in microstructure (Figure 5.5d–f). Besides refinement of microstructure, a change in morphology of eutectic silicon was also observed. The acicular shape of eutectic silicon (observed in base alloy) changed to globular (in AMCs) i.e. the aspect ratio of eutectic silicon decreased. Globular morphology of eutectic silicon was mainly observed for '15CBI-31' composite. Further, this globular eutectic silicon was observed in the vicinity of reinforced particles. Figure 5.6 presents the SEM-EDS of AMC containing 'coarse' particles with maximum reinforcement level and maximum proportion of boron carbide (i.e. '15CBI-31' composite) for a clear identification of both types of reinforcements (ilmenite and boron carbide) present in the matrix material.

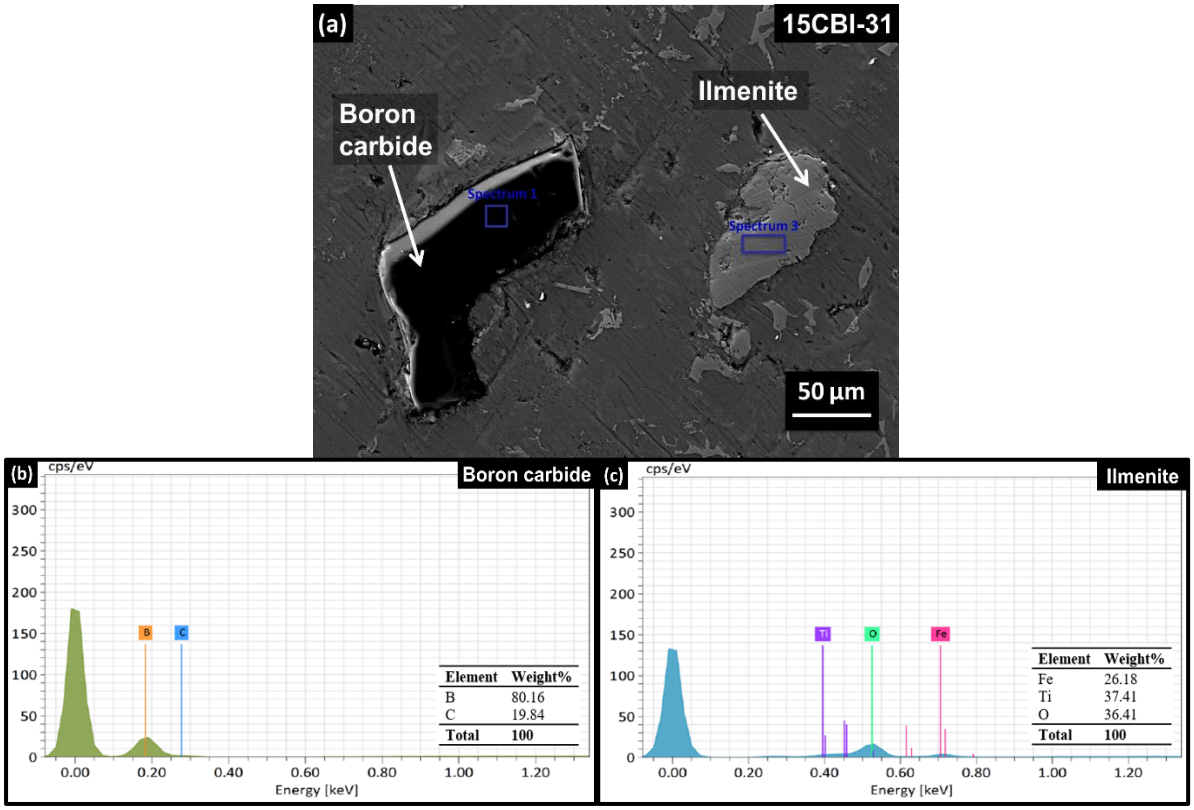

Figure 5.6 SEM image of '15CBI-31' composite with EDS of different reinforcements added to the base alloy.

The changes observed in microstructure of dual particle reinforced AMCs were attributed to the presence of two different types of reinforcements of boron carbide and ilmenite. The thermal conductivity and density of reinforced particles were mainly responsible for changes observed in the microstructure of AMCs [18,57,190]. The lower thermal conductivity of particles (Table 3.2) led to lower heat dissipation during the solidification process [80]. Due to this low dissipation of heat, particles acted as a heat sink. The presence of heat sink particles in the molten mass resulted in development of high temperature zones around the reinforced particles. These high-temperature zones were responsible for initiation of solidification of primary aluminium away from the reinforced particles. The solidification of primary aluminium led to enrichment of eutectic silicon around the reinforced particles, which solidified as the temperature dropped to eutectic point [18,57]. Due to this, eutectic silicon was found to be present in the vicinity of reinforced particles (Figures 5.3−5.5). Also, density of particles played a significant role in refinement of microstructure of AMCs. Lower is the density of reinforced particles, higher are the number of particles for a particular weight percentage, and hence lesser is the inter-particle distance in the matrix. With decrease in the inter-particle distance, the restriction to growth of grains increased which refined the

microstructure. Since the density of reinforced particles was low, their reinforcement into the matrix refined the microstructure.

Further, increase in the reinforcement level of particles also refined the microstructure. This phenomenon was attributed to the increase in high temperature zones created by reinforced particles (because of their low thermal conductivity). Due to the creation of high temperature zones, the directions available for growth of nuclei got restricted which resulted in refinement of microstructure of AMCs [190]. Similarly, a change in morphology of eutectic silicon from acicular shape to globular shape/or reduction in aspect ratio of eutectic silicon was observed. The highest refinement in microstructure and globular type eutectic silicon was observed mainly in '15CBI-31' composite. This was attributed to the combined effect of boron carbide and ilmenite particles reinforcements. The low thermal conductivity of ilmenite particles created high temperature zones in the molten mass whereas the low density of boron carbide particles helped in decreasing the inter-particle distance. Hence, the lower inter-particle distance and high temperature zones in '15CBI-31' composite resulted in maximum refinement of microstructure. In '15CBI-13' composite containing ilmenite in more proportion than boron carbide (weight percent of boron carbide to ilmenite particles in the weight ratio 1:3), particles required for pinning effect were lower (because of relatively higher density and higher mixing proportion of ilmenite particles), and hence refinement of microstructure was less as compared to '15CBI-31' composite.

5.2.2 Dual particle reinforced composites containing fine particles

Figure 5.7–5.9 present the optical micrographs of dual particle reinforced AMCs containing 'fine' particles with various mixing proportions and reinforcement levels (i.e. 'FBI' composites).

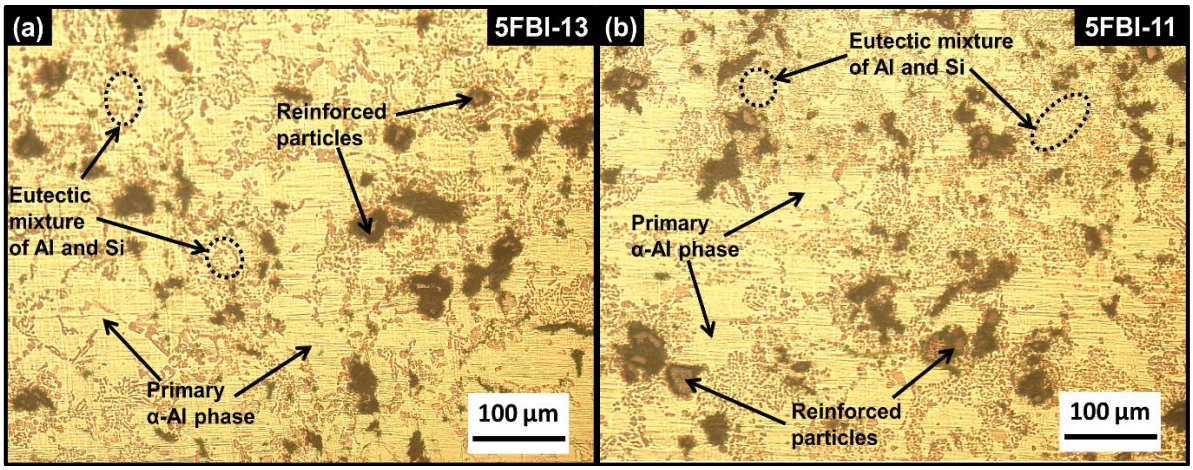

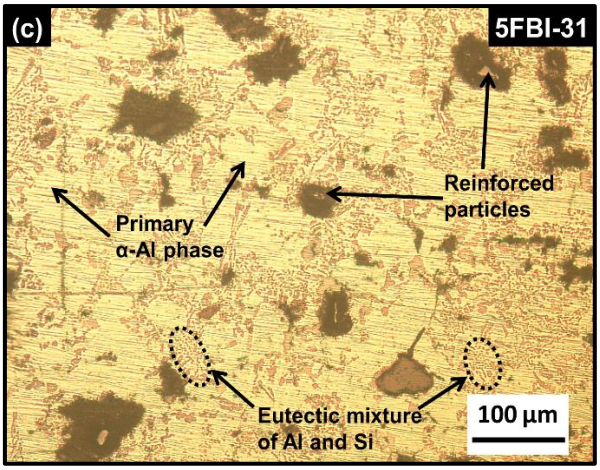

Figure 5.7 Optical micrographs of (a) '5FBI-13' composite, (b) '5FBI-11' composite, and (c) '5FBI-31' composite at 200X.

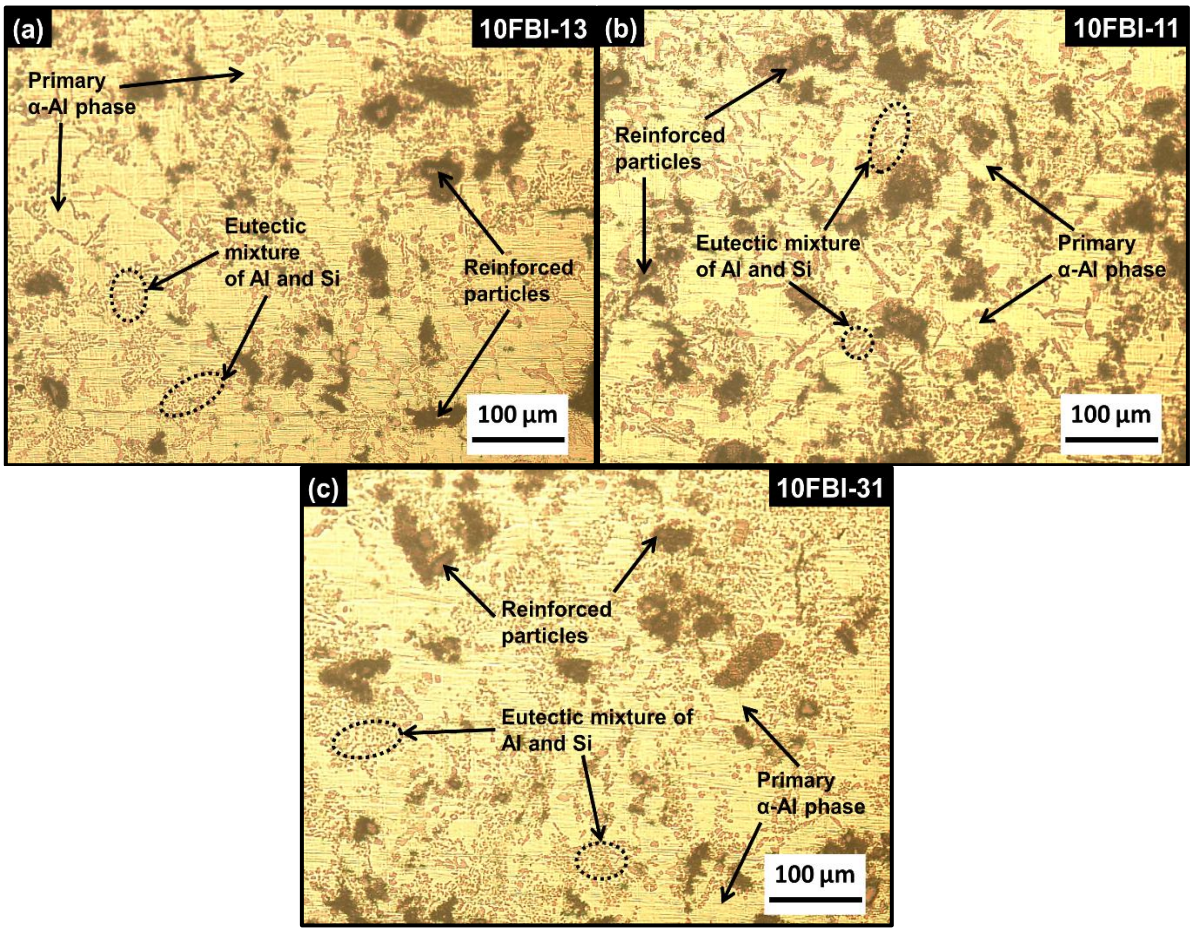

Figure 5.8 Optical micrographs of (a) '10FBI-13' composite, (b) '10FBI-11' composite, and (c) '10FBI-31' composite at 200X.

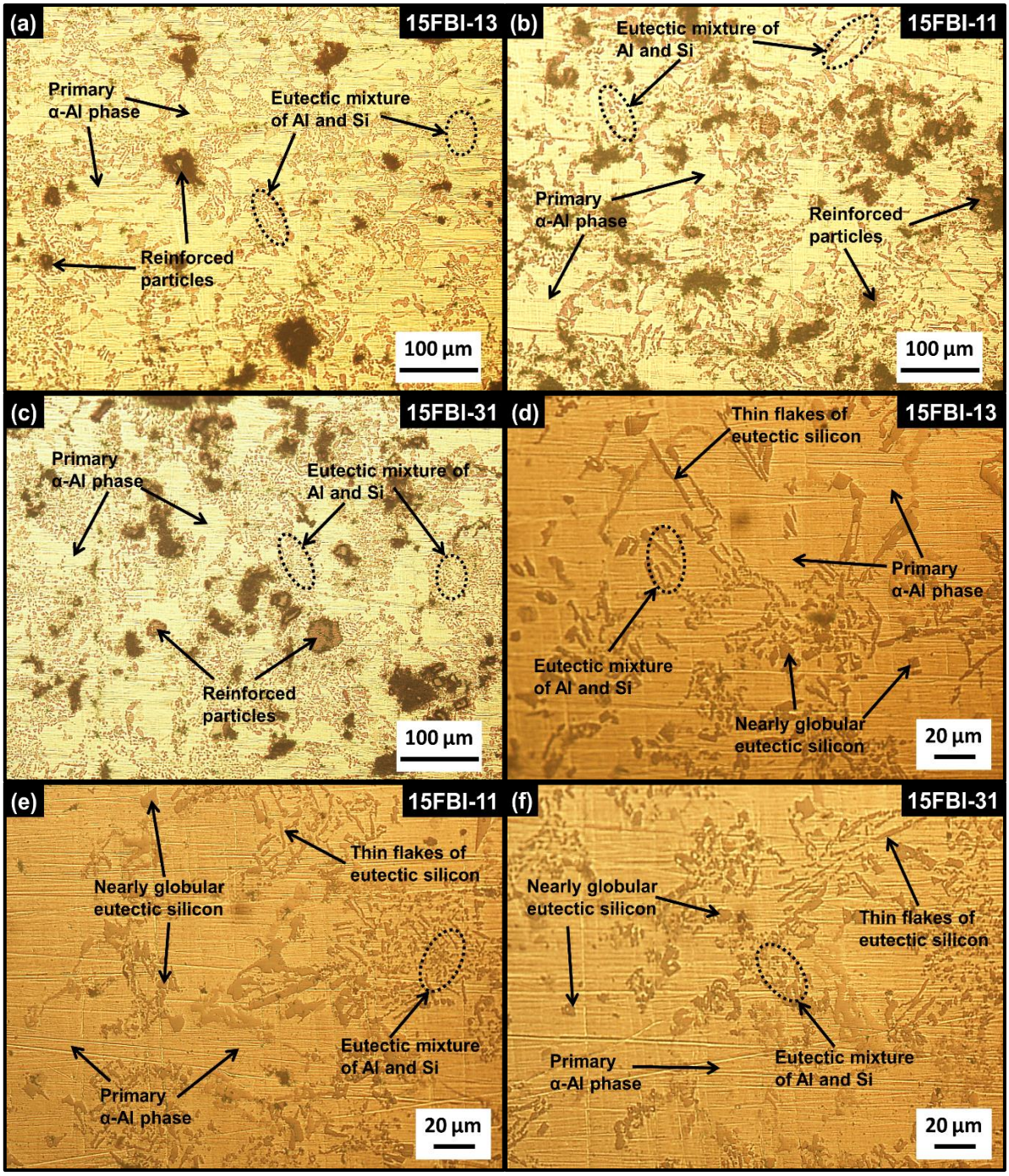

Figure 5.9 Optical micrographs of (a) '15FBI-13' composite, (b) '15FBI-11' composite, and (c) '15FBI-31' composite at 200X and optical micrographs showing silicon morphology of (d) '15FBI-13' composite, (e) '15FBI-11' composite, and (f) '15FBI-31' composite at 500X.

Figure 5.7a–c, Figure 5.8a–c, and Figure 5.9a–c presents the optical micrographs (at 200X) of AMCs containing 'fine' particles with various mixing proportions (of 1:3, 1:1, and 3:1 of the two types of particles) at reinforcement levels of 5 wt.%, 10 wt.%, and 15 wt.% respectively. The magnified optical micrographs (at 500X) of AMCs containing 'fine' particles with maximum reinforcement level and different mixing proportions are shown in Figure 5.9d–f.

Reinforcing the mixture of ceramic particles (boron carbide and ilmenite) in the matrix material (LM13 alloy) led to refinement of grain structure. The average grain size of eutectic silicon for LM13 alloy was observed to be 34.20±12.93 µm (determined using the integrated software in optical microscope). The value of average grain size of eutectic silicon decreased with increase in weight percentage at particular mixing proportion of reinforced particles. Also, the average grain size reduced with increase in proportion of boron carbide particles (in the mixture of boron carbide and ilmenite) at particular reinforcement level. Further, a change in morphology of silicon from acicular to globular was also observed. This behaviour became more prominent with increase in both the factors viz. reinforcement level and proportion of boron carbide particles in the reinforcing mixture. Thus, higher proportion of globular grains and lower average grain size were observed in '15FBI-31' composite as shown in Figure 5.9d–f.

The mixture of particles were found to be uniformly dispersed within the matrix at all the reinforcement levels and mixing proportions (Figure 5.7a–c, Figure 5.8a–c, and Figure 5.9a–c). After solidification, the eutectic mixture of aluminium and silicon was found to be present in the vicinity of both the reinforced particles (Figure 5.9d–f). The reasons for refinement in microstructure, change in morphology to globular and the presence of eutectic mixture in the vicinity of reinforced particles are same as discussed for dual particle reinforced AMCs containing 'coarse' particles ('CBI' composites) in Section 5.2.1.

For the two types of particle size categories, relatively finer grain size of eutectic silicon was obtained for AMC reinforced with 'fine' particles. Further, more change in morphology of eutectic silicon from acicular to globular was also observed for 'FBI' composites.

The grain size distribution of eutectic silicon present in dual particle reinforced AMCs containing 'coarse'/'fine' particle size with maximum reinforcement level and different mixing proportions ('15CBI' and '15FBI' composites) is represented in Figure 5.10.

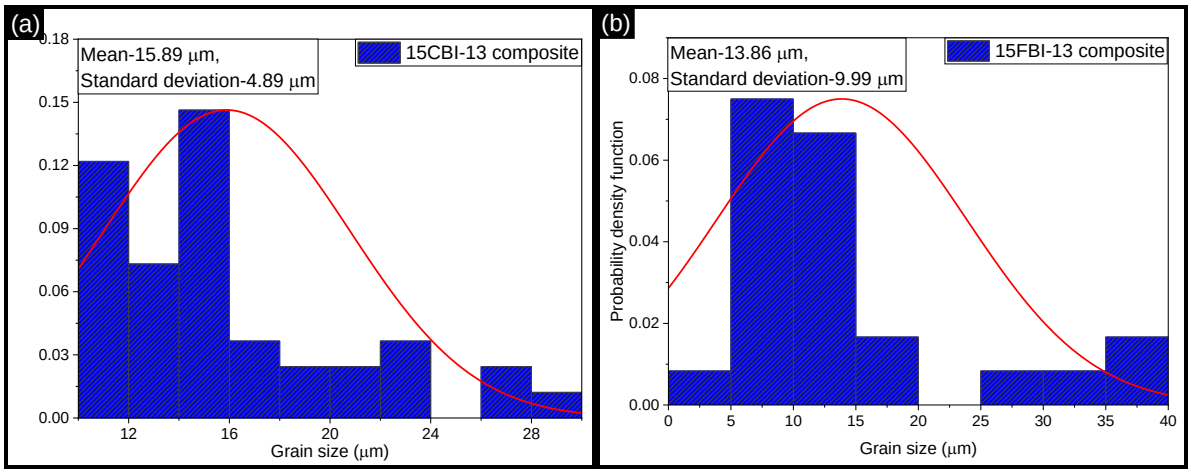

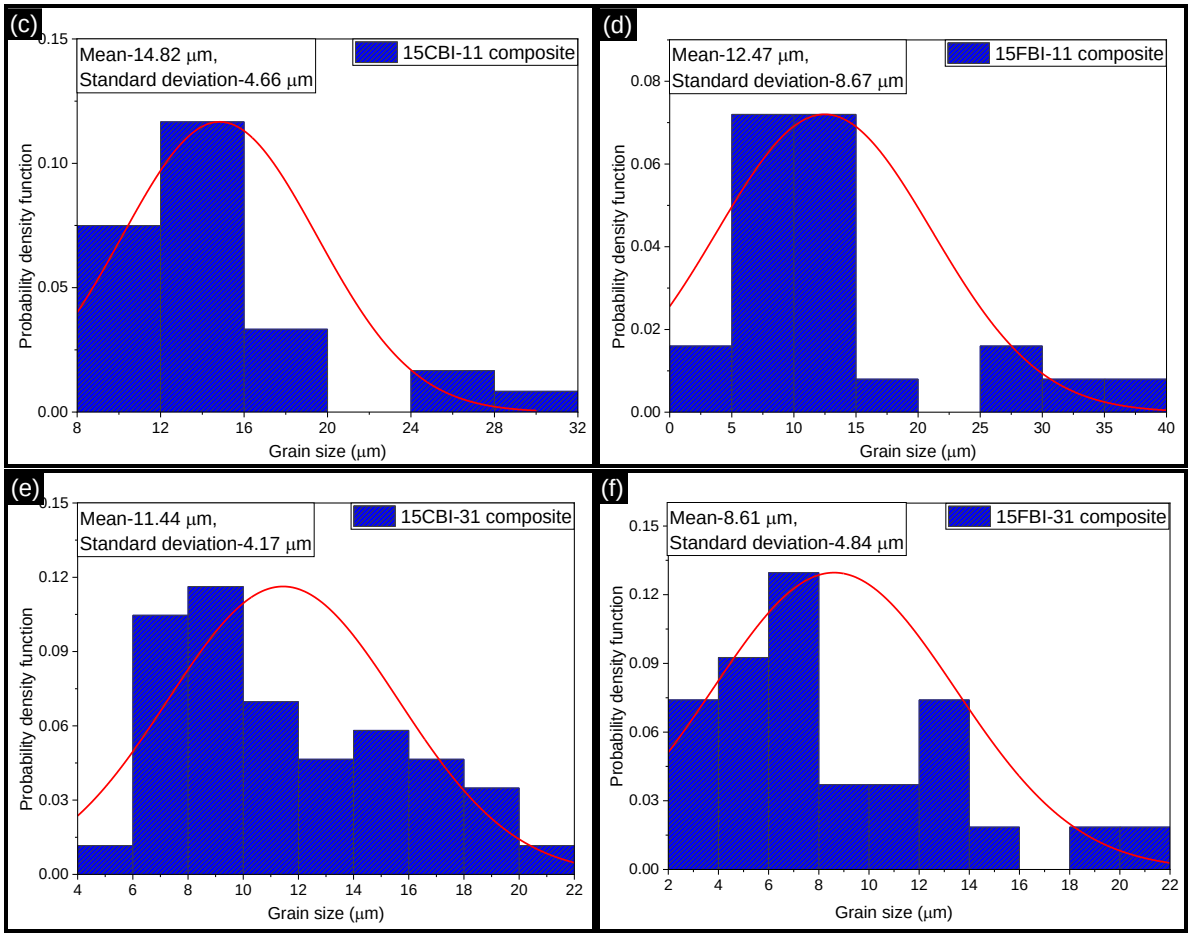

Figure 5.10 Grain size distribution of silicon in (a) '15CBI-13' composite, (b) '15FBI-13' composite, (c) '15CBI-11' composite, (d) '15FBI-11' composite, (e) '15CBI-31' composite, and (e) '15FBI-31' composite.

For a particular particle size and reinforcement level, the increase in proportion of ilmenite particles (in the mixture of ilmenite and boron carbide particles) led to rise in average grain size of eutectic silicon in the hybrid AMCs. However, a reduction in average grain size of eutectic silicon was observed with rise in reinforcement level for a particular particle size and a given mixing proportion. A comparison of dual particle reinforced AMCs ('CBI' and 'FBI' composites) on the basis of particle size revealed that reduction in particle size also led to decrement in average grain size of eutectic silicon for a particular reinforcement level and mixing proportion. The behaviour shown by average grain size of eutectic silicon with respect to particle size, reinforcement level, and mixing proportion was attributed to rise in the number of particles present in the base alloy. This resulted in increase of high temperature zones and also decrease in inter particle distance. The discussion related to the effect of high temperature zones and inter particle distance on average grain size is already done in Section 5.2.1.

5.3. Hardness analysis

5.3.1 Dual particle reinforced composites containing coarse particles

The 'Vickers hardness' and 'penetration depth of nano-indenter vs indenter load' of dual particle reinforced AMCs containing 'coarse' particles with different mixing proportions and reinforcement levels ('CBI' composites) are shown in Figure 5.11a and Figure 5.11b respectively.

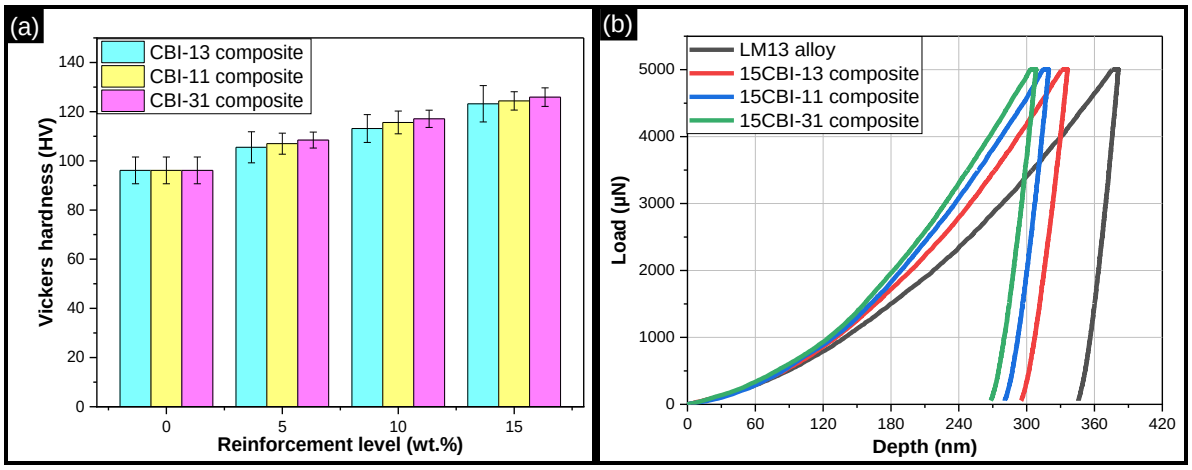

Figure 5.11 (a) Vickers hardness of 'CBI-13', 'CBI-11', and 'CBI-31' composites at different reinforcement levels and (b) load-depth curves obtained from nanohardness test for base alloy, '15CBI-13' composite, '15CBI-11' composite, and '15CBI-31' composite.

With increase in proportion of boron carbide particles in the reinforcement mixture at a particular reinforcement level, Vickers hardness showed an increasing trend and penetration depth of the nano-indenter showed a decreasing trend. The increment in reinforcement weight percentage at a particular mixing proportion also showed the same trends. A combination of both the parameters viz. 'reinforcement level and mixing proportion' resulted in attainment of high hardness and low penetration depth for '15CBI-31' composite. The improvement in hardness of 'CBI' composites was attributed to increase in restriction to the localized deformation of matrix caused by the indenter as shown in Figure 5.11b. This plastic deformation can also be influenced by refinement of microstructure and dislocation density. The increase in refinement of microstructure improved the plastic deformation in accordance to the Hall-Petch effect. However, plastic deformation shows direct correlation with the dislocation density [23,177,191]. Dislocations in composites are generated due to a mismatch in coefficient of thermal expansion (CTE) between matrix and reinforced particles. The density of the generated dislocations (DD) can be measured by using the expression given by Taya and Arsenault (Equation 5.3) [23,191].

$$DD = \frac{a*(\alpha_M - \alpha_H)(T_C - T_R)*V_H}{b*d_H*(1-V_H)} \quad \text{..... (5.3)}$$

Here α_i, T_i, V_i, d_i, a, and b are defined as coefficient of thermal expansion, temperature condition, volume fraction, average diameter of particles, geometric constant, and Burgers vector respectively. '*i'* in the subscript is used to distinguish between matrix (M), reinforcement (H), casting conditions (C: 750 ℃), and room temperature conditions (R: 25 ℃). In case of dual particle reinforced AMCs, the effective CTE of reinforcement was calculated using the 'Rule of Mixtures' and 'Total Volume Fraction' (V_H) was calculated as the sum of volume fractions of individual reinforcements. The values of different parameters and the calculated dislocation density for AMCs containing maximum reinforcement level of 'coarse' particles with various mixing proportions ('15CBI' composites) are given in Table 5.3.

Table 5.3 Different parameters and dislocation density of '15CBI' composites at different mixing proportions [23,80].

S. No.	Samples	a	$(\alpha_M - \alpha_H)$ $(\times 10^{-6}\ K^{-1})$	$(T_C - T_R)$ (K)	V_H $(\times 10^{-6}\ m^3)$	b (nm)	d_H (μm)	DD $(\times\ 10^{16}\ m^{-2})$
1.	**'15CBI-31' composite**	12	13.35	725	0.14	0.32	115.5	52.52
2.	**'15CBI-11' composite**	12	8.49	725	0.13	0.32	115.5	28.98
3.	**'15CBI-13' composite**	12	1.88	725	0.11	0.32	115.5	5.45

At a particular reinforcement level, the increase in proportion of boron carbide particles resulted in generation of higher dislocation density in AMCs. Further, the minimum grain size was obtained for AMCs containing 'coarse' particles with maximum reinforcement level and maximum proportion of boron carbide particles ('15CBI-31' composite) as discussed in Section 5.2.1. Hence, the attainment of lower grain size and higher dislocation density was responsible for highest hardness shown by '15CBI-31' composite.

5.3.2 Dual particle reinforced composites containing fine particles

Figure 5.12a and Figure 5.12b show the variation of 'Vickers hardness' and 'penetration depth of nano-indenter vs indenter load' for AMCs containing 'fine' particles at different reinforcement levels and mixing proportions ('FBI' composites) respectively. The average hardness value of LM13 alloy was found to be 96.11±5.42 HV which increased with rise in weight percentage of reinforced particles for a given mixing proportion. Further, an increasing trend in hardness values was observed with increase in the proportion of boron carbide particles at a particular reinforcement level. The load-depth curves for '15FBI' composites at different

mixing proportions revealed a decrease in penetration depth for rise in proportion of boron carbide particles as shown in Figure 5.12b. At maximum reinforcement level, the highest hardness and lowest penetration depth values were obtained for '15FBI-31' composite, followed by '15FBI-11' composite, and finally '15FBI-13' composite. The reasons responsible for enhancement in hardness values were found to be same as discussed in Section 5.3.1 for 'CBI' composites.

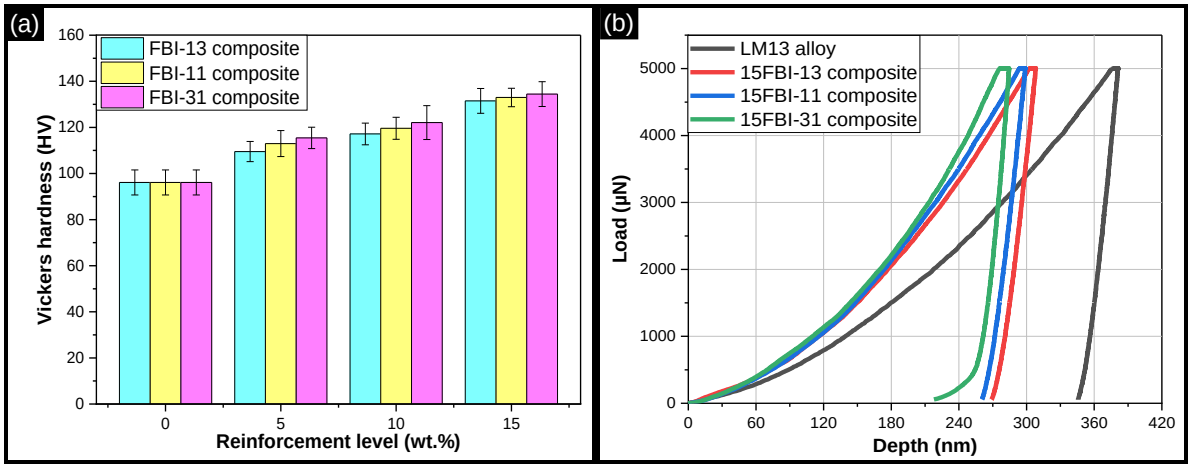

Figure 5.12 (a) Vickers hardness of 'FBI-13', 'FBI-11', and 'FBI-31' composites at different reinforcement levels and (b) load-depth curves obtained from nanohardness test for base alloy, '15FBI-13' composite, '15FBI-11' composite, and '15FBI-31' composite.

Table 5.4 presents the values of different parameters and also the calculated dislocation density for dual particle reinforced AMCs containing maximum reinforcement level of 'fine' particles with different mixing proportions ('15FBI' composite).

Table 5.4 Different parameters and dislocation density of '15FBI' composites at different mixing proportions [23,80].

S. No.	Samples	a	$(\alpha_M - \alpha_H)$ $(\times 10^{-6}\ K^{-1})$	$(T_C - T_R)$ (K)	V_H $(\times 10^{-6}\ m^3)$	b (nm)	d_H (μm)	DD $(\times\ 10^{16}\ m^{-2})$
1.	**'15FBI-31' composite**	12	13.35	725	0.14	0.32	115.5	233.3
2.	**'15FBI-11' composite**	12	8.49	725	0.13	0.32	115.5	128.7
3.	**'15FBI-13' composite**	12	1.88	725	0.11	0.32	115.5	24.2

It can be concluded from Table 5.4 that for a given reinforcement level, increase in the proportion of boron carbide led to rise in dislocation density. Similar trends were observed with increase in volume fraction of reinforced particles as given in Table 5.4. Further, it was discussed in Section 5.2.2 that lowest grain size was obtained on addition of maximum reinforcement level and maximum proportion of boron carbide of 'fine' particles in LM13 alloy

('15FBI-31' composite). Hence, the attainment of lowest grain size and highest dislocation density for '15FBI-31' composite resulted in attainment of highest hardness value.

The comparison of 'FBI' composites and 'CBI' composites for a given reinforcement level and mixing proportion revealed increment in hardness values for change in particle size from 'coarse' to 'fine'. This trend was ascribed to an increase in resistance to plastic deformation by refinement of grain structure of base alloy and increase in the dislocation density as discussed in Section 5.3.1. For a given reinforcement level and mixing proportion, the AMCs having 'fine' particle reinforcement mixture resulted in lower grain size and higher dislocation density in comparison to AMCs containing 'coarse' particle reinforcement mixture. Hence, the hardness observed for 'FBI' composites was higher than 'CBI' composites.

5.4. Coefficient of thermal expansion (CTE)

5.4.1 Dual particle reinforced composites containing coarse particles

Figure 5.13 presents the 'thermal strain versus operating temperature' and 'CTE versus operating temperature' graphs for various AMCs containing 'coarse' particles with different reinforcement levels and mixing proportions for 'CBI' composites. CTE and thermal strain values were calculated over a temperature range of 50–300 ℃. For different reinforcement levels and mixing proportions, the CTE and thermal strain of AMCs showed lower value in comparison of LM13 base alloy. Further, the rise in proportion of boron carbide in the reinforcement mixture led to reduction in CTE and thermal strain values for a given reinforcement level. Similar reduction in CTE and thermal strain values was obtained when reinforcement level was increased for a particular mixing proportion. Considering all the parameters, lowest CTE and thermal strain values were obtained for '15CBI-31' composite over the entire range of temperature i.e. 50 to 300 ℃ which were 43.71% and 41.20% lower than the base alloy respectively. This reduction in CTE value was attributed to the synergetic effect of two different reinforcements (i.e. boron carbide and ilmenite). The lower CTE value of boron carbide particles led to higher mismatch in thermal properties of matrix-reinforcement and caused restriction to expansion of base alloy as given in Table 3.2 [192]. In addition to this, the strength of interfacial bonding also played a significant role in reducing the CTE of base alloy. The attainment of strong interfacial bonding by ilmenite particles (as discussed in Section 5.1.1) also led to reduction in CTE values of 'CBI' composites.

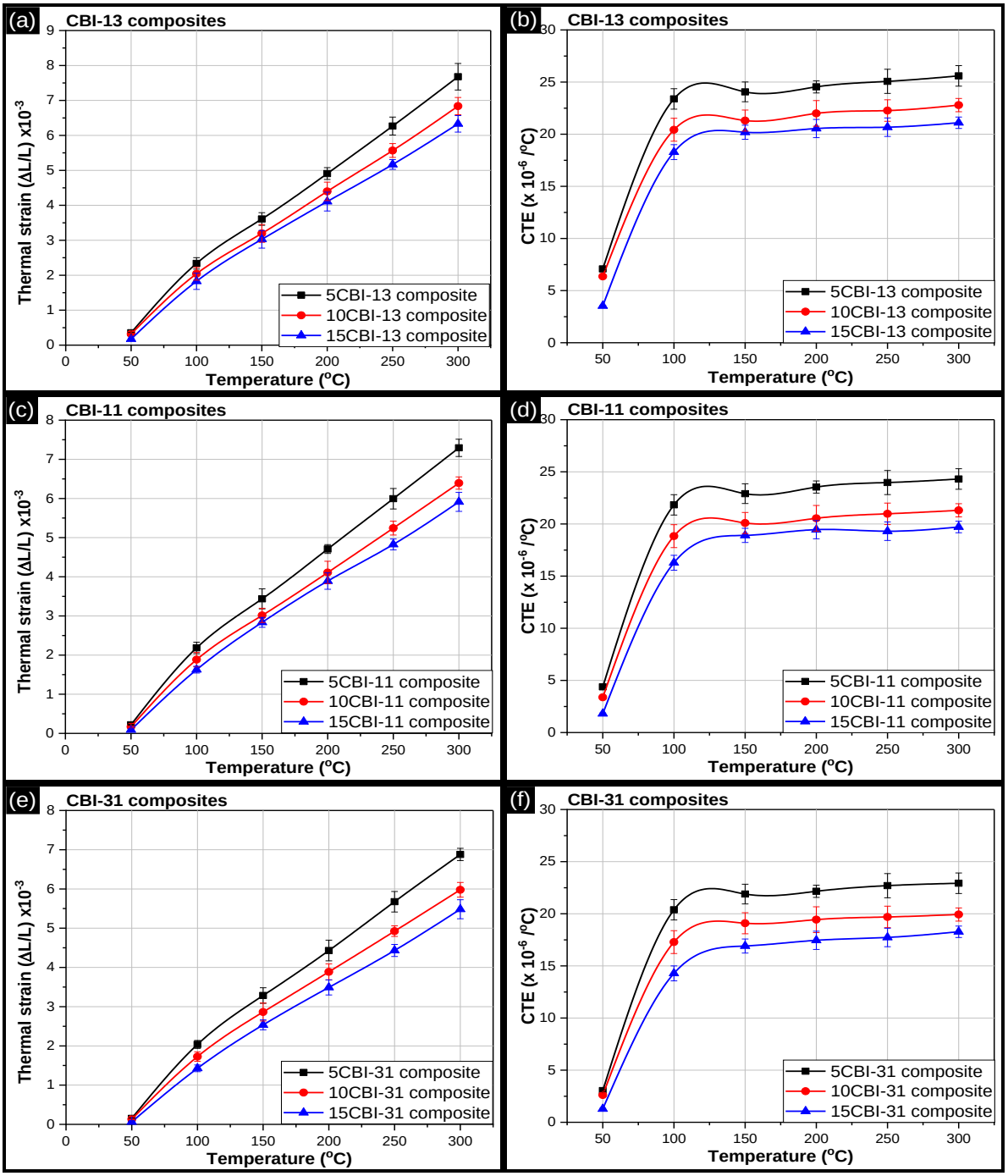

Figure 5.13 Variation in thermal strain and CTE values as a function of operating temperature for (a & b) 'CBI-13' composites, (c & d) 'CBI-11' composites, and (e & f) 'CBI-31' composites.

For thermal strain, all the samples showed a continuous rise in values with change in temperature from 50 to 300 ℃ as shown in Figure 5.13a, Figure 5.13c, and Figure 5.13e. However, in case of CTE, the trend can be categorized into two regions: (i) first region shows a sharp rise in CTE value over the temperature range of 50 to 100 ℃ and (ii) second region presents a steady rise in CTE values over the temperature range of 100 to 300 ℃ as shown in Figure 5.13b, Figure 5.13d, and Figure 5.13f. The behaviour of CTE and thermal strain shown

by ‘CBI’ composites was similar to ’CIR’ composites. In case of ‘CIR’ composites, ilmenite particles were responsible for suppressing of solubility of silicon in aluminium at high temperature conditions. The occurrence of interfacial reaction between ilmenite and silicon signified greater affinity of reinforced particles to silicon as discussed in Section 5.1.1. Hence, at high temperature conditions, the solubility of silicon was restricted by ilmenite particles in ‘CBI’ composites which resulted in steady rise of CTE over the temperature range of 100 to 300 ℃.

5.4.2 Dual particle reinforced composites containing fine particles

Figure 5.14 presents ‘thermal strain versus operating temperature’ and ‘CTE versus operating temperature’ graphs for various AMCs containing ‘fine’ particles with different reinforcement levels and mixing proportions for ‘FBI’ composites.

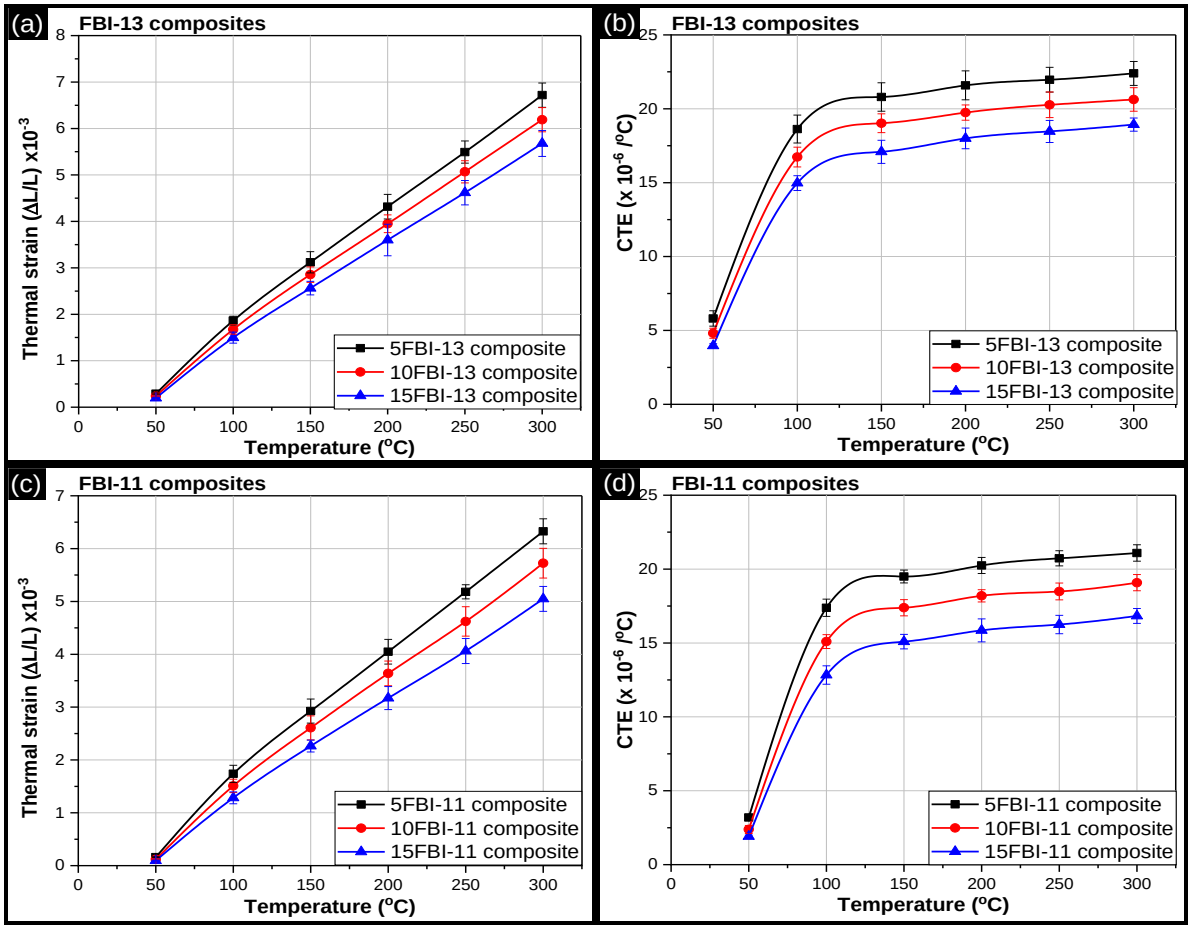

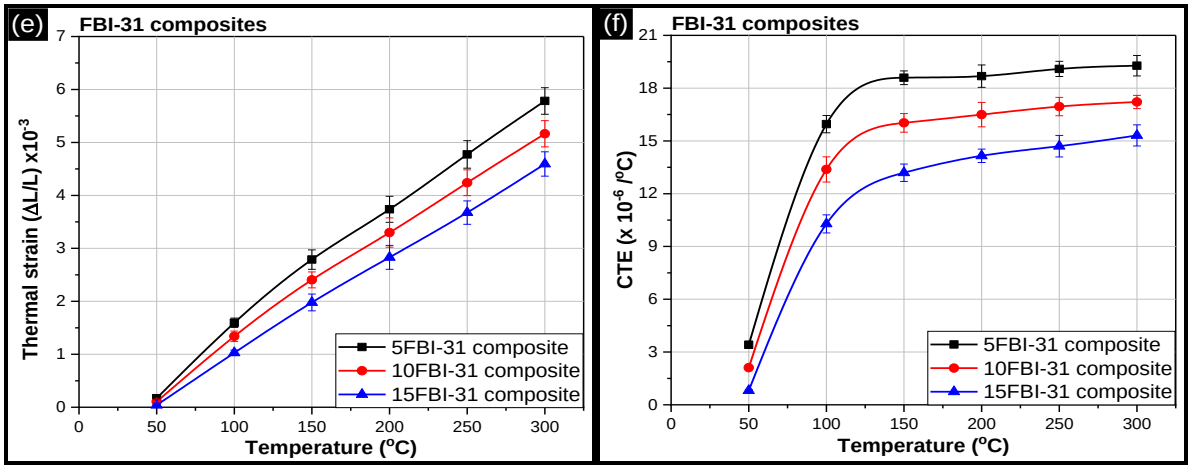

Figure 5.14 Variation in thermal strain and CTE values as a function of operating temperature for (a & b) 'FBI-13' composites, (c & d) 'FBI-11' composites, and (e & f) 'FBI-31' composites.

The addition of reinforced particles in LM13 alloy resulted in reduction of CTE and thermal strain values for all the combination of reinforcement levels and mixing proportions. For a given reinforcement level, the increase in proportion of boron carbide particles in the reinforcement mixture resulted in decrement of CTE and thermal strain values. For a particular mixing proportions, increase in reinforcement level led to decrement in CTE and thermal strain values. For any composition-operating temperature combination, 'FBI' composites showed lower value of CTE compared to base alloy. In comparison to base alloy, '15FBI-31' composite showed maximum reduction in CTE value (55.18% lower than base alloy) which was followed by '15FBI-11' composite (48.42%) and '15FBI-13' composite (40.13%). With increase in operating temperature, all samples (i.e. 'FBI' composites) showed sharp increase in CTE values till 100 ℃. However, beyond 100 ℃, a steady rise in CTE values was observed. The reasons stated for trends and improvement in CTE of 'CBI' composites are valid for 'FBI' composites also.

A comparison of CTE values of 'CBI' composites and 'FBI' composites for any given composition revealed that reduction in particle size led to decrement in CTE values of resulting AMCs. This was attributed to increase in resistance to expansion of base alloy provided by the reinforced particles across the interfacial area. With reduction in particle size, the increase in interfacial area resulted in rise of restriction to expansion which corresponded to the reduction in CTE of 'FBI' composites. CTE of AMCs also depends upon the geometrically necessary dislocations (GND). In AMCs, the dislocations can be stored in two ways: (i) by allowing the dislocations to entangle with each other and (ii) by deforming the material in a constrained surrounding. The mismatch in CTE of base alloy and reinforced particles led to deformation of matrix material in the interfacial region. This led to generation of geometrically necessary

dislocations in the base alloy [193,194]. With reduction in particles size, the deformed area of base alloy also increases which corresponds to increase in GND. This signified the increase in flow stress of base alloy which shows a direct relationship with GND. The increase in flow stress attributes to reduction in expansion of base alloy with rise in temperature [193]. Hence, 'FBI' composites containing 'fine' particles showed lower CTE value in comparison to 'CBI' composites containing 'coarse' particles.

5.5. Wear rate behaviour under room temperature conditions

5.5.1 Dual particle reinforced composites containing coarse particles

Figure 5.15, Figure 5.16, and Figure 5.17 show the wear rate behaviour (under room temperature conditions) for various AMCs containing 'coarse' particles ('CBI' composites) as a function of sliding distance for different reinforcement levels and mixing proportions under different applied loads. With increase in applied load (from 9.8 N to 49.0 N), the pressure acting between the sliding pin and steel disc increases. This causes more plastic deformation of asperity-to-asperity junction made between the two sliding surfaces, and hence, higher wear. Besides plastic deformation, frictional force also increases with increase in applied load, which increases the frictional heating. This frictional heating led to rise in surface temperature for both the counter surfaces. With rise in surface temperature, sliding material tends to soften, which accelerates the wear rate with increase in applied load [195,196].

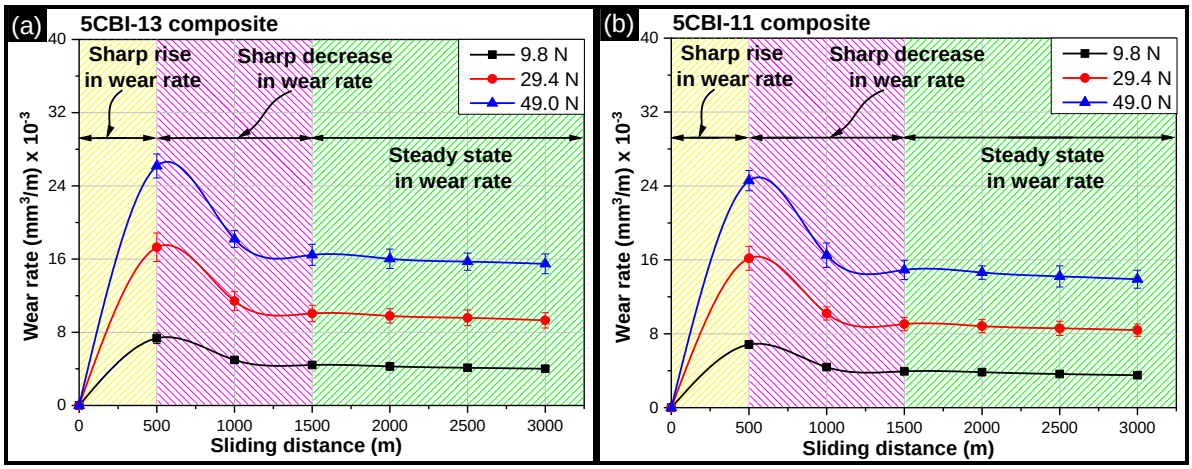

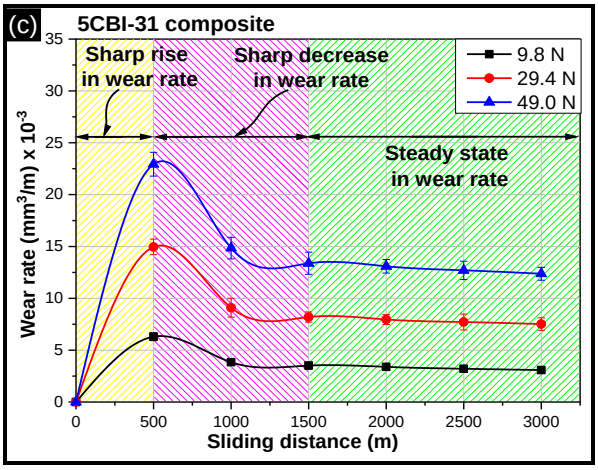

Figure 5.15 Wear rate as a function of sliding distance under various loads for (a) '5CBI-13' composite, (b) '5CBI-11' composite, and (c) '5CBI-31' composite.

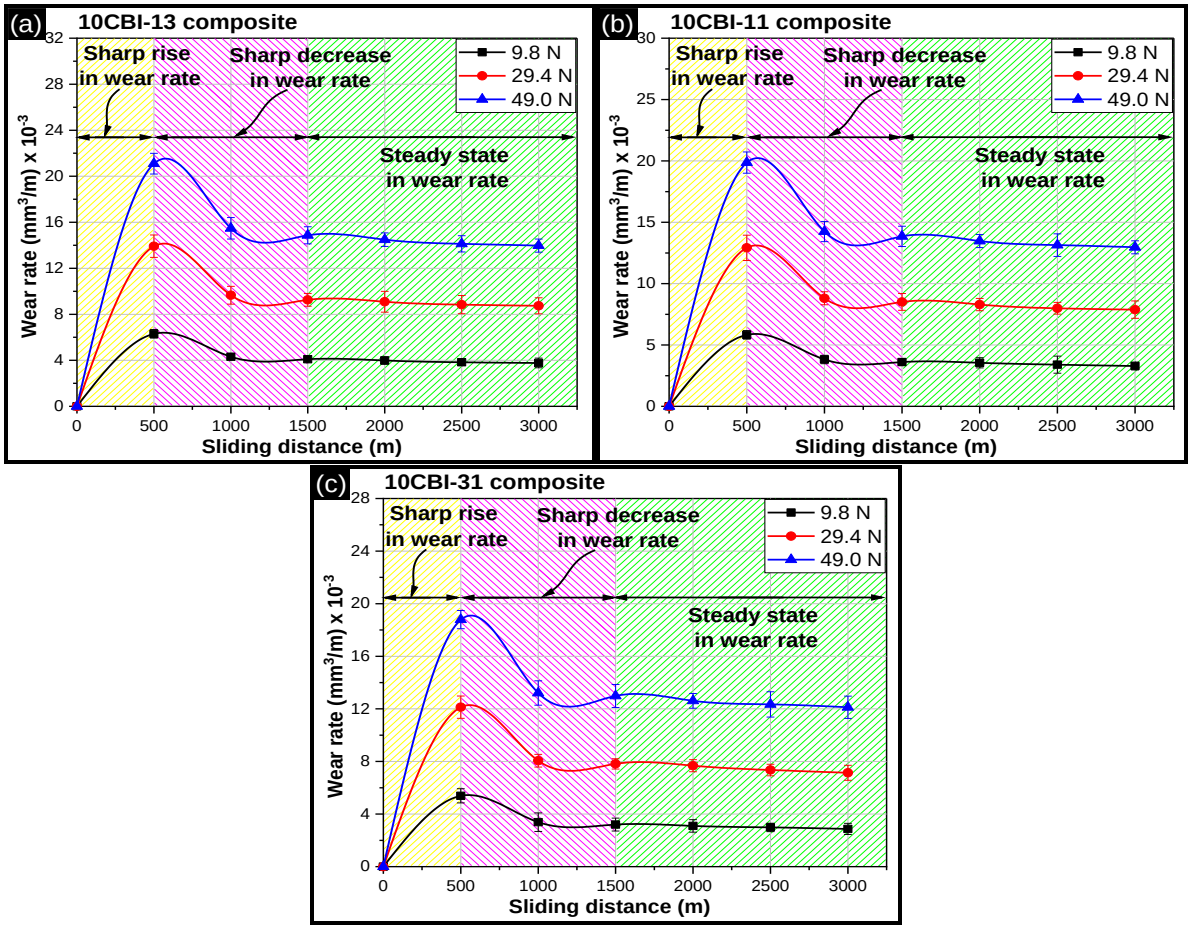

Figure 5.16 Wear rate as a function of sliding distance under various loads for (a) '10CBI-13' composite, (b) '10CBI-11' composite, and (c) '10CBI-31' composite.

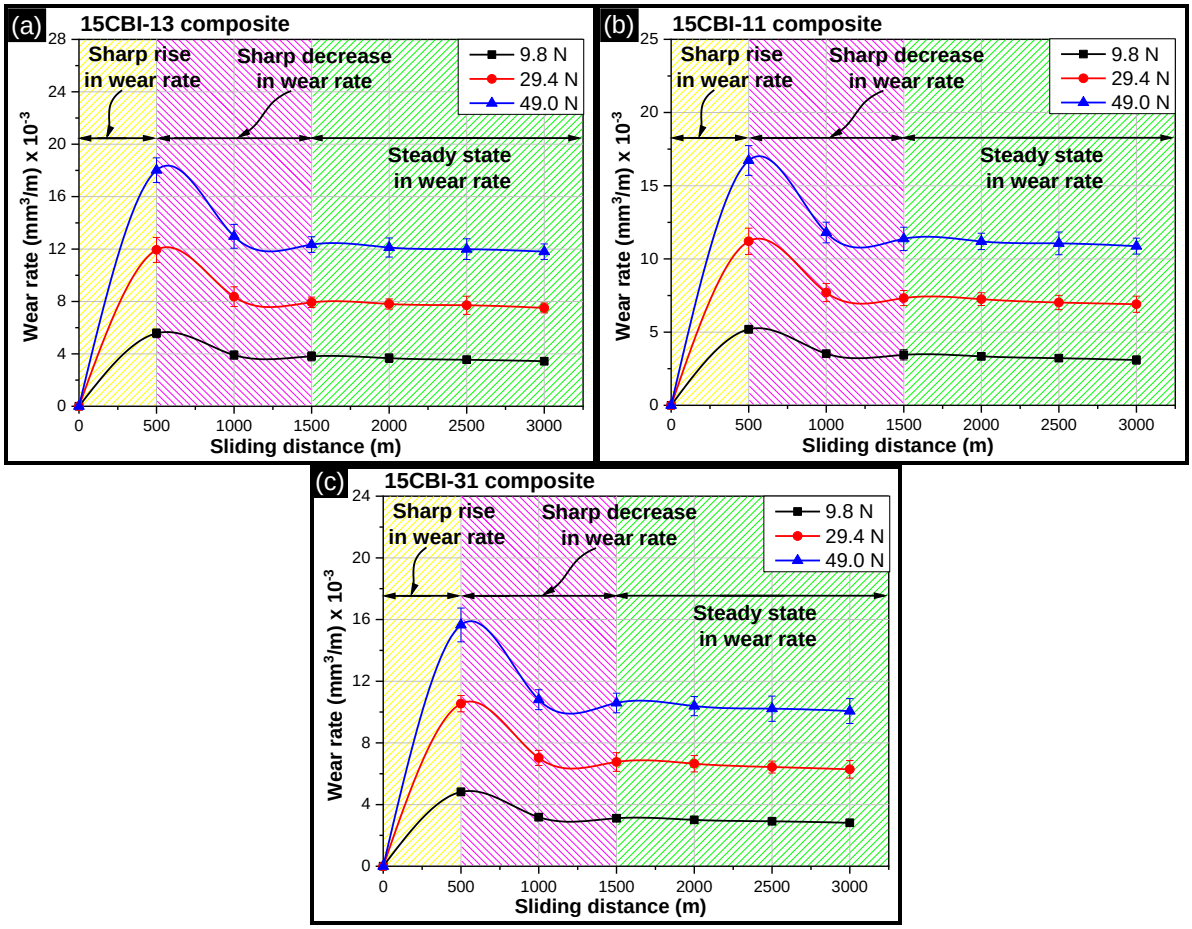

Figure 5.17 Wear rate as a function of sliding distance under various loads for (a) '15CBI-13' composite, (b) '15CBI-11' composite, and (c) '15CBI-31' composite.

In the context of sliding distance, wear rate showed a sudden rise, followed by a sudden drop, and finally a steady state. The sudden rise in wear rate (sliding distance: 0–500 m) was ascribed to the plastic deformation of asperity-to-asperity junction under the action of applied load. With further increase in sliding distance (500–1500 m), sliding surface got flattened as asperities deformed and fractured asperities filled the valleys between asperities. As a result, pressure acting on the asperities got distributed on the sliding surface, and thus, the wear rate decreased [18,196]. For the sliding distance of 1500–3000 m, the rise in temperature due to applied load led to oxidation of the sliding surfaces. This resulted in formation of mechanical mixed layer (MML). In mechanical mixed layer, the entrapped debris of pin and disc material got compacted and deposited on the pin surface [195,196]. Both, oxidation and formation of MML, prevented metal-to-metal interaction between the pin and disc, which resulted in reduction and attainment of steady state wear rate for all the samples.

At a particular applied load and sliding distance, increase in reinforcement level caused a decrease in wear rate of 'CBI' composites. Further, at particular reinforcement level and

applied load, increase in proportion of boron carbide particles in the reinforcement mixture resulted in lower wear rate. '15CBI-31' composite showed the lowest wear rate (67.74% lower than the base alloy). Table 5.5 presents the maximum reduction in wear rate at a sliding distance of 500 m of for hybrid composites containing 'coarse' particles with different reinforcement levels and mixing proportions.

Table 5.5 Percentage decrease in wear rate of AMCs containing 'coarse' particles ('CBI' composites) over the base alloy.

Applied load (N)	Percentage decrease in wear rate of 'CBI' composites at different reinforcement levels and mixing proportions (boron carbide: ilmenite) compared to the base alloy (%) for								
	5 wt.%			10 wt.%			15 wt.%		
	1:3	1:1	3:1	1:3	1:1	3:1	1:3	1:1	3:1
9.8	51	54	58	58	61	64	63	65	68
29.4	47	51	54	57	60	63	63	66	68
49.0	43	46	50	54	57	59	61	64	66

For a given reinforcement level and a given mixing proportion in the reinforcement mixture, the improvement in wear rate was ascribed to the synergic effect shown by the combination of ilmenite and boron carbide particles. Ilmenite particles were responsible for formation of strong interfacial bonding (as discussed in Section 5.1) and also resulted in early oxidation of sliding surfaces due to the low thermal conductivity of ilmenite particles. The occurrence of strong interfacial bonding led to effective transfer of load from the matrix to reinforced particles [58,177]. This resulted in minimization of shear stress acting on the matrix material. Further, the lower thermal conductivity of ilmenite reinforced particles restricted the flow of heat generated due to the friction acting between the two sliding surfaces. This increased the surface temperature at a faster rate, which corresponded to early oxidation of sliding surfaces and prevention of exposure of pin surface to the counter steel disc [80]. So, lower shear stress and less exposure to the steel disc reduced the wear rate of composite material due to the reinforced ilmenite particles. On the other hand, boron carbide particles caused an increase in hardness of the 'CBI' composites as discussed in Section 5.3. This increase in hardness provided support to the mechanical mixed layer which protected the matrix material from wear [77,183].

Further, the wear rate behaviour of '15CBI-31' composite as a function of sliding distance was compared with a commercially used brake rotor material at an applied load of 49.0 N and the results are shown in Figure 5.18. Wear rate of the two materials was comparable with '15CBI-31' composite showing 17% higher wear rate (maximum) than the brake rotor material.

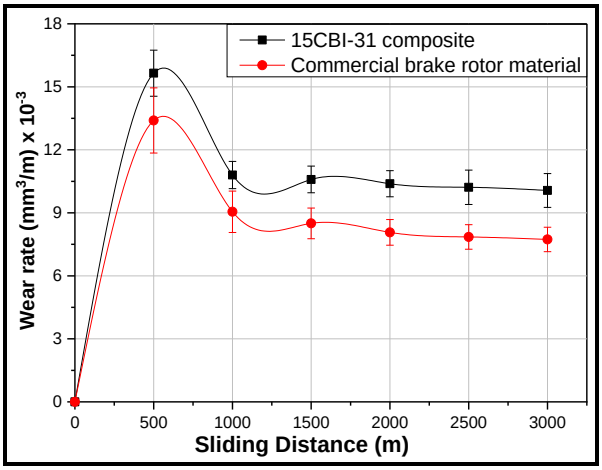

Figure 5.18 Comparison of wear rate behaviour of '15CBI-31' composite and the commercially used brake rotor material.

5.5.2 Dual particle reinforced composites containing fine particles

Figure 5.19, Figure 5.20, and Figure 5.21 show the wear rate behaviour (under room temperature conditions) for various AMCs containing 'fine' particles ('FBI' composites) as a function of sliding distance for different reinforcement levels and mixing proportions under different applied loads. All the samples showed a sharp rise in wear rate for sliding distance of 0–500 m. However, with further rise in sliding distance, a sharp decrease in wear rate was observed till 1500 m, which was followed by attainment of steady state wear rate (for 1500–3000 m). With increase in applied load, wear rate showed an increasing trend for all the samples. At a particular applied load and sliding distance, increase in reinforcement level caused a decrease in wear rate of 'FBI' composites. Further, at a particular reinforcement level and applied load, increase in proportion of boron carbide particles in the reinforcement mixture resulted in lower wear rate.

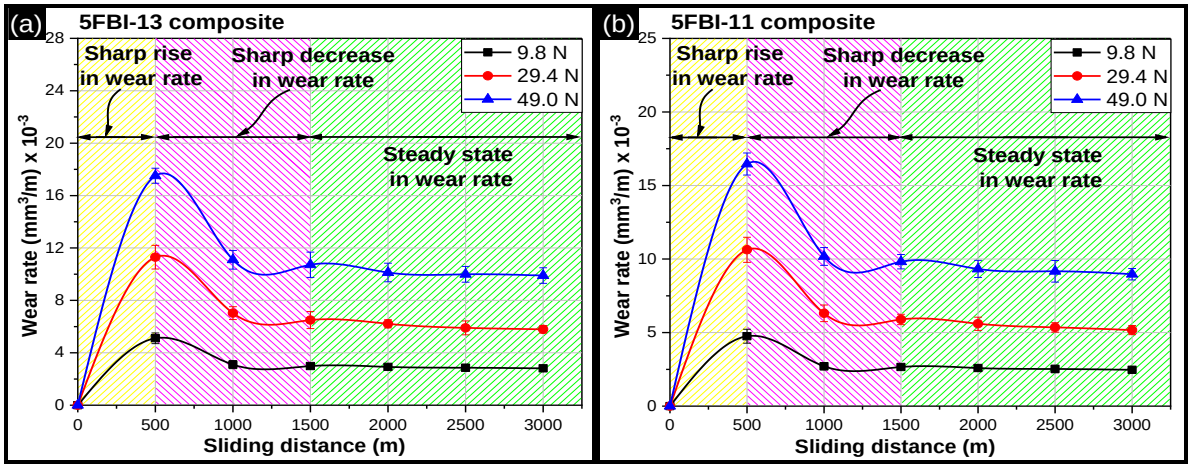

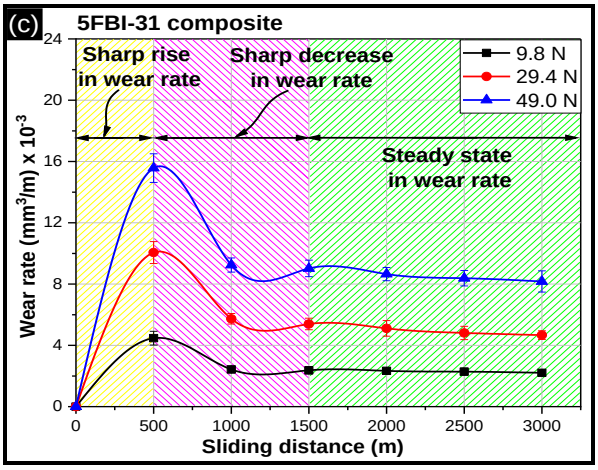

Figure 5.19 Wear rate as a function of sliding distance under various loads for (a) '5FBI-13' composite, (b) '5FBI-11' composite, and (c) '5FBI-31' composite.

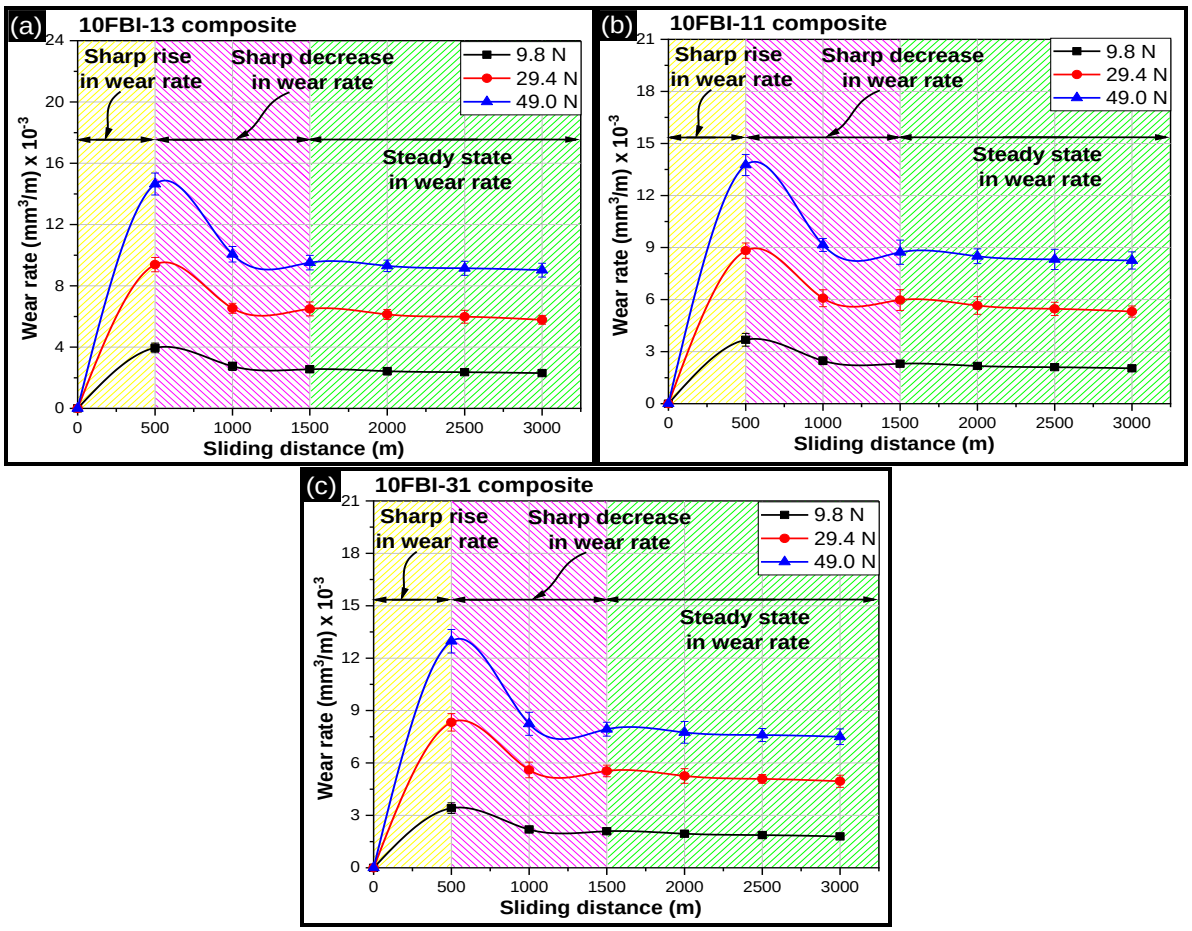

Figure 5.20 Wear rate as a function of sliding distance under various loads for (a) '10FBI-13' composite, (b) '10FBI-11' composite, and (c) '10FBI-31' composite.

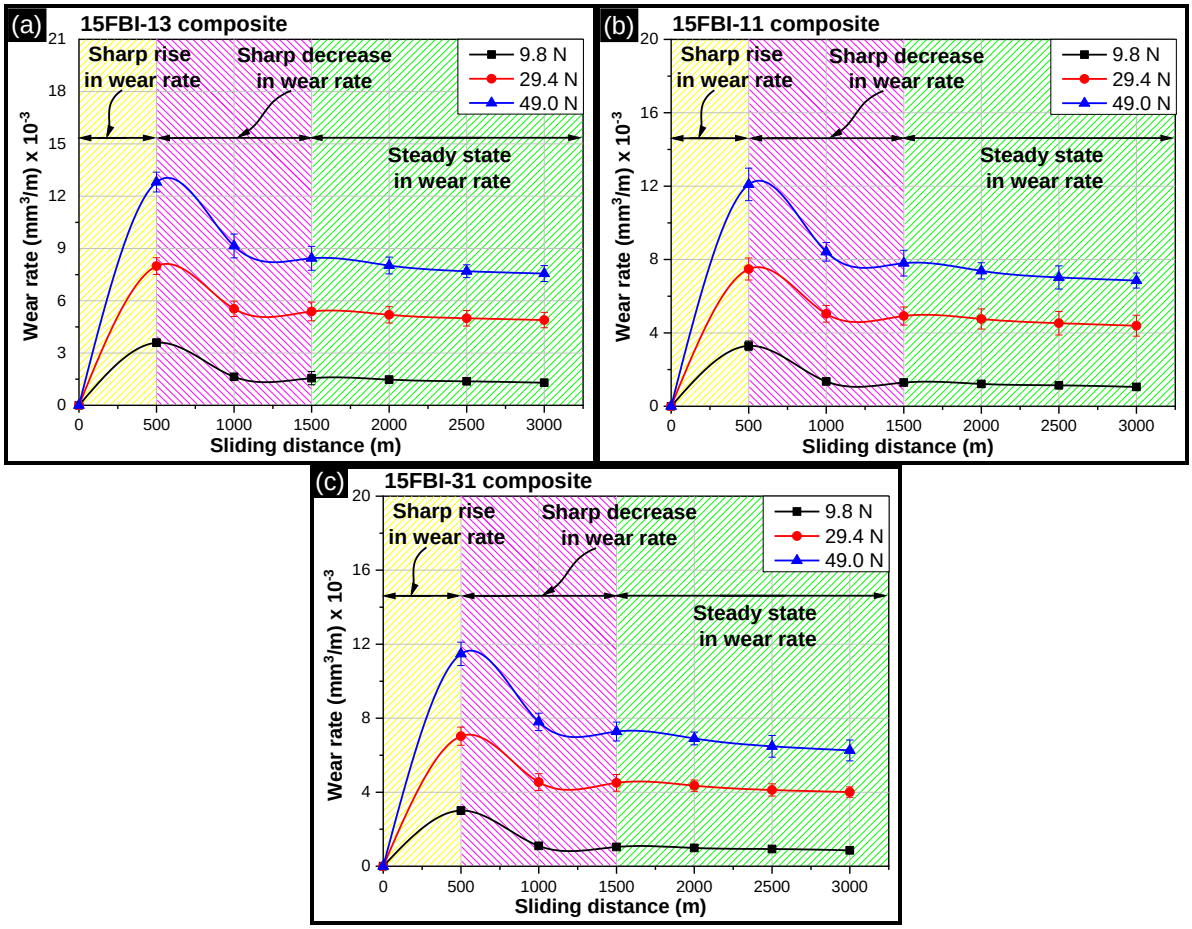

Figure 5.21 Wear rate as a function of sliding distance under various loads for (a) '15FBI-13' composite, (b) '15FBI-11' composite, and (c) '15FBI-31' composite.

'15FBI-31' composite showed the lowest wear rate (80% lower than the base alloy). For other compositions, the improvement in wear rate over a sliding distance of 500 m is given in Table 5.6. The same trend for wear rate was observed when proportion of boron carbide was increased by keeping the reinforcement level at particular value. The explanation of trends for wear rate with respect to sliding distance, applied load, reinforcement level and mixing proportion is already discussed in the Section 5.5.2.

Table 5.6 Percentage decrease in wear rate of AMCs containing 'fine' particles (i.e. 'FBI' composites) over the base alloy.

Applied load (N)	Percentage decrease in wear rate of 'FBI' composites at different reinforcement levels and mixing proportions (boron carbide: ilmenite) compared to the base alloy (%) for								
	5 wt.%			10 wt.%			15 wt.%		
	1:3	1:1	3:1	1:3	1:1	3:1	1:3	1:1	3:1
9.8	66	68	70	74	75	77	76	78	80
29.4	65	67	69	71	73	75	76	77	78
49.0	62	64	66	68	70	72	72	74	75

For a given reinforcement level and a given mixing proportion in the reinforcement mixture, the wear rate of dual particle reinforced AMCs decreased with change in particle size from 'coarse' to 'fine'. This was attributed to attainment of lower CTE value and higher hardness value by 'FBI' composites compared to 'CBI' composites (see Section 5.3 and Section 5.4). The lower CTE of 'FBI' composites signified reduction in thermal softening of sliding surface due to rise in surface temperature by frictional forces. Further, the high hardness of 'FBI' composites resulted in higher stability of MML. Hence, the combination of higher hardness and lower CTE resulted in higher resistance to wear rate for 'FBI' composites when compared to 'CBI' composites.

The comparison of wear rate behaviour as a function of sliding distance of '15FBI-31' composite with commercial brake rotor material at 49.0 N applied load condition is shown in Figure 5.22.

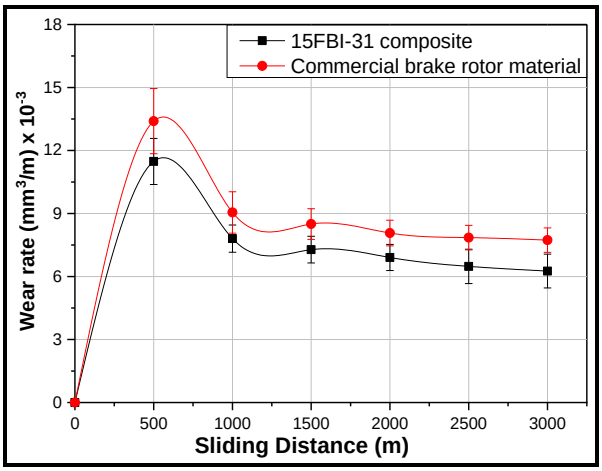

Figure 5.22 Comparison of wear behaviour of '15FBI-31' composite and commercially used brake rotor material.

The wear rate of '15FBI-31' composite was 14% lower than the commercial brake rotor material. Hence, the combination of the low-cost ilmenite particles and the high strength/hardness boron carbide particles can be considered as an effective alternative reinforcement mixture for Al-Si alloy based AMCs to substitute for the commercially used material.

5.6. Coefficient of friction under room temperature conditions

5.6.1 Dual particle reinforced composites containing coarse particles

Figure 5.23 presents the coefficient of friction (COF) values under room temperature conditions for various dual particle reinforced AMCs containing 'coarse' particles ('CBI'

composites) as a function of applied load over the entire sliding distance. For a given composition, COF values showed an increasing trend with rise in applied load. Further, for a given reinforcement level at a given load, a decreasing trend was observed in COF values with rise in proportion of boron carbide particles in the reinforcement mixture. Increase in reinforcement level at a particular mixing proportion also decreased the COF values. Lowest value of COF was obtained for '15CBI-31' composite which was 39.92% lower than the LM13 alloy.

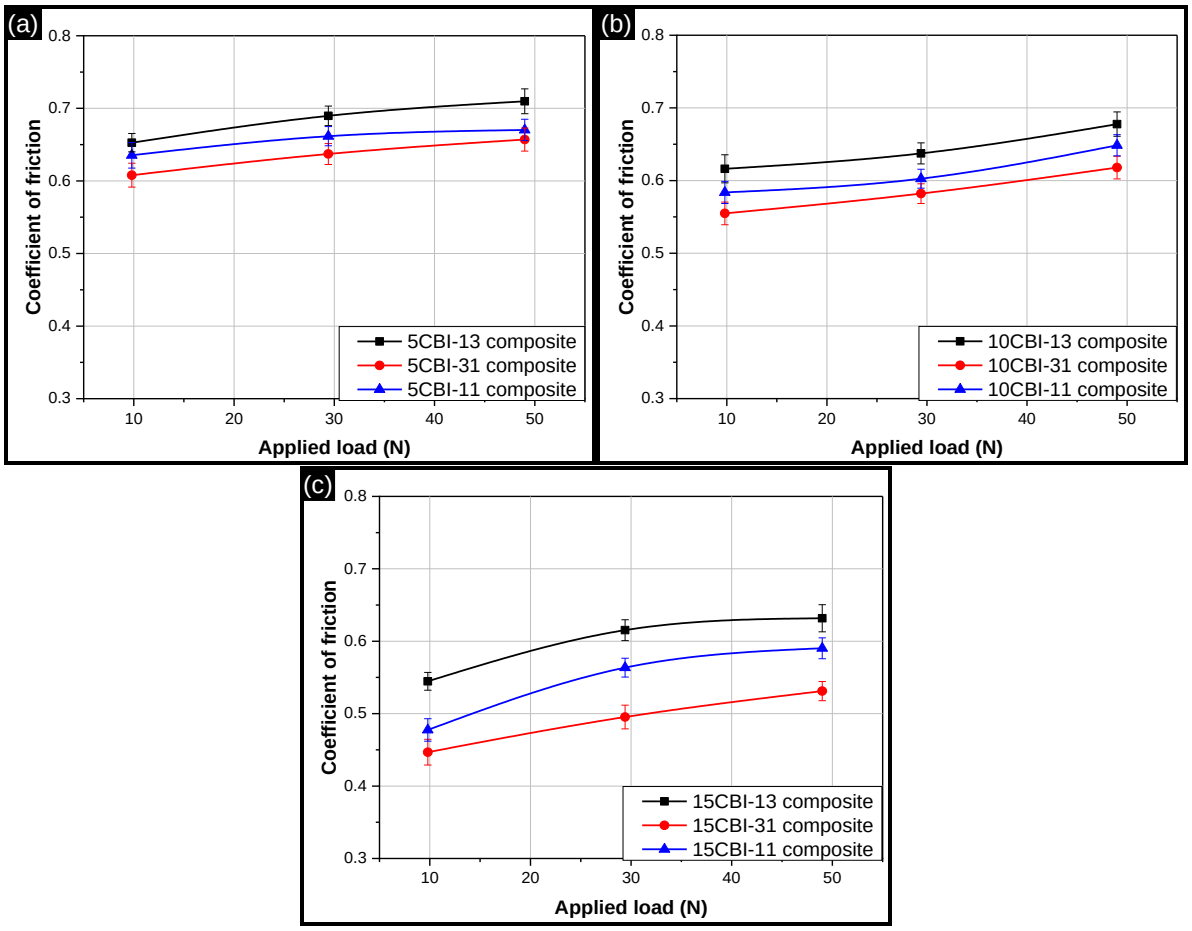

Figure 5.23 Coefficient of friction values as a function of applied load for different mixing proportions of (a) '5CBI' composites, (c) '10CBI' composites, and (d) '15CBI' composites.

Coefficient of friction value is mainly influenced by the formation of MML and wear mechanism (i.e. ploughing and adhesion of sliding surfaces) [197,198]. For a particular composition of AMCs, COF values got affected by the severity of wear mechanisms (i.e. ploughing and adhesion) occurring due to the applied load on the sliding surfaces (i.e. pin and steel disc). With increase in applied load, the severity of ploughing and adhesion increased which increased the COF values of all samples [197]. Further, the severity of wear mechanism was also dependent on the formation of MML. The formation of MML led to non-exposure of

base alloy to steel disc which corresponded to reduction in ploughing and adhesion [198]. However, the stability of MML depends on the hardness of the beneath surface i.e. higher hardness of composite surface signifies higher stability of MML [24]. The increase in hardness for composites having higher reinforcement level and higher proportion of boron carbide in the reinforcement mixture as discussed in Section 5.3.1 signified higher stability of MML and higher reduction in COF value for '15CBI-31' composite.

5.6.2 Dual particle reinforced composites containing fine particles

Figure 5.24 presents the coefficient of friction (COF) values under room temperature conditions for various dual particle reinforced AMCs containing 'fine' particles ('FBI' composites) as a function of applied load over the entire sliding distance.

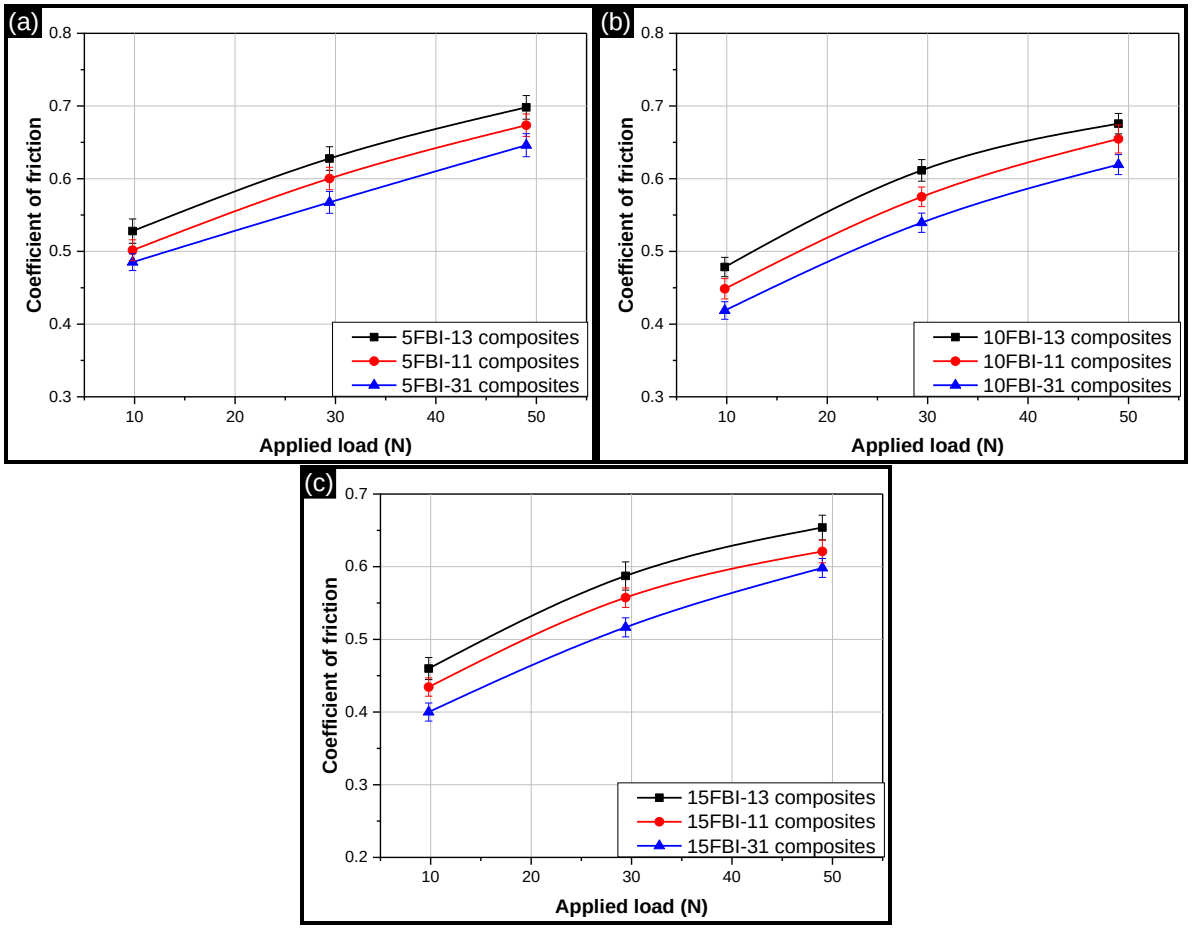

Figure 5.24 Coefficient of friction values as a function of applied load for different mixing proportion of (a) '5FBI' composites, (c) '10FBI' composites, and (d) '15FBI' composites.

For a given composition, COF values showed an increasing trend with rise in applied load. Further, for a given reinforcement level at a given load, a decreasing trend was observed in COF values with rise in proportion of boron carbide particles in the reinforcement mixture.

Increase in reinforcement level at a particular mixing proportion also decreased the COF values. Lowest value of COF was obtained for '15FBI-31' composite which was 46.21% lower than the LM13 alloy. The reasons for the trends observed in COF values for dual particle reinforced AMCs containing 'coarse' particles has already been discussed in Section 5.6.1. The same reasons hold well for dual particle reinforced AMCs containing 'fine' particles also i.e. 'FBI' composites.

For a given composition of AMC at a given applied load, the change in particle size from 'coarse' to 'fine' led to reduction in COF values. This was attributed to decrease in contact area of the base alloy with respect to counter steel disc and increase in stability of MML [199,200]. With reduction in particle size, the number of particles present in base alloy shows an increasing trend for a given composition of AMCs. This led to reduction in contact area of base alloy to the counter steel disc which resulted in decrement of deformation caused by adhesion of base alloy with the counter steel disc. Hence, a reduction in COF values were observed on addition of fine size of particles in AMCs. Further, the reduction in particle size also led to achievement of higher hardness for 'FBI' composites as has been discussed in Section 5.3.2. This enhanced the stability of MML formed in 'FBI' composites as the strength of beneath material is sufficient for supporting the MML in comparison of 'CBI' composites.

5.7. Wear-track and debris under room temperature conditions

5.7.1 Dual particle reinforced composites containing coarse particles

Figure 5.25 presents the SEM micrographs of wear-track and wear-debris of AMCs containing 'coarse' particles with maximum reinforcement level and maximum proportion of boron carbide in the reinforcement mixture (i.e. '15CBI-31' composite) tested under different applied load conditions. Figure 5.25a and Figure 5.25b show the wear track for '15CBI-31' composite at an applied load of 9.8 N and 49.0 N respectively. Both the wear-track surfaces were observed to be plastically deformed under the action of applied load. However, the mechanisms responsible for plastic deformation of surface were observed to vary with increase in applied load. At the low load condition of 9.8 N, plastic deformation mainly occurred due to micro-ploughing action caused by the counter surface asperities and the debris entrapped between the two counter surfaces. The entrapped debris ploughed the counter surface by acting as an abrasive particle [80,195]. Micro-ploughing on sliding surfaces led to generation of grooves which can be seen in Figure 5.25a–b. Besides micro-ploughing, some delamination areas were also observed on the sliding surface. These delamination areas were formed due to the merging

of multiple cracks generated under the action of applied load [58,199]. At high load conditions of 49.0 N, the plastic deformation was observed to be severe as micro-ploughing grooves were wider and the depth of delaminated area was relatively higher.

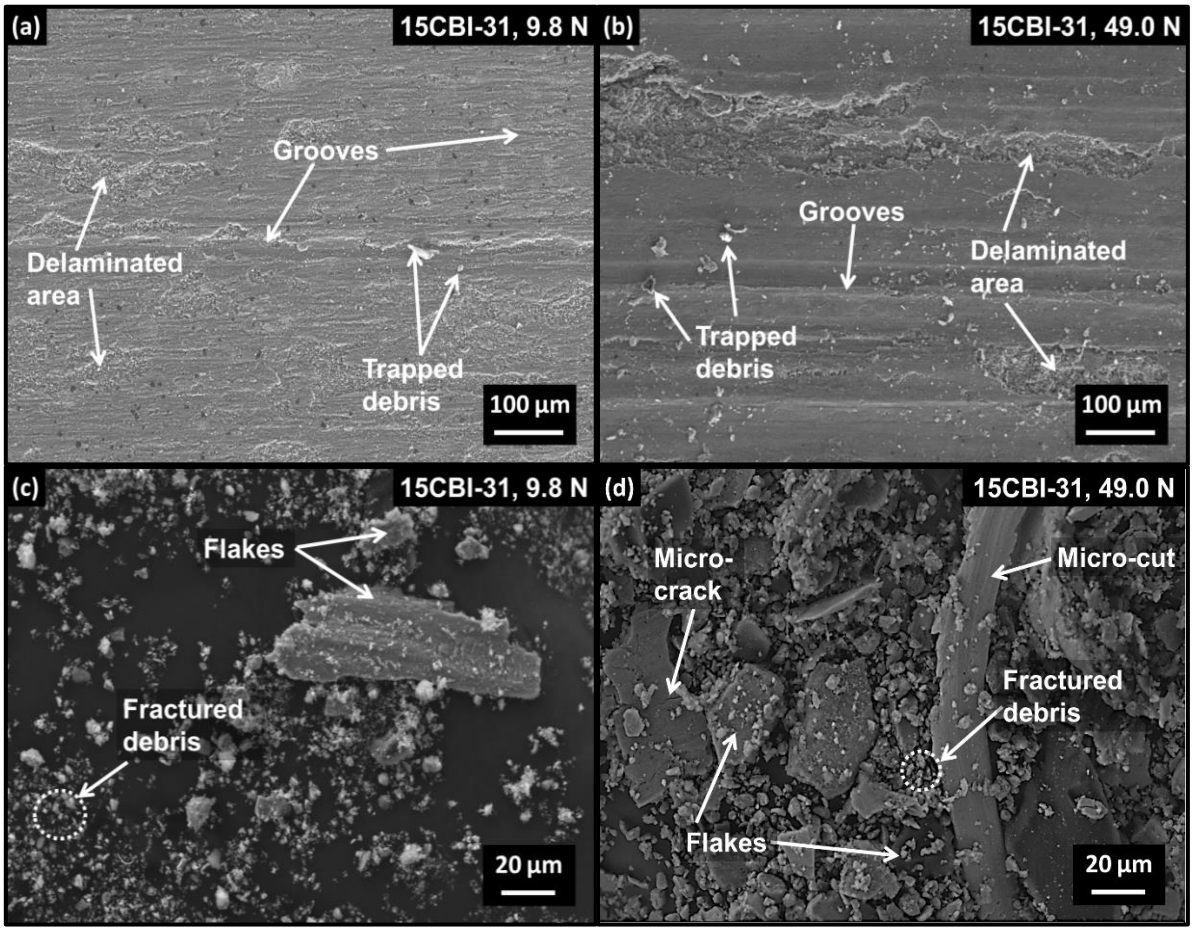

Figure 5.25 SEM images of '15CBI-31' composite for (a) wear-track at 9.8 N, (b) wear-track at 49.0 N, (c) wear-debris at 9.8 N, and (d) wear-debris at 49.0 N.

The increase in plastic deformation under high load conditions was justified by measuring the roughness of sliding surfaces. Figure 5.26 presents the roughness profiles of wear-track of '15CBI-31' composite obtained at different applied load conditions (9.8 N and 49.0 N). The average roughness value for worn surfaces was observed to be 1.89±0.34 µm and 2.41±0.26 µm respectively. The increase in roughness values with rise in applied load signified higher deformation of sliding surface. This higher deformation resulted in formation of large craters by undergoing delamination wear whereas lower deformation at 9.8 N applied load signified ploughing action caused by trapped debris.

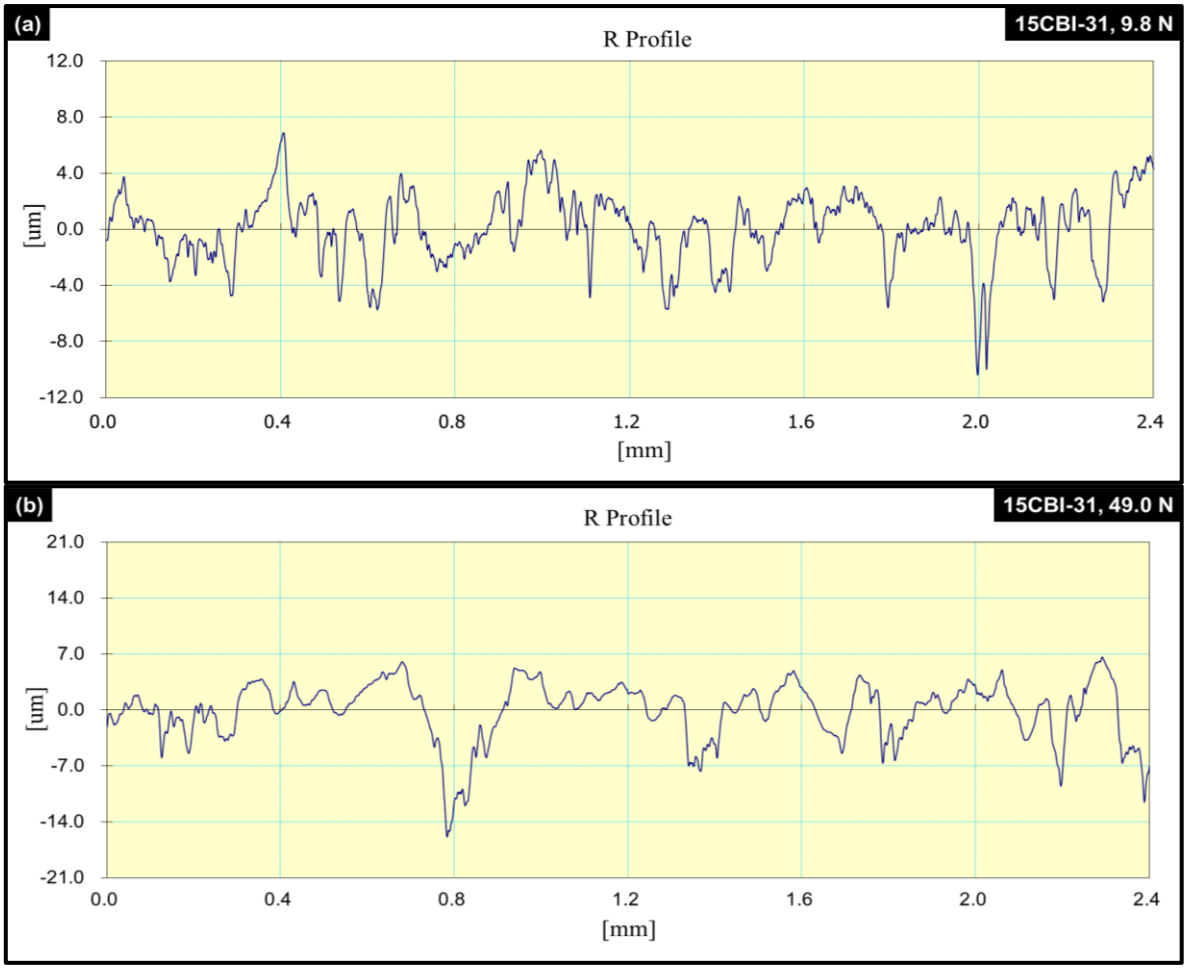

Figure 5.26 Roughness profiles of wear-track of '15CBI-31' composite at an applied load of (a) 9.8 N and (b) 49.0 N.

Figure 5.25c–d presents the wear-debris of '15CBI-31' composite at an applied load of 9.8 N and 49.0 N respectively. Wear-debris mainly consisted of flakes and fractured debris. In addition to this, some additional features such as micro-cracks and micro-cuts were also observed. In case of low load conditions, edges were formed due to material displacement caused by the micro-ploughing action [201]. Further, these edges were removed from the surface in the form of flakes-like debris. These flakes-like debris also get formed when various cracks merged at a node to delaminate the sliding surface. Since the intensity of cracks generating force was relatively higher at 49.0 N load, so higher depth of delaminated area was observed in '15CBI-31' composite at the higher load condition. The presence of micro-cracks on the debris signified the higher intensity of crack generation. Further, the occurrence of fractured debris was ascribed to crushing of entrapped debris between the two sliding surfaces. At last, the presence of micro-cut debris was ascribed to the abrasive action caused by the trapped debris.

Figure 5.27 presents the SEM-EDS of wear-track and wear-debris of '15CBI-31' composite at different applied loads.

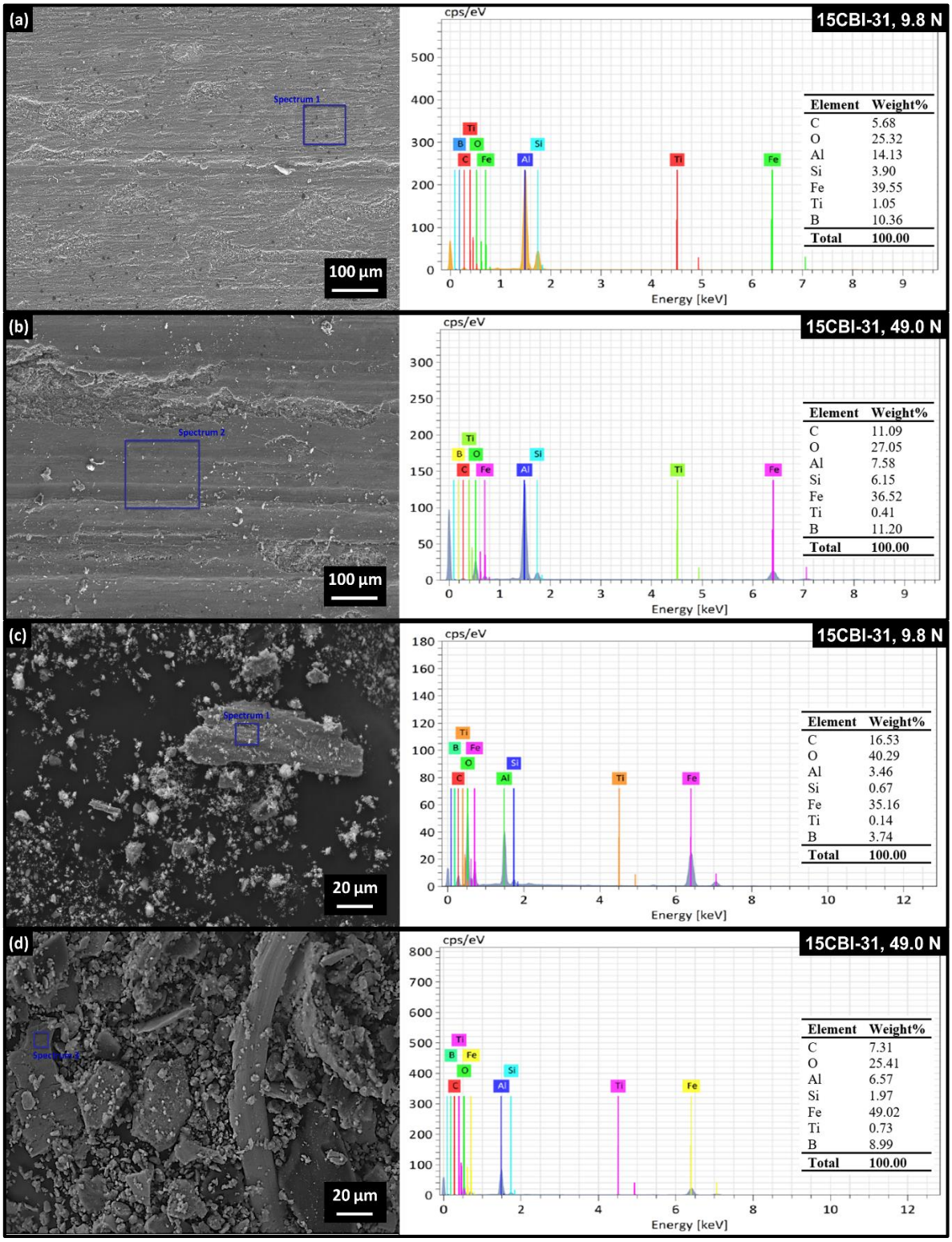

Figure 5.27 SEM-EDS of (a) wear-track at 9.8 N, (b) wear-track at 49.0 N, (c) wear-debris at 9.8 N and (d) wear-debris at 49.0 N for '15CBI-31' composite.

For all the samples, the detected elements were aluminium (Al), silicon (Si), boron (B), iron (Fe), titanium (Ti), carbon (C) and oxygen (O). Based on the weight percentage of boron and titanium present in the reinforced particles, the amount of iron, carbon and oxygen coming as a result of transfer of material and oxidation was recalculated. At the low load of 9.8 N, the amount of transfer of iron and carbon from the steel disc was 39.11 wt.% and 0.68 wt.% respectively. The amount of oxygen present due to oxidation of sliding surface because of rise in temperature was observed to be 23.96 wt.%. Further, the calculated amount of iron, carbon and oxygen for sliding surface obtained at an applied load of 49.0 N was 36.34 wt.%, 5.66 wt.% and 26.52 wt.% respectively. The presence of elements like iron and carbon confirmed the formation of mechanical mixed layer by transfer of material between the counter surfaces. Further, the percentage of oxygen (responsible for surface oxidation) and carbon increased when applied load increased from 9.8 N to 49.0 N. At the higher load of 49.0 N, the extra amount of oxygen present (26.52%) signified the increase in oxidation rate with increase in applied load. Besides this, carbon level increased from 0.68 to 5.66% which signified increased transfer of material between the counter surfaces and formation of thicker MML. Similar observations were also obtained from the elemental analysis of wear-debris.

5.7.2 Dual particle reinforced composites containing fine particles

The SEM images of wear-track and debris of AMCs containing 'fine' particles with maximum reinforcement level and maximum proportion of boron carbide particles in the reinforcement mixture ('15FBI-31' composite) tested under different applied load conditions are presented by Figure 5.28. Wear track obtained at an applied load of 9.8 N and 49.0 N are shown by Figure 5.28a and Figure 5.28b, respectively. Both the wear track surfaces showed presence of delaminated areas, grooves, micro-cracks, and trapped debris. Under the action of applied load, the asperities of composites were broken by the counter steel disc. These were either removed from the system in the form of debris or got trapped between the two sliding surfaces. In addition to this, the hard asperities of the counter steel disc and trapped debris penetrated into the sliding surface to generate grooves. The repetitive action of sliding led to larger plastic deformation of sliding surfaces which attributed to nucleation of micro-cracks. When these cracks propagated and merged at a node, the material got removed and left behind the delaminated area. At low load condition (9.8 N), ploughing was observed to be the dominant wear mechanism which got changed to delaminated wear mechanism with rise in applied load to 49.0 N as shown in Figure 5.28a–b.

The SEM micrographs of wear-debris of '15FBI-31' composite at 9.8 N and 49.0 N applied loads are shown by Figure 5.28c and Figure 5.28d respectively. The debris consisted of flake-like debris, corrugated debris, micro-cuts, micro-cracks, and fractured debris. The additional features observed on the debris at an applied load of 9.8 N were the grooves on flake-like debris. The formation of flake-like debris was formed by merging of the micro-cracks. The presence of grooves on flake-like debris signified that the material got removed after ploughing action by trapped debris. These trapped debris were also responsible for removal of material in the form of micro-cuts and the repetitive action of sliding resulted in formation of corrugated debris. The trapped debris under the action of applied load got fractured and resulted in formation of fractured debris.

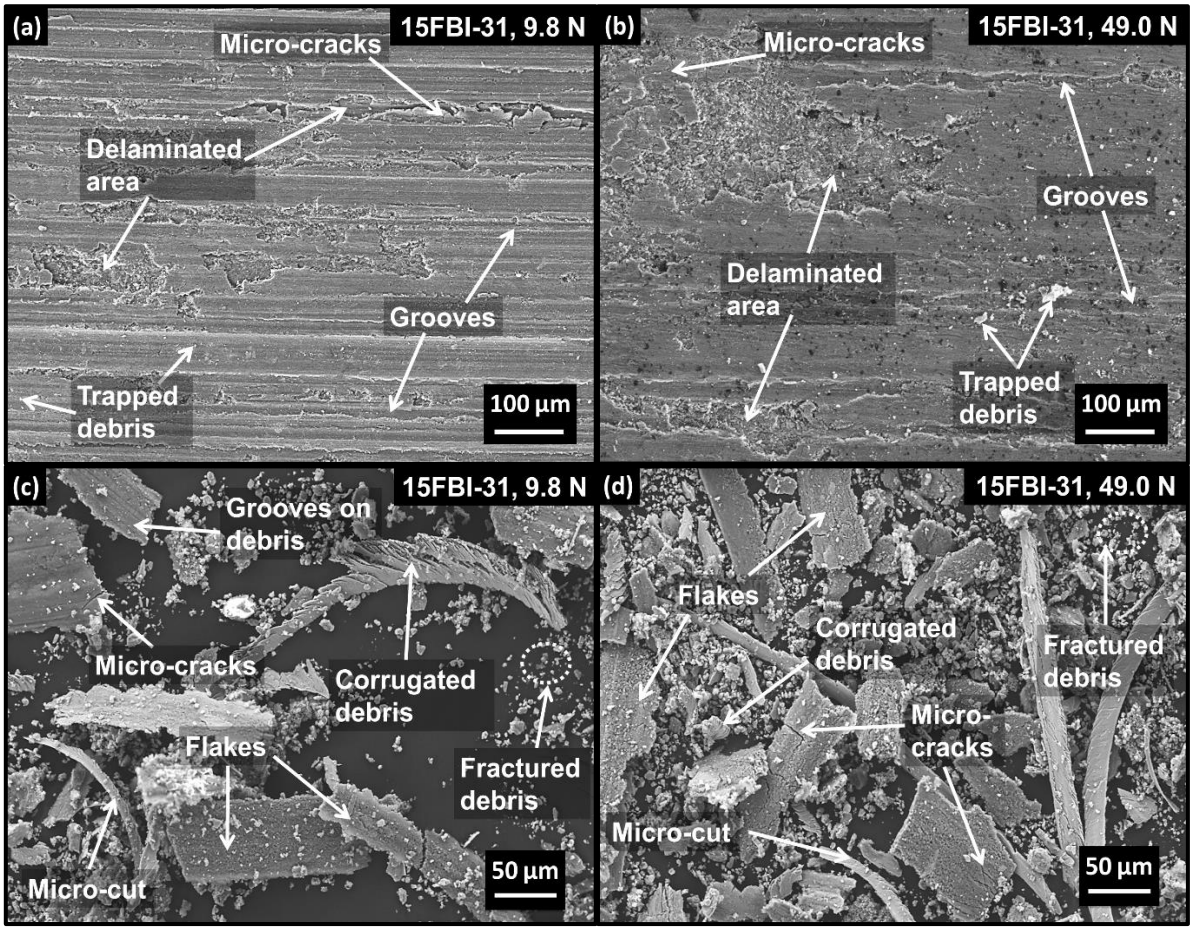

Figure 5.28 SEM images of '15FBI-31' composite showing (a) wear-track at 9.8 N, (b) wear-track at 49.0 N, (c) wear-debris at 9.8 N, and (d) wear-debris at 49.0 N.

The roughness profile obtained for the wear-track of '15FBI-31' composite under different load conditions is shown by Figure 5.29. It was observed that the average roughness (R_a value) for wear tracks under applied load of 9.8 N and 49 N was 1.43±0.28 µm and 1.97±0.36 µm respectively. An increase in roughness value indicated more deformation of the sliding surface

with increase in applied load. Due to higher deformation, large craters were formed through delamination wear at higher applied loads. On the other hand, lower deformation at 9.8 N applied load resulted in ploughing caused by trapped debris.

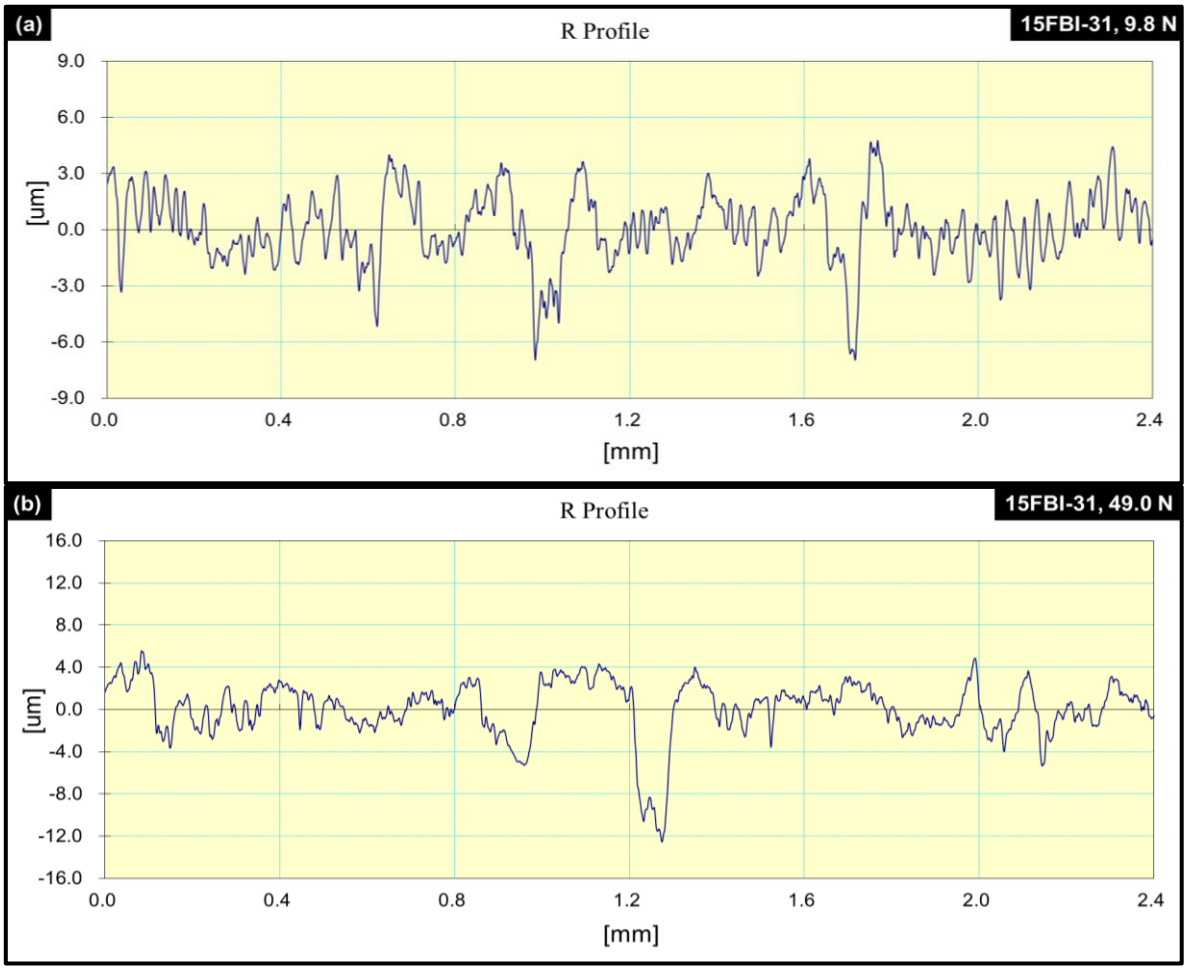

Figure 5.29 Roughness profiles of wear-track of '15FBI-31' composite at an applied load of (a) 9.8 N and (b) 49.0 N.

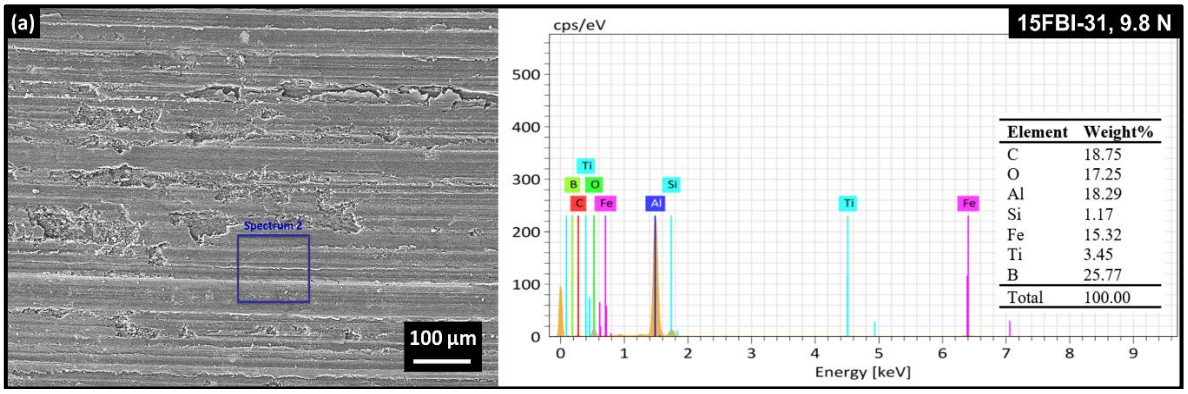

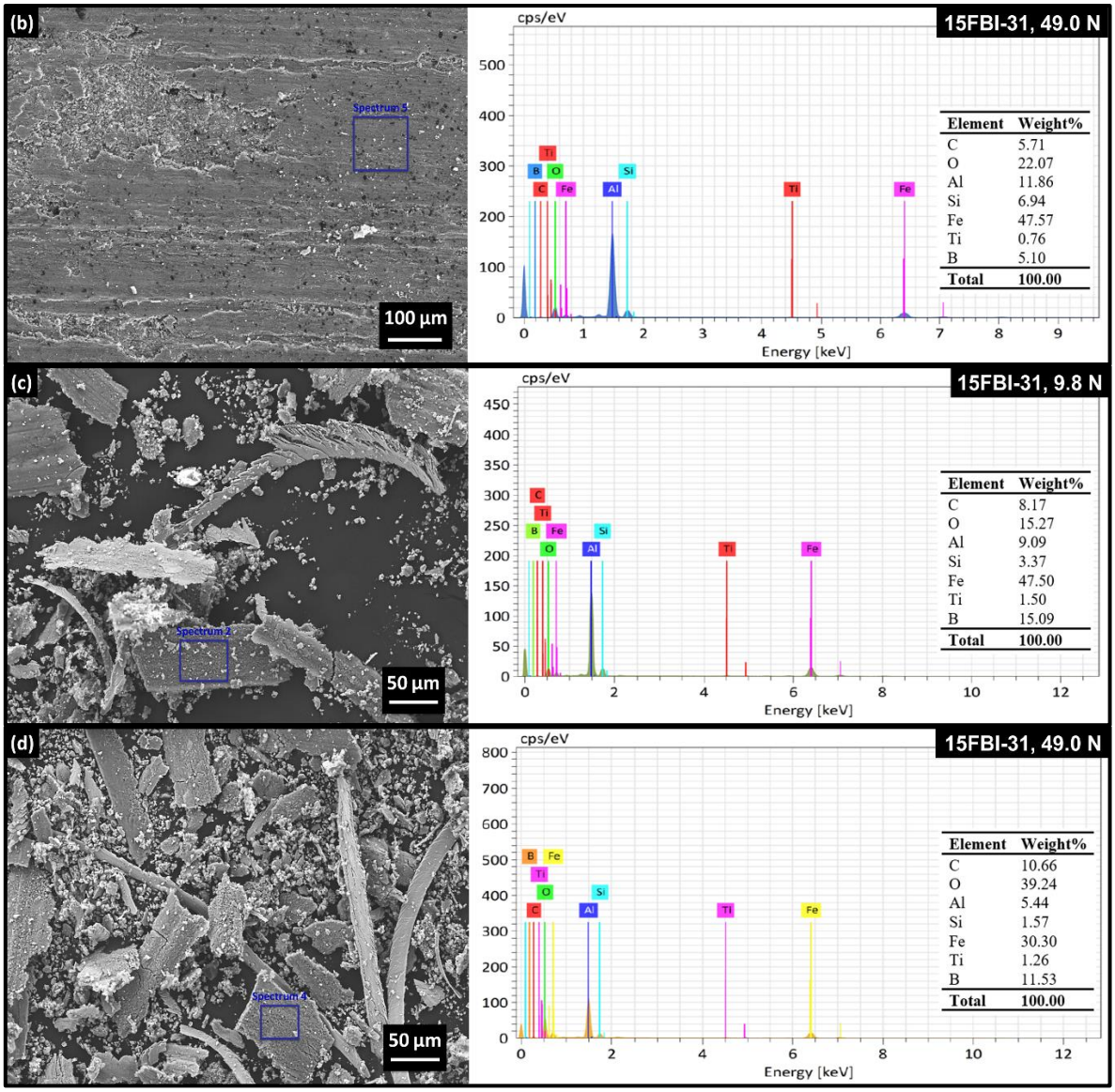

Figure 5.30 SEM-EDS of (a) wear-track at 9.8 N, (b) wear-track at 49.0 N, (c) wear-debris at 9.8 N and (d) wear-debris at 49.0 N for '15FBI-31' composite.

The SEM-EDS of wear-track and debris for '15FBI-31' composite at different applied loads is shown in Figure 5.30. The weight percentage of iron, oxygen, and carbon obtained from EDS is a combination of these elements present in the reinforced particles (i.e. $FeTiO_3$ and B_4C), oxides formed due to rise in temperature by frictional heating, and material removal from the counter steel (i.e. iron and carbon). To identify the source of different elements, the EDS analysis of reinforced particles was used as the reference. The calculated values of weight percentage of iron, oxygen and carbon on the worn surfaces at 9.8 N were 13.85%, 12.79%, and 6.26% respectively and at 49.0 N were 47.25%, 21.08%, and 3.24% respectively. For wear-debris, the values were 46.87%, 13.33%, and 0.86% at 9.8 N and 29.77%, 37.61% and 5.07% respectively at 49 N. The presence of iron and carbon elements on the wear-tracks and debris

confirmed the formation and removal of mechanical mixed layer by transfer of material from steel disc to sliding surface. The occurrence of oxygen signified the formation of various oxides due to rise in temperature by frictional heating.

5.8. Wear rate behaviour under high temperature conditions

5.8.1 Dual particle reinforced composites containing coarse particles

Figure 5.31, Figure 5.32, and Figure 5.33 present the average steady-state wear rate behaviour of AMCs containing 'coarse' particles ('CBI' composites) as a function of operating temperature for various reinforcement levels and mixing proportions at applied loads of 9.8 N, 29.4 N, and 49.0 N respectively. From the wear studies of AMCs at room temperature conditions, it was observed that the steady state wear rate condition was mainly achieved after a sliding distance of 1500 m as discussed in Section 5.5. Hence, the calculation of average steady state wear rate was done over a sliding distance range of 1500−3000 m. For all the samples, the rise in applied load led to increase in average steady-state wear rate for a particular operating temperature. Similarly, the change in operating temperature from ambient temperature to 300 ℃ resulted in rise of average steady-state wear rate for a given applied load condition. A continuous rise in average steady-state wear rate was observed till operating temperature of 200 ℃. With further rise in temperature, a sharp increase in average steady-state wear rate was observed for all the samples under all the applied load conditions. Increase in reinforcement level at a given mixing proportion and operating temperature resulted in reduction of average steady-state wear rate. Further, at a given reinforcement level and operating temperature, increase in proportion of boron carbide particles in the reinforcement mixture also led to decrease in steady-state wear rate.

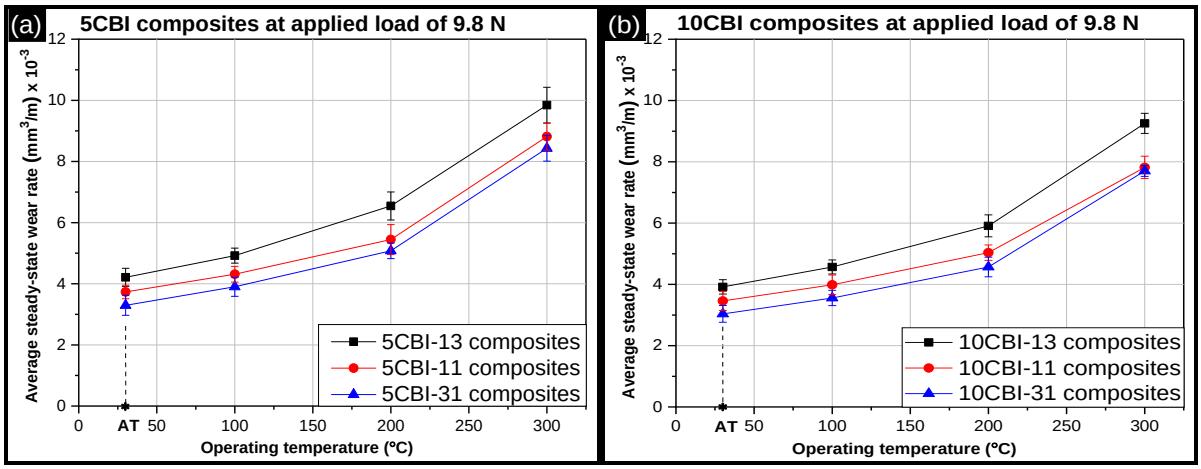

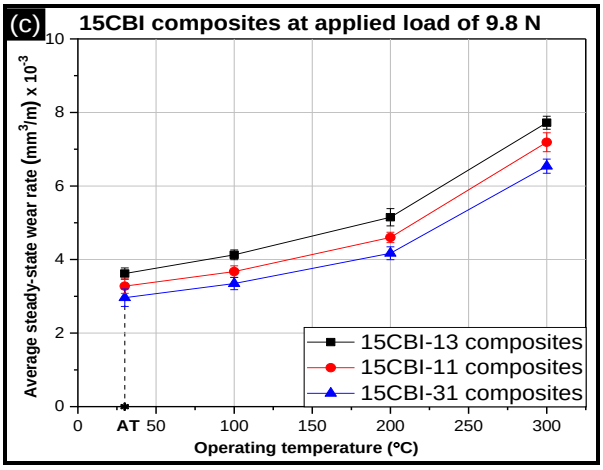

Figure 5.31 Variation in average steady-state wear rate with operating temperature for (a) '5CBI' composites, (b) '10CBI' composites, and (c) '15CBI' composites at an applied load of 9.8 N.

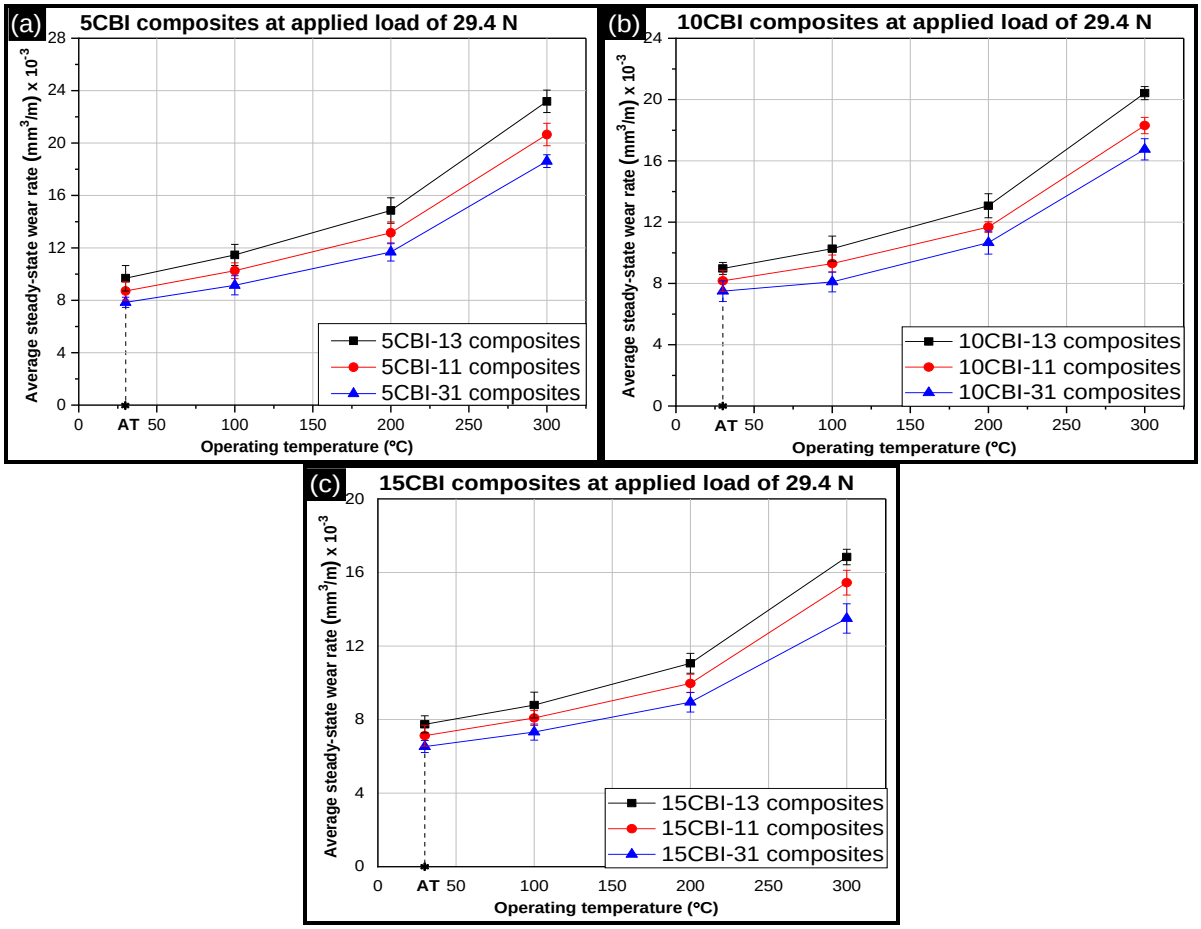

Figure 5.32 Variation in average steady-state wear rate with operating temperature for (a) '5CBI' composites, (b) '10CBI' composites, and (c) '15CBI' composites at an applied load of 29.4 N.

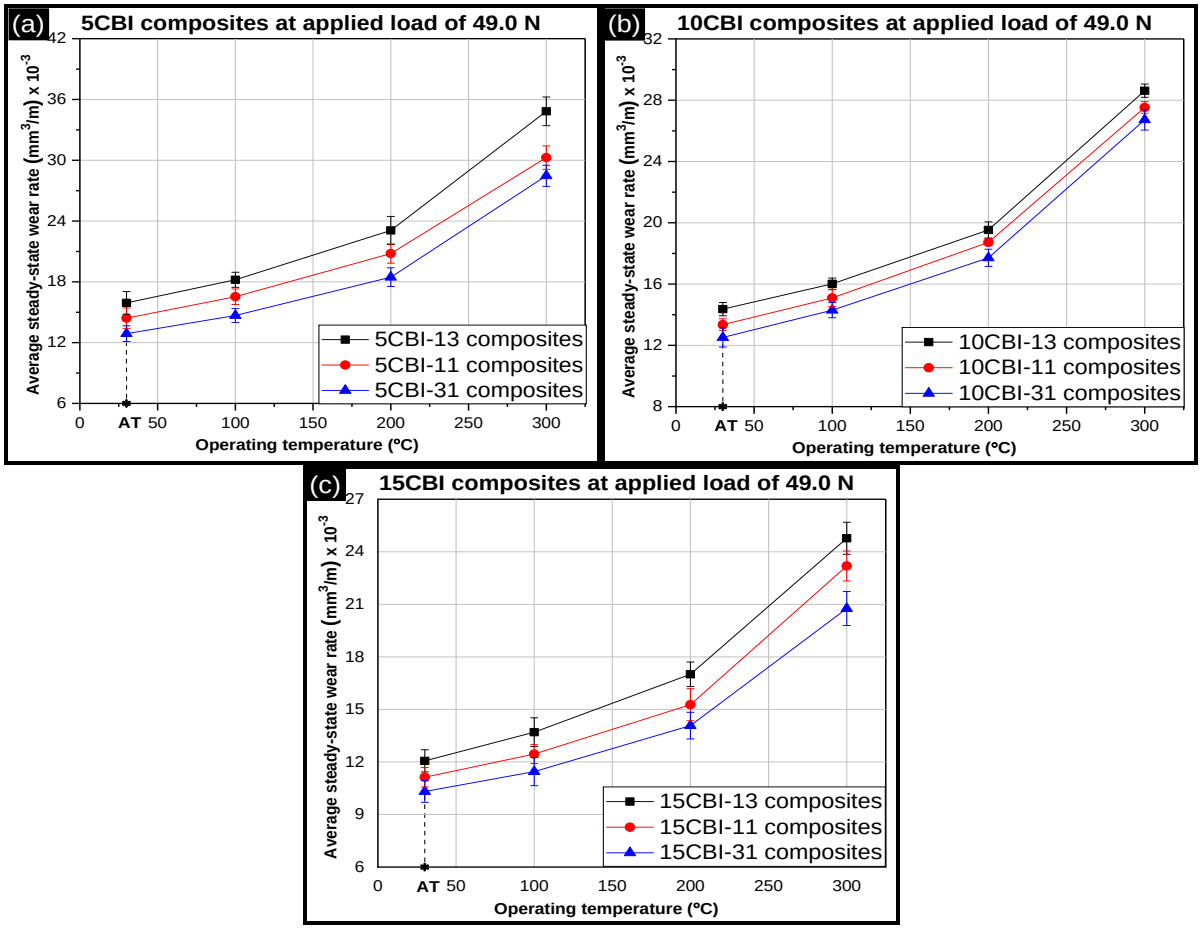

Figure 5.33 Variation in average steady-state wear rate with operating temperature for (a) '5CBI' composites, (b) '10CBI' composites, and (c) '15CBI' composites at an applied load of 49.0 N.

During sliding process, multiple point contacts are made between the two sliding surfaces [202]. These contact points are subjected to Hertzian stress under the action of applied load. The magnitude of Hertzian stress depends on the applied load, hardness of sliding surface, and contact area between the two counter surfaces. The increase in wear rate for AMC having a particular composition (here, 'CBI' composites) with increase in applied load was attributed to increment in Hertzian stress [24,203]. Further, the effect of Hertzian stress on wear rate at a given applied load can be minimized by varying the mechanical properties of the material, mainly hardness. The increase in hardness of sample provides the sliding surface with additional resistance against plastic deformation caused by Hertzian stresses [80,203]. This helps in reducing the wear rate of composites. The incorporation of reinforced particles in the base alloy led to enhancement of hardness values as discussed in Section 5.3.1. Thus, increase in reinforcement level attributes to increase in wear resistance for 'CBI' composites and attainment of lowest wear rate for '15CBI' composite. Further, the variation of mixing proportion of reinforced particles in the reinforcement mixture also showed changes in

hardness values. At a particular reinforcement level, the highest hardness value was shown by 'CBI-31' composites followed by 'CBI-11' composites, and finally 'CBI-13' composites. This trend was also followed by wear rate of composites which resulted in highest wear resistance for '15CBI-31' composite followed by '15CBI-11' and '15CBI-13' composites. Further, increase in operating temperature showed increasing trend in wear rate for all the samples. At high temperature conditions, grain coarsening of base alloy occurs which results in reduction of the hardness value. However, addition of reinforced particles creates a pinning effect which hinders the growth of grains and reduces the reduction in hardness value [24,184,204]. The highest number of hard boron carbide particles in case of 3:1 mixing proportion and highest reinforcement level of 15 wt.% in '15CBI-31' composite signified higher pinning effect and lesser reduction in hardness value. Thus, the increase in proportion of boron carbide particles and reinforcement level showed enhancement in wear resistance of hybrid aluminium matrix composites. Beyond 200 ℃, a sharp increase in wear rate was observed for 'CBI' composites. This signified that the sliding surface softened excessively due to which high plastic deformation was observed under the action of Hertzian stress.

Table 5.7 presents the improvement in average steady-state wear rate of 'CBI' composites over LM13 alloy at operating temperature of 200 ℃ and different applied load conditions.

Table 5.7 Percentage reduction in average steady-state wear rate of 'CBI' composites over LM13 alloy at operating temperature of 200 ℃.

Applied load (N)	Percentage reduction in steady-state wear rate at 200 ℃ for 'CBI' composites at different reinforcement levels and mixing proportions								
	5 wt.%			10 wt.%			15 wt.%		
	1:3	1:1	3:1	1:3	1:1	3:1	1:3	1:1	3:1
9.8	53	61	63	57	63	67	63	67	70
29.4	51	56	61	57	61	65	63	67	70
49.0	48	53	58	56	58	60	62	65	68

Figure 5.34 presents the comparison of wear characteristics of commercially used brake rotor material and '15CBI-31' composite. The comparison on the basis of average steady-state wear rate and temperature derivative of average steady state is shown in Figure 5.34a and Figure 5.34b respectively. The average steady-state wear rate of '15CBI-31' composite is 45% higher than the commercial brake rotor material. Further, the working temperature of commercial brake rotor material and '15CBI-31' composite for same wear rate was determined using the temperature derivative of average steady-state wear rate. For a derivative value of 0.031 $mm^3m^{-1}{}^{o}C^{-1}$, the working temperature of commercial brake rotor material and '15CBI-31' composite was 300 ℃ and 150 ℃ respectively.

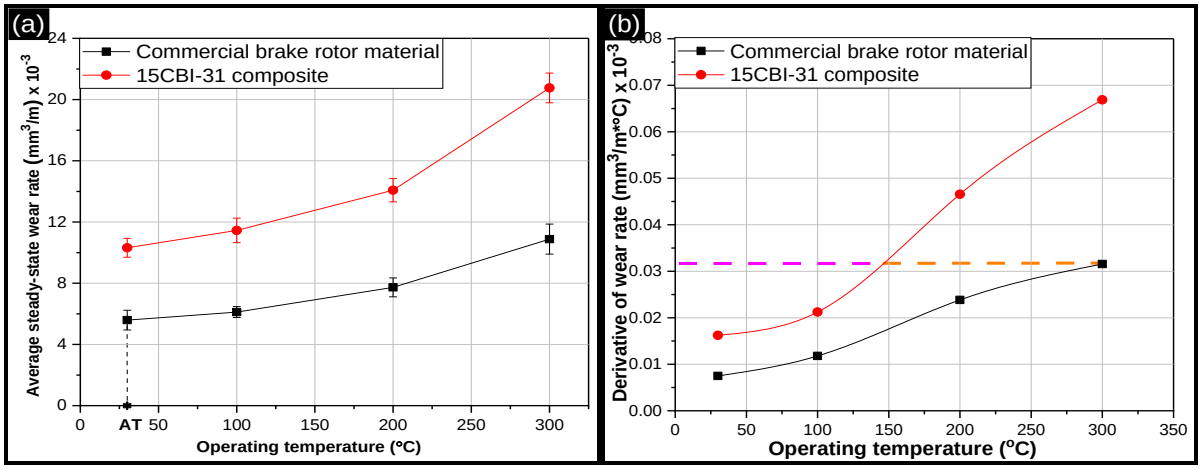

Figure 5.34 Comparison of (a) average steady-state wear rate and (b) temperature derivative of average steady-state wear rate of commercial brake rotor material and '15CBI-31' composite.

5.8.2 Dual particle reinforced composites containing fine particles

Figure 5.35, Figure 5.36, and Figure 5.37 present the average steady-state wear rate behaviour of AMCs containing 'fine' particles ('FBI' composites) as a function of operating temperature for various reinforcement levels and mixing proportions at applied loads of 9.8 N, 29.4 N, and 49.0 N respectively. It was observed that the average steady-state wear rate of 'FBI' composites showed a steady increase with rise in operating temperature till 200 ℃. Beyond 200 ℃, there was a sharp rise in wear rate. Further, the average steady-state wear rate was more under higher loads. The wear rate of 'FBI' composites decreased with increase in proportion of boron carbide particles in the reinforcement mixture at a particular reinforcement level. Similar trend was observed with rise in reinforcement level for a given mixing proportion of the two types of particles in the reinforcement mixture.

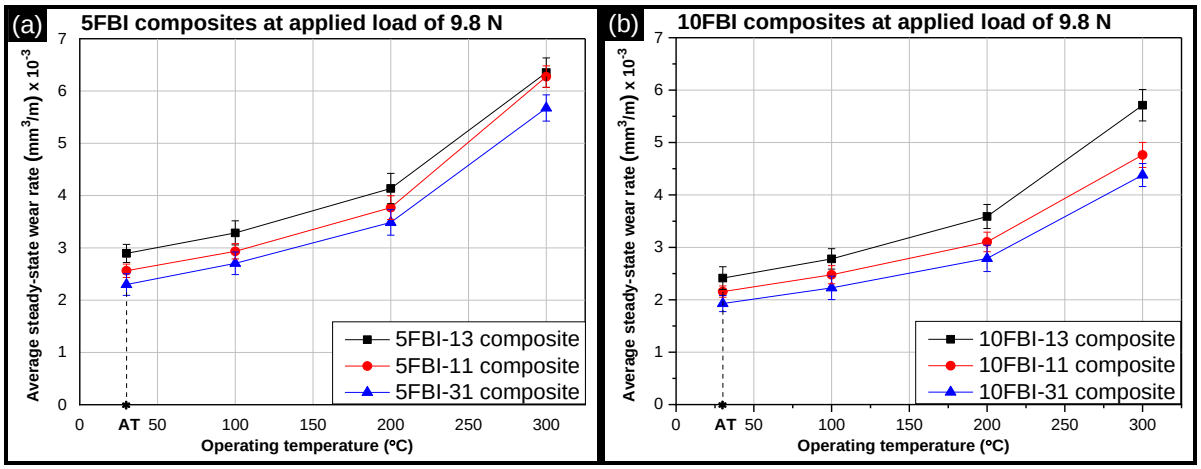

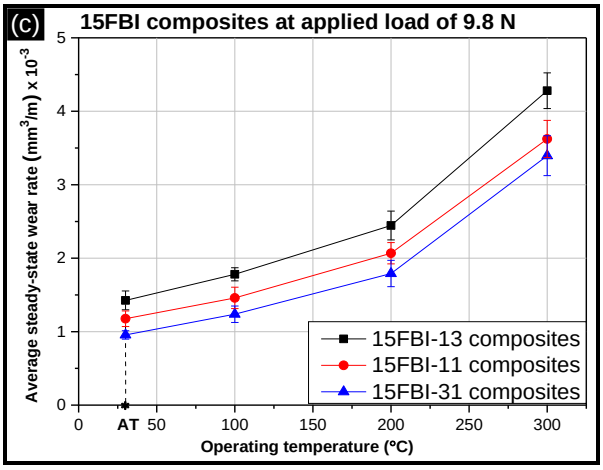

Figure 5.35 Variation in average steady-state wear rate with operating temperature for (a) '5FBI' composites, (b) '10FBI' composites and (c) '15FBI' composites at an applied load of 9.8 N.

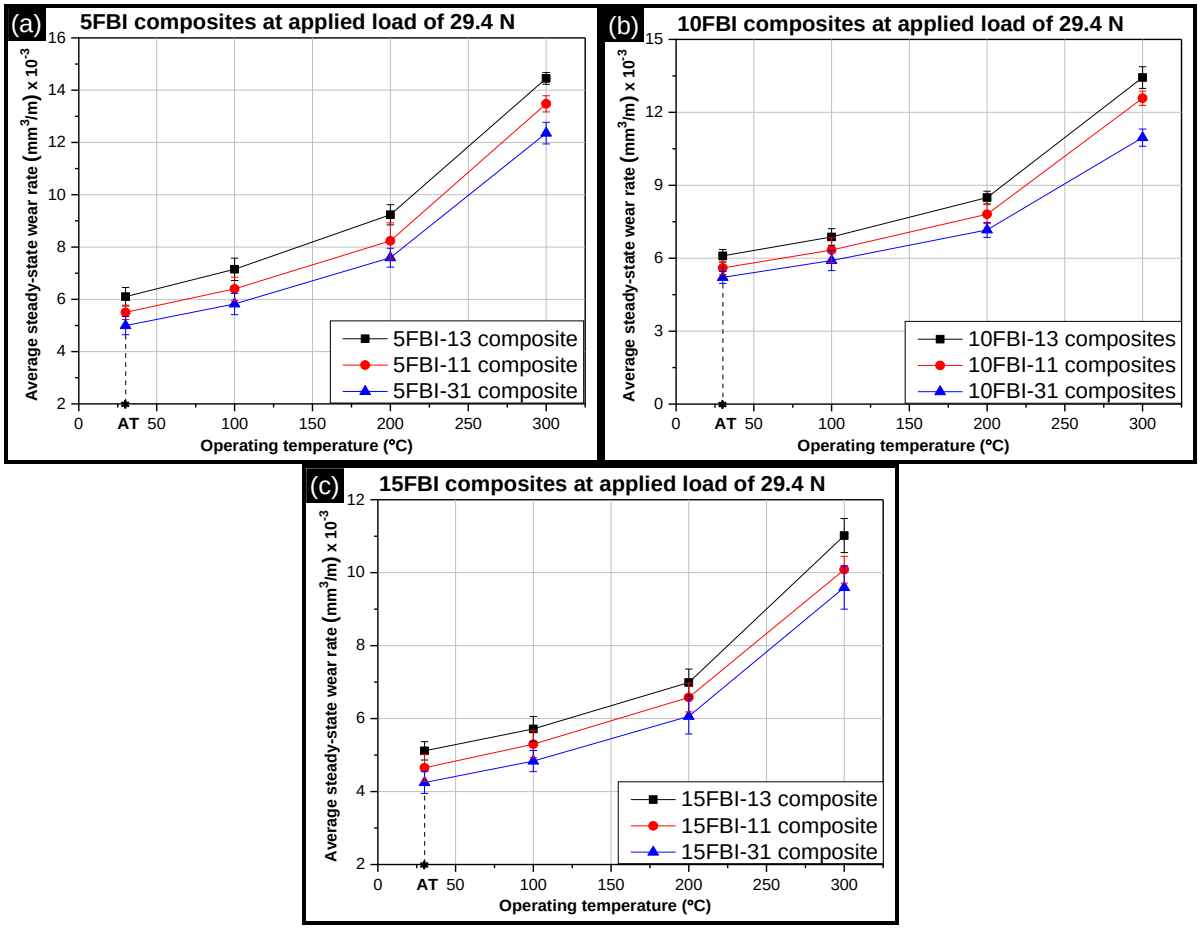

Figure 5.36 Variation in average steady-state wear rate with operating temperature for (a) '5FBI' composites, (b) '10FBI' composites and (c) '15FBI' composites at an applied load of 29.4 N.

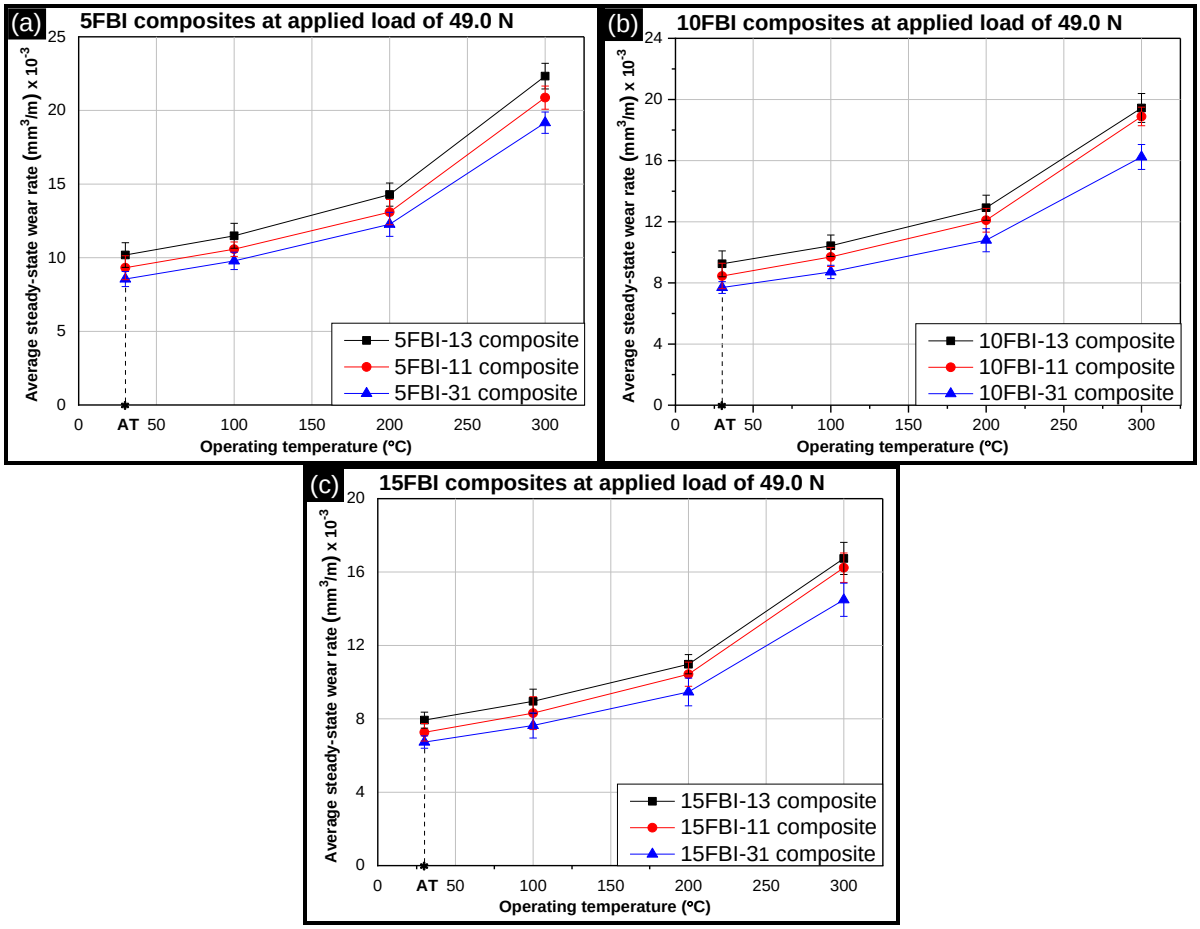

Figure 5.37 Variation in average steady-state wear rate with operating temperature for (a) '5FBI' composites, (b) '10FBI' composites and (c) '15FBI' composites at an applied load of 49.0 N.

Maximum reduction in wear rate was obtained for '15FBI-31' composite (87% decrease over base alloy at 200 ℃-9.8 N condition; Table 5.8). In Section 5.8.1, the reasons for the trends observed in wear behaviour of hybrid AMCs with 'coarse' particles under high operating temperatures is already discussed. The same reasons hold good for hybrid AMCs containing 'fine' particles ('FBI' composites) also. The improvement in wear rate for various 'FBI' composites at different applied loads and temperature condition of 200 ℃ is shown in Table 5.8.

Table 5.8 Percentage reduction in average steady-state wear rate of 'FBI' composites over LM13 alloy at operating temperature of 200 ℃.

Applied load (N)	Percentage reduction in steady-state wear rate at 200 ℃ for 'FBI' composites at different reinforcement levels and mixing proportions								
	5 wt.%			10 wt.%			15 wt.%		
	1:3	1:1	3:1	1:3	1:1	3:1	1:3	1:1	3:1
9.8	70	73	75	74	77	80	82	85	87
29.4	69	73	75	72	74	76	77	78	80
49.0	68	70	72	71	73	76	75	76	79

Further, the differences obtained in the wear rate of AMCs containing 'fine' particles ('FBIs') and those containing 'coarse' particles ('CBIs') under high temperature conditions are discussed ahead. At a given reinforcement level and mixing proportion, the change in particle size from 'coarse' to 'fine' resulted in lower wear rate for hybrid AMCs at a given operating temperature-applied load condition. With relatively finer particle size (in 'FBIs'), the number of particles reinforced in the matrix material at a given reinforcement level were relatively higher. This signified rise in pining effect caused by individual reinforced particles and lesser decrease in hardness at a given high temperature-load condition. Hence, the plastic deformation caused by the action of Hertzian stress on the sliding surface of 'FBI' composites was relatively less when compared to 'CBI' composites.

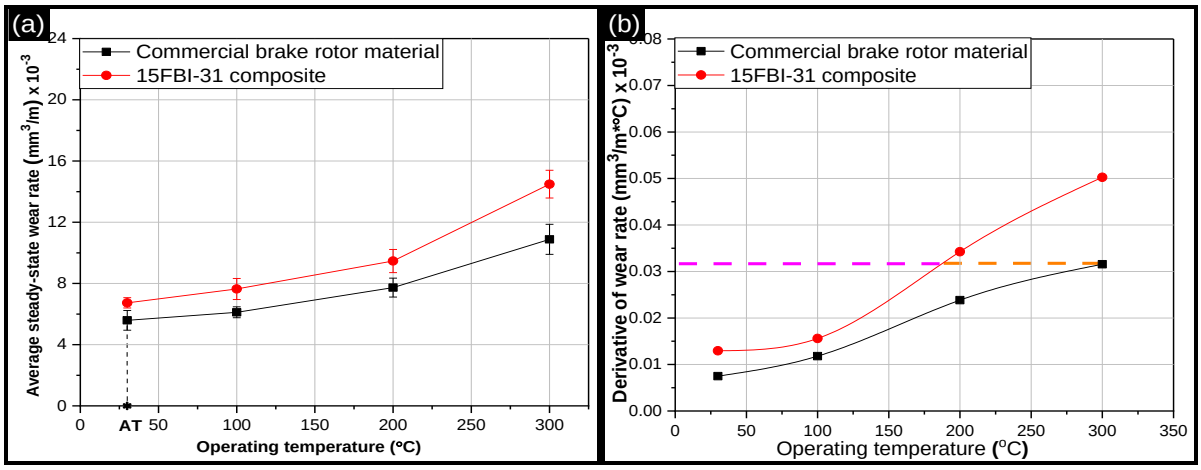

Figure 5.38 Comparison of (a) average steady-state wear rate and (b) temperature derivative of average steady-state wear rate of commercial brake rotor material and '15FBI-31' composite.

Figure 5.38 presents the comparison of '15FBI-31' composite with commercially used brake rotor material in terms of average steady-state wear rate and temperature derivative of average steady state wear rate. The wear rate of 15FBI-31 composite showed relatively higher wear rate values than the commercial brake rotor material at all operating temperatures. At 200 ℃, the wear rate of '15FBI-31' composite was 23% higher than the commercial material. For a derivative value of 0.031 $mm^3m^{-1}℃^{-1}$, the working temperature of commercial brake rotor material and '15FBI-31' composite was 300 ℃ and 186 ℃ respectively. The wear rate behaviour and working temperature of commercial brake rotor material were better than the '15FBI-31' composite developed in the present research. However, if light-weight and low production cost are important considerations, this newly processed hybrid composite can substitute for the commercial material.

5.9. Coefficient of friction under high temperature conditions

5.9.1 Dual particle reinforced composites containing coarse particles

Figure 5.39, Figure 5.40, and Figure 5.41 present the coefficient of friction (COF) values of hybrid AMCs containing 'coarse' particles ('CBI' composites) as a function of operating temperature for various reinforcement levels and mixing proportions at applied loads of 9.8 N, 29.4 N, and 49.0 N respectively. For a hybrid composite containing a particular reinforcement level and a given reinforcing mixture at a given applied load, COF values increased with increase in operating temperature. Similarly, for a particular reinforcement level and a given reinforcing mixture at a given operating temperature, COF values increased with increase in applied load. At a given applied load and given operating temperature, COF values decreased with increase in the reinforcement level. Further, at a given applied load, given operating temperature, and given reinforcement level, COF values decreased with increase in proportion of boron carbide particles in the reinforcement mixture. For any given operating temperature-applied load condition, '15CBI-31' composite showed the lowest COF value.

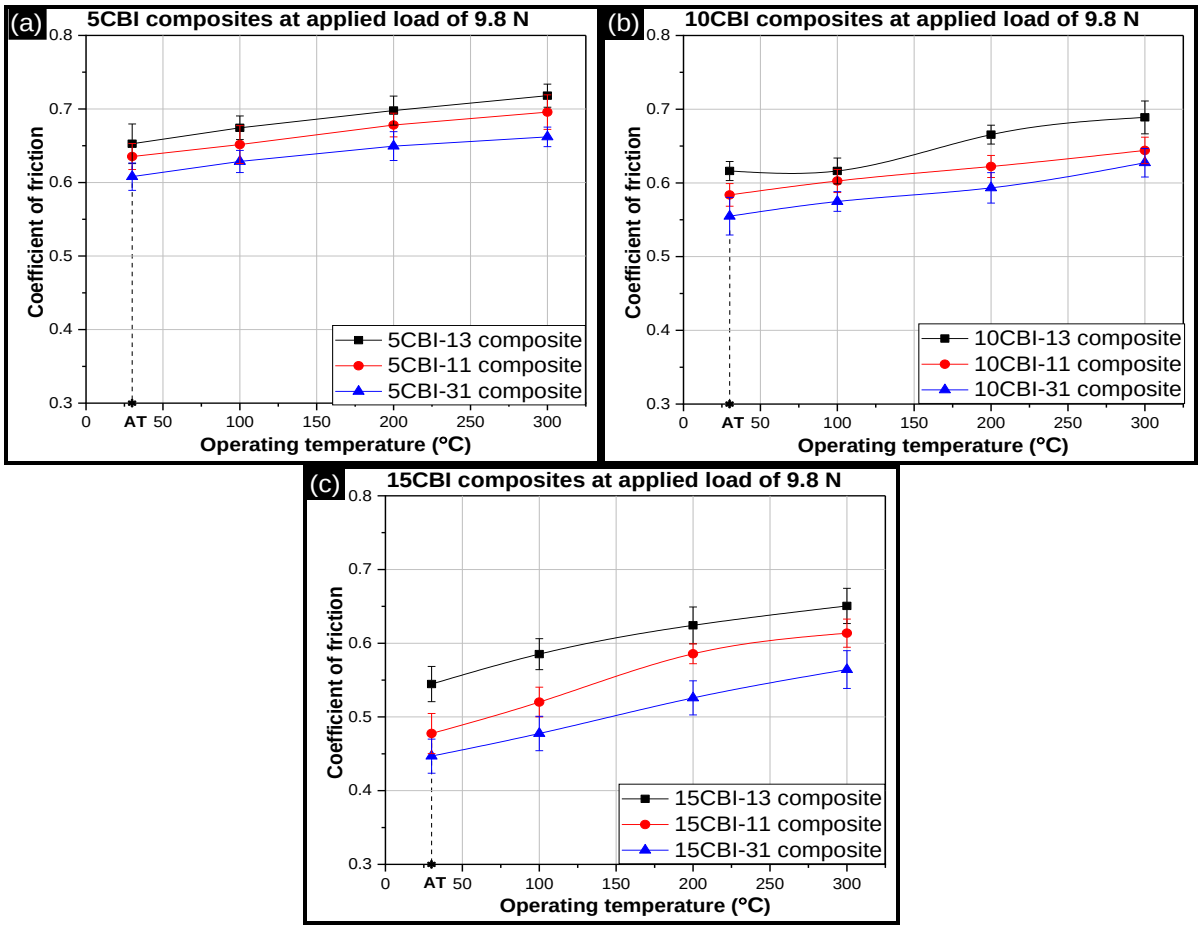

Figure 5.39 Variation in coefficient of friction values with operating temperature for (a) '5CBI' composites, (b) '10CBI' composites and (c) '15CBI' composites at various mixing proportions of reinforcement mixture and an applied load of 9.8 N.

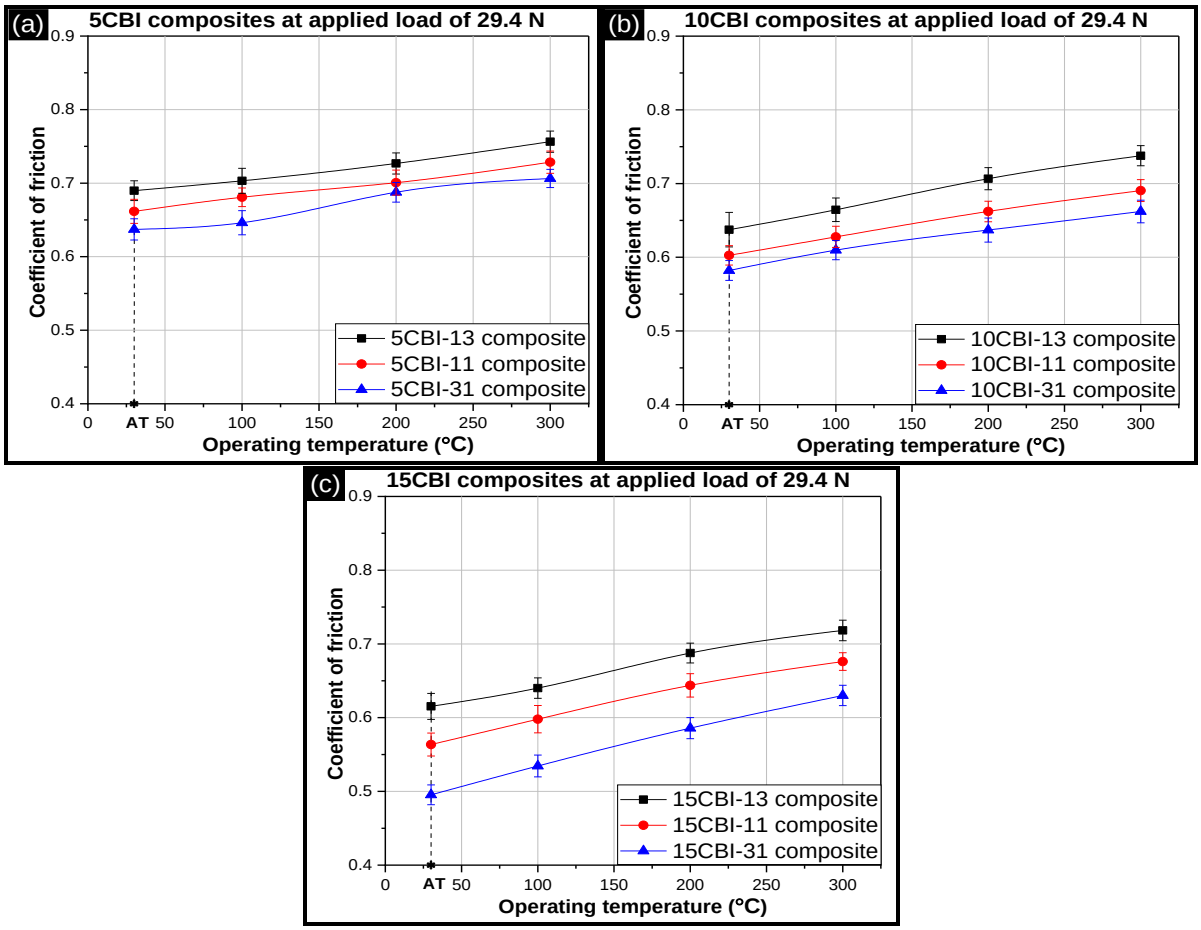

Figure 5.40 Variation in coefficient of friction values with operating temperature for (a) '5CBI' composites, (b) '10CBI' composites and (c) '15CBI' composites at various mixing proportions of reinforcement mixture and an applied load of 29.4 N.

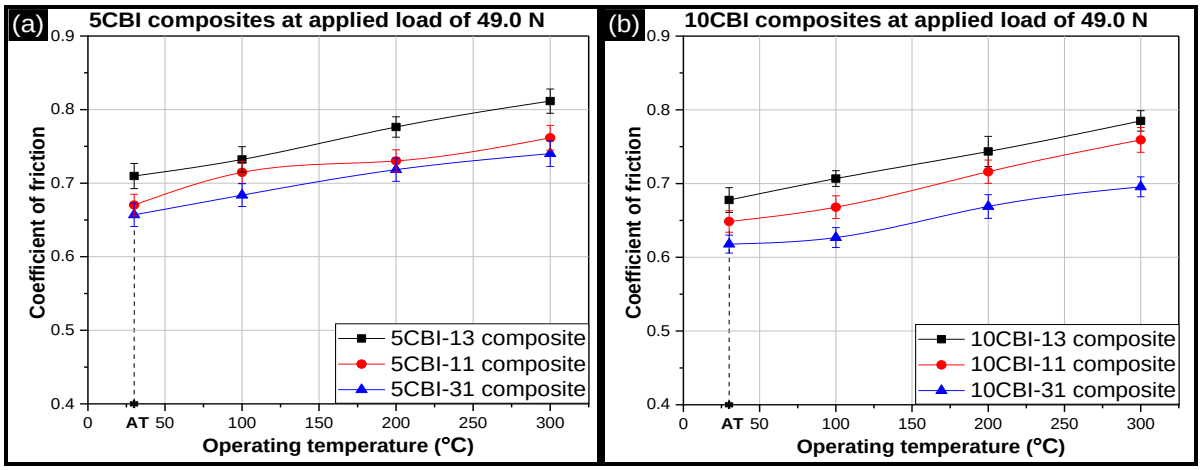

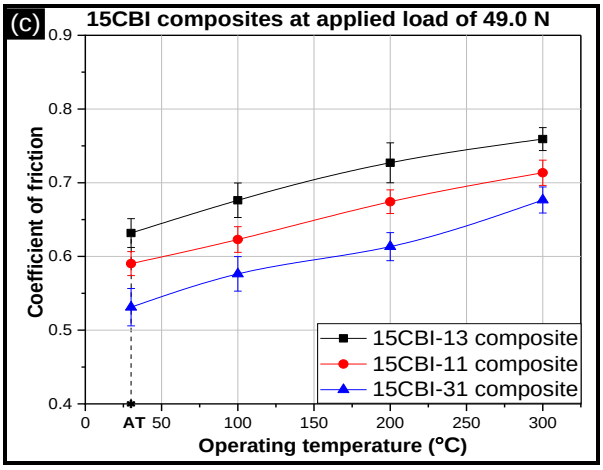

Figure 5.41 Variation in coefficient of friction values with operating temperature for (a) '5CBI' composites, (b) '10CBI' composites and (c) '15CBI' composites at various mixing proportions of reinforcement mixture and an applied load of 49.0 N.

The decrease in COF values with increase in reinforcement level and/or increase in boron carbide particles in the reinforcement mixture is process dependent parameter. COF value depends on the exposure of base alloy to the counter steel disc and formation of oxide layer. During sliding wear, multiple point contacts were made between base alloy and counter steel disc which adhered to each other. These bonded junctions were broken under the action of shear stress caused by relative motion between the two sliding surfaces. The increase in number of junctions led to rise in shear stress which correspond to increase in COF value. Further, the breaking of junctions led to dissipation of mechanical energy which resulted in generation of heat at the point of contacts [76,205]. This heat was responsible for rise in temperature at the contact of two sliding surfaces. The rise in temperature was so significant that it resulted in formation of a protective oxide layer on the composite pin surface. This oxide layer created a lubricity effect between the two sliding surfaces and helped in reducing the COF of AMCs [24,206]. Similar observations were reported in discussions on single particle reinforced AMCs in Chapter 4.

On addition of reinforced particles, the matrix material was less exposed to the counter steel disc surface. This reduced the amount of heat generated through breaking of junction points. However, the lower thermal conductivity of reinforced particles restricted the flow of heat for formation of oxide layer on the sliding surface of AMCs. Hence, the reduction in exposure of base alloy and formation of oxide layer for 'CBI' composites resulted in reduction of COF values. The attainment of lowest COF value for '15CBI-31' composite signified that the reduction in exposure of base alloy due to presence of high number of reinforced particles had more pronounced effect on COF values of AMCs. The increase in COF value with rise in

operating temperature and applied load was attributed to decrease in stability of oxide layer and increase in adhesion junctions.

5.9.2 Dual particle reinforced composites containing fine particles

Figure 5.42, Figure 5.43, and Figure 5.44 present the coefficient of friction (COF) values of hybrid AMCs containing 'fine' particles ('FBI' composites) as a function of operating temperature for various reinforcement levels and mixing proportions at applied loads of 9.8 N, 29.4 N, and 49.0 N respectively.

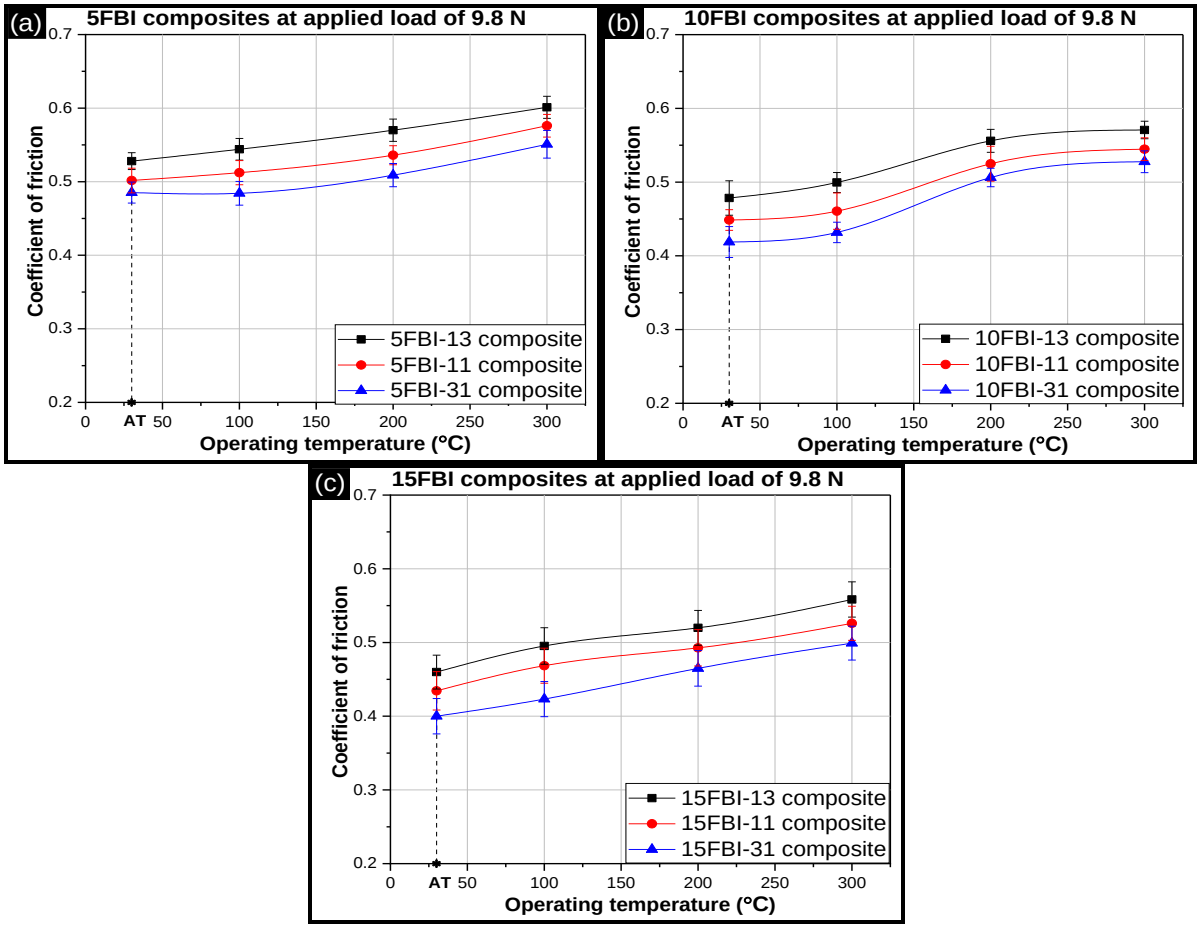

Figure 5.42 Variation in coefficient of friction values with operating temperature for (a) '5FBI' composites, (b) '10FBI' composites and (c) '15FBI' composites at various mixing proportions of reinforcement mixture and an applied load of 9.8 N.

The coefficient of friction for all the samples showed an increasing trend with rise in operating temperature for a particular applied load condition. Further, increase in applied load condition at a given operating temperature resulted in rise in COF values for all compositions of AMCs. For a particular reinforcement level, operating temperature and applied load, the rise in proportion of boron carbide particles led to decrease in COF values. Further, for a given mixing

proportion, operating temperature and applied load, increase in reinforcement level resulted in reduction of COF values. The trends observed for COF values of hybrid AMCs containing 'fine' particles ('FBI' composites) were similar to the trends observed in AMCs containing 'coarse' particles ('CBI' composites). The reasons for change in COF of hybrid AMCs containing 'fine' particles were the same as discussed in Section 5.9.1.

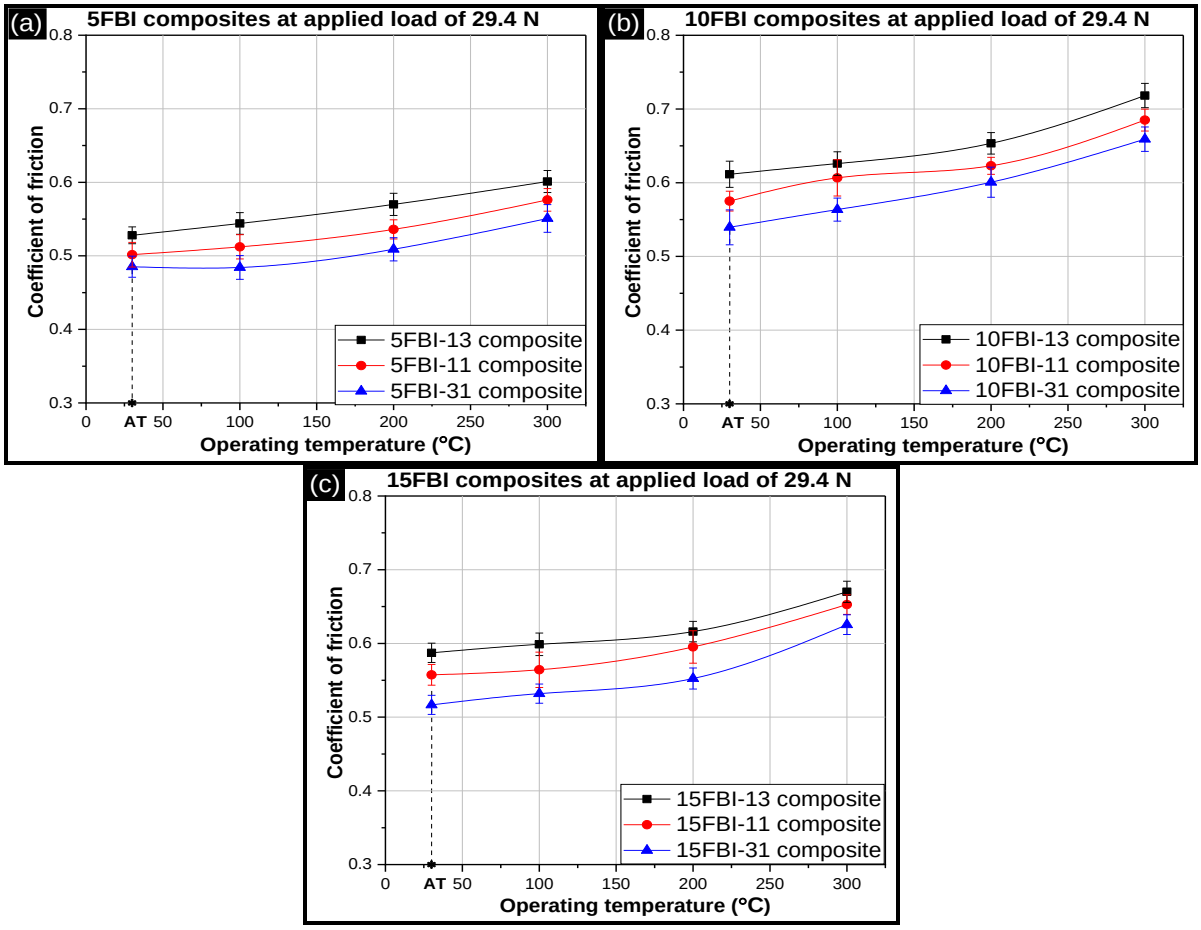

Figure 5.43 Variation in coefficient of friction values with operating temperature for (a) '5FBI' composites, (b) '10FBI' composites and (c) '15FBI' composites at various mixing proportions of reinforcement mixture and an applied load of 29.4 N.

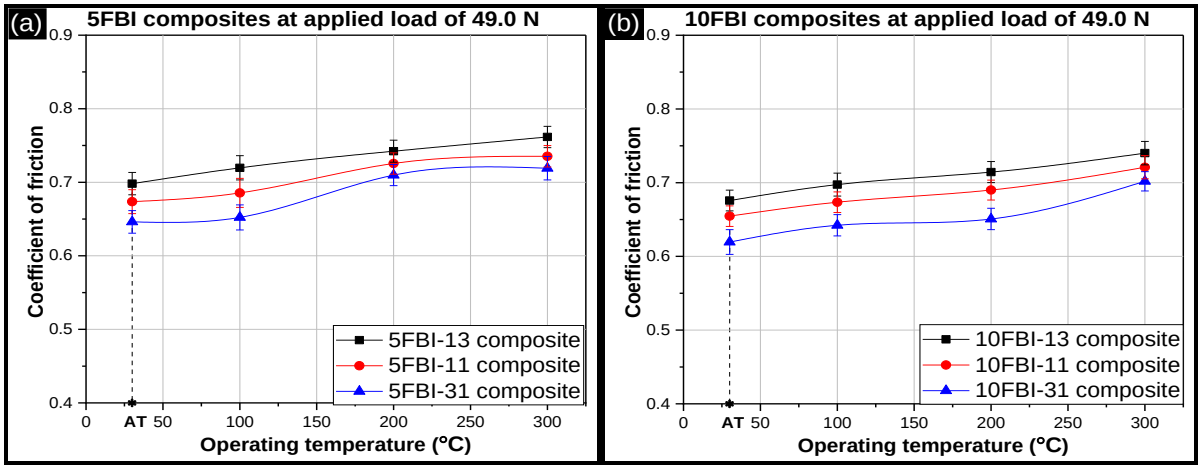

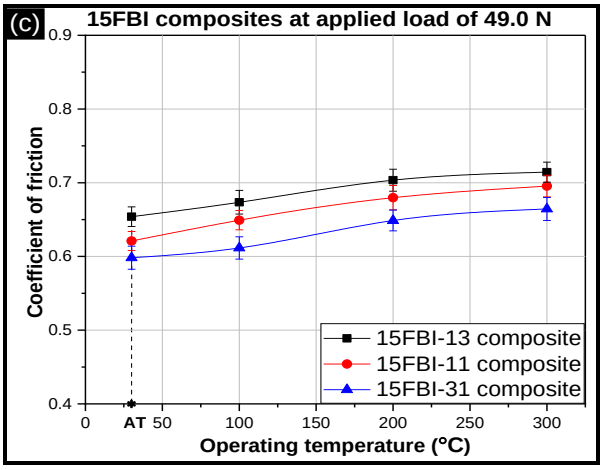

Figure 5.44 Variation in coefficient of friction values with operating temperature for (a) '5FBI' composites, (b) '10FBI' composites and (c) '15FBI' composites at various mixing proportions of reinforcement mixture and an applied load of 49.0 N.

For a given reinforcement level and mixing proportion, the change in particle size from 'coarse' to 'fine' resulted in lower COF values for hybrid AMCs at a given operating temperature-applied load condition. This behaviour was attributed to the reduction in exposure of base alloy to counter steel disc and formation of oxide layer on sliding surface due to restriction in flow of heat generated due to breaking of adhesion junctions as discussed in Section 5.9.1. Both the mechanisms were dominant in AMCs containing 'fine' particles as the number of particles per unit reinforcement level was more as compared to AMCs containing 'coarse' particles. Hence, the COF of 'FBI' composites was lower than the 'CBI' composites.

5.10. Wear-tracks and debris under high temperature conditions

5.10.1 Dual particle reinforced composites containing coarse particles

Figure 5.45 presents the SEM micrographs of wear-tracks and wear-debris of AMCs containing 'coarse' particles with maximum reinforcement level and maximum proportion of boron carbide in the reinforcement mixture ('15CBI-31' composite) tested under different applied load conditions at operating temperature of 200 ℃. Figure 5.45a and Figure 5.45b show the wear-tracks of '15CBI-31' composite at an applied load of 9.8 N and 49.0 N respectively. Both the surfaces showed presence of features like micro-cracks, craters, grooves, and trapped debris. The presence of craters indicated convergence of multiple micro-cracks. As the sliding distance increased, the micro-cracks as shown in Figure 5.45, started propagating and merged at a node causing removal of material and leaving behind craters. Some of the debris got trapped between the sliding surfaces. Under the action of applied load, these debris got hardened and acted as abrasive particles. This led to generation of grooves on the sliding

surfaces [195,196]. It can be concluded from the above discussion that delamination wear was the dominant wear mechanism for material removal from the pin surface.

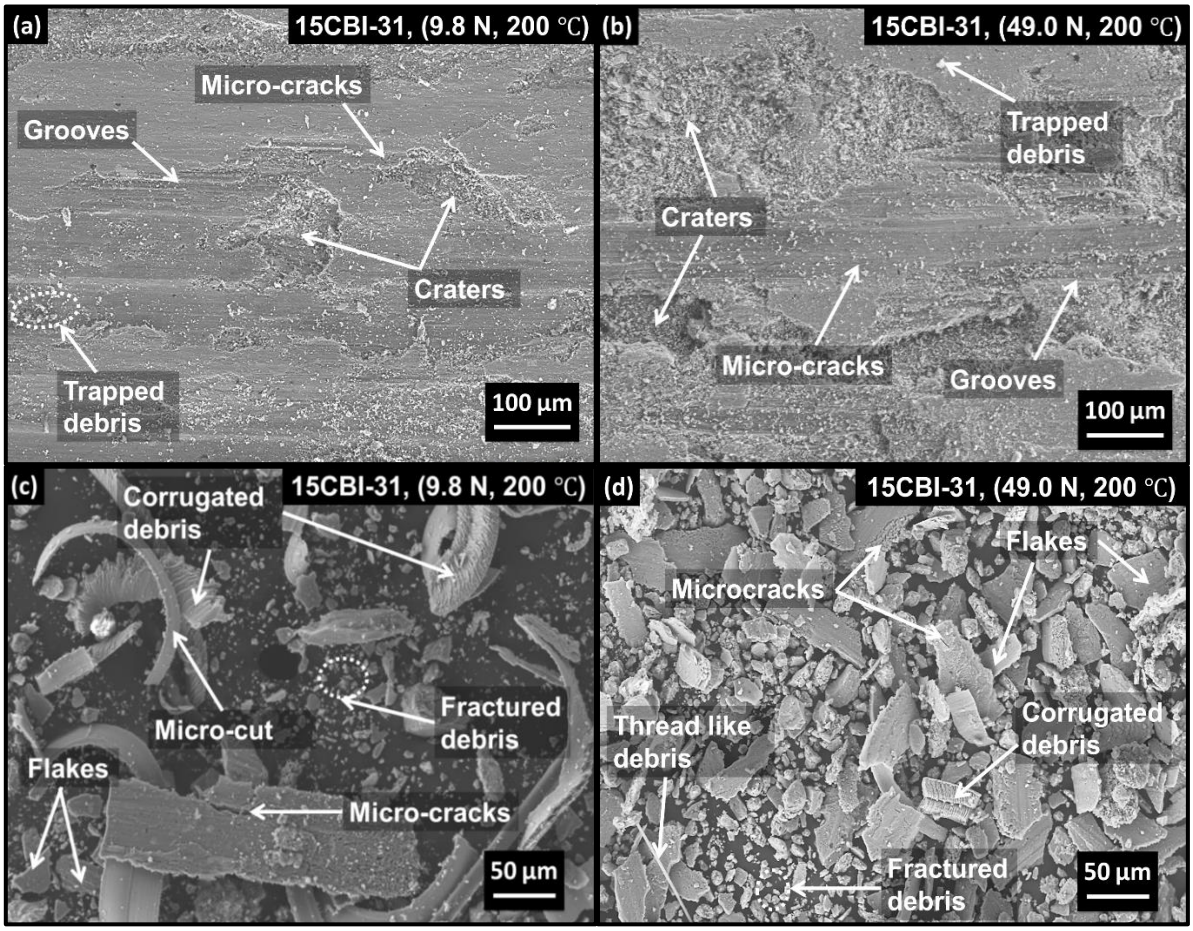

Figure 5.45 SEM images of '15CBI-31' composite for (a) wear-track at 9.8 N & 200 ℃, (b) wear-track at 49.0 N & 200 ℃, (c) wear-debris at 9.8 N & 200 ℃, and (d) wear-debris at 49.0 N & 200 ℃.

The wear-debris of '15CBI-31' composite obtained at an applied load of 9.8 N and 49.0 N are presented by Figure 5.45c and Figure 5.45d respectively. Debris at both the applied loads showed presence of features like flakes-like debris, micro-cuts, micro-cracks, corrugated debris, fractured debris, and thread-like debris. The presence of micro-cracks on flakes justified that removal of material happened due to convergence of these cracks which also resulted in formation of flake-like debris [13,202]. The presence of fractured debris, micro-cuts, and thread-like debris were attributed to entrapment of debris between the two sliding surfaces [80]. Under the influence of applied load, these entrapped debris broke into smaller debris and resulted in formation of fractured debris. Further, these debris also acted as abrasive particles which removed the material from sliding surface in the form of micro-cuts and threads [13]. The presence of corrugated debris was ascribed to the cyclic plastic deformation of the sliding

surface. This resulted in removal of material in different layers and each layer was formed after completion of one cycle [24]. The roughness profile of worn surface of '15CBI-31' composite is shown in Figure 5.46. The roughness of worn surface showed an increase in value with rise in applied load. This increase in deformation signifying the change in mechanism form abrasive to adhesive. At 9.8 N applied load, worn surface showed an average roughness value of 2.27±0.11 µm which increased to 2.80±0.25 µm at an applied load of 49.0 N.

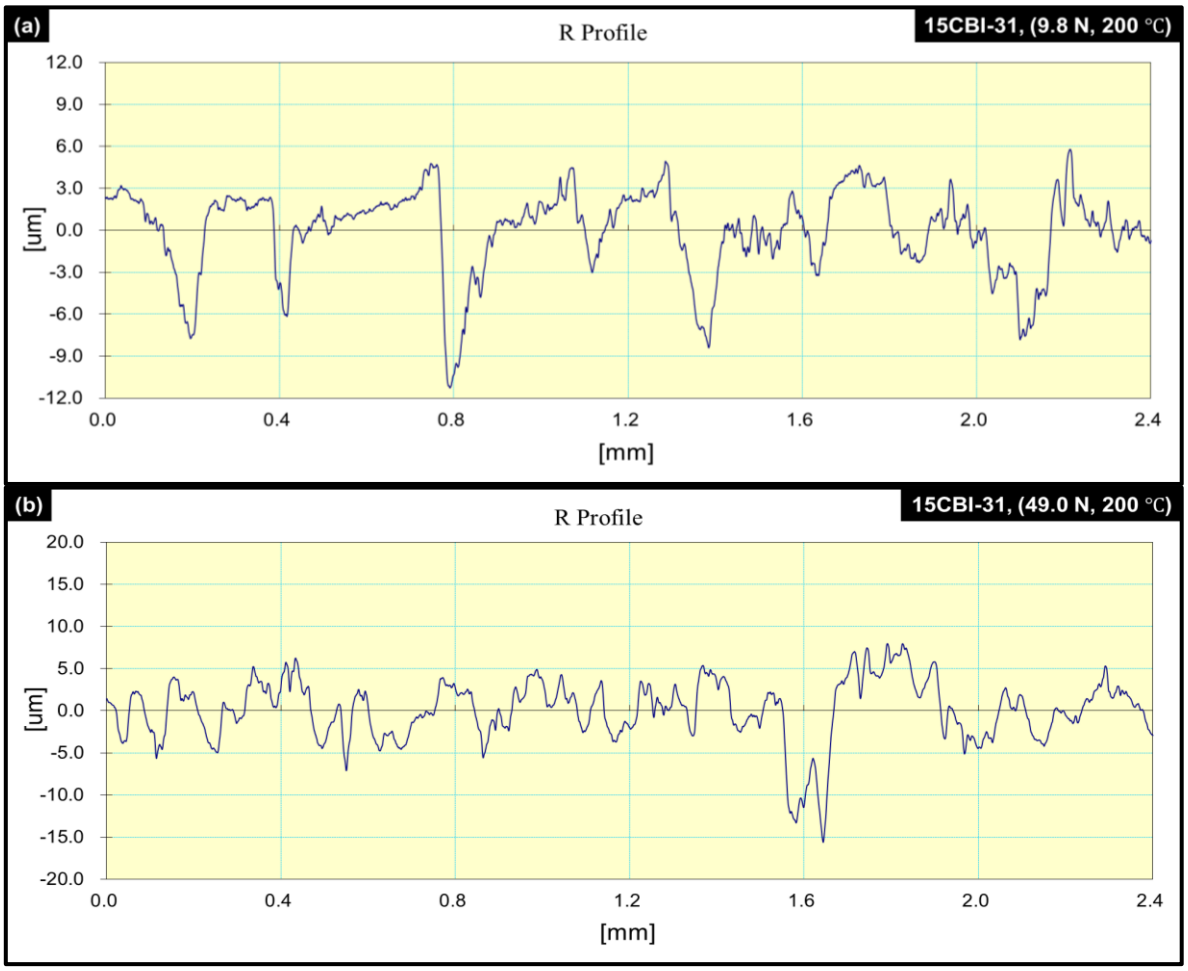

Figure 5.46 Roughness profiles of worn surfaces of '15CBI-31' composite at (a) 9.8 N & 200 ℃ and (b) 49.0 N & 200 ℃.

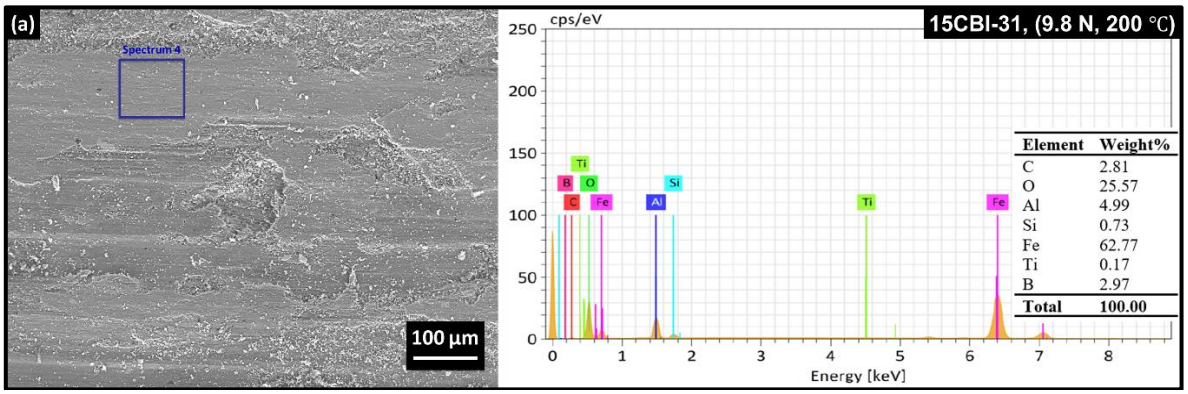

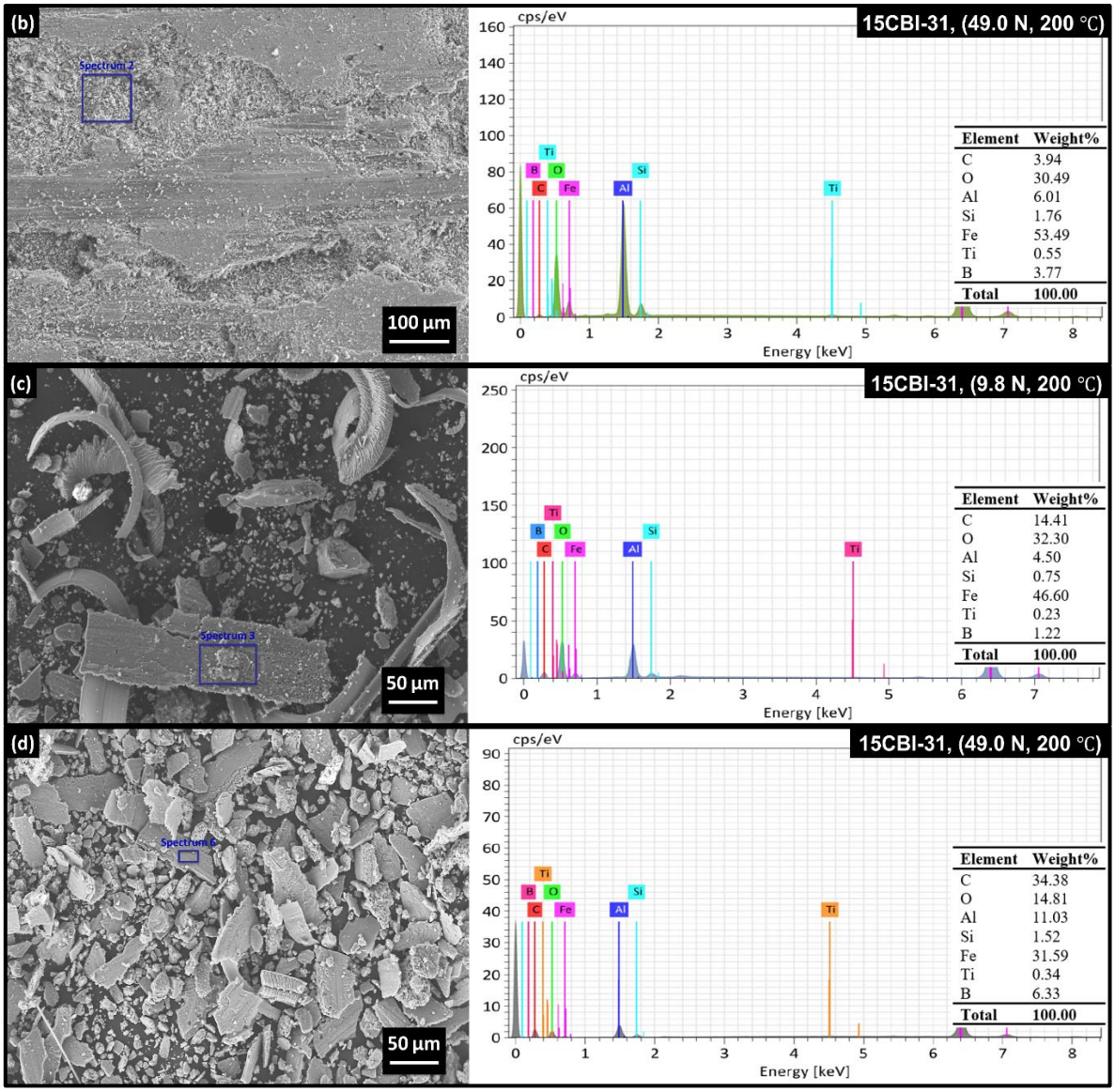

Figure 5.47 SEM-EDS analysis of '15CBI-31' composite for (a) wear-track at 9.8 N & 200 ℃, (b) wear-track at 49.0 N & 200 ℃, (c) wear-debris at 9.8 N & 200 ℃, and (d) wear-debris at 49.0 N & 200 ℃.

The SEM-EDS of wear-tracks and debris for '15CBI-31' composite at different applied loads is shown in Figure 5.47. For all the testing conditions, the elements observed on wear tracks and debris included aluminium, silicon, titanium, boron, carbon, iron, and oxygen. In elemental analysis, the source of iron and carbon was the sum total of these elements coming from reinforced particles (ilmenite and boron carbide) and counter steel disc. Similarly, the weight percentage of oxygen was the sum of oxygen present in reinforced particles of ilmenite and oxides formed due to oxidation. After deducting the amount of elements coming from reinforced particles, the revised weight percentage of iron, carbon and oxygen on sliding surface of '15CBI-31' composite at 9.8 N load was 62.69 wt.%, 1.41 wt.% and 25.35 wt.% respectively whereas for 49.0 N load, the values were 53.26 wt.%, 2.16 wt.% and 29.77 wt.%

respectively. On the other hand, the same elemental composition for debris at 9.8 N load was 46.50 wt.%, 13.83 wt.% and 32.00 wt.% respectively and for 49.0 N, the values were 31.44 wt.%, 31.39 wt.% and 14.37 wt.% respectively. The occurrence of elements like iron and carbon on wear tracks and debris signified the transfer of material between the two counter surfaces. This resulted in formation of mechanical mixed layer (MML) which restricted the exposure of pin surface to the counter steel disc for reduction in the wear rate value. Further, the existence of oxygen on the sliding surface signified the formation of various oxides on the sliding surfaces. The function of oxide formation was the same as is performed by the MML.

5.10.2 Dual particle reinforced composites containing fine particles

Figure 5.48 presents the SEM micrographs of wear-tracks and wear-debris of AMCs containing 'fine' particles with maximum reinforcement level and maximum proportion of boron carbide in the reinforcement mixture ('15FBI-31' composite) tested under different applied loads (9.8 N and 49.0 N) and operating temperature of 200 ℃. The wear-track of '15FBI-31' composite at 9.8 N applied load showed presence of grooves along with delaminated areas, trapped debris, and micro-cracks as shown in Figure 5.48a. The presence of grooves were attributed to entrapment of hard debris and reinforced particles. The hardened debris and particles were observed on the sliding surface in the form of trapped debris. These particles acted as abrasives which ploughed the surface during sliding wear. In addition to this, the thermal softening of matrix by the high operating temperature led to formation of adhesion joints between the two surfaces under the action of applied load. The continuous sliding of surfaces broke the joints and left behind the delaminated areas and micro-cracks. Delaminated areas due to wear were much more at higher load of 49.0 N.

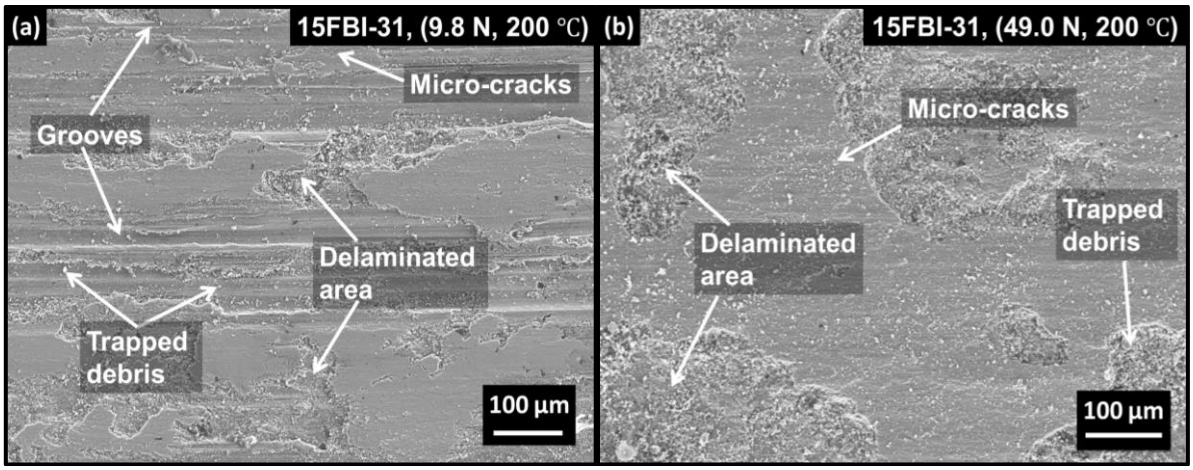

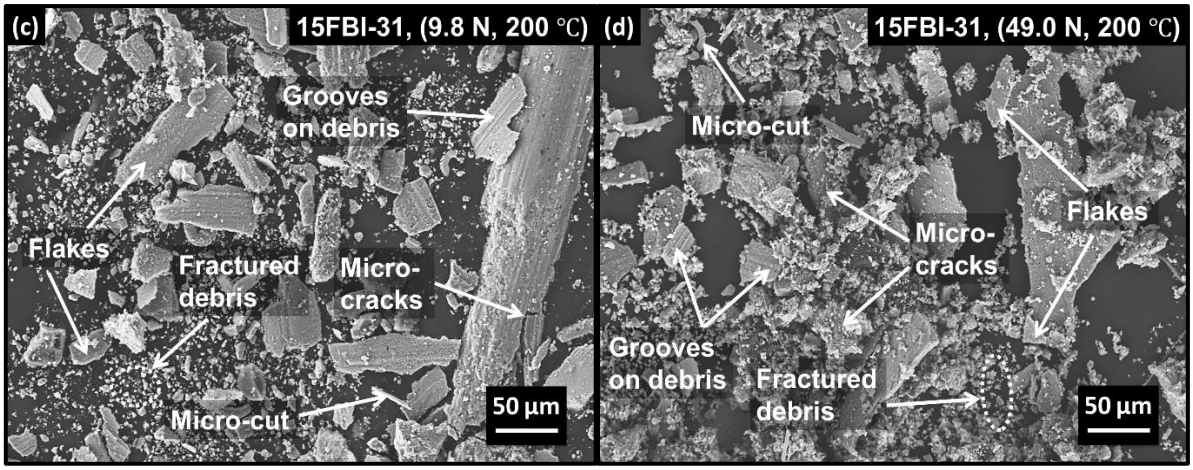

Figure 5.48 SEM images of '15FBI-31' composite for (a) wear-track at 9.8 N & 200 ℃, (b) wear-track at 49.0 N & 200 ℃, (c) wear-debris at 9.8 N & 200 ℃, and (d) wear-debris at 49.0 N & 200 ℃.

SEM images of wear-debris of '15FBI-31' composite and steel disc are shown in Figure 5.48c–d. Flake-like debris, fractured debris, micro-cuts, micro-cracks, and grooves on debris like features were observed in wear-debris obtained at both the applied load conditions. The formation of flake-like debris was attributed to merging of micro-cracks. Merging of micro-cracks were also responsible for generation of grooves on debris. In this case, surface was initially ploughed by trapped debris which got worn out after the convergence of micro-cracks. During ploughing action, trapped debris also removed the matrix material in the form of micro-cuts. These trapped debris under the action of applied load got fractured and led to formation of fractured debris. With increase in applied load, the tendency of generation and convergence of micro-cracks increased which led to formation of relatively finer debris at 49.0 N applied load in comparison to 9.8 N applied load condition. Also at higher load, there was reduction in size of fractured debris as shown in Figure 5.48c–d.

Figure 5.49 presents the roughness profiles of worn surfaces of '15FBI-31' composite at extreme load conditions of 9.8 N and 49.0 N. The worn surface of '15FBI-31' composite showed a roughness value of 1.60±0.09 µm at an applied load of 9.8 N. This roughness value increased with rise in applied load to 49.0 N. At an applied load of 49.0 N, worn surface showed a roughness value of 2.23±0.22 µm. The increase in roughness value signified the increase in plastic deformation of sliding surfaces with rise in applied load and operating temperature.

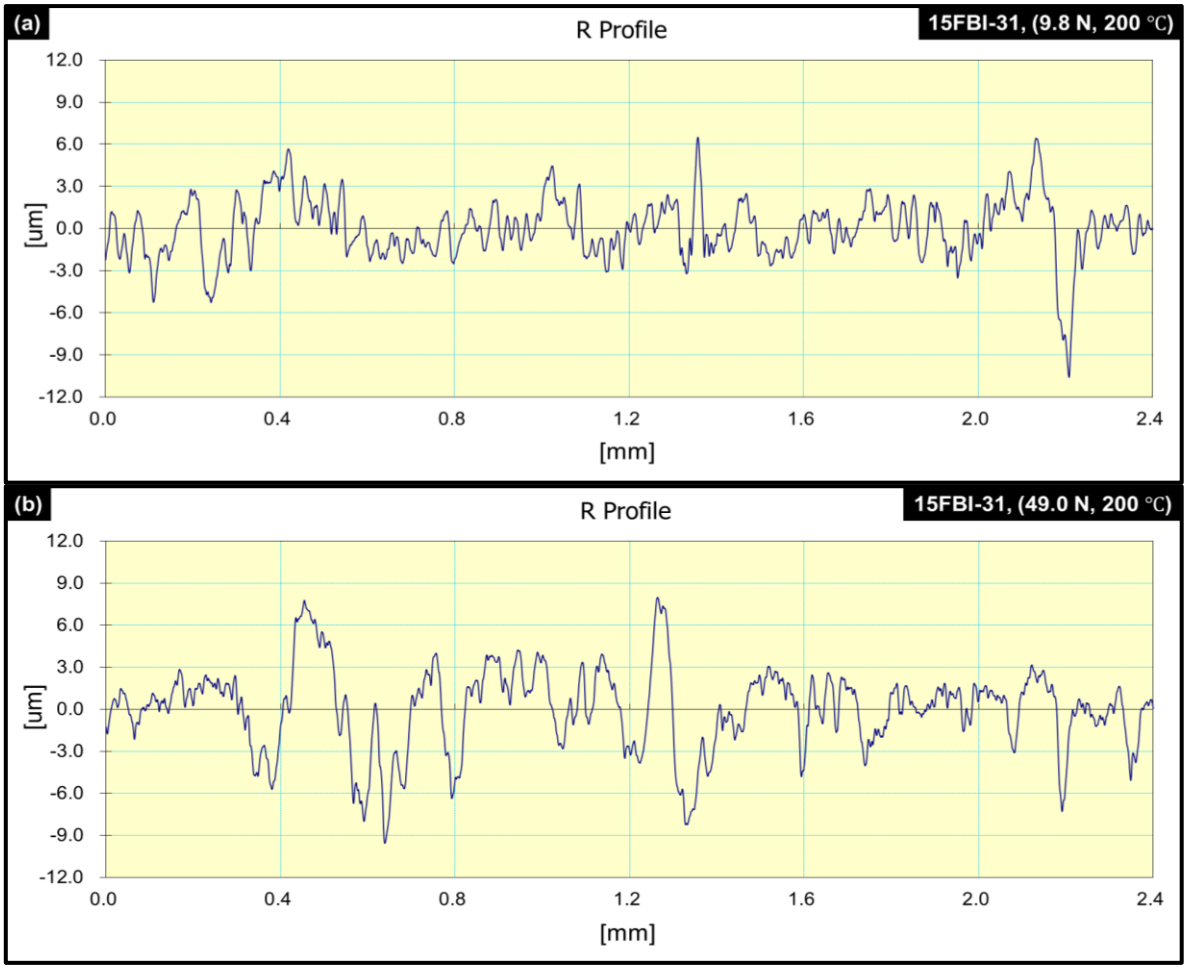

Figure 5.49 Roughness profiles of worn surfaces of '15FBI-31' composite at (a) 9.8 N & 200 ℃ and (b) 49.0 N & 200 ℃.

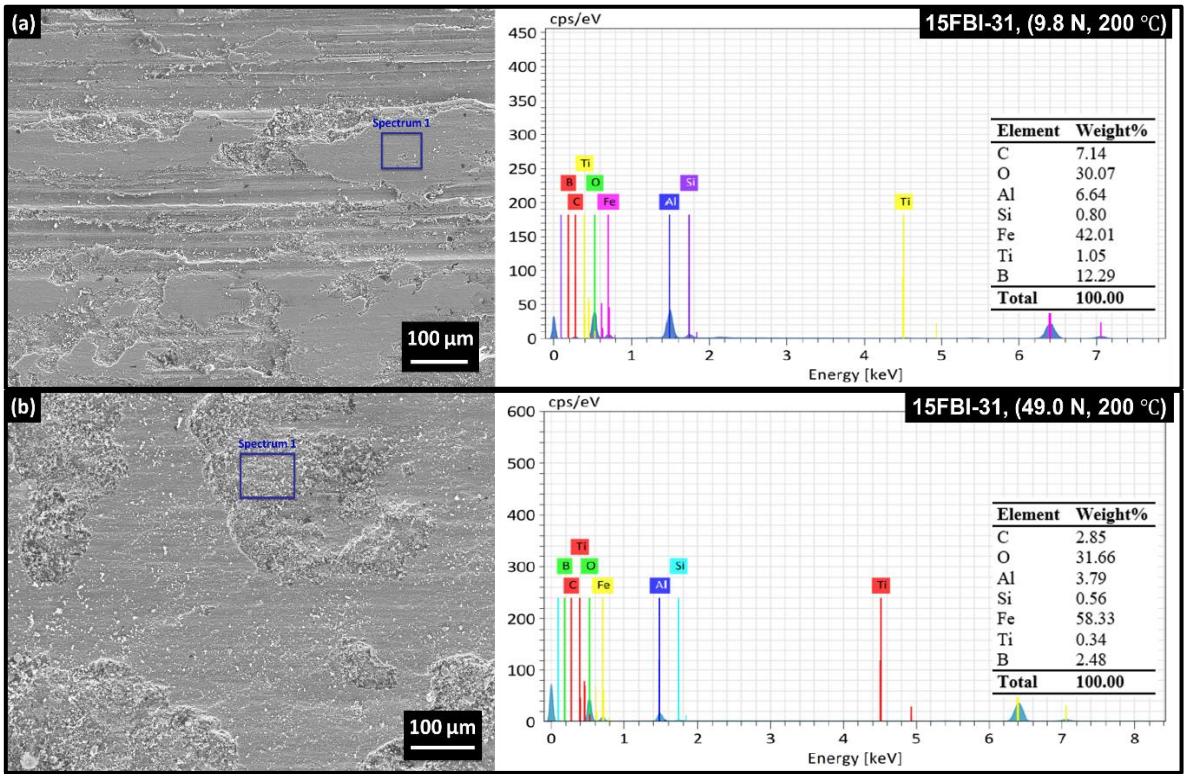

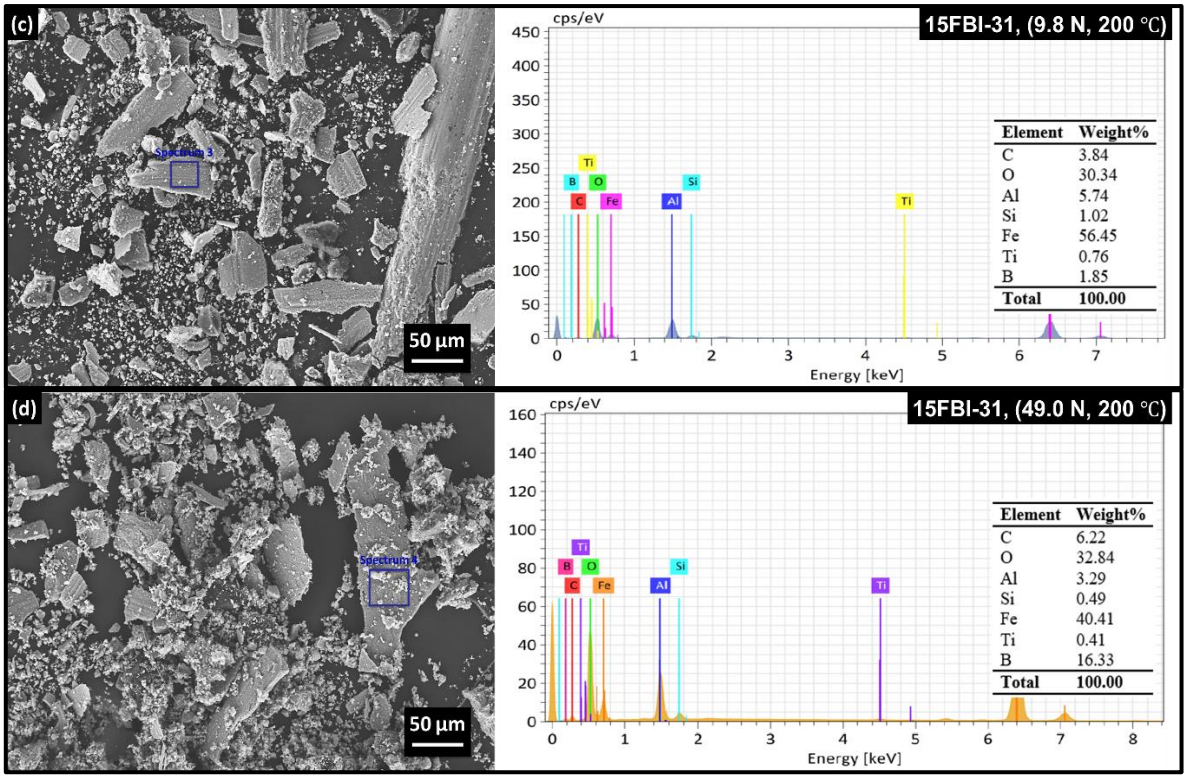

Figure 5.50 SEM-EDS analysis of '15FBI-31' composite for (a) wear-track at 9.8 N & 200 ℃, (b) wear-track at 49.0 N & 200 ℃, (c) wear-debris at 9.8 N & 200 ℃, and (d) wear-debris at 49.0 N & 200 ℃.

The SEM-EDS of wear-tracks and debris for '15FBI-31' composite at different applied loads is shown in Figure 5.50. As discussed in Section 5.10.1, the amount of elements coming from reinforced particles was deducted from the weight percentage of iron, carbon, and oxygen shown in the EDS spectrum. The revised weight percentage of iron, carbon and oxygen on the sliding surface of '15FBI-31' composite at 9.8 N applied load was noted as 41.57 wt.%, 1.19 wt.%, and 28.71 wt.% whereas for 49.0 N applied load, the values were 58.18 wt.%, 1.64 wt.%, and 31.22 wt.% respectively. For wear-debris at 9.8 N applied load, the calculated values of weight percentage of iron, carbon and oxygen were 56.13 wt.%, 2.94 wt.%, and 29.35 wt.% whereas for 49.0 N applied load, the values were 40.24 wt.%, 1.69 wt.%, and 32.31 wt.%, respectively. The presence of iron and carbon on wear-tracks and debris of '15FBI-31' composite signified transfer of material from the steel disc. This also signified formation and removal of protective mechanical mixed layer on/from the sliding surface. In addition to this, the occurrence of oxygen signified the formation of oxides of matrix and counter steel disc. The formation of oxides served the same purpose as is performed by the MML. With rise in applied load and operating temperature, the rate of material transfer and oxidation showed an increasing trend.

The next chapter presents the key findings from the present research. The main results and conclusions drawn from the analysis of various characterization procedures (SEM-EDS, XRD, and optical microscopy) and testing (nanohardness, CTE, wear rate, and friction behaviour) of different AMCs have been discussed. The main limitations of the research and the future scope have also been presented.

Chapter 6
CONCLUSIONS

Overview

This chapter summarizes the key findings of the present research work. Single particle as well as hybrid AMCs were processed by varying the type of reinforcement, reinforcement level, and also mixing proportion of boron carbide and ilmenite particles in the reinforcement mixture for hybrid composites. The developed composites were characterized and tested for their application as wear resistant materials. The main conclusions drawn from the present work are presented in this chapter. The future scope of work is also discussed.

6.1. Single particle reinforced AMCs

6.1.1 Single particle reinforced AMCs under room temperature conditions

- EDS analysis of ilmenite particles ($FeTiO_3$) showed the presence of iron, titanium, and oxygen whereas boron carbide particles (B_4C) revealed the presence of boron and carbon. Further, the chemical formula for boron carbide and ilmenite derived from the atomic percentage given by EDS was $B_{3.00–3.23}C$ and $FeTi_{1.32–1.56}O_{3.29–3.36}$ respectively. The derived chemical formulae and the occurrence of no other element confirmed 100% purity of the two reinforcing particles.
- The particle size distribution of boron carbide particles showed the average particle size as 25.52±3.48 µm for 'fine' particles and 115.64±5.70 µm for 'coarse' particles. Similarly, the average particle size for ilmenite particles was 25.24±2.85 µm and 116.60±5.72 µm respectively. Thus, the particles (both of boron carbide and ilmenite) were categorized into two broad categories of 'coarse' and 'fine'.
- XRD analysis revealed that addition of ilmenite particles to the base alloy resulted in occurrence of interfacial reaction between the matrix and reinforced ilmenite particles. This led to formation of SiO_2, FeO, and $TiSi_2$ around the interfacial region which increased the wetting nature of ilmenite particles with the matrix material. This resulted in formation of strong interfacial bonding in ilmenite based 'IR' composites in comparison to boron carbide based 'BR' composites.
- XRD analysis revealed that addition of reinforced particles to the base alloy increased the crystallinity and reduced the crystallite size of AMCs. Further, boron carbide reinforced 'BR' composites showed relatively higher crystallinity and lower crystallite size compared to ilmenite reinforced 'IR' composites. These results indicated that reinforcement of boron carbide had more significant effect for grain refinement and higher hardness of AMCs. Further, these effects were more pronounced with addition of 'fine' particles as reinforcements.
- Optical micrographs showed that both type of reinforced particles were uniformly distributed in the matrix material in the processed AMCs. Moreover, the reinforced particles were observed in the vicinity of eutectic silicon. Reinforcement of particles caused grain refinement and also change in morphology of eutectic silicon from flake type to nearly globular. These effects were more prominent in boron carbide based 'BR' composites. '15FBR' and '15FIR' composites showed a grain size reduction of 77% and 67% respectively over the base alloy.

- Vickers hardness of AMCs was higher than that of base alloy. For 'IR' and 'BR' composites, increase in reinforcement level showed an increasing trend in hardness values. Maximum increase in hardness was obtained on addition of 'fine' particles of boron carbide in the LM13 alloy. '15FBR' and '15FIR' composites showed an increase of 41% and 35% in hardness respectively over LM13 alloy.
- For any given temperature rise in the range of 50 to 300 ℃, coefficient of thermal expansion (CTE) of AMCs was lesser than base alloy and decreased with increasing reinforcement level and also with decreasing particle size, for both type of reinforcements (ilmenite and boron carbide). Maximum reduction in average CTE value of AMCs over the base alloy (for the range of 50 to 300 ℃) was 60.02% and 49.67% respectively for '15FBR' and '15FIR' composites.
- For any given temperature rise in the range of 50 to 300 ℃, CTE of 'IR' composites showed a continuous increase. However, 'BR' composites showed a typical behaviour with regards to CTE values. For rise in temperature till 100 ℃, CTE values showed a significant rise. However, beyond 100 ℃, 'BR' composites showed a steady decrease in CTE values. This behavior was attributed to the lower affinity of silicon for boron carbide particles which enhanced the solid solubility of silicon in LM13 alloy.
- The wear rate behaviour of AMCs over the entire sliding distance of 0−3000 m was categorized into three different regions showing, (a) sharp rise in wear rate, (b) sharp decrease in wear rate, and (c) steady state wear rate. For a given range of sliding distance, wear rate of AMCs increased with increase in applied load. Further, at a particular applied load, wear rate decreased with increase in reinforcement level and decrease in particle size of reinforced particles. For this reason, the highest percentage decrease in wear rate of AMCs over the base alloy was shown by '15FBR' composite (74% less than LM13 alloy) and '15FIR' composite (70% less than LM13 alloy). Here, the wear rate refers to maximum wear rate obtained at a sliding distance of 500 m and at an applied load of 29.4 N. It was concluded that both types of reinforced particles (synthetic ceramic: B_4C and natural mineral: $FeTiO_3$) were equally effective in improving the wear behaviour of resulting AMCs.
- For a given type of AMC at a given applied load, COF values decreased with increase in reinforcement level. There was further decrease in COF values at a given load with reduction in particle size of reinforcement particles from 'coarse' to 'fine'. Further, for any AMC, increase in load, increased the COF values. The highest percentage decrease in COF

values of AMCs over the base alloy was shown by '15FBR' composite (27% less than LM13 alloy) and '15FIR' composite (35% less than LM13 alloy). The lowest COF for ilmenite based 'IR' composite was attributed to formation of strong interfacial bonding between matrix and ilmenite particles. These reductions in COF values mentioned here were calculated by considering the entire sliding distance of 0−3000 m and at an applied load of 9.8 N.

6.1.2 Single particle reinforced AMCs under high operating temperature conditions

- For a given applied load and sliding distance, the wear rate of AMCs increased with rise in operating temperature from room temperature to 300 ℃. For rise in temperature till 200 ℃, a steady rise in wear rate was observed for all the samples. However, beyond 200 ℃, the rise in wear rate was significantly higher. Thus 200 ℃ was considered as the operating temperature which signified transition from 'mild' to 'severe' wear.
- The steady-state wear rate was obtained for the sliding distance of 1500−3000 m for any given operating temperature. The maximum reduction in average steady-state wear rate at transition temperature of 200 ℃ was obtained at an applied load of 29.4 N. This maximum reduction in average steady-state wear rate was shown by '15FBR' composite (82% reduction over base alloy) and '15FIR' composite (75% reduction over base alloy).
- For both types of AMCs at a given load condition, COF values increased with increase in operating temperature. Maximum reduction in COF value of AMCs over base alloy was obtained for '15FIR' composite (35% lower than base alloy) at an operating temperature of 300 ℃, applied load of 9.8 N while considering the entire sliding range of 0−3000 m. This maximum reduction in COF value of 'IR' composites again confirmed formation of strong interfacial bonding between matrix and ilmenite particles.
- The analysis of wear-tracks and debris under room temperature conditions revealed presence of grooves and delaminated area for both the loads (9.8 N and 49.0 N). However, delaminated area was more under higher applied load of 49.0 N. The presence of grooves on the sliding surface signified abrasive action performed by trapped debris whereas, delaminated area signified convergence of micro-cracks generated under the influence of applied load. Similar observations were noticed for wear-track and debris analysis at transition temperature of 200 ℃.
- EDS analysis of wear-tracks and debris showed the presence of iron and carbon. This signified the transfer of material from counter steel disc to the sliding pin surface. Further,

the presence of oxygen revealed formation of oxides due to rise in temperature by frictional heating. Both these mechanisms led to formation of MML on the sliding surface which helped in reducing the wear rate of fabricated AMCs.

6.2. Dual particle reinforced AMCs (Hybrid AMCs)

6.2.1 Dual particle reinforced hybrid AMCs under room temperature conditions

- XRD analysis revealed the formation of coherent bonding between the major constituents of base alloy (aluminium and silicon) and the reinforced particles (shown through lattice misfit). However, in case of 'IR' composites, in addition to occurrence of lattice misfit, interfacial reaction also occurred between ilmenite and matrix material. This was evident from the formation of interfacial products between ilmenite and silicon (SiO_2, Fe_3O_4, and TiO_2). This signified strong interfacial bonding between matrix and ilmenite particles as compared to that between matrix and boron carbide particles.
- Refined microstructure, change in morphology of eutectic silicon, and uniform distribution of reinforced particles was obtained for all the hybrid composites ('BI' composites). Refinement of eutectic silicon and attainment of globular morphology for eutectic silicon improved with (a) increase in reinforcement level, (b) increase in proportion of boron carbide particles in the reinforcement mixture at a given reinforcement level, and/or (c) change in particle size from 'coarse' to 'fine' particles. '15FBI-31' hybrid composite showed maximum reduction of 75% in grain size over the base alloy (grain size decreased from 34.20 µm for base alloy to 8.61 µm for '15FBI-31' hybrid composite).
- Vickers hardness of 'BI' hybrid composites increased with rise in reinforcement level and increase in proportion of boron carbide particles in the reinforcement mixture at a given reinforcement level. This behaviour was attributed to decreased grain size and increased dislocation density due to addition of reinforced particles. Further increase in hardness was obtained with change in particle size from 'coarse' to 'fine'. For this reason, '15FBI-31' composite showed the maximum improvement of 50% in hardness over the base alloy (hardness value increased from 96.11 HV for base alloy to 134.44 HV for '15FBI-31' hybrid composite).
- For a given composition of AMCs, the CTE showed an increasing trend with rise in the operating temperature. A sharp increase in CTE values was observed for temperature increase till 100 ℃. However, beyond 100 ℃, a steady rise in CTE values was observed.

This behaviour was attributed to decrease in solubility of silicon in aluminium under the presence of ilmenite particles at temperatures in excess of 100 ℃.

- The CTE of hybrid AMCs decreased with increase in reinforcement level, increase in proportion of boron carbide particles in the reinforced mixture, and change in particle size from 'coarse' to fine'. This decrease was attributed to (a) large mismatch in thermal properties of matrix and boron carbide particle, and (b) strong interfacial bonding between matrix and ilmenite particles. '15FBI-31' composite showed the lowest CTE value (considering the entire temperature range) which was 55% lower than the base alloy.
- The wear rate and COF values of 'BI' hybrid composites were lower than the base alloy under all the testing conditions. Wear rate and COF values of AMCs decreased with rise in reinforcement level, rise in proportion of boron carbide particles in the reinforcement mixture, and/or reduction in particle size. Thus, the lowest wear rate and COF values were shown by '15FBI-31' composite (80% and 46% lower than base alloy respectively at 9.8 N and room temperature conditions). These improvements were because of (a) early oxidation of sliding surface and formation of strong interfacial bonding by ilmenite particles, and (b) increased stability provided to mechanical mixed layer by boron carbide particles.

6.2.2 Dual particle reinforced hybrid AMCs under high operating temperature conditions

- For a given operating temperature, wear rate and COF values of hybrid composites showed an increasing trend with rise in applied load. Similarly, for a given applied load, wear rate and COF values showed an increasing trend with rise in operating temperature. The rise in wear rate was steady till the operating temperature of 200 ℃. However, there was a steep increase in wear rate with further rise in operating temperature. For this reason, operating temperature of 200 ℃ was considered as the 'transition' temperature where wear rate changed from 'mild' to 'severe'.
- At the transition temperature of 200 ℃ , the maximum reduction in steady-state wear rate and COF values was shown by '15FBI-31' composite (considering sliding distance of 1500–3000 m and applied load of 9.8 N). Wear rate and COF values reduced by 87% and 46% respectively over the base alloy. Wear rate behaviour improved due to increase in pinning effect by reinforced particles which reduced the effect of increased temperature on hardness of AMCs. COF values reduced due to reduction in exposure of base alloy to steel disc and the formation of oxide layer on the sliding surface.

- The wear rate of '15FBI-31' composite was comparable to that of commercially used brake rotor material (23% more than commercial material at 200 ℃ and 49.0 N). Though, the wear rate of the processed composite is slightly higher but its advantages like light-weight, low materials cost and low processing cost make it a good substitute for the commercially used material.
- Wear-tracks and debris analysis at transition temperature of 200 ℃ revealed that different mechanisms were responsible for plastic deformation of hybrid composites under different applied load conditions. At low load of 9.8 N, plastic deformation was mainly caused by ploughing action by trapped debris whereas at high load condition of 49.0 N, delamination action was mainly responsible for plastic deformation. Also, rise in surface roughness of sliding surfaces with increase in applied load signified the increase in plastic deformation of sliding surfaces.
- For all the samples, the elemental composition of wear-tracks and debris showed presence of iron, carbon, and oxygen. The presence of iron and carbon signified the formation of mechanical mixed layer (MML) by transfer of material from the counter steel disc to the sliding surface. The presence of oxygen indicated that significant rise in surface temperature occurred which caused formation of different oxides. The formation of MML and oxides helped in reducing the wear rate of AMCs.

6.3. Major conclusions

- Attempts to process dual particle reinforced hybrid AMCs containing a combination of a synthetic ceramic (boron carbide particles) and a natural mineral (ilmenite particles) using stir casting process were successful.
- Micrographs of AMCs revealed nearly uniform distribution of reinforced particles in the matrix material without any agglomeration, for both, single as well as dual particle reinforced AMCs. This indicated that the processing methodology was very effective in developing the composites.
- For each property under a given test condition, the hybrid composites ('15FBI-31' showed the best properties) showed superior results than the single particle reinforced AMCs ('15FBR' and '15FIR' composites respectively showed the best properties for single particle reinforced AMCs). This signified that each type of reinforced particles in the hybrid AMCs played a significant and diverse role in improving the properties. Boron carbide particles due to their inherent high hardness improved the hardness of AMCs and

also improved the stability of MML. Boron carbide particles also resulted in more grain refinement of eutectic silicon and changed its morphology to nearly globular. For these reasons, boron carbide was very effective in reducing the wear rate of resulting composites. On the other hand, ilmenite particles because of their inherent low thermal conductivity caused early oxidation of the pin surface and provided a protective oxide film on the surface of resulting AMCs. Also, ilmenite showed interfacial reaction with silicon of matrix material forming strong interfacial bonding between matrix-reinforced ilmenite particles. For these reasons, ilmenite was very effective in reducing the COF values of resulting composites.

- Under high temperature conditions, the reduction caused in wear rate by boron carbide particles was attributed to grain size reduction which resulted in higher restriction to crack propagation. Also, due to the low density of reinforced boron carbide particles, a large number of particles were reinforced which caused pinning effect and provided resistance to softening of the matrix at high temperatures. On the other hand, ilmenite particles provided protection to the base alloy by formation of oxide layer during the wear test, and formed strong interfacial bonding with the matrix.
- Single particle reinforced ilmenite based AMCs showed comparable wear rate (23% higher at 49.0 N and room temperature) with single particle reinforced boron carbide based AMCs. At high operating temperatures of 100 ℃, 200 ℃, and 300 ℃ at applied load of 49.0 N, the wear rates were 16%, 23%, and 30% higher respectively for ilmenite based AMCs as compared to boron carbide based AMCs. It may be noted that the cost of boron carbide is about 25 times higher than the price of ilmenite. The naturally occurring ilmenite mineral can act as an economical substitute for boron carbide reinforcement for developing economical AMCs.
- '15FBI-31' hybrid composite showed the best wear characteristics (among all type of processed composites in the present research) under all the testing conditions. Under room temperature conditions, the maximum wear rate (measured at a sliding distance of 500 m and applied load of 49.0 N) of '15FBI-31' hybrid composite was 14% lower than the commercially used brake rotor material. However, at the high operating temperature of 200 ℃ (transition temperature) and applied load of 49.0 N, the wear rate of '15FBI-31' composite was 22% higher than the brake rotor material.

6.4. Scope of future work

The focus of the present research work was to investigate the room temperature and the high temperature dry sliding wear characteristics of single as well as dual particle reinforced AMCs. The possibilities for further research in the present work are as follows:

- Vickers hardness, nanohardness, CTE, wear characteristics and friction properties of different types of AMCs were investigated in the present work. In addition to these characteristics, other properties like tensile strength, compressive strength, percentage elongation etc. can be determined in future research which will widen application of processed composites for different engineering applications.
- The present research showed that single particle reinforced AMCs containing naturally occurring mineral particles showed comparable wear characteristics and COF values as compared to AMCs containing synthetic ceramic particles. This result opens up new routes for adding various abundantly available naturally occurring minerals (sillimanite, rutile, corundum etc.) as reinforcements in metal matrix composites. Similarly, the abundantly available rare earth oxides can also act as effective reinforcement.
- In the present research, the stir-cast composites were not subjected to any type of heat treatment processes before their testing and characterization. However, in future work, the processed AMCs can be subjected to standard heat treatment processes viz. T4 and T6 treatments to note the improvement in various properties.

References

[1] Spikes, H. (2018) Stress-augmented thermal activation: Tribology feels the force. *Friction*, **6**, 1–31.

[2] Popov, V.L. and Pohrt, R. (2018) Adhesive wear and particle emission: Numerical approach based on asperity-free formulation of Rabinowicz criterion. *Friction*, **6**, 260–73.

[3] Zhang, Z., Yin, N., Chen, S. and Liu, C. (2021) Tribo-informatics: Concept, architecture, and case study. *Friction*, **9**, 642–55.

[4] Liu, H., Yang, B., Wang, C., Han, Y. and Liu, D. (2023) The mechanisms and applications of friction energy dissipation. *Friction*, **11**, 839–64.

[5] Lontin, K. and Khan, M. (2021) Interdependence of friction, wear, and noise: A review. *Friction*, **9**, 1319–45.

[6] Samal, P., Vundavilli, P.R., Meher, A. and Mahapatra, M.M. (2020) Recent progress in aluminum metal matrix composites: A review on processing, mechanical and wear properties. *Journal of Manufacturing Processes*, **59**, 131–52.

[7] Hasan, M.S., Wong, T., Rohatgi, P.K. and Nosonovsky, M. (2022) Analysis of the friction and wear of graphene reinforced aluminum metal matrix composites using machine learning models. *Tribology International*, **170**, 107527.

[8] Anandkumar, R., Almeida, A. and Vilar, R. (2012) Microstructure and sliding wear resistance of an Al-12wt.% Si/TiC laser clad coating. *Wear*, **282**–**283**, 31–9.

[9] Behnamian, Y., Serate, D., Aghaie, E., Zahiri, R., Tolentino, Z., Niazi, H. et al. (2022) Tribological behavior of ZK60 magnesium matrix composite reinforced by hybrid MWCNTs/B_4C prepared by stir casting method. *Tribology International*, **165**, 107299.

[10] Daniel, S.A.A., Sakthivel, M., Gopal, P.M. and Sudhagar, S. (2018) Study on tribological behaviour of Al/SiC/MoS_2 hybrid metal matrix composites in high temperature environmental condition. *Silicon*, **10**, 2129–39.

[11] Mahdavi, S. and Akhlaghi, F. (2011) Effect of the graphite content on the tribological behavior of Al/Gr and Al/30SiC/Gr composites processed by in- situ powder metallurgy (IPM) method. *Tribology Letters*, **44**, 1–12.

[12] Singh, S., Singh, A., Singh, I. and Dvivedi, A. (2012) Optimization of the process parameters for drilling of metal matrix composites (MMC) using taguchi analysis. *Advanced Materials Research*, **410**, 249–52.

[13] Gupta, R., Sharma, S., Nanda, T. and Pandey, O.P. (2020) A comparative study of dry sliding wear behaviour of sillimanite and rutile reinforced LM27 aluminium alloy composites. *Materials Research Express*, **7**, 016540.

[14] Ao, M., Liu, H. and Dong, C. (2019) The effect of La_2O_3 addition on intermetallic-free aluminium matrix composites reinforced with TiC and Al_2O_3 ceramic particles. *Ceramics International*, **45**, 12001–9.

[15] Liu, Y., Wang, R., Peng, C., Cai, Z., Zhou, Z., Li, X. et al. (2021) Microstructures and mechanical properties of in-situ TiB_2/Al−xSi−0.3Mg composites. *Transactions of Nonferrous Metals Society of China*, **31**, 331–44.

[16] Monikandan, V.V., Rajendrakumar, P.K. and Joseph, M.A. (2020) High temperature tribological behaviors of aluminum matrix composites reinforced with solid lubricant particles. *Transactions of Nonferrous Metals Society of China*, **30**, 1195–210.

[17] Singh, R.K., Telang, A. and Das, S. (2020) Microstructure, mechanical properties and two-body abrasive wear behaviour of hypereutectic Al—Si—SiC composite. *Transactions of Nonferrous Metals Society of China*, **30**, 65–75.

[18] Gupta, R., Sharma, S., Nanda, T. and Pandey, O.P. (2020) Wear studies of hybrid AMCs reinforced with naturally occurring sillimanite and rutile ceramic particles for brake-

rotor applications. *Ceramics International*, **46**, 16849–59.
[19] Prabhu, S.R., Shettigar, A.K., Herbert, M.A. and Rao, S.S. (2019) Microstructure and mechanical properties of rutile-reinforced AA6061 matrix composites produced via stir casting process. *Transactions of Nonferrous Metals Society of China*, **29**, 2229–36.
[20] Shayan, M., Eghbali, B. and Niroumand, B. (2020) Fabrication of AA2024−TiO_2 nanocomposites through stir casting process. *Transactions of Nonferrous Metals Society of China*, **30**, 2891–903.
[21] Abbas, A. and Huang, S.-J. (2020) Qualitative and quantitative investigation of as-cast and aged CNT/AZ31 metal matrix composites. *JOM*, Springer US. **72**, 2272–82.
[22] Arulraj, M., Davim, J.P. and Hashmi, M.S.J. (2022) Prediction of tensile strength in squeeze casted hybrid aluminium matrix composites using conventional statistical approach. *Advances in Materials and Processing Technologies*, **8**, 2216–28.
[23] Sharma, S., Gupta, R., Nanda, T. and Pandey, O.P. (2021) Influence of two different range of sillimanite particle reinforcement on tribological characteristics of LM30 based composites under elevated temperature conditions. *Materials Chemistry and Physics*, **258**, 123988.
[24] Gupta, R., Nanda, T. and Pandey, O.P. (2022) Effect of high operating temperatures on the wear characteristics of boron carbide and ilmenite reinforced LM13 alloy based composites. *Journal of Tribology*, **144**, 101703.
[25] Garg, P., Jamwal, A., Kumar, D., Sadasivuni, K.K., Hussain, C.M. and Gupta, P. (2019) Advance research progresses in aluminium matrix composites: Manufacturing & applications. *Journal of Materials Research and Technology*, **8**, 4924–39.
[26] Torralba, J.M., Costa, C.E. and Velasco, F. (2003) P/M aluminum matrix composites: An overview. *Journal of Materials Processing Technology*, **133**, 203–6.
[27] Shirvanimoghaddam, K., Hamim, S.U., Akbari, M.K., Fakhrhoseini, S.M., Khayyam, H., Pakseresht, A.H. et al. (2017) Carbon fiber reinforced metal matrix composites: Fabrication processes and properties. *Composites Part A: Applied Science and Manufacturing*, **92**, 70–96.
[28] Zhang, B., Li, W., Li, H. and Zhang, H. (2018) Spontaneous infiltration and wetting behaviors of a Zr-based alloy melt on a porous SiC substrate. *International Journal of Minerals, Metallurgy and Materials*, **25**, 817–23.
[29] Munir, K.S., Kingshott, P. and Wen, C. (2015) Carbon nanotube reinforced titanium metal matrix composites prepared by powder metallurgy - A review. *Critical Reviews in Solid State and Materials Sciences*, **40**, 38–55.
[30] Hewitt, S.A. and Kibble, K.A. (2009) Effects of ball milling time on the synthesis and consolidation of nanostructured WC-Co composites. *International Journal of Refractory Metals and Hard Materials*, **27**, 937–48.
[31] Ghomashchi, M.R. and Vikhrov, A. (2000) Squeeze casting: An overview. *Journal of Materials Processing Technology*, **101**, 1–9.
[32] Arunachalam, R., Kumar, P. and Muraliraja, R. (2019) A review on the production of metal matrix composites through stir casting – Furnace design, properties, challenges, and research opportunities. *Journal of Manufacturing Processes*, **42**, 213–45.
[33] Rosso, M. (2006) Ceramic and metal matrix composites: Routes and properties. *Journal of Materials Processing Technology*, **175**, 364–75.
[34] Kumar, A., Kumar, S. and Mukhopadhyay, N.K. (2018) Introduction to magnesium alloy processing technology and development of low-cost stir casting process for magnesium alloy and its composites. *Journal of Magnesium and Alloys*, **6**, 245–54.
[35] Hashim, J., Looney, L. and Hashmi, M.S.J. (1999) Metal matrix composites: Production by the stir casting method. *Journal of Materials Processing Technology*, **92**, 1–7.
[36] Dewidar, M.M., Yoon, H.C. and Lim, J.K. (2006) Mechanical properties of metals for

biomedical applications using powder metallurgy process: A review. *Metals and Materials International*, **12**, 193–206.
[37] Akhlaghi, F. and Pelaseyyed, S.A. (2004) Characterization of aluminum/graphite particulate composites synthesized using a novel method termed "in-situ powder metallurgy." *Materials Science and Engineering A*, **385**, 258–66.
[38] Uthayakumar, M., Aravindan, S. and Rajkumar, K. (2013) Wear performance of Al–SiC–B_4C hybrid composites under dry sliding conditions. *Materials & Design*, **47**, 456–64.
[39] Omrani, E., Moghadam, A.D., Menezes, P.L. and Rohatgi, P.K. (2016) Influences of graphite reinforcement on the tribological properties of self-lubricating aluminum matrix composites for green tribology, sustainability , and energy efficiency — A review. *The International Journal of Advanced Manufacturing Technology*, **83**, 325–46.
[40] Suresha, S. and Sridhara, B.K. (2010) Wear characteristics of hybrid aluminium matrix composites reinforced with graphite and silicon carbide particulates. *Composites Science and Technology*, **70**, 1652–9.
[41] Elango, G., Raghunath, B.K., Palanikumar, K. and Thamizhmaran, K. (2014) Sliding wear of LM25 aluminium alloy with 7.5% SiC+2.5% TiO_2 and 2.5% SiC+7.5% TiO_2 hybrid composites. *Journal of Composite Material*, **48**, 2227–36.
[42] Ebrahimian-hosseinabadi, M., Azari-dorcheh, K. and Vaghefi, S.M.M. (2006) Wear behavior of electroless Ni–P–B_4C composite coatings. *Wear*, **260**, 123–7.
[43] Anandkumar, R., Almeida, A., Colaço, R., Vilar, R., Ocelik, V. and Hosson, J.T.M. De. (2007) Microstructure and wear studies of laser clad Al-Si/$SiC_{(p)}$ composite coatings. *Surface and Coatings Technology*, **201**, 9497–505.
[44] Harichandran, R., Selvakumar, N. and Venkatachalam, G. (2017) High temperature wear behaviour of nano/micro B_4C reinforced aluminium matrix composites fabricated by an ultrasonic cavitation-assisted solidification process. *Transactions of the Indian Institute of Metals*, **70**, 17–29.
[45] Pozdniakov, A. V, Lotfy, A., Qadir, A., Shalaby, E., Khomutov, M.G., Churyumov, A.Y. et al. (2017) Development of Al-5Cu/B_4C composites with low coefficient of thermal expansion for automotive application. *Materials Science & Engineering A*, **688**, 1–8.
[46] Nie, C., Gu, J., Liu, J. and Zhang, D. (2008) Investigation on microstructures and interface character of B_4C particles reinforced 2024Al matrix composites fabricated by mechanical alloying. *Journal of Alloys and Compounds*, **454**, 118–22.
[47] Baradeswaran, A. and Perumal, A.E. (2013) Influence of B_4C on the tribological and mechanical properties of Al 7075-B_4C composites. *Composites Part B: Engineering*, **54**, 146–52.
[48] Alidokht, S.A., Abdollah-zadeh, A. and Assadi, H. (2013) Effect of applied load on the dry sliding wear behaviour and the subsurface deformation on hybrid metal matrix composite. *Wear*, **305**, 291–8.
[49] Wilson, N.C., Muscat, J., Mkhonto, D., Ngoepe, P.E. and Harrison, N.M. (2005) Structure and properties of ilmenite from first principles. *Physical Review B*, **71**, 075202.
[50] Torres, B., Lieblich, M., Ibáñez, J. and García-Escorial, A. (2002) Mechanical properties of some PM aluminide and silicide reinforced 2124 aluminium matrix composites. *Scripta Materialia*, **47**, 45–9.
[51] Sharma, S., Nanda, T. and Pandey, O.P. (2018) Effect of dual particle size (DPS) on dry sliding wear behaviour of LM30/sillimanite composites. *Tribology International*, **123**, 142–54.
[52] Panwar, R.S. and Pandey, O.P. (2013) Study of wear behavior of zircon sand-reinforced LM13 alloy composites at elevated temperatures. *Journal of Materials Engineering and*

Performance, **22**, 1765–75.
[53] Lee, T., Lee, J., Lee, D., Jo, I., Lee, S.K. and Ryu, H.J. (2020) Effects of particle size and surface modification of SiC on the wear behavior of high volume fraction Al/SiC_p composites. *Journal of Alloys and Compounds*, **831**, 154647.
[54] Sharma, S., Nanda, T. and Pandey, O.P. (2018) Effect of particle size on dry sliding wear behaviour of sillimanite reinforced aluminium matrix composites. *Ceramics International*, **44**, 104–14.
[55] Rao, T.B. (2021) Microstructural, mechanical, and wear properties characterization and strengthening mechanisms of Al7075/SiCnp composites processed through ultrasonic cavitation assisted stir-casting. *Materials Science and Engineering A*, **805**, 140553.
[56] Kim, C.S., Cho, K., Manjili, M.H. and Nezafati, M. (2017) Mechanical performance of particulate-reinforced Al metal-matrix composites (MMCs) and Al metal-matrix nano-composites (MMNCs). *Journal of Materials Science*, **52**, 13319–49.
[57] Fadavi Boostani, A., Tahamtan, S., Jiang, Z.Y., Wei, D., Yazdani, S., Azari Khosroshahi, R. et al. (2015) Enhanced tensile properties of aluminium matrix composites reinforced with graphene encapsulated SiC nanoparticles. *Composites Part A: Applied Science and Manufacturing*, **68**, 155–63.
[59] Lakshmikanthan, A., Bontha, S., Krishna, M., Koppad, P.G. and Ramprabhu, T. (2019) Microstructure, mechanical and wear properties of the A357 composites reinforced with dual sized SiC particles. *Journal of Alloys and Compounds*, **786**, 570–80.
[59] Bindumadhavan, P.N., Wah, H.K. and Prabhakar, O. (2001) Dual particle size (DPS) composites: effect on wear and mechanical properties of particulate metal matrix composites. *Wear*, **248**, 112–20.
[60] Ray, A.K., Venkateswarlu, K., Chaudhury, S.K., Das, S.K., Ravi Kumar, B. and Pathak, L.C. (2002) Fabrication of TiN reinforced aluminium metal matrix composites through a powder metallurgical route. *Materials Science and Engineering A*, **338**, 160–5.
[61] Shirvanimoghaddam, K., Khayyam, H., Abdizadeh, H., Akbari, M.K., Pakseresht, A.H., Ghasali, E. et al. (2016) Boron carbide reinforced aluminium matrix composite: Physical, mechanical characterization and mathematical modelling. *Materials Science and Engineering A*, **658**, 135–49.
[62] Miracle, D.B. (2005) Metal matrix composites – From science to technological significance. *Composites Science and Technology*, **65**, 2526–40.
[63] Bajakke, P.A., Malik, V.R. and Deshpande, A.S. (2019) Particulate metal matrix composites and their fabrication via friction stir processing–a review. *Materials and Manufacturing Processes*, **34**, 833–81.
[64] Sivakumar, R., Kumar, B.R.S., Subramaniyan, G.G., Sivaraja, M., Natarajan, M.P., Patil, P.P. et al. (2022) Microstructure and mechanical behaviour of Ti-6Al-4V matrix reinforced with WC_p developed by squeeze casting. *Journal of Nanomaterials*, 6381265.
[65] Singh, S., Singh, I. and Dvivedi, A. (2013) Multi objective optimization in drilling of Al6063/10% SiC metal matrix composite based on grey relational analysis. *Proceedings of the Institution of Mechanical Engineers, Part B: Journal of Engineering Manufacture*, **227**, 1767–76.
[66] Rohatgi, P. (1991) Cast aluminum-matrix composites for automotive applications. *Journal of Minerals, Metals and Materials Society*, **43**, 10–5.
[67] Allison, E.J. and Cole, G.S. (1993) Metal matrix composites in the automotive industry: Opportunities and challenges. *Journal of Minerals, Metals and Materials Society*, **45**, 19–24.
[68] Cole, G.S. and Sherman, A.M. (1995) Lightweight materials for automotive applications. *Materials Characterization*, **35**, 3–9.
[69] Deuis, R.L., Subramanian, C. and Yellupb, J.M. (1997) Dry sliding wear of aluminium

composites - A review. *Composites Science and Technology*, **57**, 415–35.
[70] Sujith, S. V., Mahapatra, M.M. and Mulik, R.S. (2020) Microstructural characterization and experimental investigations into two body abrasive wear behavior of Al-7079/TiC in-situ metal matrix composites. *Proceedings of the Institution of Mechanical Engineers, Part J: Journal of Engineering Tribology*, **234**, 588–607.
[71] Ravi, B., Naik, B.B. and Prakash, J.U. (2015) Characterization of aluminium matrix composites (AA6061/B_4C) fabricated by stir casting technique. *Materials Today: Proceedings*, **2**, 2984–90.
[72] Suthar, J. and Patel, K.M. (2018) Processing issues, machining, and applications of aluminum metal matrix composites. *Materials and Manufacturing Processes*, **33**, 499–527.
[73] Arslan, E., Totik, Y., Demirci, E.E., Vangolu, Y., Alsaran, A. and Efeoglu, I. (2009) High temperature wear behavior of aluminum oxide layers produced by AC micro arc oxidation. *Surface & Coatings Technology*, **204**, 829–33.
[74] Umanath, K., Palanikumar, K. and Selvamani, S.T. (2013) Analysis of dry sliding wear behaviour of Al6061/SiC/Al_2O_3 hybrid metal matrix composites. *Composites Part B: Engineering*, **53**, 159–68.
[75] Ren, Q., Cui, G., Li, T., Hassani, M., Liu, Y. and Kou, Z. (2021) High-temperature wear behavior of cobalt matrix composites reinforced by LaF_3 and CeO_2. *Tribology Letters*, **69**, 149.
[76] Munagala, V.N.V., Torgerson, T.B., Scharf, T.W. and Chromik, R.R. (2019) High temperature friction and wear behavior of cold-sprayed Ti6Al4V and Ti6Al4V-TiC composite coatings. *Wear*, **426**–**427**, 357–69.
[77] Zhu, H., Jar, C., Song, J., Zhao, J., Li, J. and Xie, Z. (2012) High temperature dry sliding friction and wear behavior of aluminum matrix composites (Al_3Zr+α-Al_2O_3)/Al. *Tribology International*, **48**, 78–86.
[78] Kumar, C.A.V. and Rajadurai, J.S. (2016) Influence of rutile (TiO_2) content on wear and microhardness characteristics of aluminium-based hybrid composites synthesized by powder metallurgy. *Transactions of Nonferrous Metals Society of China*, **26**, 63–73.
[79] Kumar, S., Panwar, R.S. and Pandey, O.P. (2013) Effect of dual reinforced ceramic particles on high temperature tribological properties of aluminum composites. *Ceramics International*, **39**, 6333–42.
[80] Gupta, R., Nanda, T. and Pandey, O.P. (2021) Comparison of wear behaviour of LM13 Al−Si alloy based composites reinforced with synthetic (B_4C) and natural (ilmenite) ceramic particles. *Transactions of Nonferrous Metals Society of China*, **31**, 3613–25.
[81] Chen, G., Song, Z., Chen, J., Peng, J. and Srinivasakannan, C. (2013) Evaluation of the reducing product of carbonthermal reduction of ilmenite ores. *Journal of Alloys and Compounds*, **577**, 610–4.
[82] Al-Sabagh, A.M., Abdou, M.I., Migahed, M.A., Fadl, A.M., Farag, A.A., Mohammedy, M.M. et al. (2018) Influence of ilmenite ore particles as pigment on the anticorrosion and mechanical performance properties of polyamine cured epoxy for internal coating of gas transmission pipelines. *Egyptian Journal of Petroleum*, **27**, 427–36.
[83] Elwan, M., Fathy, A., Wagih, A., Essa, A.R.S., Abu-Oqail, A. and EL-Nikhaily, A.E. (2020) Fabrication and investigation on the properties of ilmenite ($FeTiO_3$)-based Al composite by accumulative roll bonding. *Journal of Composite Materials*, **54**, 1259–71.
[84] Zhang, Z., Topping, T., Li, Y., Vogt, R., Zhou, Y., Haines, C. et al. (2011) Mechanical behavior of ultrafine-grained Al composites reinforced with B_4C nanoparticles. *Scripta Materialia*, **65**, 652–5.
[85] Han, Z., Li, G., Tian, J. and Gu, M. (2002) Microstructure and mechanical properties of boron carbide thin films. *Materials Letters*, **57**, 899–903.

[86] Shirvanimoghaddam, K., Khayyam, H., Abdizadeh, H., Akbari, K., Pakseresht, A.H., Abdi, F. et al. (2015) Effect of B_4C, TiB_2 and $ZrSiO_4$ ceramic particles on mechanical properties of aluminium matrix composites: experimental investigation and predictive modelling. *Ceramics International*, **42**, 6206–20.
[87] Das, S., Das, S. and Das, K. (2007) Abrasive wear of zircon sand and alumina reinforced Al-4.5 wt.%Cu alloy matrix composites- A comparative study. *Composites Science and Technology*, **67**, 746–51.
[88] Arora, R., Kumar, S., Singh, G. and Pandey, O.P. (2015) Influence of particle size and temperature on the wear properties of rutile-reinforced aluminium metal matrix composite. *Journal of Composite Materials*, **49**, 843–52.
[89] Sharma, S., Nanda, T. and Pandey, O.P. (2019) Effect of elevated temperatures and applied pressure on the tribological properties of LM30/sillimanite aluminium alloy composites. *Journal of Composite Materials*, **53**, 1521–39.
[90] Avinash, L., Ramprabhu, T. and Bontha, S. (2016) The effect on the dry sliding wear behavior of gravity cast A357 reinforced with dual size silicon carbide particles. *Applied Mechanics and Materials*, **829**, 83–9.
[91] Tirth, V. (2017) Dry sliding wear behavior of 2218 Al-alloy-Al_2O_3(TiO_2) hybrid composites. *Journal of Tribology*, **140**, 021603.
[92] Abbass, M.K. and Fouad, M.J. (2015) Wear characterization of aluminum matrix hybrid composites reinforced with nanoparticles of Al_2O_3 and TiO_2. *Journal of Material Science and Engineering B*, **5**, 361–71.
[93] Aamir, M., Giasin, K., Tolouei-Rad, M. and Vafadar, A. (2020) A review: Drilling performance and hole quality of aluminium alloys for aerospace applications. *Journal of Materials Research and Technology*, **9**, 12484–500.
[94] Singh, J. and Chauhan, A. (2019) A review of microstructure, mechanical properties and wear behavior of hybrid aluminium matrix composites fabricated via stir casting route. *Sādhanā*, **44**, 1–18.
[95] Idusuyi, N. and Olayinka, J.I. (2019) Dry sliding wear characteristics of aluminium metal matrix composites: A brief overview. *Journal of Materials Research and Technology*, **8**, 3338–46.
[96] Cao, H., Ye, X., Li, H., Qi, F., Wang, Q., Ouyang, X. et al. (2021) Microstructure, mechanical and tribological properties of multilayer Ti-DLC thick films on Al alloys by filtered cathodic vacuum arc technology. *Materials and Design*, **198**, 109320.
[97] Hegde, S. and Prabhu, K.N. (2008) Modification of eutectic silicon in Al–Si alloys. *Journal of Materials Science*, **43**, 3009–27.
[98] Javidani, M. and Larouche, D. (2014) Application of cast Al-Si alloys in internal combustion engine components. *International Materials Reviews*, **59**, 132–58.
[99] Das, A. and Kotadia, H.R. (2011) Effect of high-intensity ultrasonic irradiation on the modification of solidification microstructure in a Si-rich hypoeutectic Al-Si alloy. *Materials Chemistry and Physics*, **125**, 853–9.
[100] Summer, F., Pusterhofer, M., Grün, F. and Gódor, I. (2020) Tribological investigations with near eutectic AlSi alloys found in engine vane pumps – Characterization of the material tribo-functionalities. *Tribology International*, **146**, 106236.
[101] Vijeesh, V. and Prabhu, K.N. (2014) Review of microstructure evolution in hypereutectic Al-Si alloys and its effect on wear properties. *Transactions of the Indian Institute of Metals*, **67**, 1–18.
[102] Gupta, R., Sharma, S., Nanda, T. and Pandey, O.P. (2019) A comparative study of dry sliding wear behaviour of sillimanite and rutile reinforced LM27 aluminium alloy composites. *Materials Research Express*, **7**, 016540.
[103] Gupta, R., Nanda, T. and Pandey, O.P. (2023) Tribological properties of hybrid

aluminium matrix composites reinforced with boron carbide and ilmenite particles for brake rotor applications. *Archives of Civil and Mechanical Engineering*, **23**, 1–18.
[104] Sharma, V., Kumar, S., Panwar, R.S. and Pandey, O.P. (2012) Microstructural and wear behavior of dual reinforced particle (DRP) aluminum alloy composite. *Journal of Materials Science*, **47**, 6633–46.
[105] Ahlatci, H., Kocer, T., Candan, E. and Cimenoglu, H. (2006) Wear behaviour of Al/(Al_2O_{3p}+SiC_p) hybrid composites. *Tribology International*, **39**, 213–20.
[106] Ghasali, E., Yazdani-rad, R., Asadian, K. and Ebadzadeh, T. (2017) Production of Al-SiC-TiC hybrid composites using pure and 1056 aluminum powders prepared through microwave and conventional heating methods. *Journal of Alloys and Compounds*, **690**, 512–8.
[107] Sethi, J., Das, S. and Das, K. (2019) Study on thermal and mechanical properties of yttrium tungstate-aluminium nitride reinforced aluminium matrix hybrid composites. *Journal of Alloys and Compounds*, **774**, 848–55.
[108] Tang, F., Wu, X., Ge, S., Ye, J., Zhu, H., Hagiwara, M. et al. (2008) Dry sliding friction and wear properties of B_4C particulate-reinforced Al-5083 matrix composites. *Wear*, **264**, 555–61.
[109] Mohammad Sharifi, E., Karimzadeh, F. and Enayati, M.H. (2011) Fabrication and evaluation of mechanical and tribological properties of boron carbide reinforced aluminum matrix nanocomposites. *Materials and Design*, **32**, 3263–71.
[110] Shabani, M.O. and Mazahery, A. (2011) Prediction of wear properties in A356 matrix composite reinforced with B_4C particulates. *Synthetic Metals*, **161**, 1226–31.
[111] Rajesh, G.L., Auradi, V. and Kori, S.A. (2016) Mechanical behaviour and dry sliding wear properties of ceramic boron carbide particulate reinforced Al6061 matrix composites. *Transactions of the Indian Ceramic Society*, **75**, 112–9.
[112] Nieto, A., Yang, H., Jiang, L. and Schoenung, J.M. (2017) Reinforcement size effects on the abrasive wear of boron carbide reinforced aluminum composites. *Wear*, **390**–**391**, 228–35.
[113] Singh, R., Shadab, M., Dash, A. and Rai, R.N. (2019) Characterization of dry sliding wear mechanisms of AA5083/B_4C metal matrix composite. *Journal of the Brazilian Society of Mechanical Sciences and Engineering*, **41**, 98.
[114] Shinde, D.M., Poria, S. and Sahoo, P. (2020) Dry sliding wear behavior of ultrasonic stir cast boron carbide reinforced aluminium nanocomposites. *Surface Topography: Metrology and Properties*, **8**, 025033.
[115] Hynes, N.R.J., Raja, S., Tharmaraj, R., Pruncu, C.I. and Dispinar, D. (2020) Mechanical and tribological characteristics of boron carbide reinforcement of AA6061 matrix composite. *Journal of the Brazilian Society of Mechanical Sciences and Engineering*, **42**, 155.
[116] Nagaral, M., Deshapande, R.G., Auradi, V., Boppana, S.B., Dayanand, S. and Anilkumar, M.R. (2021) Mechanical and wear characterization of ceramic boron carbide-reinforced Al2024 alloy metal composites. *Journal of Bio- and Tribo-Corrosion*, **7**, 1–12.
[117] Saessi, M., Alizadeh, A. and Abdollahi, A. (2021) Wear behavior and dry sliding tribological properties of ultra-fine grained Al5083 alloy and boron carbide-reinforced Al5083-based composite at room and elevated temperatures. *Transactions of Nonferrous Metals Society of China*, **31**, 74–91.
[118] Lee, D., Kim, J., Lee, S.K., Kim, Y., Lee, S.B. and Cho, S. (2021) Effect of boron carbide addition on wear resistance of aluminum matrix composites fabricated by stir casting and hot rolling processes. *Metals*, **11**, 989.
[119] V a, A.B., R, S., V, B., Auradi, V. and Nagaral, M. (2022) Mechanical and wear

characterisation of boron carbide particles reinforced Al2030 alloy composites developed by two stage stir cast method. *Advances in Materials and Processing Technologies*, **8,** 4320–34.

[120] Sarkar, S., Mohan, S. and Panigrahi, S.C. (2008) Effect of particle distribution on the properties of aluminum matrix in-situ particulate composites. *Journal of Reinforced Plastics and Composites*, **27**, 1177–87.

[121] Sarkar, S., Lohar, A.K. and Panigrahi, S.C. (2009) Vertical centrifugal casting of aluminum matrix particle reinforced composites. *Journal of Reinforced Plastics and Composites*, **28**, 1013–20.

[122] Rasidhar, L., Krishna, A.R. and Rao, C.S. (2013) Fabrication and investigation on properties of ilmenite ($FeTiO_3$) based Al-nanocomposite by stir casting process. *International Journal of Bio-Science and Bio-Technology*, **5**, 193–9.

[123] Rasidhar, L., Ramakrishna, A. and Rao, S.C. (2013) Experimental investigation on mechanical properties of ilmenite based Al nanocomposites. *International Journal of Engineering Science and Technology*, **5**, 1025–30.

[124] Rasidhar, L., Krishna, A.R., Rao, C.S. and Lakshmi, K.V. (2014) Development and evaluation of mechanical properties of Al/ilmenite nanocomposite. *Applied Mechanics and Materials*, **704**, 32–8.

[125] Thirumalai Kumaran, S. and Uthayakumar, M. (2014) Investigation on the dry sliding friction and wear behavior of AA6351-SiC-B_4C hybrid metal matrix composites. *Proceedings of the Institution of Mechanical Engineers, Part J: Journal of Engineering Tribology*, **228**, 332–8.

[126] Show, B.K., Mondal, D.K. and Maity, J. (2014) Dry sliding wear behavior of aluminum-based metal matrix composites with single (Al_2O_3) and hybrid (Al_2O_3+SiC) reinforcements. *Metallography, Microstructure, and Analysis*, **3**, 11–29.

[127] Muley, A. V, Aravindan, S. and Singh, I.P. (2015) Mechanical and tribological studies on nano particles reinforced hybrid aluminum based composite. *Manufacturing Review*, **2**, 26–34.

[128] Singh, G. and Goyal, S. (2018) Dry sliding wear behaviour of AA6082-T6/SiC/B_4C hybrid metal matrix composites using response surface methodology. *Proceedings of the Institution of Mechanical Engineers, Part L: Journal of Materials: Design and Applications*, **232**, 952–64.

[129] Ekka, K.K., Chauhan, S.R. and Varun. (2016) Study on the sliding wear behaviour of hybrid aluminium matrix composites using Taguchi design and neural network. *Proceedings of the Institution of Mechanical Engineers, Part L: Journal of Materials: Design and Applications*, **230**, 537–49.

[130] Das, D.K., Mishra, P.C., Singh, S. and Pattanaik, S. (2014) Fabrication and heat treatment of ceramic- reinforced aluminium matrix composites - A review. *International Journal of Mechanical and Materials Engineering*, **1**, 1–15.

[131] Fenghong, C., Chang, C., Zhenyu, W., Muthuramalingam, T. and Anbuchezhiyan, G. (2019) Effects of silicon carbide and tungsten carbide in aluminium metal matrix composites. *Silicon*, **11**, 2625–32.

[132] Suresh, S., Gowd, G.H. and Kumar, M.L.S.D. (2019) Mechanical and wear behavior of Al 7075/Al_2O_3/SiC/mg metal matrix nanocomposite by liquid state process. *Advanced Composites and Hybrid Materials*, **2**, 530–9.

[133] AM, R., Kaleemulla, M., Doddamani, S. and KN, B. (2019) Material characterization of SiC and Al_2O_3–reinforced hybrid aluminum metal matrix composites on wear behavior. *Advanced Composites Letters*, **28**, 1–10.

[134] Hillary, J.J.M., Ramamoorthi, R. and Chelladurai, S.J.S. (2020) Dry sliding wear behaviour of Al6061-5%SiC-TiB_2 hybrid metal matrix composites synthesized by stir

casting process. *Materials Research Express*, **7**, 126519.
[135] Pranavi, U., Reddy, P.V., Venukumar, S. and Cheepu, M. (2022) Evaluation of mechanical and wear properties of Al5059/B4C/Al_2O_3 hybrid metal matrix composites. *Journal of Composites Science*, **6**, 86.
[136] Das, S., Das, K. and Das, S. (2009) Abrasive wear behavior of Al-4.5 wt% Cu/(zircon sand+silicon carbide) hybrid composite. *Journal of Composite Materials*, **43**, 2665–72.
[137] Rajmohan, T., Palanikumar, K. and Ranganathan, S. (2013) Evaluation of mechanical and wear properties of hybrid aluminium matrix composites. *Transactions of Nonferrous Metals Society of China*, **23**, 2509–17.
[138] Patel, S.K., Kumar, R. and Nateriya, R. (2014) Microstructural analysis, micro hardness and tensile strength of silicon carbide and zirconium silicate dual reinforced particle ADC-12 alloy composite. *International Journal of Applied Science and Engineering Research*, **3**, 723–33.
[139] Arif, S., Alam, M.T., Ansari, A.H., Shaikh, M.B.N. and Siddiqui, M.A. (2018) Analysis of tribological behaviour of zirconia reinforced Al-SiC hybrid composites using statistical and artificial neural network technique. *Materials Research Express*, **5**, 056506.
[140] Palanikumar, K., Eaben Rajkumar, S. and Pitchandi, K. (2019) Influence of primary B_4C particles and secondary mica particles on the wear performance of Al6061/B_4C/mica hybrid composites. *Journal of Bio- and Tribo-Corrosion*, **5**, 1–12.
[141] Sharma, S., Singh, J., Gupta, M.K., Mia, M., Dwivedi, S.P., Saxena, A. et al. (2021) Investigation on mechanical, tribological and microstructural properties of Al-Mg-Si-T6/SiC/muscovite-hybrid metal-matrix composites for high strength applications. *Journal of Materials Research and Technology*, **12**, 1564–81.
[142] Kishore, G., Parthiban, A., Krishnan, A.M., Krishnan, B.R. and Vijayan, V. (2021) Experimental investigation of mechanical and wear properties of AL7075/Al_2O_3/MICA hybrid composite. *Journal of Inorganic and Organometallic Polymers and Materials*, **31**, 1026–34.
[143] Ahamad, N., Mohammad, A., Sadasivuni, K.K. and Gupta, P. (2021) Wear, optimization and surface analysis of Al-Al_2O_3-TiO_2 hybrid metal matrix composites. *Proceedings of the Institution of Mechanical Engineers, Part J: Journal of Engineering Tribology*, **235**, 93–102.
[144] Hariharan, S.R., Mahendran, S., Meignanamoorthy, M. and Ravichandran, M. (2022) Microstructure, mechanical and wear behavior of LM24/SiC/MoS_2 hybrid composites produced via liquid metallurgy process. *Surface Topography: Metrology and Properties*, **10**, 015015.
[145] Maleki, A., Niroumand, B. and Shafyei, A. (2006) Effects of squeeze casting parameters on density, macrostructure and hardness of LM13 alloy. *Materials Science and Engineering: A*, **428**, 135–40.
[146] Hosseini, V.A., Shabestari, S.G. and Gholizadeh, R. (2013) Study on the effect of cooling rate on the solidification parameters, microstructure, and mechanical properties of LM13 alloy using cooling curve thermal analysis technique. *Materials & Design*, **50**, 7–14.
[147] Maleki, A., Shafyei, A. and Niroumand, B. (2009) Effects of squeeze casting parameters on the microstructure of LM13 alloy. *Journal of Materials Processing Technology*, **209**, 3790–7.
[148] Abdou, M.I., Al-Sabagh, A.M., Ahmed, H.E. and Fadl, A.M. (2018) Impact of barite and ilmenite mixture on enhancing the drilling mud weight. *Egyptian Journal of Petroleum*, **27**, 955–67.
[149] Poovazhagan, L., Kalaichelvan, K. and Sornakumar, T. (2016) Processing and

performance characteristics of aluminum-nano boron carbide metal matrix nanocomposites. *Materials and Manufacturing Processes*, **31**, 1275–85.
[150] Singh, G. and Goyal, S. (2018) Microstructure and mechanical behavior of AA6082-T6/SiC/B_4C-based aluminum hybrid composites. *Particulate Science and Technology*, **36**, 154–61.
[151] Gates, J.D., Dargusch, M.S., Walsh, J.J., Field, S.L., Hermand, M.J.P., Delaup, B.G. et al. (2008) Effect of abrasive mineral on alloy performance in the ball mill abrasion test. *Wear*, **265**, 865–70.
[152] Cueva, G., Sinatora, A., Guesser, W.L. and Tschiptschin, A.P. (2003) Wear resistance of cast irons used in brake disc rotors. *Wear*, **255**, 1256–60.
[153] Seong, H.G., Lopez, H.F., Robertson, D.P. and Rohatgi, P.K. (2008) Interface structure in carbon and graphite fiber reinforced 2014 aluminum alloy processed with active fiber cooling. *Materials Science and Engineering A*, **487**, 201–9.
[154] Tham, L.M., Gupta, M. and Cheng, L. (2001) Effect of limited matrix-reinforcement interfacial reaction on enhancing the mechanical properties of aluminium-silicon carbide composites. *Acta Materialia*, **49**, 3243–53.
[155] Molinari, A., Lonardelli, I., Demetrio, K. and Menapace, C. (2010) Effect of the particle size on the thermal stability of nanostructured aluminum powder: Dislocation density and second-phase particles controlling the grain growth. *Journal of Materials Science*, **45**, 6739–46.
[156] Wu, J.H., Yen, M.S., Kuo, M.C. and Chen, B.H. (2013) Physical properties and crystallization behavior of silica particulates reinforced poly(lactic acid) composites. *Materials Chemistry and Physics*, **142**, 726–33.
[157] Saghafian, H., Shabestari, S.G., Ghadami, S. and Ghoncheh, M.H. (2017) Effects of iron, manganese, and cooling rate on microstructure and dry sliding wear behavior of LM13 aluminum alloy. *Tribology Transactions*, **60**, 888–901.
[158] Lasa, L. and Rodriguez-Ibabe, J.M. (2003) Wear behaviour of eutectic and hypereutectic Al-Si-Cu-Mg casting alloys tested against a composite brake pad. *Materials Science and Engineering A*, **363**, 193–202.
[159] Karantzalis, A.E., Lekatou, A., Georgatis, E. and Mavros, H. (2010) Solidification behaviour of ceramic particle reinforced Al-alloy matrices. *Journal of Materials Science*, **45**, 2165–73.
[160] Clauser, C. and Huenges, E. (1995) Thermal conductivity of rocks and minerals. *Rock Physics and Phase Relations: A Handbook of Physical Constants*, **3**, 105–26.
[161] Grasso, S., Hu, C., Vasylkiv, O., Suzuki, T.S., Guo, S., Nishimura, T. et al. (2011) High-hardness B_4C textured by a strong magnetic field technique. *Scripta Materialia*, **64**, 256–9.
[162] Karantzalis, A.E., Lekatou, A., Georgatis, E., Poulas, V. and Mavros, H. (2010) Microstructural observations in a cast Al-Si-Cu/TiC composite. *Journal of Materials Engineering and Performance*, **19**, 585–90.
[163] Kim, J.K. and Rohatgi, P.K. (2000) Nucleation on ceramic particles in cast metal-matrix composites. *Metallurgical and Materials Transactions A*, **31**, 1295–304.
[164] Ravikumar, K., Kiran, K. and Sreebalaji, V.S. (2017) Characterization of mechanical properties of aluminium/tungsten carbide composites. *Measurement*, **102**, 142–9.
[165] Shen, Y.L., Williams, J.J., Piotrowski, G., Chawla, N. and Guo, Y.L. (2001) Correlation between tensile and indentation behavior of particle-reinforced metal matrix composites: An experimental and numerical study. *Acta Materialia*, **49**, 3219–29.
[166] Linton, J., Navrotsky, A. and Fei, Y. (1998) The thermodynamics of ordered perovskites on the $CaTiO_3$-$FeTiO_3$ join. *Physics and Chemistry of Minerals*, **25**, 591–6.
[167] Tiwari, S., Das, S. and Ch, V.A.N. (2019) Mechanical properties of Al–Si–SiC

composites. *Materials Research Express*, **6**, 076553.
[168] Jiang, T., Li, S., Yu, C., Fu, J., Wei, B., Luo, L. et al. (2019) The evolution on the microstructure and thermal expansion behavior of Al–50Si alloy with different P contents. *Journal of Materials Science: Materials in Electronics*, **30**, 6786–94.
[169] Lalet, G., Kurita, H., Heintz, J.M., Lacombe, G., Kawasaki, A. and Silvain, J.F. (2014) Thermal expansion coefficient and thermal fatigue of discontinuous carbon fiber-reinforced copper and aluminum matrix composites without interfacial chemical bond. *Journal of Materials Science*, **49**, 397–402.
[170] Ren, S., He, X., Qu, X., Humail, I.S. and Li, Y. (2007) Effect of Mg and Si in the aluminum on the thermo-mechanical properties of pressureless infiltrated SiC_p/Al composites. *Composites Science and Technology*, **67**, 2103–13.
[171] Zhang, Q., Wu, G., Jiang, L. and Chen, G. (2003) Thermal expansion and dimensional stability of Al-Si matrix composite reinforced with high content SiC. *Materials Chemistry and Physics*, **82**, 780–5.
[172] Wang, J.T., Xie, L., Wang, Z.G., Gu, H., Luo, K.Y., Lu, Y.L. et al. (2020) Influence of laser shock peening on the coefficient of thermal expansion of Al (7075)-based hybrid composites. *Journal of Alloys and Compounds*, **844**, 156088.
[173] Habibnejad-korayem, M., Mahmudi, R., Ghasemi, H.M. and Poole, W.J. (2010) Tribological behavior of pure Mg and AZ31 magnesium alloy strengthened by Al_2O_3 nano-particles. *Wear*, **268**, 405–12.
[174] Xiao, P., Gao, Y., Xu, F., Yang, C., Li, Y., Liu, Z. et al. (2018) Tribological behavior of in-situ nanosized TiB_2 particles reinforced AZ91 matrix composite. *Tribiology International*, **128**, 130–9.
[175] Chen, H. and Alpas, A.T. (2000) Sliding wear map for the magnesium alloy Mg-9Al-0.9Zn (AZ91). *Wear*, **246**, 106–16.
[176] Zhou, H., Yao, P., Xiao, Y., Fan, K., Zhang, Z., Gong, T. et al. (2019) Friction and wear maps of copper metal matrix composites with different iron volume content. *Tribiology International*, **132**, 199–210.
[177] Hosseini, N., Karimzadeh, F., Abbasi, M.H. and Enayati, M.H. (2012) A comparative study on the wear properties of coarse-grained Al6061 alloy and nanostructured Al6061-Al_2O_3 composites. *Tribology International*, **54**, 58–67.
[178] Nemati, N., Emamy, M., Penkov, O. V, Kim, J. and Kim, D. (2016) Mechanical and high temperature wear properties of extruded Al composite reinforced with $Al_{13}Fe_4$ CMA nanoparticles. *Materials and Design*, **90**, 532–44.
[179] Mandal, D., Dutta, B.K. and Panigrahi, S.C. (2004) Wear and friction behavior of stir cast aluminium-base short steel fiber reinforced composites. *Wear*, **257**, 654–64.
[180] Jerome, S., Ravisankar, B., Mahato, P.K. and Natarajan, S. (2010) Synthesis and evaluation of mechanical and high temperature tribological properties of in-situ Al-TiC composites. *Tribology International*, **43**, 2029–36.
[181] Chang, F., Gu, D., Dai, D. and Yuan, P. (2015) Selective laser melting of in-situ Al4SiC4+SiC hybrid reinforced Al matrix composites: Influence of starting SiC particle size. *Surface & Coatings Technology*, **272**, 15–24.
[182] Rajaram, G., Kumaran, S., Rao, T.S. and Kamaraj, M. (2010) Studies on high temperature wear and its mechanism of Al–Si/graphite composite under dry sliding conditions. *Tribology International*, **43**, 2152–8.
[183] Zhou, Z., Liu, X., Zhuang, S., Yang, X., Wang, M. and Sun, C. (2019) Preparation and high temperature tribological properties of laser in-situ synthesized self-lubricating composite coatings containing metal sulfides on Ti6Al4V alloy. *Applied Surface Science*, **481**, 209–18.
[184] Nyanor, P., El-Kady, O., Yehia, H.M., Hamada, A.S., Nakamura, K. and Hassan, M.A.

(2021) Effect of carbon nanotube (CNT) content on the hardness, wear resistance and thermal expansion of in-situ reduced gaphene oxide (rGO)-reinforced aluminum matrix composites. *Metals and Materials International*, **27**, 1315–26.

[185] Giovanni, M.T. Di, Menezes, J.T.O. De, Cerri, E. and Castrodeza, E.M. (2020) Influence of microstructure and porosity on the fracture toughness of Al-Si-Mg alloy. *Journal of Materials Research and Technology*, **9**, 1286–95.

[186] Torres, H., Varga, M., Adam, K. and Ripoll, M.R. (2016) The role of load on wear mechanisms in high temperature sliding contacts. *Wear*, **364**–**365**, 73–83.

[187] Kumar, S., Sharma, A., Arora, R. and Pandey, O.P. (2019) The microstructure and wear behaviour of garnet particle reinforced Al matrix composites. *Journal of Materials Research and Technology*, **8**, 5443–55.

[188] Hayun, S., Dilman, H., Dariel, M.P. and Frage, N. (2009) The effect of aluminum on the microstructure and phase composition of boron carbide infiltrated with silicon. *Materials Chemistry and Physics*, **118**, 490–5.

[189] Sujith, S. V., Kim, H., Mulik, R.S., Park, H. and Lee, J. (2022) Synergistic effect of in-situ Al-7075/Al_3Ti metal matrix composites prepared via stir-assisted ultrasonic melt processing under dynamic nucleation. *Metals and Materials International*, **28**, 2288–303.

[190] Wannasin, J. and Flemings, M.C. (2005) Fabrication of metal matrix composites by a high-pressure centrifugal infiltration process. *Journal of Materials Processing Technology*, **169**, 143–9.

[191] Prasad, D.S., Shoba, C. and Ramanaiah, N. (2014) Investigations on mechanical properties of aluminum hybrid composites. *Journal of Materials Research and Technology*, **3**, 79–85.

[192] Nyanor, P., El-Kady, O., Yehia, H.M., Hamada, A.S. and Hassan, M.A. (2021) Effect of bimodal-sized hybrid TiC–CNT reinforcement on the mechanical properties and coefficient of thermal expansion of aluminium matrix composites. *Metals and Materials International*, **27**, 753–66.

[193] Yan, Y. and Geng, L. (2007) Effects of particle size on the thermal expansion behavior of SiC_p/Al composites. *Journal of Materials Science*, **42**, 6433–8.

[194] Gao, H. and Huang, Y. (2001) Taylor-based nonlocal theory of plasticity. *International Journal of Solids and Structures*, **38**, 2615–37.

[195] He, T., Lu, T., Ciftci, N., Tan, H., Uhlenwinkel, V., Nielsch, K. et al. (2020) Mechanical properties and tribological behavior of aluminum matrix composites reinforced with Fe-based metallic glass particles: Influence of particle size. *Powder Technology*, **361**, 512–9.

[196] Bhowmik, A., Dey, D. and Biswas, A. (2022) Characteristics study of physical, mechanical and tribological behaviour of SiC/TiB_2 dispersed aluminium matrix composite. *Silicon*, **14**, 1133–46.

[197] Samal, P., Mandava, R.K. and Vundavilli, P.R. (2020) Dry sliding wear behavior of Al 6082 metal matrix composites reinforced with red mud particles. *SN Applied Sciences*, **2**, 313–23.

[198] Jojith, R. and Radhika, N. (2019) Mechanical and tribological properties of LM13/TiO_2/MoS_2 hybrid metal matrix composite synthesized by stir casting. *Particulate Science and Technology*, **37**, 570–82.

[199] Lin, F., Wang, J., Wu, H., Jia, F., Lu, Y., Ren, M. et al. (2021) Synergistic effects of TiC and graphene on the microstructure and tribological properties of Al2024 matrix composites. *Advanced Powder Technology*, **32**, 3635–49.

[200] Zamani, N.A.B.N., Iqbal, A.A. and Nuruzzaman, D.M. (2020) Tribo-mechanical characterization of self-lubricating aluminium based hybrid metal matrix composite

fabricated via powder metallurgy. *Materialia*, **14**, 100936.
[201] Manikandan, R., Arjunan, T. V. and P, A.R.N.O. (2020) Studies on micro structural characteristics, mechanical and tribological behaviours of boron carbide and cow dung ash reinforced aluminium (Al 7075) hybrid metal matrix composite. *Composites Part B: Engineering*, **183**, 107668.
[202] Bolelli, G. and Lusvarghi, L. (2006) Heat treatment effects on the tribological performance of HVOF sprayed Co-Mo-Cr-Si coatings. *Journal of Thermal Spray Technology*, **15**, 802–10.
[203] Lanzutti, A., Lekka, M., de Leitenburg, C. and Fedrizzi, L. (2019) Effect of pulse current on wear behavior of Ni matrix micro-and nano-SiC composite coatings at room and elevated temperature. *Tribology International*, **132**, 50–61.
[204] Torgerson, T.B., Harris, M.D., Alidokht, S.A., Scharf, T.W., Aouadi, S.M., Chromik, R.R. et al. (2018) Room and elevated temperature sliding wear behavior of cold sprayed Ni-WC composite coatings. *Surface and Coatings Technology*, **350**, 136–45.
[205] Bolelli, G. and Lusvarghi, L. (2007) Tribological properties of HVOF as-sprayed and heat treated Co-Mo-Cr-Si coatings. *Tribology Letters*, **25**, 43–54.
[206] Chen, W., Feng, P., Dong, L., Ahangarkani, M., Ren, S. and Fu, Y. (2018) The process of surface carburization and high temperature wear behavior of infiltrated W-Cu composites. *Surface and Coatings Technology*, **353**, 300–8.